University of Canterbury

Ph.D Thesis

Parameterized effective Hamiltonians as a diagnostic tool for *ab initio* analyses of lanthanide crystal field effects

Author:
Alexander J. Salkeld

Supervisor:
Prof. Mike Reid

Co-supervisor:
Prof. Jon-Paul Wells

Submitted in Partial Fulfillment of the Requirements for the Degree
Doctor of Philosophy in Physics

February 28, 2016

Abstract

Parameterised effective Hamiltonians are fitted to *ab initio* energy level calculations of a number of lanthanide materials, in order to extract the equivalent spectroscopic parameters from the *ab initio* models, particularly from the $4f^{n-1}5d$ excited configurations.

By studying parameter variations as a function of impurity–ligand separation in $SrCl_2$:Yb^{2+}, $CsCaBr_3$:Yb^{2+}, and CaF_2:Yb^{2+}, a number of trends are observed. The Coulomb and d spin–orbit parameters exhibit variation with impurity–ligand separation which is attributed to the nephelauxetic effect. The crystal field parameters can be shown to vary with power–law dependence in many of the calculations. In $SrCl_2$:Yb^{2+}, this power–law variation is observed to exactly match the point–charge model for the crystal field. An inaccuracy is also identified at the spin–free level of calculation for this material, where the crystal field influence described by the *ab initio* model decreases with increased ligand proximity, rather than increasing as is expected physically.

Effective Hamiltonian parameters are fitted to an experimental excitation spectrum for CaF_2:Yb^{2+}. These values are compared to the extracted *ab initio* parameters. The *ab initio* parameters are observed to overstate the strengths of the Coulomb interaction, and the d crystal field.

Parameters for $4f^n$+$4f^{n-1}5d$ effective Hamiltonians are fitted to the *ab initio* energy levels of several lanthanide systems of greater complexity: Lu_2O_3:Pr^{3+}, CaF_2:Pr^{3+}, BaF_2:Tb^{3+}, and CaF_2:Eu^{2+}. The Coulomb parameters, and in particular the F^2 Coulomb parameter, tend towards large values in most of these systems, indicating that further corrections due to the missing electron correlation effects from the Hartree–Fock calculations are required. The α electron correlation parameter extracted from the *ab initio* calculations is typically 2–3 times the size of those fitted to experimental levels. This is suggested to be the result of the *ab initio* calculation potentially overlooking important contributions to the electron correlation from continuum states.

Acknowledgements

There are many people to whom I owe gratitude for their contributions and support, which have allowed me to reach this milestone.

I am particularly indebted to my supervisors Prof. Mike Reid and Prof. Jon-Paul Wells, whose guidance, support and direction have been central to the completion of this thesis. They have dedicated many hours to this project, answered my questions, encouraged me, chased me down when necessary, and assisted wherever they can.

I could not have asked for better supervisors.

To my fellow colleagues of this research group, Dr. Pubudu Senanayake, Dr. Rosa Hughes-Currie, and Dr. Konstantin Ivanovskikh: thank you for being a part of this journey, and it has been a pleasure working with you.

I give thanks for the contributions of Zoila Barandiarán, Luis Seijo, and Goar Sánchez-Sanz, who so kindly made data from their *ab initio* calculations available for our analyses.

The support of the Department of Physics and Astronomy at the University of Canterbury is acknowledged, for the provision of a departmental scholarship and teaching opportunities.

To the many denizens and frequenters of Office 713, and its subsequent incarnation as Office 601: you have all helped make this journey an interesting and enjoyable one. Our various discussions, "Cake Friday" gatherings, and assorted hijinks have all helped maintain a little sanity, punctuating the extensive amount of hard work that was happening, of course!

Many thanks go to Sebastian Horvath and Alex Neiman for the number of consultations on physics, computer code, and whatever else was going wrong at the time.

Special thanks to Lancia Hubley for proofreading this thesis, and to Chrissy Emeny and Alana Hyland for supplying large quantities of thesis–cookies, and writing–survival food.

Lastly, a great many thanks to my parents and family, who have provided their love and support for me throughout my studies. I could not have achieved this without the motivation and encouragement you provide.

To survive a thesis:

Beat two eggs with 200 g (1 cup) of sugar until thick and creamy. Melt 125 g of butter with 60 g (1/2 cup) of cocoa. Stir gently into the egg/sugar mixture with 40 g (1/3 cup) of flour. Pour into a lined cake tin and bake at 170 °C for 30 minutes, or until just–cooked when tested with a skewer.

Contents

List of Figures

List of Tables

Chapter 1

Introduction

Semi–empirical parameterised effective Hamiltonian calculations have been useful computational tools to reproduce and predict the observed energy level structure of a wide range of materials, including the spectra of transition and rare earth ions [1]. Full first principles, or *ab initio*, approaches to calculations have typically lagged behind empirical approaches in their usefulness [2, 3], due in part to the computational complexity, even for fairly simple systems. However, modern computing lifts these restrictions, and *ab initio* analyses are now not only possible on f–shell materials, but are also able to reasonably accurately reproduce observed spectral features [4–6].

In this thesis we explore the use of semi–empirical effective Hamiltonian energy level calculations as a diagnostic tool for the interpretation of *ab initio* quantum chemistry energy level calculations. By empirically fitting a parameterised effective Hamiltonian to the energy levels of the *ab initio* calculation, we can extract the equivalent physical parameters from these calculations. This allows us to take advantage of the transferability and predictive power of the physical parameters [7] in the analysis of the *ab initio* calculations, where the values of these physical parameters are not typically exposed directly. The parameters also allow us to compare the calculation to experimental observations at a lower level than to the whole observed spectra or energy levels, and to parameters of similar materials [8].

In this thesis, we apply this diagnostic tool to a number of published *ab initio* studies. The first group of *ab initio* studies focus on the modelling of an impurity–trapped exciton state and the $5d$ levels with which it interacts. This exciton state is a feature that occurs in a number of materials containing divalent europium or ytterbium ions. The equiva-

lent physical parameters for these models are extracted from the *ab initio* calculations. Secondly, we explore a series of *ab initio* calculations for lanthanide materials with an increasing complexity of parameterised description (that is, an increasingly filled f electron shell), in order to test the equivalent physical parameters of these calculations. These calculations all contain $4f^{n-1}5d$ excited configurations, from which we aim to extract the effective Hamiltonian parameters, as these parameters frequently cannot be fitted to experimental observations.

1.1 Lanthanide phosphors and spectroscopy

The lanthanide series is comprised of the elements with atomic numbers 57 – 71 (lanthanum to lutetium). These elements form the bulk of the rare earth metals – the remainder being the elements with atomic number 21 (scandium) and 39 (yttrium). The lanthanide ions typically have trivalent oxidation states, with the valence orbitals occuring in the $4f$ shell (with the exception of lutetium, which has a d valence shell). Additionally, europium and ytterbium readily form divalent oxidation states, and some lanthanides have higher oxidation states. These materials have an abundance of optically–active energy levels, which makes them useful in a wide variety of applications, such as laser and scintillator materials [9, 10], medical imaging [10], as candidates for usage in quantum memory storage [11], and in nanoparticle–based medical applications [12], to name a few.

An understanding of the processes and interactions present in these materials is essential, in order to design or select a material to suit the intended role. The lanthanides have been the subject of extensive studies in order to examine and catalog these physical properties, from spectroscopy of single lanthanides in a collection of hosts [15, 16], to assays of the entire series of lanthanide ions [13, 17–22]. Figure 1.1 demonstrates one such study by Carnall et al. [13]. Here, the $4f^N$ energy levels for the entire series of lanthanide ions are presented. This format of presentation is based on a compilation of spectra of the trivalent lanthanide ions in a $LaCl_3$ host by Dieke [17], and is called a Dieke diagram. The energy levels here are calculated from parameters fitted to observed spectra of the lanthanides doped as substitutional impurities into a LaF_3 host lattice [13].

One of the properties of the lanthanide ions is that the $4f^N$ valence orbitals lie closer to the nucleus than the full–shell $5s$ and $5p$ orbitals. This is demonstrated in Figure 1.2, using computed radial probability distributions for the electron shells of an ytterbium ion, from Cowan's RCN code [23]. These full outer shells effectively shield the $4f$ valence orbitals

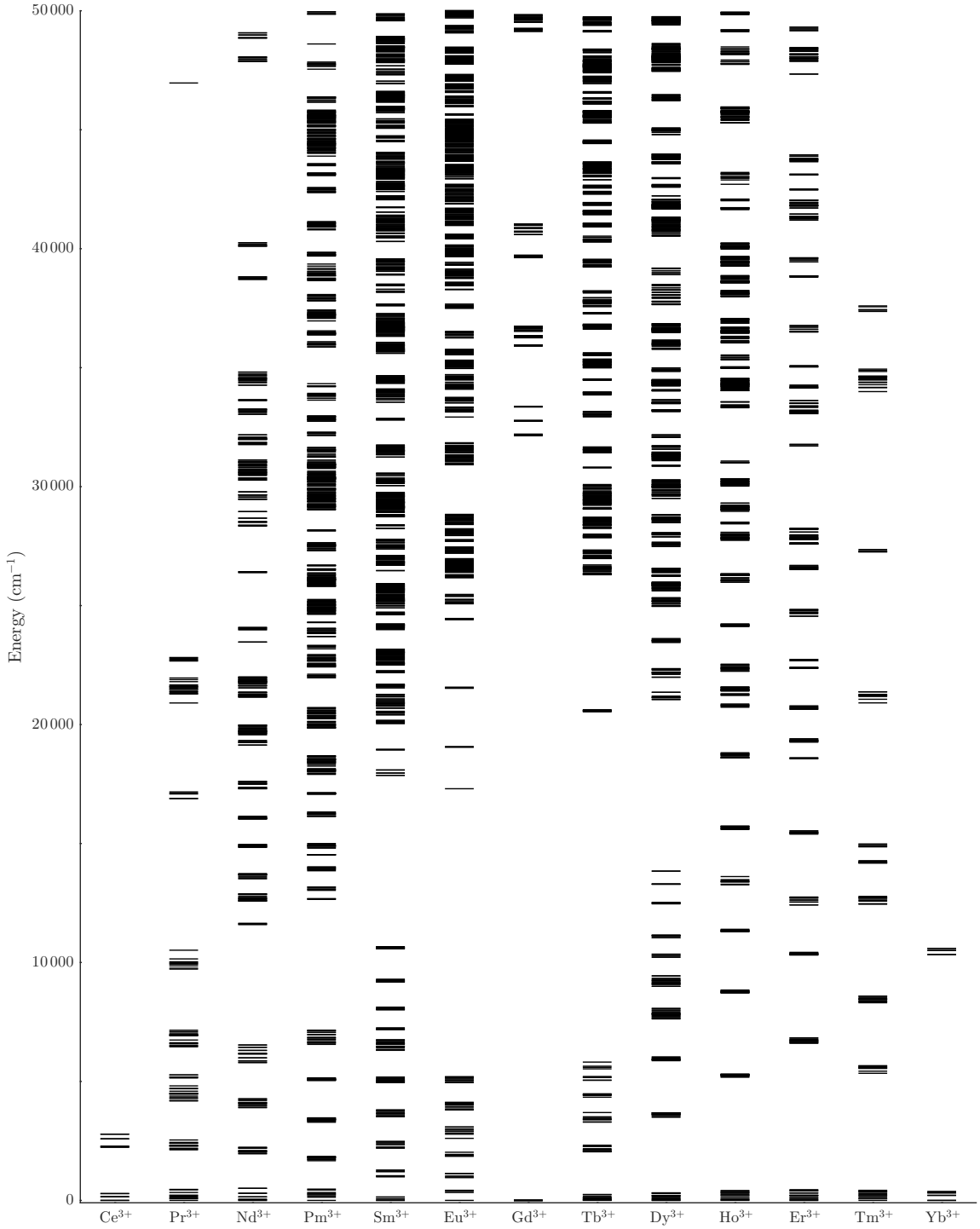

Figure 1.1 A Dieke diagram generated using energy levels calculated by the parameters of Carnall et al., from spectroscopic studies of trivalent lanthanide ions embedded in LaF_3 [13, 14].

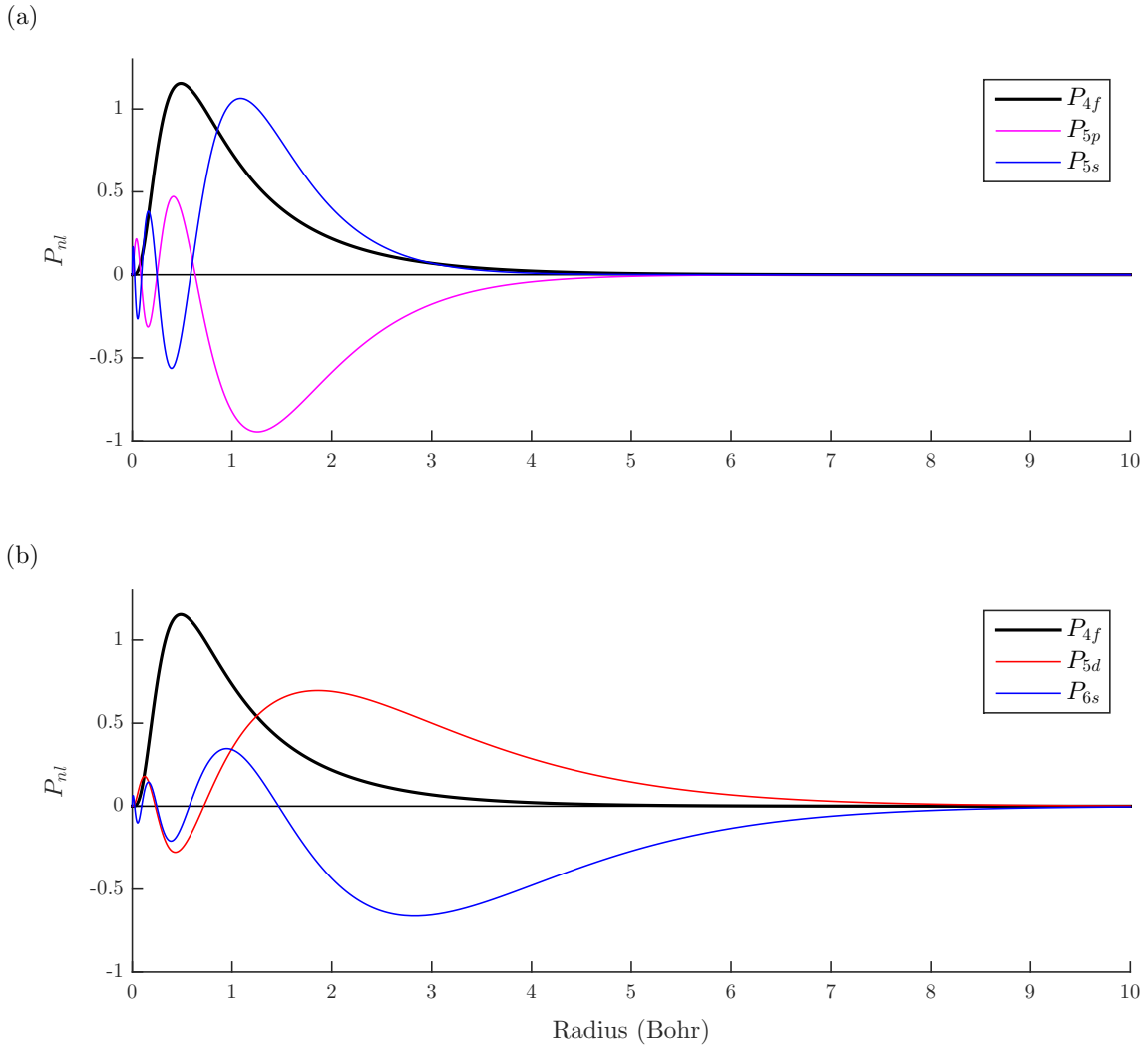

Figure 1.2 Hartree–Fock radial wavefunction distributions for a free Yb^{2+} ion, calculated using R. D. Cowan's RCN code [23]. The radial distribution is defined in Equation 2.13. (a) The $4f$, $5p$ and $5s$ electron orbitals of the ground state ion. The $5s$ and $5p$ orbitals are completely occupied, and the electrons spend a large amount of time, probabilistically, further from the nucleus than the $4f$ electrons. This partially shields the $4f$ electrons from outlying charges, such as any excited electrons of the same atom, or charges of a neighbouring atom. The strength of interaction with these external charges is effectively decreased by this shielding. (b) The $4f$, $5d$ and $6s$ excited state electron orbitals of the Yb^{2+} ion. The change in the $4f$ orbital shape between ground and excited states is negligible. The excited electron orbitals have a small overlap with the $4f$ orbital. They exist considerably further from the nucleus, with maxima occuring beyond the maxima of the full–shell $n = 5$ electron orbitals.

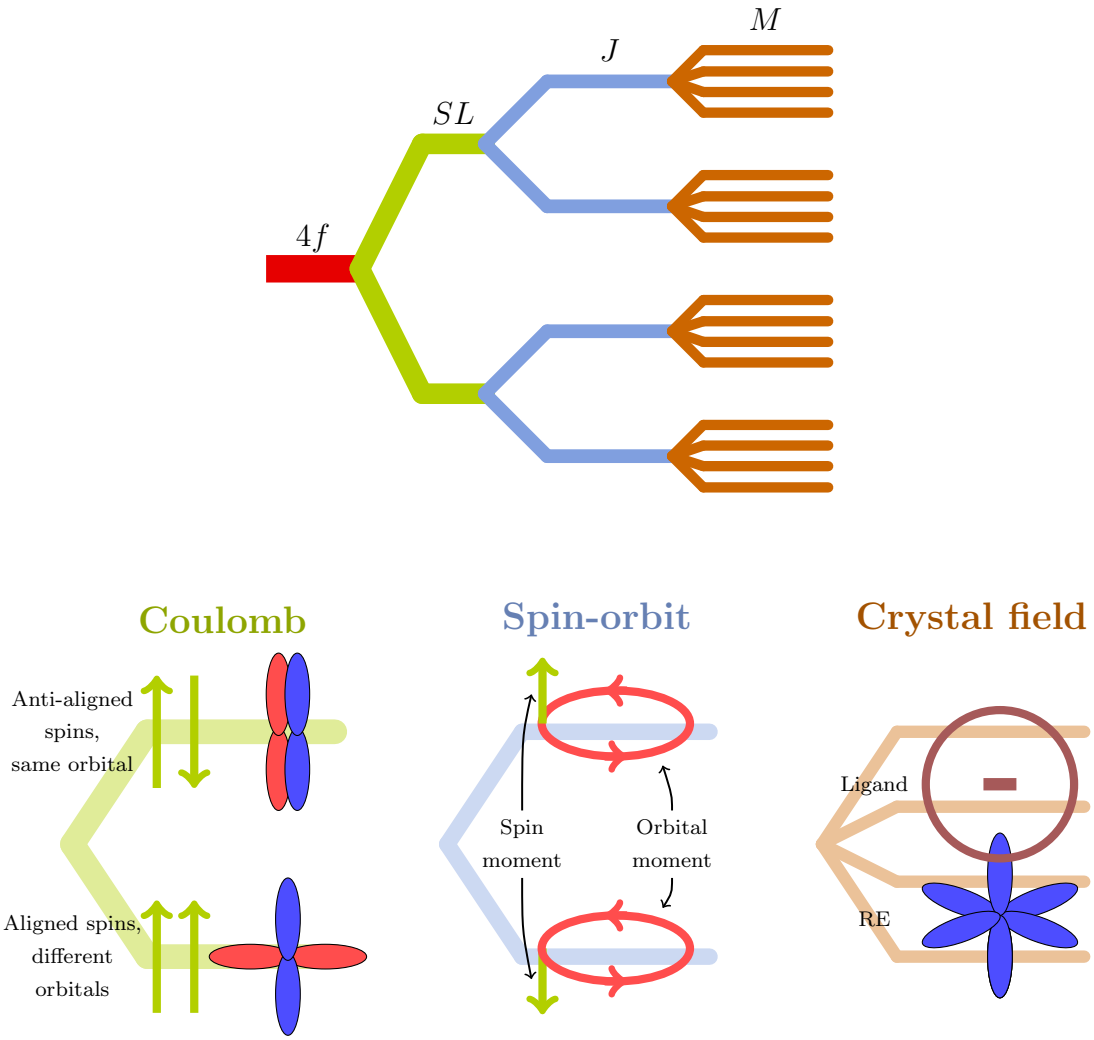

Figure 1.3 A schematic of a $4f^N$ configuration energy level splitting, by interaction type. The strongest electron interactions for the $4f^N$ configuration are usually Coulomb interactions. By Hund's rules, it is energetically favourable to align electron spins in different orbitals, rather than to pair electrons into the same orbital. The spin–orbit interactions are typically the next strongest interactions. Lastly, the Coulombic interactions between the $4f$ electrons and the ligands, the so–called crystal field, splits the energy levels based on the symmetry of the impurity site. These are typically weak interactions, as the $4f$ valence shell is shielded from the host lattice by the full $5s$ and $5p$ shells. The schematic is based on a figure by Reid [24].

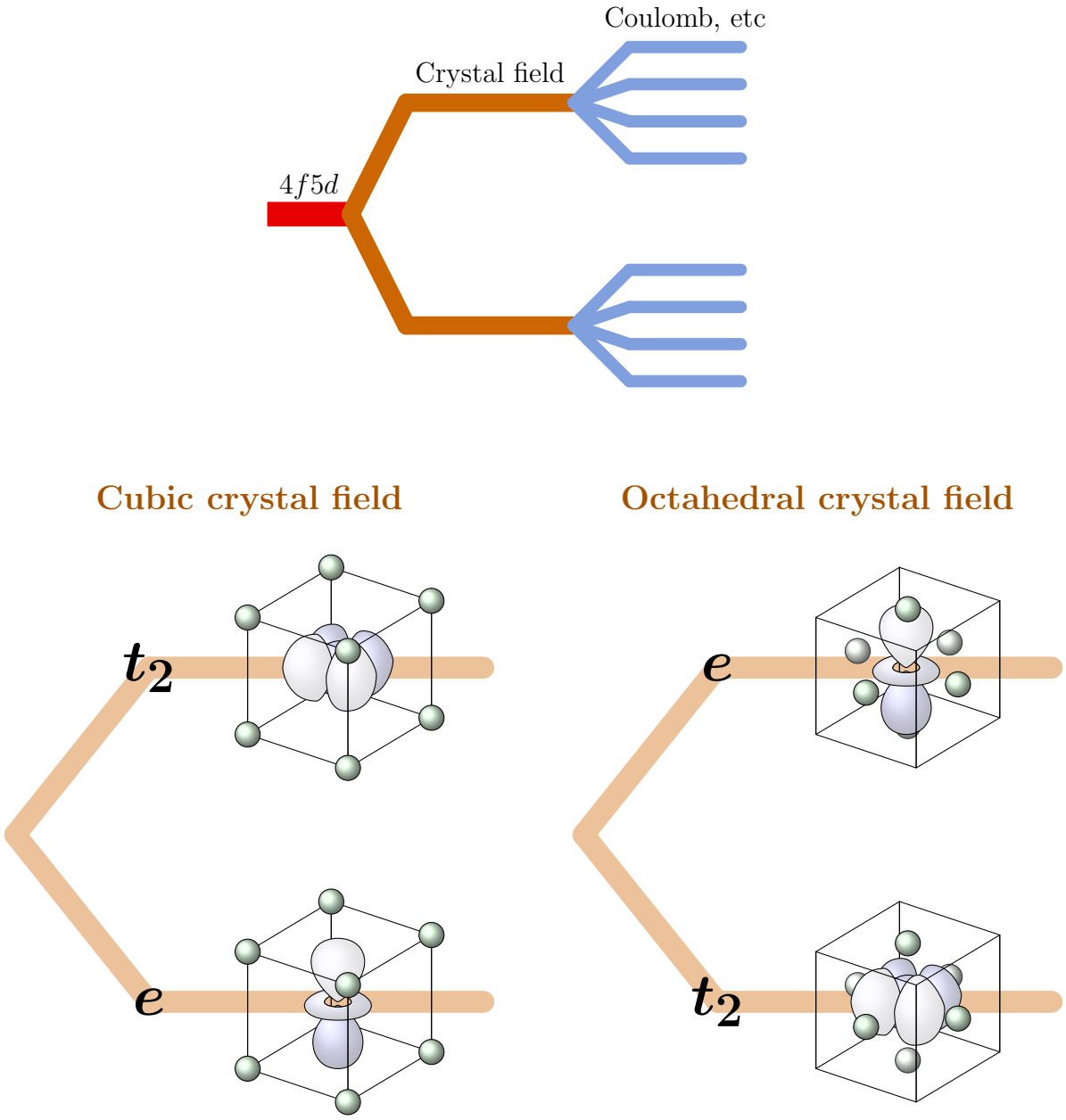

Figure 1.4 A schematic of a $4f^{N-1}5d$ configuration energy level splitting, by interaction type. The strongest electron interactions for the $4f5d$ configuration are usually the d crystal field interactions, as the d electron is more delocalised than the full $5s$ and $5p$ shells, and hence interacts strongly with the host. Which d crystal field orbital is energetically favourable is determined by the symmetry of the impurity site. Under cubic or octahedral symmetry the d crystal field splits the energy levels into e and t_2 irreducible representations (irreps). Under cubic symmetry, the t_2 irrep orbitals are closer to the ligands, and hence have a stronger interaction with them, and are therefore higher in energy. Under octahedral symmetry, the reverse is true. The shapes of all d orbitals in an octahedral host can be found in Figure 2.13 of Henderson and Imbusch [1]. The schematic is based on a figure by Reid [24].

from most interactions with any neighbouring ligands, meaning that the lanthanide $4f$ levels have similar interactions with a variety of host materials. The strongest interactions experienced by these electrons are typically the Coulomb interactions within the $4f$ shell, followed by the spin–orbit interactions of each individual electron in the shell. Each of these interactions break the degeneracy of the $4f$ electrons, as is demonstrated in Figure 1.3. The interpretation of each of these interactions will be discussed in detail in the next chapter.

The excited state configurations, for example $4f^{N-1}5d$ or $4f^{N-1}6s$, have a valence electron in an orbital which extends far beyond the full shells, and hence interacts very strongly with the host environment. Frequently, this interaction with the host material will be the strongest interaction in the configuration. This is illustrated in Figure 1.4.

1.1.1 Impurity–trapped excitons

One of the features of the lanthanide materials that is not yet fully understood are the trap states that cause the anomalous emission observed in some materials containing divalent europium or ytterbium as dopants. These materials display a characteristic anomalous broad emission band, instead of the expected emission bands from the d levels to the ground f configurations. These have been the subject of many studies [25–32], attempting to explain the presence of this anomalous emission band. Some interpretations offered have included a charge transfer processes [33], a Jahn-Teller distortion [34], and the impurity–trapped exciton model [9, 25, 27]. There is also a contention that the anomalous emission band is due to an intervalence charge transfer process between clustered Yb^{2+} and Yb^{3+} ions [35].

The impurity–trapped exciton consists of a bound electron/hole pair, with the hole trapped in the valence f shell of the impurity ion. Upon excitation of an electron to the $5d$ shell, this exciton state can be formed by a non–radiative process, where the $5d$ electron becomes delocalised from the impurity. This is observed in host materials with a band–gap such that the $5d$ levels lie close to, or partially in, the conduction band of the host material [15]. The hole is unable to move around the lattice, as the ions neighbouring the impurity site typically do not have equivalent valence orbitals from which to source an electron (unless the concentration of impurity ions is sufficiently high that clusters may form). The impurity ion is effectively ionised, but not to the extent that the electron is completely dissociated from the ion. Instead, the electron exists in a highly delocalised

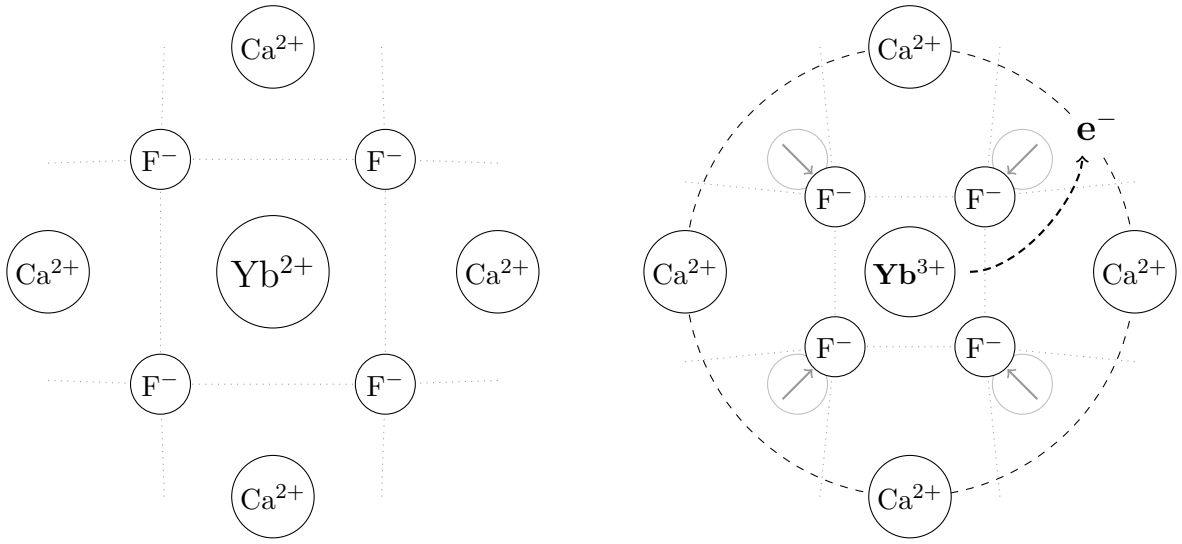

Figure 1.5 A schematic of an impurity–trapped electron in CaF_2:Yb^{2+}. The lanthanide impurity is effectively ionised by the displacement of the electron, except the electron remains loosely bound to the Yb^{3+} ion, existing in an extended orbital across the next–nearest neighbour metal cations, Ca^{2+}. The schematic is based on Figure 3e of Dorenbos [27].

orbital, distributed across the next–nearest–neighbour cations in the host lattice. The contraction of the lattice around the higher–charge ion is consistent with the Stokes shift observed in the broad emission band [28]. A schematic of this model is demonstrated in Figure 1.5, based on Figure 3e of Dorenbos [27]. A schematic of the energy structure of the exciton in CaF_2 is presented in Figure 1.6, based on the work of Moine et al. [28–31]. This structure of trap state can also be observed in the actinide series, and has been reproduced by *ab initio* calculation methods [36].

The exciton state itself has a very long radiative lifetime, on the order of a few milliseconds. Evidence for the presence of higher energy exciton states with much faster radiative decay rates was discovered by Moine et al. [28, 30], and explored in detail in an excited state absorption experiment [37–40].

1.2 The parameterised effective Hamiltonian

Theoretical calculations of electronic energy level structure and simulated spectra are frequently–used tools to aid in the interpretation, and understanding, of experimental observations. Parameterised effective Hamiltonian operators provide a piece–by–piece

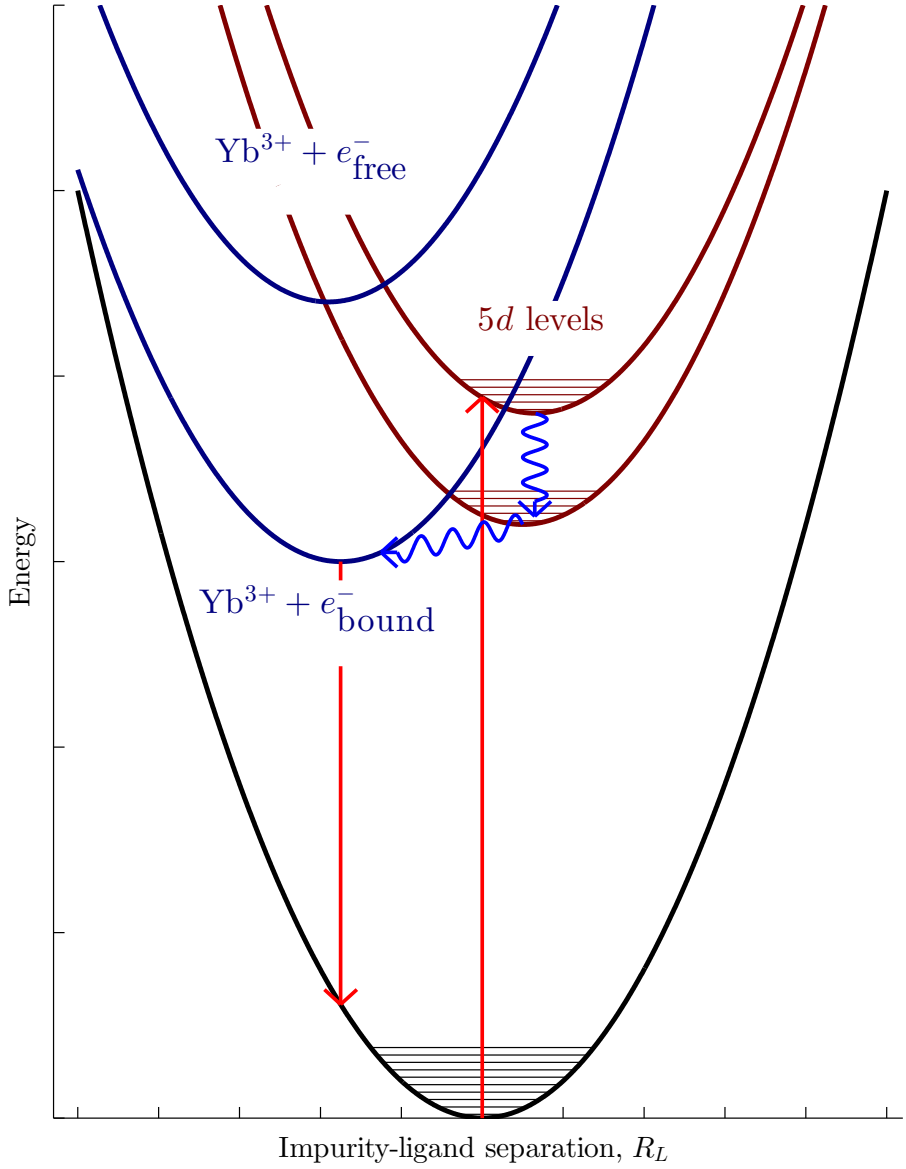

Figure 1.6 Energy diagram of an impurity–trapped electron in CaF_2:Yb^{2+}. Upon excitation to the excited $4f^{13}5d$ configuration, the excited electron relaxes non–radiatively to a $5d$ state which has a forbidden transition to the ground configuration. The electron instead becomes delocalised in an extended orbital across the next–nearest neighbour metal cations, tunneling into the energetically favourable exciton state. The impurity–ligand separation of this state is almost equivalent to that of Yb^{3+}, so effectively, the exciton is a delocalised electron bound to a Yb^{3+} ion. The schematic is based on the work of Moine et al. [28–31].

decomposition of the contributing physical interactions present in the observed spectra. A useful property of these parameters is the presence of clear trends in behaviour as electron shells are filled. This provides the ability to reliably predict the expected properties of new materials, based on analyses of similar materials [7, 8, 20].

While in theory, any observable system should be able to be reproduced precisely by a spanning set of arbitrary operators, the advantage to parameterising physical interactions is immediately obvious, as these provide a directly comparable measure of the strengths or weights of the physical interactions. The drawback however, is that after a fitting process, the individual contributions of interactions towards a parameter cannot be distinguished (for example, the interactions that contribute purely diagonal terms to the Hamiltonian).

The parametric approach has been in use since the 1930s [41], with the methods introduced by Slater and Bethe in 1929 (for atomic spectra, and crystal fields respectively [1, 41]), and treated using conventional quantum mechanics in Condon and Shortley's *The Theory of Atomic Spectra* [42]. The techniques, at this stage, were still extremely involved for complicated systems containing many electrons in valence shells. The introduction of tensor operators, coefficients of fractional parentage, and the application of group theory techniques by Racah, in the 1940s, allowed for much more efficient calculations, particularly with regards to the complexity that f–shell atoms otherwise presented [41]. Advances have continued to have been made, with the addition of correction terms whenever a deficiency in the method has been encountered. Such terms include configuration interaction corrections, magnetic coupling of the spin and orbital angular momenta between pairs of electrons, and the introduction of electron correlation terms. This theory shall be discussed in detail in the next chapter.

1.3 *Ab initio* calculations

The alternative to the semi–empirical approach is to use first principles or *ab initio* formalisms. Instead of fitting parameters empirically, these approaches rely upon an adequate quantum mechanical description of the system. A typical *ab initio* calculation method starts with a Hartree–Fock calculation – that is, the basis for the system is optimised using iterative methods, until self–consistency is achieved [43]. Corrections for the assumptions made by the Hartree–Fock method are then applied, using these resulting basis functions. Each level of correction brings the system closer to the true solution to the Schrödinger equation, and for a sufficiently large basis, the system can converge to

the true solution. The drawback to these methods is the computational cost. The system of coeffecients being optimised at some levels of the calculations can easily consist of on the order of 10^5 parameters [43].

Due to this large requirement in computational resources, *ab initio* approaches were typically overlooked in favour of semi–empirical processes [2, 3]. With advances in modern computing, however, *ab initio* calculations are increasingly viable for more complicated systems. Several recent studies successfully reproduce observed spectral features of f-shell materials [4–6, 44], including actinides [36, 45], and very large molecules or chemical systems [43].

One of the useful features for comparisons of the semi–empirical effective Hamiltonian calculations is the ability to individually examine the constituent interactions of the Hamiltonian. As the solution for the *ab initio* calculation is obtained for the entire Hamiltonian in an iterative process, the contributions from individual interactions are not explicitly calculated.

It is possible to directly calculate the crystal field parameters from *ab initio* energy levels and eigenvectors for simple systems, such as trivalent cerium ions [8, 46], as this system only has a single valence electron, and hence, a minimal number of parameters. This method has been applied to a number of fluoride crystals [47], the YSO crystal [48], and has also been used to calculate intensity parameters [49]. Direct calculation of crystal field parameters is useful when the number of energy levels of the configuration of interest is comparable or less than the number parameters, which precludes the use of empirical fitting methods. This is, however, very difficult for more complicated systems, due to the increasing number of electrons present, and hence complexity of the electron interactions.

As an alternative, it is possible to extract the physical parameters from *ab initio* energy levels by empirical means, if the number of energy levels is sufficiently large, as demonstrated by Duan et al. [50]. Typically, the *ab initio* calculations will provide a very large number of energy levels, and this makes them ideal candidates to provide reference energy levels for the empirical fitting processes. This can potentially allow us to fit parameters which cannot be fitted to observed spectra, such as is typical for $4f^{N-1}5d$ configuration parameters, owing to the lack of observed levels from these states.

1.4 Outline

This work aims to explore the use of parameterised effective Hamiltonian operators as a diagnostic tool to explore the physical interpretation of first principles or *ab initio* energy level calculations, and simulated spectra. Parameterisation of physical interactions allows for a direct means of comparison between calculations for similar lanthanide ions, or host materials; or to experimental observations.

The chapters in this thesis are arranged as follows:

- Chapter 2 is a review of the theory required to perform the semi–empirical effective Hamiltonian energy level calculations. All terms of the effective Hamiltonian and their physical interpretation are introduced.
- Chapter 3 presents the calculation process used throughout this thesis, and the code contributed for the purpose of labelling states in this project. The simulation of absorption spectra is also discussed, and a brief overview is given of the quantum chemical software package, MOLCAS, which is used in most of the reference *ab initio* calculations.
- Chapter 4 provides details of calculations of two materials containing divalent ytterbium ions: $SrCl_2$ and $CsCaBr_3$. Effective Hamiltonian parameters are extracted from *ab initio* energy level calculations for these materials, both from the calculated vibronic potential curve minima, and from instantaneous vertical transitions at a number of impurity–ligand separations. These parameters are compared with existing semi–empirical parameter calculations of these materials.
- Chapter 5 provides details of the fitting of effective Hamiltonian parameters to experimental CaF_2:Yb^{2+} spectra, and the extraction of parameters from *ab initio* calculations of the same material. The parameters are used to recreate the absorption spectra by simulation.
- Chapter 6 provides details of the extraction of fd configuration parameters from La_2O_3:Pr^{3+}, Lu_2O_3:Pr^{3+}, CaF_2:Pr^{3+}, BaF_2:Tb^{3+}, and CaF_2:Eu^{2+}. These materials represent an increasing complexity of lanthanide system, compared to the effectively–two–electron divalent ytterbium system, where semi–empirical approaches to reproducing the energy level structure of experimental observations are limited by the complexity of these systems. Comparisons are made between the extracted parameters, and those calculated from theoretical definitions.

- Finally, in Chapter 7, we shall summarise the analyses of the previous chapters and discuss the contribution made to this field of study by the work in this thesis.

Chapter 2

Background theory

In addition to experimental observations of optical processes in rare–earth elements doped into host materials, it is useful to have a means of determining the expected or observed behaviour from a theoretical viewpoint. Optical processes in these materials depend upon the energy level structure of the rare–earth dopant. These energy levels can be calculated purely theoretically, from first principles or *ab initio* treatments of the system. Alternatively, a semi–empirical approach can be taken, using a parameterised effective Hamiltonian, and predicted parameters based on previous analyses of similar dopants or host materials. Furthermore, the parameters can be fitted to experimental observations of the energy level structure to allow empirical measurements of these parameters to be made.

This chapter briefly reviews the rather extensive theory on effective Hamiltonian calculations, focussing on the aspects that are of particular relevance to this thesis. The notation used here is primarily that of Cowan [23], and Lindgren and Morrison [51]. Other sources, such as Wybourne [3], Judd [41], Henderson and Imbusch [1], Weissbluth [52], Liu [14], and Newman and Ng [2], also provide equivalent interpretations.

We shall cover the definitions of terms used in the subsequent theory; the definition and construction of effective Hamiltonians; and the calculation of matrix elements and corresponding parameters for both single– and many–valence–electron systems.

We shall also discuss some of the limitations to aspects of the effective Hamiltonian construction.

2.1 Definitions

2.1.1 n–j symbols

The terms in this theory make use of the geometric properties of Wigner's 3–j and 6–j symbols. The 3–j symbol is defined in terms of Clebsch–Gordon (vector coupling) coefficients:

$$\begin{pmatrix} j_1 & j_2 & j_3 \\ m_1 & m_2 & m_3 \end{pmatrix} = (-1)^{j_1-j_2-m_3} \left(2j_3+1\right)^{-1/2} \langle j_1 m_1, j_2 m_2 | j_3 \; -m_3 \rangle \,. \tag{2.1}$$

The actual computation of this symbol is shown in appendix A.1. The 3–j symbol will be zero unless $m_1 + m_2 + m_3 = 0$, and the triangular condition, $|j_1 - j_2| \leq j_3 \leq j_1 + j_2$, is met.

The 6–j symbol is used for coupling three angular momenta, j_1, j_2, j_3, together to a resultant momenta, J, and can be defined in terms of the coupling coefficients for this:

$$\begin{aligned} &\langle (j_1 j_2)\, J_{12}, j_3,\; J \mid j_1, (j_2 j_3)\, J_{23},\; J \rangle \\ &\qquad = (-1)^{j_1+j_2+j_3+J} \left[(2J_{12}+1)\,(2J_{23}+1)\right]^{1/2} \begin{Bmatrix} j_1 & J_{12} & j_2 \\ j_3 & J_{23} & J \end{Bmatrix}, \end{aligned} \tag{2.2}$$

where the coefficients recouple between states where j_1 and j_2 are coupled together first, and where j_2 and j_3 are coupled together first. The calculation of the 6–j symbol values are shown in appendix A.1.

The 6–j symbol,

$$\begin{Bmatrix} j_1 & j_2 & j_3 \\ j_4 & j_5 & j_6 \end{Bmatrix},$$

is zero unless the following triangular conditions are met:

$$\begin{aligned} |j_1 - j_2| \leq j_3 \leq j_1 + j_2 \\ |j_4 - j_5| \leq j_3 \leq j_4 + j_5 \\ |j_4 - j_2| \leq j_6 \leq j_4 + j_2 \\ |j_1 - j_5| \leq j_6 \leq j_1 + j_5. \end{aligned} \tag{2.3}$$

Lastly, the 9–j symbol is used to couple four angular momenta together. It is particularly useful in changing between LS coupling and jj coupling. For example, in a two–electron

system the coefficients between LS and jj coupling are given by:

$$\begin{aligned}&\langle (s_1 s_2)\, S,\, (l_1 l_2)\, L,\, J \mid (s_1 l_1)\, j_1,\, (s_2 l_2)\, j_2,\, J \rangle \\ &\qquad = \left[(2j_1+1)\,(2j_2+1)\,(2S+1)\,(2L+1)\right]^{1/2} \begin{Bmatrix} s_1 & s_2 & S \\ l_1 & l_2 & L \\ j_1 & j_2 & J \end{Bmatrix}\end{aligned} \tag{2.4}$$

Again, the calculation of this symbol is given in appendix A.1.

2.1.2 Wigner–Eckart theorem

The Wigner–Eckart theorem separates a physical process into a part which depends solely upon the symmetry, and a part that depends upon the physical interaction [52]. For example, using a single operator, acting upon a single angular momentum state:

$$\left\langle \gamma j m \mid t^k_q \mid \gamma' j' m' \right\rangle = (-1)^{j-m} \begin{pmatrix} j & k & j' \\ -m & q & m' \end{pmatrix} \left\langle \gamma j \mid\mid \mathbf{t}^k \mid\mid \gamma' j' \right\rangle . \tag{2.5}$$

Here, the symmetry is contained within the 3–j symbol, and the physical interaction is described by the reduced matrix element, $\left\langle \gamma j \mid\mid \mathbf{t}^k \mid\mid \gamma' j' \right\rangle$. The value of the reduced matrix element is typically easily computed, or found in existing tabulations.

Using the Wigner–Eckart theorem, the matrix elements of the frequently used Racah spherical tensors, $\mathbf{C}^k$, are given by:

$$\begin{aligned}\left\langle lm \middle| C^k_q \middle| l' m' \right\rangle &= \sqrt{\frac{4\pi}{2k+1}} \int Y^l_m(\Omega)^*\, Y^k_q(\Omega)\, Y^{l'}_{m'}(\Omega)\, d\Omega \\ &= (-1)^{l-m} \begin{pmatrix} l & k & l' \\ -m & q & m' \end{pmatrix} \left\langle l \middle|\middle| \mathbf{C}^k \middle|\middle| l' \right\rangle .\end{aligned} \tag{2.6}$$

The reduced matrix element, $\left\langle l \middle|\middle| \mathbf{C}^k \middle|\middle| l' \right\rangle$, is independent of m quantum numbers, and is defined:

$$\left\langle l \middle|\middle| \mathbf{C}^k \middle|\middle| l' \right\rangle = (-1)^l \left[(2l+1)\,(2l'+1)\right]^{1/2} \begin{pmatrix} l & k & l' \\ 0 & 0 & 0 \end{pmatrix} . \tag{2.7}$$

2.1.3 Coupling tensors to operators of specified rank

We can use the Wigner–Eckart theorem to easily determine matrix elements for coupled operators acting upon coupled states. This is a useful result, as both the Coulomb and

spin–orbit operators can be expressed in terms of coupled operators. To evaluate reduced matrix elements for coupled tensor operators acting upon coupled states, we use the expression [51]:

$$\left\langle (\gamma_1 j_1 \gamma_2 j_2)\, J \mid\mid \left\{ \mathbf{t}^{k_1}(1)\, \mathbf{u}^{k_2}(2) \right\}^K \mid\mid (\gamma_1' j_1' \gamma_2' j_2')\, J' \right\rangle = \left\langle \gamma_1 j_1 \mid\mid \mathbf{t}^{k_1} \mid\mid \gamma_1' j_1' \right\rangle \left\langle \gamma_2 j_2 \mid\mid \mathbf{u}^{k_2} \mid\mid \gamma_2' j_2' \right\rangle \times \left((2J+1)(2K+1)(2J'+1) \right)^{1/2} \begin{Bmatrix} j_1 & j_1' & k_1 \\ j_2 & j_2' & k_2 \\ J & J' & K \end{Bmatrix}. \tag{2.8}$$

For the case where $K = 0$, the operator coupling is the scalar product between the operators. In this case, the matrix elements become [51]:

$$\begin{aligned} &\left\langle (\gamma_1 j_1 \gamma_2 j_2)\, JM \mid\ \mathbf{t}^k(1) \cdot \mathbf{u}^k(2) \mid (\gamma_1' j_1' \gamma_2' j_2')\, J'M' \right\rangle \\ &= (-1)^{j_1' + j_2 + J}\, \delta(J, J')\, \delta(M, M') \begin{Bmatrix} j_1 & j_1' & k \\ j_2' & j_2 & J \end{Bmatrix} \left\langle \gamma_1 j_1 \mid\mid \mathbf{t}^k \mid\mid \gamma_1' j_1' \right\rangle \left\langle \gamma_2 j_2 \mid\mid \mathbf{u}^k \mid\mid \gamma_2' j_2' \right\rangle. \end{aligned} \tag{2.9}$$

2.2 Energy level calculations

A calculation of the energy level structure of a dopant ion in a given material requires that the Schrödinger equation for that system be solved:

$$H\psi_i = E_i \psi_i. \tag{2.10}$$

Here, H is the Hamiltonian operator describing all interactions of the system, ψ_i are the wavefunctions describing each possible electron state, and E_i are the energy eigenvalues corresponding to each ψ_i.

Describing a full quantum mechanical wavefunction of a system containing a large number of electrons is an inhibitively long process, even for an individual atom of sufficient size. To fully consider all electrons involved in a crystal lattice (or similarly, all electrons in a large molecule or compound) about an arbitrary centre of interest is highly impractical. It is also unnecessary, as in most cases the splittings of energy levels in the valence shells are all that need to be considered [23].

There are two possible approaches to performing energy level calculations: either using first principles (or *ab initio*) formalism, or using empirical methods. In the empirical approach, the physical interactions that comprise the Hamiltonian can be parameterised.

These parameters are varied to allow the resulting energy levels to be fitted to the energy levels of the observed spectra, providing an empirical solution. Typically an effective Hamiltonian is used, acting upon only a subset of the states of the full Hamiltonian. This subset is chosen to consist of the configurations of interest. This empirical approach relies upon the availability of a sufficient number of target energy levels, in order to allow the physical parameters to vary freely.

The fitting process is typically a least–squares fitting of the calculated energy levels compared to a selection of experimental or *ab initio* energy levels. The accuracy of the resultant fit can be described by the standard deviation:

$$\sigma = \sqrt{\frac{\sum \left(E_{\mathrm{calc},i} - E_{\mathrm{ref},i}\right)^2}{N - n}}, \tag{2.11}$$

where i indexes over all supplied energy levels, $E_{\mathrm{ref},i}$. The energy of the corresponding calculated level is $E_{\mathrm{calc},i}$. The quantities N and n are the number of supplied energy levels, and number of free parameters respectively.

The *ab initio* methods instead optimise the basis states of the Schrödinger equation in order to obtain a solution. As the basis set becomes sufficiently large, these methods can converge to the exact solution of the Schrödinger equation. Typical calculations can involve the optimisation of on the order of 10^5 coefficients [43].

2.2.1 The effective Hamiltonian

For a Hamiltonian H, with eigenstates ψ_i and eigenvalues E_i, an effective Hamiltonian H_{eff} is defined so that within a subspace of the space acted upon by the full Hamiltonian, it has eigenstates ϕ_i with the same eigenvalues as H:

$$\begin{aligned} H\psi_i &= E_i\psi_i, \\ H_{\mathrm{eff}}\phi_i &= E_i\phi_i. \end{aligned} \tag{2.12}$$

The effective Hamiltonian is constructed from a sum of orthogonal operators representing the interactions that occur in the system, acting upon the chosen eigenfunctions. The matrix elements of the operators correspond to the angular components of the interactions, while the weighting parameters measure the radial component of each interaction. This matrix representation is then diagonalised to provide the eigenvectors, and corresponding energy eigenvalues, for each state in the system.

In theory, an effective Hamiltonian should be able to be produced for any system, and be able to accurately reproduce the energies of the full Hamiltonian, given a sufficient number of orthogonal operators and parameters. In practice, we want to do so with the minimum number of parameters required to obtain a good reproduction of the energy levels of the full system, as having large numbers of free parameters can complicate the fitting process. This is especially noticeable when weakly defined parameters or interactions with very small contributions or corrections to the system are present [53].

2.2.2 Central–field approximation

Under the central–field model, all electrons experience a spherically symmetric Coulomb potential from the nucleus, and other electrons in the atom. This means that the distribution of probability density for an electron depends only upon the radial coordinate. Hence the wavefunctions (or spin–orbitals), ϕ_i, can be described by products of a radial probability density, a spherical harmonic function, and a spin state:

$$\phi_i(\mathbf{r}_i) = \frac{1}{r_i} P_{n_i l_i}(r_i) \cdot Y_{l_i m_{l_i}}(\theta_i \phi_i) \cdot \sigma_{m_{s_i}}(s_{i_z}), \tag{2.13}$$

where $\mathbf{r}_i = (r_i, \theta_i, \phi_i)$.

This approximation provides completely degenerate energy levels for each electron configuration. The interactions between electrons cause departures from this model, as they contain significant non–spherical effects. The effective Hamiltonian parameters provide a perturbation from this spherically symmetric approximation, to correct for these non–spherical interactions [51].

2.2.3 Effective Hamiltonian for singly–occupied electron orbitals

The effective Hamiltonian, in general, can be considered to be constructed from two parts:

$$H_{\text{eff}} = H_{\text{ion}} + H_{\text{CF}}. \tag{2.14}$$

The first is the effective Hamiltonian for a free ion, and the second is the so–called crystal field Hamiltonian, which incorporates the interactions between the ion and the host material in which the ion is imbedded.

2.2.3.1 The free–ion effective Hamiltonian

The initial part of this thesis deals with materials doped with divalent ytterbium. The ground state of divalent ytterbium has a fully occupied $4f$ valence shell. Since all valence electrons are fully degenerate, the ground state Hamiltonian, $H_{4f^{14}}$, is trivial.

The excited state, $4f^{13}5d^1$, has a single d electron and a hole in the f shell. The hole can be treated as a positively charged electron which simply has the effect of changing the sign of some matrix elements.

This system can be described by the N–electron Hamiltonian,

$$H = -\sum_i \nabla_i^2 - \sum_i \frac{2Z}{r_i} + \sum\sum_{i>j} \frac{2}{r_{ij}} + \sum_i \zeta_i(r_i)(\mathbf{l}_i \cdot \mathbf{s}_i). \tag{2.15}$$

This is simply the sum of all one–electron Hamiltonians, in addition to the Coulomb interaction between different electrons. This is expressed in Bohr units (a_0) for distances and rydbergs for energies. For the two–electron case, this Hamiltonian can be easily expressed in terms of a small number of parameters.

The first two terms in Equation 2.15 contribute only diagonal matrix elements, uniform for each configuration, to the Hamiltonian. Primarily, this controls where the barycentres, or average energies, of the configurations lie. This can be expressed:

$$H_{\text{config.}} = E_{\text{avg}} \cdot I + \Delta_E\left(fd\right)\delta_E\left(fd\right), \tag{2.16}$$

where E_{avg} is the energy of the $4f^{14}$ ground state, $\Delta_E\left(fd\right)$ is the difference in energy between the d electron configuration average and the ground state, and $\delta_E\left(fd\right)$ is a matrix for which the only non–zero elements are an identity matrix block for the d states.

The third term in Equation 2.15 is the Coulomb interaction between electrons, or in this case, the electron and hole. This contributes the following terms:

$$H_{\text{Coulomb}} = \sum_k F^k\left(fd\right) f_k\left(fd\right) + \sum_k G^k\left(fd\right) g_k\left(fd\right). \tag{2.17}$$

The last term in Equation 2.15 is the spin–orbit interaction. Additional magnetic interactions can occur between pairs of electrons occupying the same shell, contributing additional operators to the corresponding Hamiltonians. Part of the effect of these additional magnetic interactions is already included in this spin–orbit operator, so this is technically an *effective* spin–orbit operator.

There are two spin–orbit terms in the excited ytterbium system:

$$H_{\mathrm{so}} = \zeta\left(f\right) A_{\mathrm{so}}\left(f\right) + \zeta\left(d\right) A_{\mathrm{so}}\left(d\right), \tag{2.18}$$

corresponding to f spin–orbit and d spin–orbit interactions.

In Chapters 4 and 5, we will use an extended model which includes the $4f^{13}6s$ excited state, in addition to the $4f^{13}5d$ levels. This requires the addition of the following terms:

$$H_{4f^{13}6s^1} = \Delta_E\left(fs\right)\delta_E\left(fs\right) + G^3\left(fs\right) g_3\left(fs\right), \tag{2.19}$$

and

$$H_{\mathrm{CI}} = \sum_k R^k\left(fd\,fs\right) r_k\left(fd\,fs\right). \tag{2.20}$$

As with Equation 2.16, the $\Delta_E\left(fs\right)\delta_E\left(fs\right)$ term positions the average configuration energy for the s states. The $G^3\left(fs\right) g_3\left(fs\right)$ term is the only non–zero Coulomb interaction between the f and s orbitals. The last Hamiltonian operator, H_{CI}, provides the non–zero Coulomb terms that act between the fd configurations and the fs configurations. These terms are a form of configuration interaction (CI).

So far, this provides the free–ion effective Hamiltonian of Yb^{2+}. The last step is to construct the crystal field Hamiltonian.

2.2.3.2 The crystal field Hamiltonian

As the lanthanide ion is introduced as an impurity to a crystalline host, it has the same symmetry as the site which it occupies. The crystal field terms of the effective Hamiltonian decrease the symmetry of the spherically–symmetric free–ion Hamiltonian to the symmetry of the impurity site. This can significantly break the degeneracy of the energy levels, depending on the site symmetry involved.

The crystal field interactions in the effective Hamiltonian are written as a sum of spherical tensor operators,

$$H_{\mathrm{CF}} = \sum_{k,q} B_q^k C_q^{(k)}. \tag{2.21}$$

The B_q^k parameters represent the strengths of each interaction, and the $C_q^{(k)}$ operators are Racah spherical tensor operators. These are defined as

$$C_q^{(k)} = \sqrt{\frac{4\pi}{2k+1}} Y_{k,q}, \tag{2.22}$$

where $Y_{k,q}$ are spherical harmonic functions.

The combinations of k and q values that give non–zero matrix elements depends upon the symmetry of the impurity site. Additionally, the B_q^k parameters for $q < 0$ can be expressed in terms of the $q > 0$ parameters:

$$B_{-q}^k = (-1)^q \, B_q^{k*}. \tag{2.23}$$

For f electrons in octahedral site symmetry, there are only a few non–zero elements, and only two independent crystal field parameters [53–55]:

$$H_{\mathrm{CF}} = B^4 \left[C_0^{(4)} + \sqrt{\frac{5}{14}} \left(C_4^{(4)} + C_{-4}^{(4)} \right) \right] + B^6 \left[C_0^{(6)} - \sqrt{\frac{7}{2}} \left(C_4^{(6)} + C_{-4}^{(6)} \right) \right], \tag{2.24}$$

where the the ratios of $q = 0$ terms to the $q = \pm 4$ terms are required in order to maintain invariance under all rotation operations of the cubic group [3]. Lower symmetry sites require more terms to fully describe their effect upon the Hamiltonian. For example, S_6 site symmetry requires the crystal field Hamiltonian to be [14]:

$$\begin{aligned} H_{\mathrm{CF},\, S_6} = {} & B_0^2 C_0^{(2)} + B_0^4 C_0^{(4)} + \mathrm{Re}\left(B_3^4\right) \left(C_3^{(4)} - C_{-3}^{(4)} \right) + i \, \mathrm{Im}\left(B_3^4\right) \left(C_3^{(4)} + C_{-3}^{(4)} \right) \\ & + B_0^6 C_0^{(6)} + \mathrm{Re}\left(B_3^6\right) \left(C_3^{(6)} - C_{-3}^{(6)} \right) + i \, \mathrm{Im}\left(B_3^6\right) \left(C_3^{(6)} + C_{-3}^{(6)} \right) \\ & + \mathrm{Re}\left(B_6^6\right) \left(C_6^{(6)} + C_{-6}^{(6)} \right) + i \, \mathrm{Im}\left(B_6^6\right) \left(C_6^{(6)} - C_{-6}^{(6)} \right), \end{aligned} \tag{2.25}$$

involving parameters with real and imaginary components. To describe the lowest site symmetry, C_1, 27 parameters are required. A list of the required parameters for each site symmetry can be found in Table 1.7 of Liu and Jacquier [14, 56].

A useful quantity for comparing crystal field parameters between different host site symmetries is the scalar crystal field strength, N_ν, defined by Auzel and Malta [57]:

$$N_\nu = \left[\sum_{k,q} \left(B_q^k \right)^2 \left(\frac{4\pi}{2k+1} \right) \right]^{1/2}. \tag{2.26}$$

This quantity is a norm representing a distance in the space of the spherical harmonics Y_q^k [57]. As a scalar quantity, this can provide a means to easily compare crystal field interactions of different site symmetries, which cannot be directly compared otherwise, due to the differences in constituent crystal field parameters [57, 58].

2.2.3.3 The superposition model

The superposition model allows us to interpret the effect on an ion of each ligand associated with that ion individually, and that the combined influence of all ligands behaves

as a sum of the effects of the individual ligands. The effect of each individual ligand can be written in terms of an intrinsic crystal field parameter, $\overline{B}_k(R_L)$, which measures the strength of the interaction with reference to the axis formed by the ligand and the ion:

$$V_L = \sum_k \overline{B}_k(R_L)\, C_0^{(k)}. \tag{2.27}$$

This intrinsic parameter is independent of the actual geometry of the site symmetry, but can then be transformed in terms of axes based on the site symmetry of the ion, so that all ligand–ion interactions are directly comparable. This transformation allows the calculation of the B_q^k crystal field parameters from the individual intrinsic parameters of the ligands:

$$B_q^k = \sum_L \overline{B}_k(R_L)\, g_{k,q}(\theta_L, \phi_L), \tag{2.28}$$

where the coefficients are:

$$g_{k,q}(\theta_L, \phi_L) = (-1)^q\, C_{-q}^k(\theta_L, \phi_L), \tag{2.29}$$

which depend only on the geometry of the ligand relative to the axis of the site symmetry of the ion. These expressions can be found in reference [2].

If a point–charge electrostatic model is considered, the intrinsic parameter varies in R_L with a power–law dependence:

$$\overline{B}_k(R_L) = \overline{B}_k(R_0)\left(\frac{R_0}{R_L}\right)^{t_k}, \tag{2.30}$$

where, $t_2 = 3$, $t_4 = 5$, and $t_6 = 7$ [2, 14]. This is not observed experimentally, however. Actual observations for rare–earth ions with chloride ligands have shown the crystal field paramaters to have an R_L dependence described by the exponents $t_4 = 12 - 16$ and $t_6 = 5 - 7$ for a range of rare–earths [14, 59], indicating that the theoretical point–charge model does not adequately describe the effect of the crystal field.

2.2.4 Calculation of matrix elements and parameters for the two–electron, singly–occupied–valence system

2.2.4.1 Coulomb and configuration interaction terms

For a two–electron antisymmetric wavefunction, the Coulomb matrix elements of the effective Hamiltonian are given by:

$$\begin{aligned}\langle\phi \mid \frac{1}{r_{12}} \mid \phi\rangle = &\langle (n_a l_a)_1 (n_b l_b)_2 , SL|\frac{1}{r_{12}}| (n_a l_a)_1 (n_b l_b)_2 , SL\rangle \\ &+ (-1)^{l_a+l_b-L+S}\langle (n_a l_a)_1 (n_b l_b)_2 , SL|\frac{1}{r_{12}}| (n_a l_a)_2 (n_b l_b)_1 , SL\rangle, \end{aligned} \tag{2.31}$$

where the indices refer to the electron upon which the operator is acting.

The expression r_{12}^{-1} can be expanded in terms of spherical harmonic functions [51]:

$$\frac{1}{r_{12}} = \sum_k \frac{r_<^k}{r_>^{k+1}} \mathbf{C}^k (1) \cdot \mathbf{C}^k (2) . \tag{2.32}$$

We can use this expansion, and Equation 2.9, to write Equation 2.31 in terms of reduced matrix elements. The matrix elements on the RHS of Equation 2.31 are given by:

$$\begin{aligned}&\langle (n_a l_a)_1 (n_b l_b)_2 , SL|\frac{1}{r_{12}}| (n_c l_c)_1 (n_d l_d)_2 , SL\rangle \\ &= \sum_k R^k (l_a l_b, l_c l_d) (-1)^{l_c+l_d+L} \left\{ \begin{array}{ccc} l_a & l_b & L \\ l_c & l_d & k \end{array} \right\} \langle l_a \mid\mid \mathbf{C}^k \mid\mid l_c\rangle \langle l_b \mid\mid \mathbf{C}^k \mid\mid l_d\rangle \\ &= \sum_k r_k R^k (l_a l_b, l_c l_d) , \end{aligned} \tag{2.33}$$

where the coefficients, $R^k (l_a l_b, l_c l_d)$, are the Slater integrals:

$$R^k (l_a l_b, l_c l_d) = \int\int P_a (r_1) P_b (r_2) \frac{r_<^k}{r_>^{k+1}} P_c (r_1) P_d (r_2) dr_1 dr_2, \tag{2.34}$$

and, using Equation 2.7, the matrix elements, r_k, are:

$$\begin{aligned} r_k = &(-1)^{l_a-l_c+L} \left[(2l_a+1)(2l_b+1)(2l_c+1)(2l_d+1)\right]^{1/2} \\ &\times \left(\begin{array}{ccc} l_a & k & l_c \\ 0 & 0 & 0 \end{array} \right) \left(\begin{array}{ccc} l_b & k & l_d \\ 0 & 0 & 0 \end{array} \right) \left\{ \begin{array}{ccc} l_a & l_b & L \\ l_d & l_c & k \end{array} \right\} . \end{aligned} \tag{2.35}$$

Equation 2.31 only has diagonal terms, so $l_a = l_c$, and $l_b = l_d$. The corresponding Slater integrals which appear in the expression, $R^k (l_a l_b, l_a l_b)$ and $R^k (l_a l_b, l_b l_a)$, are called the direct and exchange parameters, and are labelled F^k and G^k, respectively. The corresponding r_k matrix elements are relabelled as f_k and g_k, as seen in Equation 2.17.

General elements referring to configurations with $l_a \neq l_c$ or $l_b \neq l_d$ measure the configuration–interaction strength. These interactions typically have very little influence on the overall effective Hamiltonian, as they consist solely of off–diagonal elements.

There are very few values of k for which there are non–zero matrix elements for any of the Coulomb interactions. These can be found by examining the triangular conditions for the the 6–j symbol (Equations 2.3). For example, we will calculate the configuration interaction matrix elements for the $4f^{13}6s$ and $4f^{13}5d$ orbitals in Chapter 4. Substituting in the appropriate angular momenta, we see from the triangular condition on the 6–j symbol that the only non–zero terms will be the $k = 2$ and $k = 3$ matrix elements.

Direct–like term:

$$\begin{aligned} r_k\left(fdfs\right) : |s - d| \leq k \leq s + d \\ 2 \leq k \leq 2 \end{aligned} \tag{2.36}$$

Exchange–like term:

$$\begin{aligned} r_k\left(fdsf\right) : |f - s| \leq k \leq f + s \\ 3 \leq k \leq 3 \end{aligned} \tag{2.37}$$

Similarly, for the fd Coulomb terms, non–zero f_k terms are limited to $k = 2, 4$ and g_k terms to $k = 1, 3, 5$.

2.2.4.2 Spin–orbit terms

From the definition in Equation 2.15, the spin–orbit matrix elements and parameters are given by:

$$\langle SLJM \mid \zeta_i\left(r_i\right)\left(\mathbf{l}_i \cdot \mathbf{s}_i\right) \mid S'L'J'M' \rangle = \zeta_i A_{\mathrm{so}}. \tag{2.38}$$

The spin–orbit parameter for an orbital, ζ_i is defined by the radial integral:

$$\zeta_i \equiv \zeta_{n_i l_i} = \frac{\alpha^2}{2} \int_0^\infty \frac{1}{r} \left(\frac{dV^i}{dr}\right) |P_{n_i l_i}(r)|^2 dr, \tag{2.39}$$

where α is the fine–structure constant, and $P_{n_i l_i}$ is the radial probability distribution of the orbital i. These integrals can be evaluated numerically using Hartree–Fock radial probability distributions, like those in Figure 1.2.

The matrix elements of the spin–orbit interaction are computed by substituting a unit double–tensor operator, $\mathbf{V}^{11}$, into the spin–orbit expression. Equation 2.9 is then used to

write the expression in terms of two separate reduced matrix elements:

$$A_{\mathrm{so}} = (-1)^{S'+L+J}\,\delta\left(J,J'\right)\delta\left(M,M'\right)\left\{\begin{array}{ccc} S & S' & 1 \\ L' & L & J \end{array}\right\} \times \left\langle l \,||\, \mathbf{l} \,||\, l\right\rangle \left\langle s \,||\, \mathbf{s} \,||\, s\right\rangle \left\langle SL \,||\, \mathbf{V}^{(11)} \,||\, S'L'\right\rangle, \tag{2.40}$$

where:

$$\left\langle l \,||\, \mathbf{l} \,||\, l\right\rangle = \left[\left(2l+1\right)\left(l+1\right)l\right]^{1/2}, \tag{2.41}$$

and:

$$\left\langle s \,||\, \mathbf{s} \,||\, s\right\rangle = \sqrt{\frac{3}{2}}. \tag{2.42}$$

The $\sqrt{3/2}$ factor is normally incorporated into the reduced matrix elements of $\mathbf{V}^{11}$. For most practical applications, these reduced matrix element values are read as SL matrix elements, from sources such as Nielson and Koster's tabulated coefficients [60]. The Wigner–Eckart theorem is then used to compute these as $SLJM$ matrix elements.

2.2.4.3 Crystal field terms

As with the spin–orbit terms, in practice, the crystal field matrix elements are calculated by means of reduced matrix elements of a unit tensor operator: the unit single tensor operator, $\mathbf{U}^k$. The matrix elements and parameters of the crystal field Hamiltonian can be expressed:

$$\left\langle l\gamma SLJM \mid H_{\mathrm{CF}} \mid l\gamma' S'L'J'M'\right\rangle = \sum_{k,q} B_q^k\,(-1)^{J-M}\left(\begin{array}{ccc} J & k & J' \\ -M & q & M' \end{array}\right) \times \left\langle l\gamma SLJ \,||\, \mathbf{U}^{(k)} \,||\, l\gamma' S'L'J'\right\rangle \left\langle l \,||\, \mathbf{C}^{(k)} \,||\, l\right\rangle, \tag{2.43}$$

where:

$$\left\langle l \,||\, \mathbf{C}^{(k)} \,||\, l\right\rangle = (-1)^l\left(2l+1\right)\left(\begin{array}{ccc} l & k & l \\ 0 & 0 & 0 \end{array}\right), \tag{2.44}$$

as per Equation 2.7. Again, the SL reduced matrix elements of $\mathbf{U}^k$ are normally read from existing tabulations [60], and used to calculate $SLJM$ matrix elements using the Wigner–Eckart theorem.

2.2.5 N–electron effective Hamiltonian

Using the definitions of matrix elements and associated parameters discussed above, we can construct an effective Hamiltonian for the two–electron $4f^{13}5d^1$ and $4f^{13}6s^1$ configurations of divalent ytterbium doped into a crystal host. To extend the effective Hamiltonian model to other lanthanide materials, for which the valence orbitals contain more than one electron, more interactions need to be considered. Additionally, while the calculations of the matrix elements for the crystal field Hamiltonian extend directly to the N–electron case due to the introduction of the unit tensor operator, those discussed for the Coulomb interaction do not.

2.2.5.1 Coulomb interactions

As with the spin–orbit and crystal field matrix elements above, the computation of N–electron Coulomb matrix elements involves the use of pre–calculated reduced matrix elements for a two–particle operator. The matrix elements for the N–electron system are built up in terms of the coefficients of fractional parentage between the N and N$-$1 states, and reduced matrix elements of the N$-$1 states. This process is repeated recursively to determine the matrix elements of the N state from the tabulated reduced matrix values. The exact expressions for this can be found in any of the sources mentioned at the beginning of the chapter [23, 51, 52].

Additionally, for configurations with doubly–occupied (or higher) f orbitals, we introduce the following additional terms to correct for electron correlation:

$$H_{\text{Trees}} = \alpha L\left(L+1\right) + \beta G\left(G_2\right) + \gamma G\left(R_7\right). \tag{2.45}$$

These are called the Trees parameters. For a $4f^N$ Hamiltonian, the only Coulomb terms present are the direct F^k terms, where k is even. For equivalent electrons, the reduced matrix elements of the exchange terms are zero, due to the triangular condition on the 3–j symbol. The Trees parameters represent a perturbation of the Coulomb interaction, expanded in terms of the unit tensor operator, $\mathbf{u}^k$, which allow for non–zero terms for odd k values. The perturbation also produces terms for even values of k, but these are simply assumed to be incorporated into the F^k terms, or ignored, as the effects cannot be distinguished.

2.2.5.2 Magnetic interactions

As mentioned previously, the spin–orbit terms in Equation 2.15 are actually effective operators, incorporating any of the two–electron interactions present that behave in the same manner as the one–electron spin–orbit operator, $\mathbf{l}_i \cdot \mathbf{s}_i$.

A fuller description of the magnetic interactions for an N–electron atom is [61]:

$$\begin{aligned} V_m =& \zeta \sum_i \frac{1}{r_i^3} \mathbf{l}_i \cdot \mathbf{s}_i - \frac{\alpha^2}{2} \sum_{i \neq j} \left(\frac{\mathbf{r}_{ij}}{r_{ij}^3} \times \mathbf{p}_i \right) \cdot (\mathbf{s}_i + 2\mathbf{s}_j) \\ &+ \frac{\alpha^2}{2} \sum_{i \neq j} \frac{1}{r_{ij}^3} \left(\mathbf{s}_i \cdot \mathbf{s}_j - 3 \frac{(\mathbf{s}_i \cdot \mathbf{r}_{ij})\,(\mathbf{s}_j \cdot \mathbf{r}_{ij})}{r_{ij}^2} \right), \end{aligned} \tag{2.46}$$

where i and j index over all valence electrons. There are three main groups of interactions here. The first term is the spin–own–orbit (or simply spin–orbit) interaction, the second is the spin–other–orbit interaction, and the last is a spin–spin dipole interaction between pairs of electrons.

The calculation of the spin–orbit matrix elements discussed previously already extends to the N–electron case. The spin–other–orbit and spin–spin terms in the effective Hamiltonian are given by a set of two–electron operators weighted by the Marvin parameters M^0, M^2 and M^4:

$$H_{\mathrm{soo}} = \sum_{i=0,2,4} M^i m_i. \tag{2.47}$$

The definitions of these parameters are given by Blume and Watson [61]. As with all other derivations here, the matrix elements for these operators are evaluated by expanding tabulated reduced matrix elements [60] using the Wigner–Eckart theorem.

Additionally, magnetic configuration–interaction can be accounted for by using the additional parameters [14]:

$$H_{\mathrm{mag-CI}} = \sum_{i=2,4,6} P^i p_i. \tag{2.48}$$

The p_i and m_i matrix elements can be calculated from the same reduced matrix elements.

Other magnetic interactions can be introduced to the Hamiltonian, such as orbit–orbit interaction between pairs of electrons, but the effects of these are typically very small in magnitude [51].

2.2.5.3 Three–body interactions

For $4f^N$ systems with $N > 2$, a set of three–body operators are added to the effective Hamiltonian:

$$H_{\text{Three-body}} = \sum_i t_i T^i. \tag{2.49}$$

To second order perturbation, there are six three–electron operators, $i = 2, 3, 4, 6, 7, 8$. To higher orders, there are an additional eight operators, $i = 11, 12, 14, 15, 16, 17, 18, 19$. Tables of the matrix elements for these operators have been published [2, 14, 62].

2.3 Limitations and additional corrections

2.3.1 Limitations

An important consideration is that the effective Hamiltonian is not restricted to a particular physical model. This means that the crystal field parameters can absorb effects from any non–spherical interaction with the lattice, not just point–charge effects. Hence there is no way to determine what interactions are present and contributing, using empirical means. Similarly, any interactions that have equivalent actions (non–orthogonal operators) are completely indistinguishable once fitted. Thus, while an empirical fitting of the effective Hamiltonian can provide a good reproduction of experimentally observed energy levels, it does not allow these quantities to be measured individually.

2.3.2 Additional corrections

The crystal field Hamiltonian works for the majority of states in most lanthanide systems. However, the energies of some multiplets cannot be resolved using just the crystal field terms above. Two approaches can be used to adjust the calculation to account for these discrepencies: extending the basis set, or introducing a number of effective operators [53].

One procedure that is used is to consider all products of two unit tensors, coupled to give operators of specified angular momentum:

$$H_{\text{CCF}} = \sum_{k_1 k_2 k q} B_q^k \left(k_1 k_2\right) \sum_{i>j} \left(\mathbf{U}^{(k1)}\left(i\right) \mathbf{U}^{(k2)}\left(j\right)\right)_q^{(k)}. \tag{2.50}$$

This is called the correlation crystal field Hamiltonian [53]. For $4f^N$ configurations, the selection rules on the angular momenta, k_1, k_2 and k, allow for non–zero elements for $k = 2$ up to $k = 12$. These operators are not orthogonal, but can be orthogonalised by an appropriate change of weight of the two–electron matrix elements [63]. These orthogonal operators are denoted:

$$H_{\mathrm{CCF}} = \sum_{ikq} G^k_{iq} g^{(k)}_{iq}. \tag{2.51}$$

This can add a total of 637 parameters to the effective Hamiltonian. Obviously, this is far too many parameters to attempt to fit to experimental energy observations. The number of parameters can be restricted to a more useful size by considering a number of different models [53]. This includes considering only the spin–correlated crystal field, which consist of a very small subset of the $\mathbf{g}^{(k)}_{iq}$ operators, or by imposing the superposition model restrictions upon the chosen selection of parameters. Care must be taken when choosing appropriate correlation crystal field parameters to include as a correction to the system, as some may have very little influence [63].

2.4 Simulating spectra

In Chapter 5, we will simulate absorption spectra using the eigenvalues and eigenvectors of effective Hamiltonians fitted to energy levels of Yb^{2+} in CaF_2 and SrF_2. The actual process of calculating dipole moments and transition intensities in order to simulate a spectrum is a non–trivial procedure, and is covered in various references [1, 14, 23, 52, 64, 65]. A brief overview shall be given here, to provide a background for the simulations performed in this thesis.

2.4.1 Transition Intensities

To determine the intensities of optical transitions (those involving the interaction of electrons with electromagnetic radiation), the matrix elements of the appropriate dipole operator acting upon the eigenvectors described by the effective Hamiltonian of the system must be calculated. The electric and magnetic dipole operators are:

$$-e\mathbf{D}^{(1)}_q = -er\mathbf{C}^{(1)}_q, \tag{2.52}$$

and:

$$\mathbf{M}^{(1)}_q = \frac{-e\hbar}{2mc}\left(\mathbf{L}^{(1)}_q + 2\mathbf{S}^{(1)}_q\right). \tag{2.53}$$

The polarisation of the radiation is given by q, and may take the values $q = 0, \pm 1$. The operators $\mathbf{C}_q^{(1)}$, $\mathbf{L}_q^{(1)}$ and $\mathbf{S}_q^{(1)}$ are the spherical harmonic tensor, orbital angular momentum, and spin angular momentum operators, respectively.

The matrix elements of the dipole operators can be used to determine the dipole line strengths. For a transition from initial state, I, to a final state, F, the line strengths are:

$$S_{FI,q}^{\mathrm{ED}} = \sum_i \sum_f e^2 \left| \langle Ff \mid \mathbf{D}_q^{(1)} \mid Ii \rangle \right|^2, \tag{2.54}$$

and:

$$S_{FI,q}^{\mathrm{MD}} = \sum_i \sum_f \left| \langle Ff \mid \mathbf{M}_q^{(1)} \mid Ii \rangle \right|^2, \tag{2.55}$$

where i and f index over the components of I and F. For isotropic (unpolarized) light, the line strengths are simply averaged over all polarisations:

$$\overline{S}_{FI} = \frac{1}{3} \sum_q S_{FI,q}. \tag{2.56}$$

For unpolarised or linearly polarised light, the magnetic and electric dipole interactions can simply be summed together when calculating overall dipole interactions [64]. These dipole line strengths are a measure of the strength of the spectrum line for all allowed ΔM transitions [23]. By Fermi's Golden Rule, the intensity of the transition is proportional to line strength: $I \propto S$ [23, 52]. These line strengths can be used to calculate all observable properties of the spectrum, such as oscillator strengths and absorption cross sections, given the degeneracy of each state.

The selection rules governing which transitions are allowed are determined by the polarities of the dipole operators. For example, the electric dipole operator has odd parity, and so is zero for all $4f \rightarrow 4f$ (even–parity) transitions, unless treated using an effective dipole operator [64] to account for the breaking of inversion symmetry close to the impurity site [1]. The $4f \rightarrow 5d$ transitions have odd parity, and hence the zero–phonon transition is electric dipole allowed. In addition, the Wigner–Eckart theorem used to determine the reduced matrix elements of the dipole operator provides additional selection rules based on the triangular condition of the 3–j symbol, (section 2.1.1):

$$\Delta J = 0, \ \pm 1,$$

except for:

$$J_{\mathrm{initial}} = J_{\mathrm{final}} = 0,$$

which is also forbidden. Additionally, if the system can be represented well by SL coupling, similar selection rules will be introduced on the S and L quantum numbers due to the coupling scheme. This will happen to any good quantum numbers of the system, if it can be represented by any pure coupling scheme. Coupling schemes and quantum numbers will be discussed in the next chapter.

2.4.2 Vibronic transitions

In addition to the zero–phonon transition intensities discussed above, the observed spectra can exhibit broadening of the lines due to the presence of vibronic transitions. Transitions within a configuration, such as $4f \rightarrow 4f$, exhibit very little vibronic behaviour, as the initial and final states have very similar coupling to the host lattice [64]. The spectra examined in this thesis mainly consist of $4f \rightarrow 5d$ transitions, where the initial and final states have different configurations, and hence vastly different interactions with the host lattice. This allows for transitions between a large number of vibronic states, which gives broad spectral peaks. A schematic of this is demonstrated in Figure 2.1.

The intensity of vibronic transitions associated with a zero–phonon transition can be characterised by use of the Huang–Rhys parameter:

$$\begin{aligned} S &= \left(\frac{M\omega}{\hbar}\right)^{1/2} \left(Q_0^{(b)} - Q_0^{(a)}\right) \\ &= \frac{E_{\text{dis}}}{\hbar\omega} \\ &\equiv m' + \frac{1}{2}. \end{aligned} \tag{2.57}$$

Here, M is the effective ionic mass, ω is the vibronic frequency, and the Q_0 are ion–ligand displacements at vibrational equilibrium, as shown in Figure 2.1. The vibronic quantum number, m', corresponds to a (possibly hypothetical) excited vibronic state with maximum integral overlap with the lowest vibronic state of the ground electronic state. The Huang–Rhys parameter is not necessarily confined to integral values.

The intensities of transitions to the vibronic states can be calculated from the zero–phonon intensity by [1]:

$$I(E) = I_0 \sum_m \frac{\exp(-S)\, S^m}{m!}\, \delta(E_0 + m\hbar\omega - E), \tag{2.58}$$

where E_0 is the zero–phonon line energy. The effect of different values of the Huang–Rhys parameter is demonstrated in Figure 2.2. For $S = 0$, there is no shift of configuration

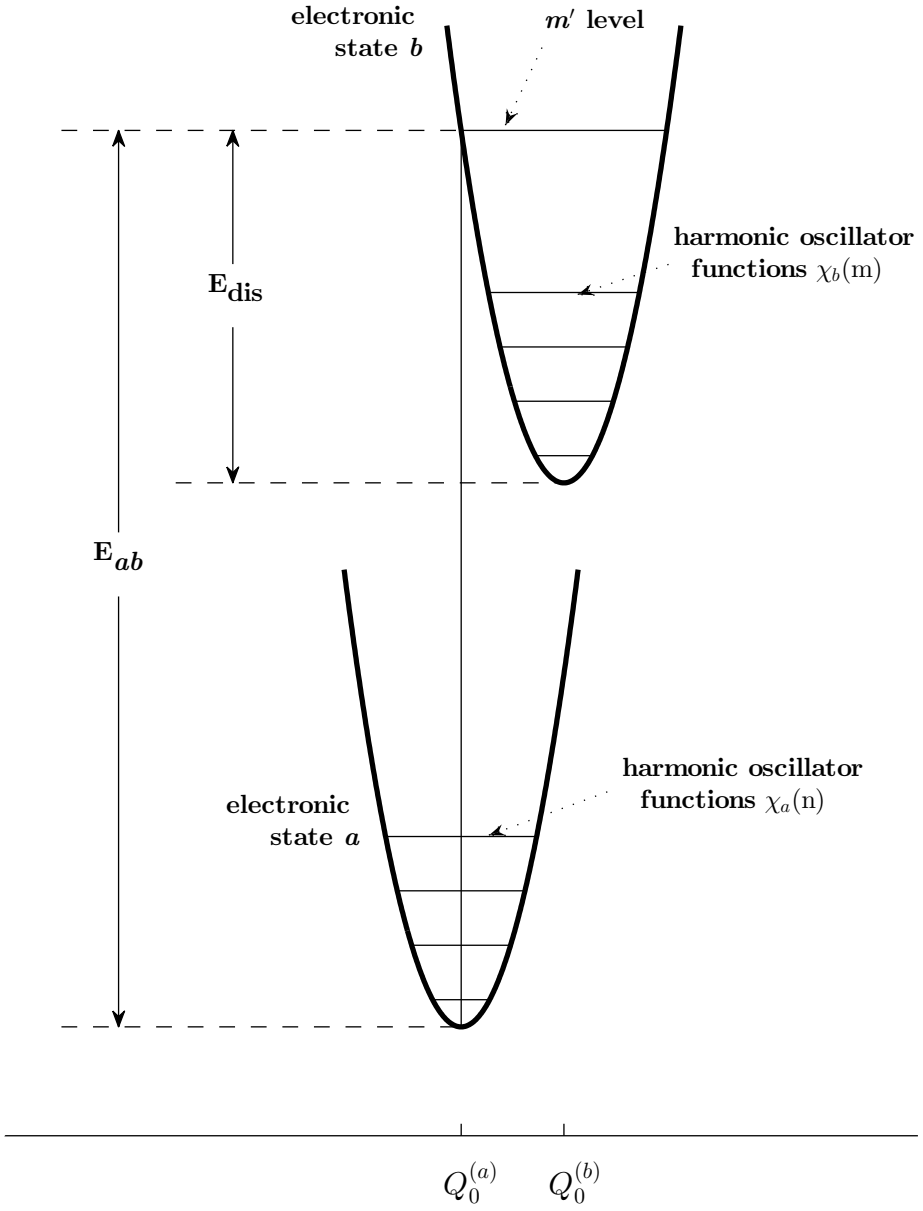

Figure 2.1 Schematic of vibronic structure of a transition between different configurations, from Henderson and Imbusch [1]. Due to the difference in equilibrium ion–ligand lengths, Q_0, between the two configurations, transitions from the ground vibrational state of electronic state a have a higher transition probability to vibronic states around the m' vibrational state of electronic state b. This is observed as a broadening of peaks in the absorption spectrum, and a shift of the peak maximum away from the zero–phonon line, for a sufficiently large change in Q_0.

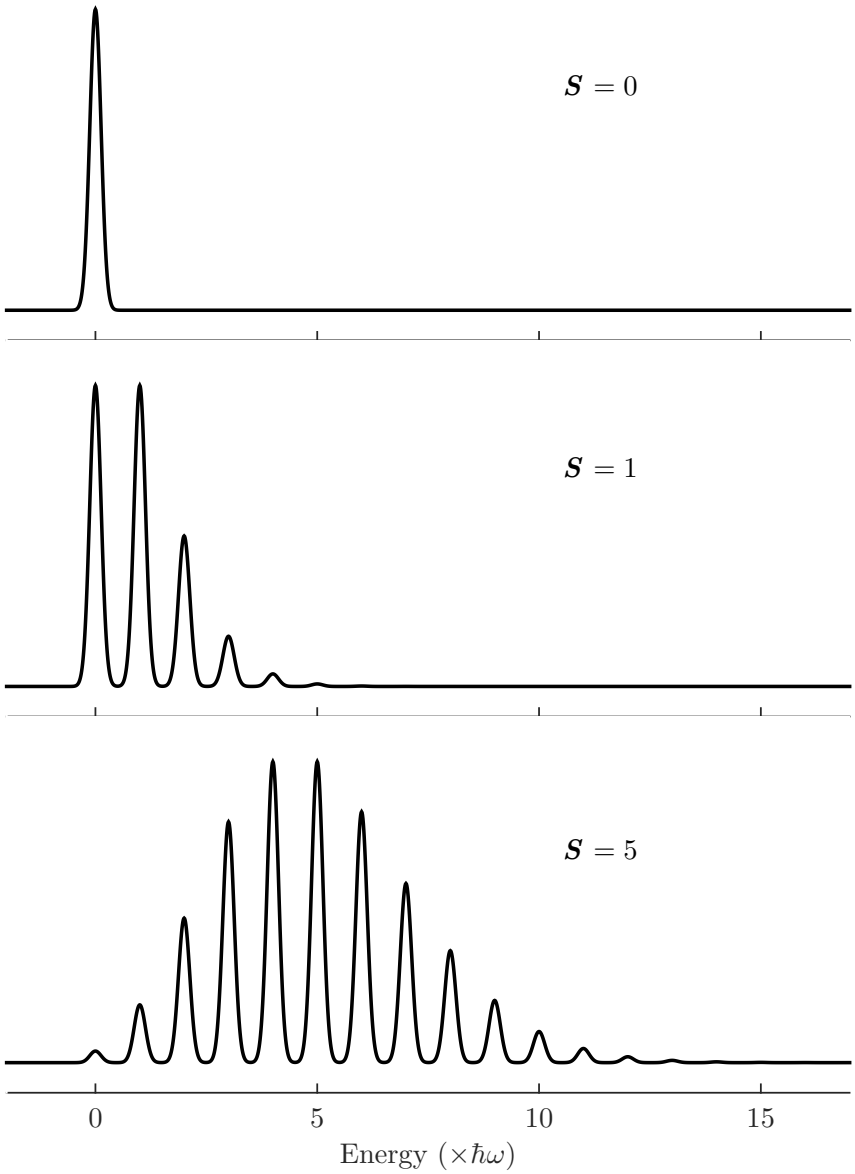

Figure 2.2 Demonstration of the effect of the Huang–Rhys parameter. A Huang–Rhys parameter of zero corresponds to a configuration shift of zero, and hence the transition is solely comprised of the zero–phonon transition. For higher S values, the transition intensity is spread from the zero–phonon line to higher vibronic states [1]. The intensity normalisation used here is not consistent between S values.

equilibrium position between the initial and final electronic states, so the matrix elements between all but the ground vibronic states are zero. Increasing the value of S spreads the transition intensity from the zero–phonon line to higher vibronic levels. The envelope of the intensities of states described by Equation 2.58 is a Pekarian function. As seen in Figure 2.2, this function has a very pronounced asymmetric shape for low values of S, but at higher S values, the envelope becomes increasingly symmetric. For sufficiently large values of S, a Gaussian function can approximate this shape [1].

The vibronic bands simulated in Chapter 5 have been constructed in two ways. The main method used is to utilise the Gaussian curve approximation, and simply convolve the dipole line strengths, $\overline{S}_{FI}$, with Gaussian functions:

$$\left(\overline{S}_{FI} * g\right)_i (E) = \int_{-\infty}^{\infty} \overline{S}_{FI,i}\, \delta\left(\mathcal{E}, \Delta E_i\right) g_i \left(E - \mathcal{E}\right) \delta\mathcal{E}, \tag{2.59}$$

where $g_i(E)$ is the Gaussian function associated with the i^{th} transition. The shape of the Gaussian functions are controlled by the full width half maximum (FWHM) value. The FWHM parameters are chosen to match the vibronic progressions associated with each zeron–phonon line transition. The simulated spectrum is then simply the sum of contributions from each transition.

For the calculations where the progression of intensities of the vibronic states have been calculated, the dipole strengths are still convolved with a narrow Gaussian function to approximate the broadening, but the shape of the simulated absorption bands better resemble the Pekarian function envelopes.

Chapter 3

Calculation details

Much of the detail covered in the previous chapter can be automated to perform most of the calculation steps. Several such implementations exist. The software used for this thesis was the f–shell empirical suite, written and maintained by Prof. M. F. Reid, and augmented by many co–workers.

This chapter covers the details of the workflow associated with performing effective Hamiltonian fits using the f–shell empirical suite of software. Theory on the quantum number labels for the states is covered, as this is an important consideration for the fitting processes used. The irreducible representation (irrep) labelling functionality that was added to this software package to address these considerations for this project is introduced and discussed.

3.1 Coupling schemes and state labels

Angular momenta coupling schemes and associated state label systems have been discussed extensively in the literature [3, 23, 51, 52]. For systems where Coulomb interactions are far more significant than the spin–orbit interaction, SL coupling can be used, where the electron spins are coupled to a total spin angular momentum, and orbital angular momenta are coupled to a total orbital angular momentum. These are then coupled together to give the total angular momentum, J. In these schemes, the total spin angular momentum, S, and total orbital angular momentum, L, are good quantum numbers and will adequately describe basis states of the Hamiltonian. Schematically, this is shown $\{(s_1, s_2)\, S, (l_1, l_2)\, L\}\, JM$, where the brackets provide the coupling order. This can be

abbreviated to $|SLJM\rangle$ or $\left|^{2S+1}LJM\right\rangle$.

On the other hand, if the spin–orbit interaction is strong, then the spin angular momentum and orbital angular momentum are coupled together to a combined angular momentum, j, for each electron. These angular momenta are then coupled to the total angular momentum of the state: $\{(l_1, s_1)\, j_1, (l_2, s_2)\, j_2\}\, JM$. In this scheme, called jj–coupling, the j are good quantum numbers, and can be used to label the states: $|jjJM\rangle$.

Additionally, the angular momenta can be coupled in varying orders. Two other coupling schemes that can be observed are: $\{[(l_1, s_1)\, j_1, l_2]\, K, s_2\}\, JM$, called jK–coupling; and $\{[(l_1, l_2)\, L, s_1]\, K, s_2\}\, JM$, called LK–coupling [23]. These describe systems with different relative magnitudes of the spin–orbit, Coulomb, and crystal field interactions.

Lanthanides are generally not well–described by any of these behaviours. Instead, a more accurate description of the coupling scheme is intermediate to the SL and jj schemes. The degree of intermediate coupling for a material can be shown by assigning a variable to scale between the coupling schemes. The energy levels of states can then be fitted to the curves described by varying this parameter between pure SL and pure jj coupling schemes. This is discussed in detail in Cowan [23].

The absence of a pure coupling scheme can result in a lack of useful quantum numbers with which to label states in these materials. In this case, the usual practice is to label states using a list of weights of the greatest constituent basis states of the eigenvector, from either a LS– or jj–coupled scheme [23]. We can also make use of group theory to provide additional labels for these states.

3.2 Irreducible representations

A matrix representation of a group is any set of matrices which satisfies the multiplication table for that group. An irreducible representation (irrep) is a representation that cannot be expressed in terms of a sum of lower dimension representations. The notation for a general representation is Γ.

In the calculations performed here, the effective Hamiltonian is a matrix representing the point group at the impurity ion site. The effective Hamiltonian consists of sets of degenerate eigenfunctions, each set of which is an irrep of the point group. The decomposition of the effective Hamiltonian matrix into its point group irreps provides the minimum level

of degeneracy in that system. There can also be occurrences of 'accidental' degeneracy, where two irreps are degenerate due to the combination of parameter values, rather than due to the underlying symmetry. The irreps of the effective Hamiltonian representation can be used as quantum numbers to label each set of degenerate states [1, 41, 66]. These can be used regardless of whether the other quantum numbers are good labels or not, as the irreps can be identified by the transformation properties of the eigenvectors, rather than just the composition of the eigenvectors.

The irreps can be assigned in a systematic fashion, using the percentage contribution of the JM basis states to the eigenvectors, and tabulated decompositions of the symmetry group into said JM states, as demonstrated in Butler (1981) [66].

3.3 The f–shell empirical software suite

The f–shell empirical suite of software is an implementation of the theory discussed in the previous chapter.

The process for performing an energy level calculation is outlined in Figure 3.1. To perform an energy level calculation, the matrix elements for all relevant interaction matrix representations must be calculated. The starting point is the specification of the electron configuration. The program readcr is used to read in the tabulated reduced matrix elements for these configurations from Nielson and Koster [60], and Hansen et al. [62]. The programs sljcalc and jmcalc expand these matrices to SLJ level, and $SLJM$ levels respectively, using successive applications of the Wigner–Eckart theorem. These states can also be recoupled as $jjJM$ states (or states of any other coupling scheme), by exporting the matrix elements to other matrix–manipulating software, and performing a change of basis. This does not alter the energy eigenvalues calculated using the effective Hamiltonian. This will, however, affect the eigenvectors of the Hamiltonian, which, in turn, will affect the transition intensities and simulated spectra.

The effective Hamiltonian is constructed and diagonalised in the cfit program. If all that is required are the energy eigenvalues of the system, this is the end point of the calculation. Otherwise, the eigenvectors can be saved, and passed to the vtrans program, which calculates matrix elements of dipole operators. Lastly, these matrix elements, along with a specified refractive index, and polarization of radiation can be provided to the inten program, to calculate dipole line strengths for transitions between specified ranges of

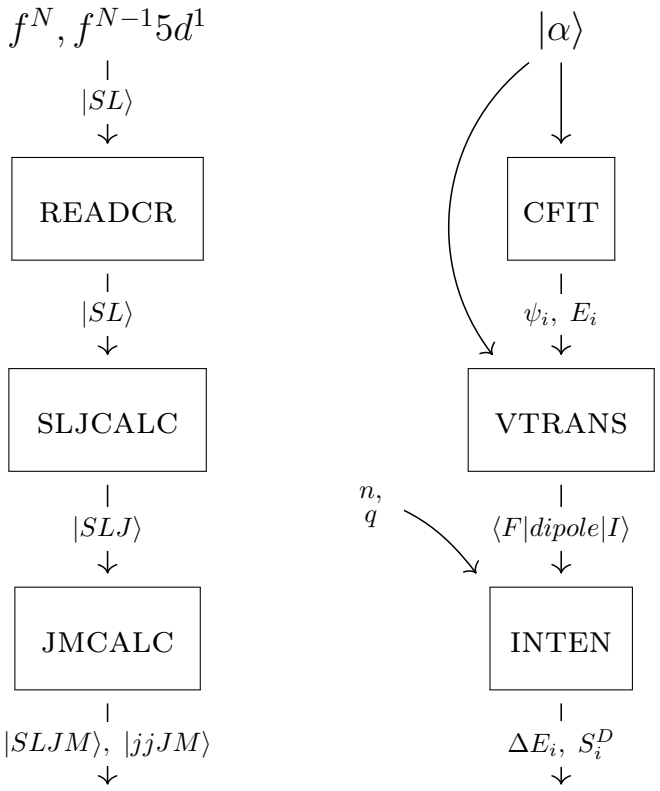

Figure 3.1 Workflow diagram of the f–shell empirical software suite. The label α stands for the quantum numbers labelling the states used as inputs into the cfit program, eg. $SLJM$ or $jjJM$. All other symbols hold the same definitions as introduced in the previous chapter. The values n and q refer to the refractive index of the material, and polarisation of the radiation, respectively.

states. These dipole line strengths can be used to generate a simulated spectrum with either the internal software, or extracted to be used externally.

3.3.1 Irrep–labelling function

For the purposes of the work in this thesis, the state labelling scheme provided by the f–shell empirical suite was not sufficient for the process of fitting high symmetry energy levels to reference calculations, or experimental observations. The software reduces the effective Hamiltonian to a block–diagonal form, to reduce the system requirements for diagonalisation as much as possible. In theory, this is achieved by rearranging the order of states in the matrix representation. In practice, these states are assigned a position in the block that they should occupy, as a pair of labels (block, level), so that no actual

alteration of the effective Hamiltonian needs to occur. Each block is then diagonalised in turn. The block and level labels are a sufficient description of states for low symmetry systems with which to assign reference energy levels against, in order to fit the parameters (provided the initial parameters are a good estimate). However, they are not useful in higher symmetry (eg. octahedral) systems, as the level label for a state is not fixed for all parameter values.

3.3.1.1 An example: $SrCl_2$:Yb^{2+}

Figure 3.2 contains a sample of the output from the cfit program for a calculation of $SrCl_2$:Yb^{2+} that will be shown in Chapter 4. We shall refer to this as an example for this section. The lanthanide impurity in this example occupies a cubic symmetry site. This is isomorphic to the octahedral symmetry group, O. For octahedral site symmetry, the possible constituent irreps can be the one dimensional A_1 or A_2 irreps, the three dimensional T_1 or T_2 irreps, or the two dimensional E irrep. The transformation properties of these irreps can be found in character tables for the O group [52].

Looking at the SL labels of the first set of triply–degenerate eigenvectors, indexed 4, 5 and 6, the primary constituents are ^3P states, and so even though the eigenvectors 4 and 6 have a large ^3H component, we can still approximate these eigenvectors with the ^3P SL label. For most of the eigenvectors in this output, there is a sufficiently dominant term with which to label the states. However some of the higher energy eigenvectors are less distinct. For example, the constituents of eigenvectors 115, 116 and 117, from the same calculation, are too mixed to be assigned an appropriate SL label.

We can see that these two states are triply degenerate, but cannot directly assign them an octahedral irrep label, as the octahedral group has two triply degenerate irreps. To distinguish between them, we need to look at the composition of the eigenvectors in terms of constituent basis states. The J quantum number is the label for the group SO_3, and M for the group SO_2. The basis states are therefore labelled $|SO_3\ SO_2\rangle$.

The vector coupling coefficients for a number of group progressions are tabulated by Butler [66]. The group progression $SO_3 - O - D_4 - C_4$ indicates the action of the octahedral symmetry group on states of the SO_3 (angular momentum) group. This action will split representations of the SO_3 group into irreps of the octahedral group [1, 66], which provide the observed degeneracies in the sample. In turn, the D_4 group acts on the irreps of the O group, and the C_4 group acts on the irreps of D_4 group. Each of these decompositions

introduce additional irrep or quantum labels that we may use to identify the irreps. We can identify the $|SO_3\ O\ D_4\ C_4\rangle$ state for each set of degenerate eigenvectors in Figure 3.2 by using the vector coupling coefficients:

$$|SO_3\ O\ D_4\ C_4\rangle_a = \sum_b {}_b\langle SO_3\ SO_2 \mid SO_3\ O\ D_4\ C_4\rangle_a\, |SO_3\ SO_2\rangle_b\,. \tag{3.1}$$

This will, in turn, allow us to assign an O group irrep label to each set of degenerate eigenvectors.

Table 3.1 Octahedral group irreps.

Irrep	Label	Dimension
1	T_1	3
$\tilde{1}$	T_2	3
2	E	2
0	A_1	1
$\tilde{0}$	A_2	1

From the tables of Butler [66], we have the set of expressions for the first T_2 irrep:

$$\begin{aligned}
\big|2\ \tilde{1}\ 1\ \ 1\big\rangle &= -\,|2\ \ 1\rangle \\
\big|2\ \tilde{1}\ 1\ \text{-}1\big\rangle &= +\,|2\ \text{-}1\rangle \\
\big|2\ \tilde{1}\ \tilde{2}\ \ 2\big\rangle &= +\frac{1}{\sqrt{2}}\,|2\ \ 2\rangle - \frac{1}{\sqrt{2}}\,|2\ \text{-}2\rangle\,.
\end{aligned} \tag{3.2}$$

We compare these with the main constituents of the eigenvectors, 4, 5 and 6, from Figure 3.2, considering first just the ${}^3P$ SL components:

$$\begin{aligned}
(6):&\quad -0.77\left(-\left|{}^3P\ \ 2\ \ 1\right\rangle\right) \\
(4):&\quad +0.77\left(+\left|{}^3P\ \ 2\ \text{-}1\right\rangle\right) \\
(5):&\quad -0.77\left(+\frac{1}{\sqrt{2}}\left|{}^3P\ \ 2\ \ 2\right\rangle - \frac{1}{\sqrt{2}}\left|{}^3P\ \ 2\ \text{-}2\right\rangle\right).
\end{aligned} \tag{3.3}$$

Equations 3.2 and 3.3 are similar up to a magnitude and a sign (which arises due to an ambiguity in phase during the diagonalisation). We can therefore label eigenvectors 4, 5 and 6 as components of the T_2 octahedral irrep, according to the vector coupling scheme in Equation 3.2.

If we look at the full readout, we have a sizeable contribution from the ${}^3H$ multiplet:

$$\begin{aligned}
(6):&\quad +0.77\left|{}^3P\ \ 2\ \ 1\right\rangle + 0.44\left|{}^3H\ \ 6\ \ 1\right\rangle \\
(4):&\quad +0.77\left|{}^3P\ \ 2\ \text{-}1\right\rangle + 0.44\left|{}^3H\ \ 6\ \text{-}1\right\rangle \\
(5):&\quad -0.54\left|{}^3P\ \ 2\ \ 2\right\rangle + 0.54\left|{}^3P\ \ 2\ \text{-}2\right\rangle.
\end{aligned} \tag{3.4}$$

```
      BLK LEV                                                                                    THEORY

  1*   5   1  ( 1.00) 100%   73 [1S       0  0>                                                674.000000
  2*   3   1  ( 0.77)  59%   76 [(2F )3P  2  0>  ( 0.50)  25%   88 [(2F )3H  6  0>  27737.368280
  3    1   1  (-0.54)  29%  121 [(2F )3P  2 -2>  (-0.54)  29%   30 [(2F )3P  2  2>  27737.368280
  4*   4   1  ( 0.77)  59%   99 [(2F )3P  2 -1>  ( 0.44)  20%  111 [(2F )3H  6 -1>  27768.676460
  5    1   2  (-0.54)  29%   30 [(2F )3P  2  2>  ( 0.54)  29%  121 [(2F )3P  2 -2>  27768.676460
  6    2   1  ( 0.77)  59%   51 [(2F )3P  2  1>  ( 0.44)  20%   63 [(2F )3H  6  1>  27768.676460
  7*   4   2  (-0.44)  19%  166 [(2F )3H  5 -5>  (-0.42)  17%   98 [(2F )3P  1 -1>  30407.012201
  8    3   2  ( 0.55)  30%   87 [(2F )3H  5  0>  (-0.43)  19%   93 [(2F )1H  5  0>  30407.012201
  9    2   2  ( 0.44)  19%    3 [(2F )3H  5  5>  ( 0.42)  17%   50 [(2F )3P  1  1>  30407.012201
 10*   1   3  (-0.43)  19%  123 [(2F )3D  3 -2>  ( 0.43)  19%   32 [(2F )3D  3  2>  30518.968087

...

115*   4  29  (-0.44)  19%  113 [(2F )1D  2 -1>  (-0.36)  13%  103 [(2F )3F  2 -1>  51660.485451
116    2  29  ( 0.44)  19%   65 [(2F )1D  2  1>  ( 0.36)  13%   55 [(2F )3F  2  1>  51660.485451
117    1  29  ( 0.35)  12%  136 [(2F )1H  5 -2>  ( 0.35)  12%   45 [(2F )1H  5  2>  51660.485451
```

Figure 3.2 CFIT output sample, from a calculation of $SrCl_2$:Yb^{2+}. Each line represents an eigenvector/eigenvalue pair of the effective Hamiltonian. The first label is simply an integer indexing over all eigenvectors. An asterisk indicates the beginning of a new set of degenerate energy eigenvectors (the eigenvectors are sorted in energy order). The next two integers are block (BLK) and position/level (LEV) labels. For each eigenvector, the largest two (or one, if there is only one) constituent basis states are then listed with the coefficient in brackets, the percentage composition (coefficient squared), the basis state index and ket.

Note that the readout itself is truncated to a maximum of two constituent states for convenience (this may be overridden where necessary), and therefore there is also a similar contribution to eigenvector 5 from the ^3H multiplet, in addition to the contributions from many other mixed states. These contributions are present due to the crystal field operators in the Hamiltonian.

The $C^4_{\pm4}$ operators present in the Hamiltonian can couple any states related by $\Delta J = 0, \pm4$, $\Delta M = 0, \pm4$; and similarly, the $C^6_{\pm4}$ operators couple states with $\Delta J = 0, \pm6$, $\Delta M = 0, \pm4$. Since all states that are coupled together by the operators of the effective Hamiltonian will appear in the same block of states when block–diagonalised by CFIT, the Hamiltonian can only be block–diagonalised into four blocks. Each block corresponds to a sequence of states linked by the M quantum number. For example, a block label of '4' corresponds to eigenvectors comprised of any states with the M quantum numbers:

$$M = -1 + n \times 4, \quad \text{for } n \in \mathbb{Z}. \tag{3.5}$$

For convenience, we shall simply refer to all of these possible quantum numbers as belonging to $M = -1$.

If we look at eigenvectors 4 and 115, the M quantum numbers of the states are both $M = -1$. Both of these states belong to the fourth block assigned by CFIT. The other eigenvector listed in the example with a block label of '4' is eigenvector 7. This has one state with $|1\ {-1}\rangle$, and one with $|5\ {-5}\rangle$, both of which are part of the sequence described in Equation 3.5.

Similarly, by inspection, blocks '1', '2' and '3' refer to the eigenvectors comprised of states belonging to the progressions $M = 2$, $M = 1$, and $M = 0$, respectively. We can now write the irreps of the octahedral group in terms of the M quantum number progessions from which they are composed. The T_2 irrep becomes any triply degenerate set of eigenvectors with the M quantum numbers: $M = -1$, 1, and 2, or equivalently, the block labels: 1, 2, and 4. The composition of the remaining irreps are shown in Table 3.2.

The actual block label is an arbitrary assignment based on the order that the algorithm processes the mixed states into blocks. It is therefore necessary to manually assign the block labels for the point group irreps for each different system fitted. The important factor here is that the block labels are consistent for a given effective Hamiltonian.

Table 3.2 Octahedral group irreps, labelled by M quantum number, and by the equivalent block labels in the sample calculation. Note that the block labels are specific to this particular calculation.

O Irrep	M quantum number ($\pm 4 \times n$)	Blocks
T_1	-1, 0, 1	2, 3, 4
T_2	-1, 1, 2	1, 2, 4
E	0, 2	1, 3
A_1	0	3
A_2	2	1

3.3.1.2 Parity irrep label

Lastly, the point group of the impurity site symmetry in the example is actually O_h, which is the direct product group: $O_h = O \otimes C_i$, where C_i is the inversion symmetry group. This has the irreps Γ_g for even parity, and Γ_u for odd parity. As the valence shell of the ground state for the Yb^{2+} system is a closed shell, it has even parity. The excited state has odd parity, as a transition of a single electron to a different configuration will change the parity of a state. Therefore, the irrep label for the eigenvector sets 4, 5, and 6; and 115, 116, and 117 is:

$$\Gamma_{\tilde{1}} \otimes \Gamma_u = T_{2u}. \tag{3.6}$$

By this process, irrep labels can be assigned to all eigenvectors of the system.

3.3.1.3 Implementation

Functionality was added to CFIT to track the M quantum labels by means of the block labels of the sets of degenerate energy eigenvectors, as discussed here. This system works at all levels of energy degeneracy. For example, the spin–orbit free calculations that are conducted in this thesis result in multiplets, $\left|^{2S+1}L\right\rangle$, with $2S+1$ degenerate energy levels, which can be easily (if somewhat tediously, for high spin systems) identified by $2S + 1$ block labels. Such systems tend to have very little mixing between states, and so may contain many blocks to be diagonalised.

At low symmetries, however, there is little benefit to using this scheme, as the states are thoroughly mixed by the crystal field operators. In this situation, there are only one or two blocks to diagonalise. Here, the states are better labelled by the index of the

eigenvector.

3.4 The fitting process

The procedure to extract parameters from *ab initio* energy levels via least–squares fitting, used throughout this thesis, is as follows:

- Identify which electron configurations are present, and hence which effective Hamiltonian parameters are required.
- Calculate the matrix elements for these operators, using the sequence of programs from the left–hand side of Figure 3.1.
- Select an initial set of parameter values, either by calculating the values from their definitions, or by using existing parameters from the same, or a similar, material.
- Diagonalise the matrix, using CFIT.
- Identify the block labels associated with each Q quantum number, using the output of this initial diagonalisation.
- Construct a list of target energy levels for the fitting process, using the energy levels supplied by the references, and the block labels identified above to label the symmetry group irrep with which each energy level is associated.
- Select which parameters should be varied, and set the limiting number of iterations after which the least–squares process is aborted (in case of a failure to converge to a solution).
- Run the least–squares fitting procedure, using CFIT.

Multiple least–squares fits can be run in sequence in a single execution of CFIT, allowing different sets of parameters to be varied, using the resultant parameter values from the previous fit as the starting points for the subsequent fit. This does not typically provide a large benefit in terms of correcting the values of the parameters, or to improve the overall quality of the fit, but it may help steer the process to avoid converging to unwanted local minima, or situations where the process fails to converge.

3.5 The MOLCAS suite

The MOLCAS suite of software is a package for performing *ab initio* quantum chemical calculations [43], which is utilised by a number of the sources of reference data in this thesis [4–6, 36, 44, 45, 67, 68]. This software is not used directly in any part of this thesis, but a brief outline shall be given, as some of the nomenclature of these calculations are used throughout this thesis to indicate the level of the calculation currently being analysed.

The procedure for performing a calculation is outlined in reference [43]. The basis wavefunction for these calculations consists of linear combinations of antisymmetrized products of molecular orbitals, which in turn are composed of linear combinations of atomic orbitals, described by a linear combination of Gaussian functions centered on the atomic nuclei. The starting point is typically to optimise the coefficients of the wavefunction, for example using a Hartree–Fock self–consistent calculation, or similar method [43]. Additional levels of calculation can then be implemented to apply corrections to account for missing interactions in the original level of calculation.

The method typically employed in the reference calculations is to use a complete (or restricted) active space self–consistent field (CASSCF or RASSCF) method to optimise the coefficients of the wavefunction [5, 44, 68]. At this level of calculation, spin–orbit, electron correlation and configuration interaction corrections are not included. Even without these interactions, the calculation can be accurate to within a few percent of the true wavefunction at this level [43]. Long range interactions with the lattice are typically modelled in two different ways. The simplest method is use a Madelung embedding, which models the potential provided by the lattice as a large array of point charges. This approach has limitations when the valence electron orbitals of the impurity are in close proximity to, or have significant overlap with, the valence electrons of the ligands [4]. A more accurate approach is to describe the closest lattice constituents with an *ab initio* model potential embedding (AIMP). This provides a more accurate spatial description of the valence electrons of the ligands [69]. Point charges are still used to describe more distant lattice constituents [5].

The calculations are then corrected for dynamic electron correlation, which is ignored in the self–consistent field stage. The software uses the Møller–Plesset perturbation method to second order in energy (MP2) to achieve this. This level of calculation is referred in the references as multistate complete (or random) active space, Møller–Plesset perturbation to 2nd order (MS-CASPT2 / MS-RASPT2).

Finally spin–orbit and configuration interaction effects are included. In the reference calculation for the $SrCl_2$:Yb^{2+}, these were included using an external program [5], but the remaining references typically used the MOLCAS software for this level of calculation [44]. These interactions are achieved by projecting the wavefunction onto a spin–orbit Hamiltonian, and then diagonalising the system. In the references used, the labels used for this level of calculation are spin–orbit, configuration interaction level (SO-CI) [5] or restricted active space state interaction spin–orbit level (RASSI-SO) [44, 68].

Chapter 4

Spectroscopic parameters of *ab initio* $SrCl_2$:Yb^{2+} and $CsCaBr_3$:Yb^{2+}

Ab initio methods for calculating energy levels do not directly expose electron interaction strengths to the user. One method for extracting parameters from an *ab initio* energy level calculation is to fit the parameters to the energy levels of the calculation, as if they were experimental levels. This works well when a large number of energy levels are available, relative to the number of parameters to be fitted. Another method is by direct calculation from the calculated energy levels and eigenvector components [46]. This can be useful in systems where the number of parameters exceeds the number of non–degenerate energy levels, for example, when considering Ce^{3+} in a low–symmetry site. Even ignoring free–ion parameters, the crystal field parameters outnumber the observed energy levels, and so the parameters cannot be obtained by a fitting process [46].

In this chapter, we shall discuss the process of fitting an effective Hamiltonian to *ab initio* energy levels, in order to extract the crystal field parameters from that calculation. The two materials examined in this section are $SrCl_2$:Yb^{2+}, and $CsCaBr_3$:Yb^{2+}. These systems have a large number of energy levels available, and have high–symmetry cubic (Figure 4.1) and octahedral sites (Figure 4.2), respectively, which means very few crystal field parameters are required. They were also chosen for the detail of the *ab initio* calculations available. The energy levels and data from the *ab initio* calculations were provided by Sánchez-Sanz et al. [5, 70].

The material, $SrCl_2$:Yb^{2+}, is of particular interest, as the *ab initio* calculations show interesting structure of the energy levels at higher energies, which could potentially provide

a model for the impurity–trapped exciton present in similar systems. An effective Hamiltonian acting upon the space $4f^{14} \rightarrow 4f^{13}5d/4f^{13}6s$ is constructed, and used to model the ground and excited states of this material, using the $6s$ parameters to model the exciton trap state.

4.1 Ytterbium (II) effective Hamiltonian

The effective Hamiltonian for this system is constructed as detailed in Chapter 2. The ground state of divalent ytterbium has a full $4f$ valence shell, so the ground state Hamiltonian is trivial (ie. a single state):

$$H_{4f^{14}} = E_{\text{avg}}. \tag{4.1}$$

The Yb^{2+} impurity substitutes at the 2+ metal cation site present in each of the host materials. The $SrCl_2$ host has cubic symmetry at the Sr^{2+} site, while $CsCaBr_3$ has octahedral symmetry at the Ca^{2+} site. The structures of these crystals are shown in Figures 4.1 and 4.2. The materials retain their symmetry when the metal ions are substituted with the lanthanide ion, as no charge compensation is required [71]. Both octahedral and cubic symmetries are described by the octahedral point group, O_h, as cubic symmetry is isomorphic to octahedral symmetry [1]. Using Equations 2.16 - 2.20, and Equation 2.24 for the octahedral crystal field contributions, the excited state Hamiltonians are:

$$\begin{aligned} H_{4f^{13}5d} = {} & \Delta_E\left(fd\right) + \sum_{k=2,4} F^k f_k\left(fd\right) + \sum_{k=1,3,5} G^k g_k\left(fd\right) + \zeta\left(f\right)_d A_{so}\left(f\right)_d + \zeta\left(d\right) A_{so}\left(d\right) \\ & + B^4\left(f\right)_d \left[C_0^{(4)} + \sqrt{\frac{5}{14}}\left(C_4^{(4)} + C_{-4}^{(4)}\right)\right] + B^6\left(f\right)_d \left[C_0^{(6)} - \sqrt{\frac{7}{2}}\left(C_4^{(6)} + C_{-4}^{(6)}\right)\right] \\ & + B^4\left(d\right) \left[C_0^{(4)} + \sqrt{\frac{5}{14}}\left(C_4^{(4)} + C_{-4}^{(4)}\right)\right], \end{aligned} \tag{4.2}$$

and:

$$\begin{aligned} H_{4f^{13}6s} = {} & \Delta_E\left(fs\right) + G^3 g_3\left(fs\right) + \sum_{k=2,3} R^k r_k\left(fdfs\right) + \zeta\left(f\right)_s A_{so}\left(f\right)_s \\ & + B^4\left(f\right)_s \left[C_0^{(4)} + \sqrt{\frac{5}{14}}\left(C_4^{(4)} + C_{-4}^{(4)}\right)\right] + B^6\left(f\right)_s \left[C_0^{(6)} - \sqrt{\frac{7}{2}}\left(C_4^{(6)} + C_{-4}^{(6)}\right)\right]. \end{aligned} \tag{4.3}$$

The resultant effective Hamiltonian, acting upon the space, $4f^{14} \rightarrow 4f^{13}5d/4f^{13}6s$, is simply:

$$H_{\text{eff}}^{\text{Yb}^{2+}} = H_{4f^{14}} + H_{4f^{13}5d} + H_{4f^{13}6s}. \tag{4.4}$$

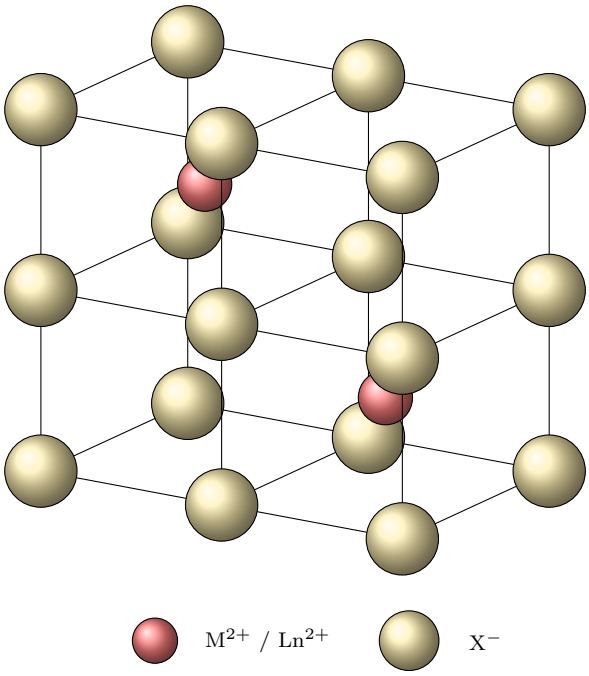

Figure 4.1 A schematic of the cubic structure of $SrCl_2$. The Yb^{2+} impurity substitutes for a Sr^{2+} ion at the metal cation site in the MX_2 lattice.

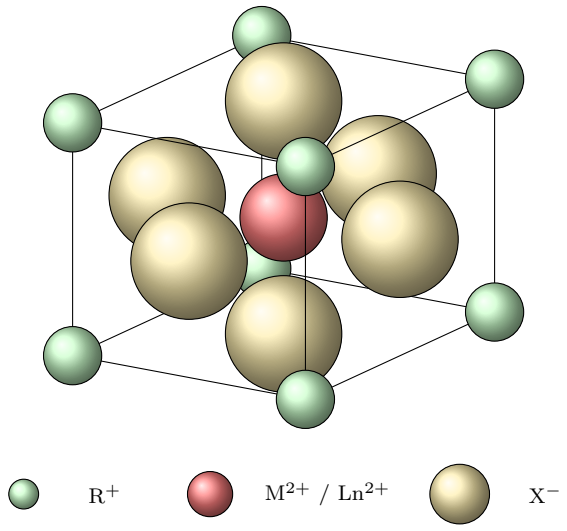

Figure 4.2 A schematic of the octahedral structure of $CsCaBr_3$. The Yb^{2+} impurity substitutes for a Ca^{2+} ion at the metal cation site in the RMX_3 lattice.

The duplicate terms in Equations 4.2 and 4.3; $\zeta(f)_{d/s}$, $B^4(f)_{d/s}$ and $B^6(f)_{d/s}$, are present because each configuration needs a term to describe the $4f^{13}$ component. For any other system (where the ground state has more than one state) these terms may be different from their ground state counterparts, due to the change in configuration. This effect is immediately obvious for duplicate Coulomb parameters (which are not required in this case), but should not be a large effect for the $4f$ crystal field terms, as the $4f$ electrons are largely shielded from the ligands. We therefore assume that $B^k(f)_d = B^k(f)_s = B^k(f)$, and by the same argument, $\zeta(f)_d = \zeta(f)_s = \zeta(f)$. To test this, the spin–orbit parameters from the two configurations were allowed to vary independently in a number of the fits detailed in this chapter. The resulting fits provided a change between the $5d$ and $6s$ configuration f–spin–orbit parameter values on the order of 30 cm^{-1}, which is approximately 1% of the parameter value.

4.1.1 Irreps

The SL basis for this effective Hamiltonian consists of a single state for the $4f^{14}$ ground state; ten states for the $4f^{13}5d$ configuration, corresponding to $S = 0, 1$ and $L = P, D, F, G, H$ quantum numbers; and two states from the $4f^{13}6s$ configuration: $S = 0, 1$ with $L = F$. These provide 25 possible SLJ basis states. Using Table 3.8 of Henderson and Imbusch [1], these SLJ states can be decomposed into irreps of the octahedral group. The resulting system consists of the octahedral irreps shown in Table 4.1.

Table 4.1 Octahedral group irreps present in the $4f^{14} \leftrightarrow 4f^{13}5d/4f^{13}6s$ system.

	Configuration			
Irrep	$4f^{14}$	$4f^{13}5d$	$4f^{13}6s$	Total
A_{1g}	1			1
A_{1u}		6	1	7
A_{2u}		5	2	7
E_u		12	2	14
T_{1u}		18	3	21
T_{2u}		17	4	21

4.2 $SrCl_2$:Yb^{2+}

The first material we shall examine is $SrCl_2$:Yb^{2+}. Details of a rather extensive *ab initio* calculation of energy levels for this system at varying separations between the Yb^{2+} impurity and the surrounding Cl^- ions, R_{Cl} (R_L, in the notation used in Chapter 2), have been provided by Sánchez-Sanz et al. [5, 6, 72]. Figure 4.3 shows the calculated energy levels from this data, at the spin–orbit inclusive level *ab initio* calculation. These energy levels show the presence of double–well potentials occuring in the higher energy excited states. These states are mainly comprised of basis states of the $4f^{13}6s$ configuration. At long impurity–ligand separations they have predominantly $6s$ character, but at shorter distances they become A_{1u} symmetry combinations composed of $5s$ orbitals on the next–nearest–neighbour Sr^{2+} ions, with a contribution from interstitial charge density [5, 73]. It was demonstrated in [6] that all of the states were crucial in explaining the different band–widths observed in the absorption spectrum [74].

In this calculation the A_{1u} potential curve minima have higher energies than the minima of the states with predominantly $6s$ or $5d$ character. Thus, while the exciton–like state is not energetically favourable, it could be described as a "precursor" to the impurity–trapped exciton states that occur in SrF_2:Yb^{2+} and CaF_2:Yb^{2+} at lower energy than the $4f^{13}5d$ configuration [27, 28].

The calculations of Sánchez-Sanz et al. [5] were directly compared with absorption [74] and emission [71] spectra. The calculation results give a good match to the observed spectra, but they do not directly provide information about the magnitudes of the physical interactions involved in the system. Therefore, they cannot be compared with the crystal field analysis of Pan et al. [71]. The advantage of determining the crystal field parameters of the system is that the corresponding interactions have predictable behaviour across the lanthanide series, allowing for the parameters determined for this system to be extrapolated to other lanthanide systems. In simple systems with high symmetry and one valence electron, such as the BaF_2:Ce^{3+} system [4, 46] it is relatively easy to relate the energy levels to crystal field parameters. For such a system at lower symmetry sites, where there are insufficient observable levels to fit the crystal field parameters, it is possible to extract the parameters from an *ab initio* calculation of the energy level structure by way of a direct calculation utilising the eigenfunctions [8, 46]. However, for a many–electron system such as $SrCl_2$:Yb^{2+} the relationship is much more complicated because there are many more parameters in the effective Hamiltonian, and we shall instead obtain the parameters by a least–squares fitting procedure.

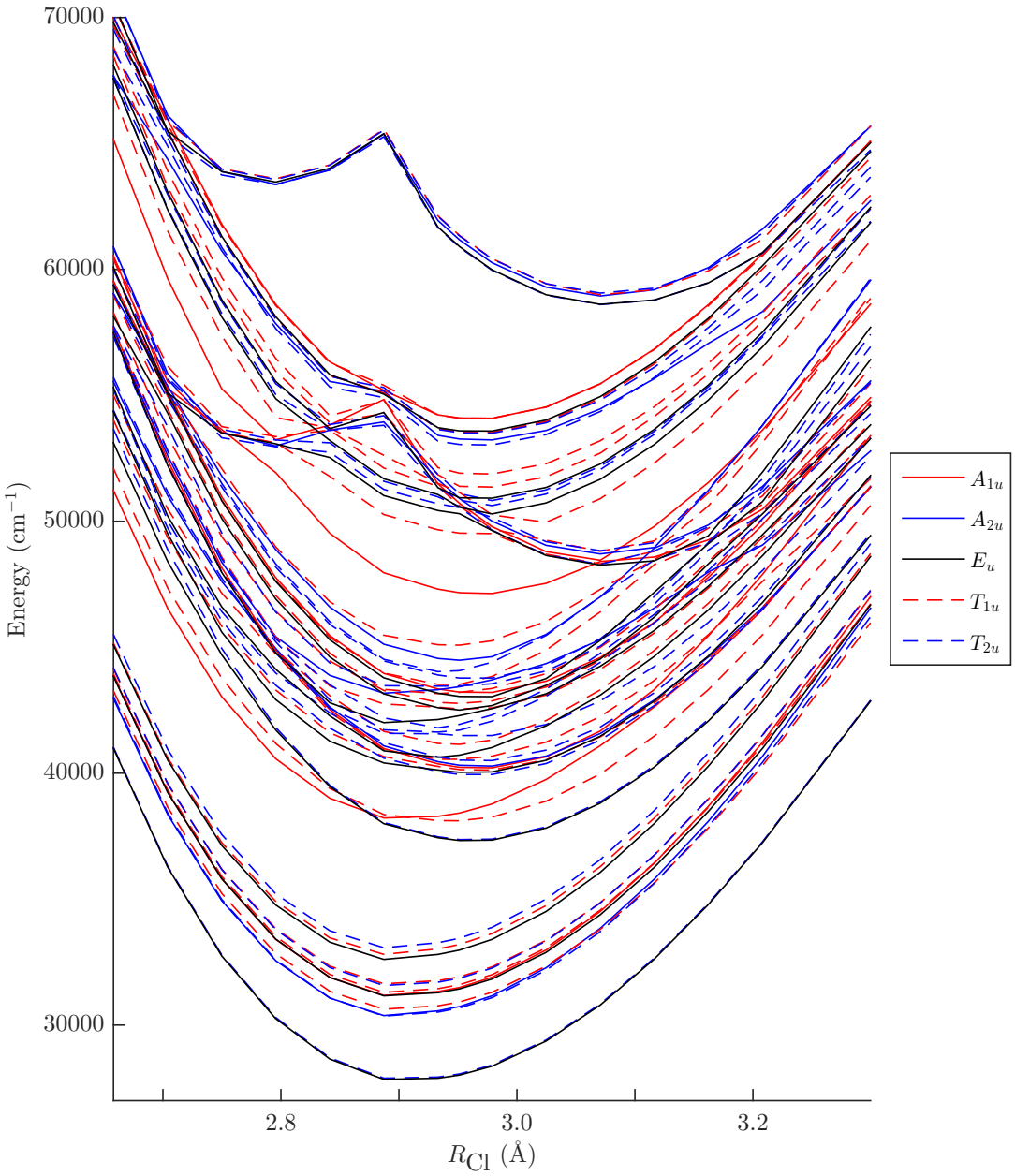

Figure 4.3 Energy levels of excited–state $SrCl_2$:Yb^{2+} calculated by Sánchez-Sanz et al. [5], as a function of impurity–ligand separation (R_{Cl}). The double–well potential curves occur on states with predominantly $6s$ character at longer impurity–ligand separations, and A_{1u} symmetry combinations of $5s$ electron orbitals on the neighbouring Sr^{2+} cations at shorter ligand–impurity separations. These double-well potential curves are a good candidate for a model of an exciton–like trap state, near the conduction band. The $4f^{14}$ curve (A_{1g} irrep), which has a minimum at $R_{Cl} = 2.9514$ Å, is omitted.

4.2.1 Fit to the *ab initio* energy level minima

The fitted energy level calculations were performed using the f–shell empirical software suite, as outlined in Chapter 3. In order to fit the system to the *ab initio* energy levels, a suitable set of initial values were required for the parameters. Common practice is to calculate initial values from the free–ion definitions of the parameters, as given in Chapter 2, or to use fitted parameters from an existing fit to the same or similar impurity, and host material. Pan et al. have fitted a $4f^{14} \rightarrow 4f^{13}5d^1$ effective Hamiltonian to experimental absorption spectra for $SrCl_2$:Yb^{2+} [71]. The parameters from this fitting have been used as a starting point for the same terms in our calculation. The additional parameters introduced by the $4f^{13}6s^1$ component of the effective Hamiltonian are calculated from the definitions in Equation 2.34 [23].

From the triangular conditions imposed by the 6–j symbols, the non–zero Coulomb term is:

$$G^3\left(fs\right) = 3168 \text{ cm}^{-1},$$

as only an operator with an angular momentum of $k = 3$ can couple an f ($l = 3$) state and an s ($l = 0$) state together. For the Coulomb configuration interaction, we recall from the triangular conditions in Equations 2.36 and 2.37 that there are matrices with non–zero elements for $k = 2$ and $k = 3$. The corresponding parameters of the antisymmetrized matrices are:

$$R^2\left(fd, fs\right) = R^2\left(ds\right) = -305 \text{ cm}^{-1}$$
$$R^3\left(fd, sf\right) = R^3\left(ds\right) = 1468 \text{ cm}^{-1}.$$

These values are calculated using Hartree–Fock radial wavefunctions for the appropriate electron orbitals. The wavefunctions (shown in Figure 1.2) were calculated using an implementation of R. D. Cowan's rcn program to solve the restricted Hartree–Fock equations [23]. Table 4.2 contains the initial parameters used for the least–squares fit: those from the fit performed by Pan et al. [71], and those calculated from the free–ion definitions.

The minima of the potential energy curves at each level of the *ab initio* calculation were extracted to use as the target energy levels for the fitting process. At the CASSCF level calculation, there is only one clear minimum for each potential curve. For the CASPT2 and SO-CI levels, there are clear double–well potentials present in the calculation. Fits for these levels were made to both the minima occuring at the shorter and longer impurity–ligand separations (R_{Cl}) of the double–well region, in turn.

Table 4.2 Initial parameter values for the effective Hamiltonian of $SrCl_2$:Yb^{2+}. The fitted parameters are from a calculation of $SrCl_2$:Yb^{2+} by Pan et al. [71]. The free–ion parameters are calculated from the parameter definitions [23]. All parameter values are in cm^{-1}. For the fit by Pan et al., the ratios of F^k the parameters were held fixed, as were the ratios of the G^k parameters.

Parameter	Pan et al. [71] (fitted)	Free–ion [23] (calculated)
$\Delta_E(fd)$	38382	
$\zeta(f)$	2950	2899
$\zeta(d)$	1211	1290
$F^2(fd)$	14355	23210
$F^4(fd)$	7222	10646
$G^1(fd)$	4693	10059
$G^3(fd)$	5382	8046
$G^5(fd)$	4349	6085
$\Delta_E(fs)$		
$G^3(fs)$		3168
$R^2(ds)$		−305
$R^3(ds)$		1468
$B^4(f)$ [a]	−725	
$B^6(f)$ [b]	292	
$B^4(d)$ [a]	−20442	
N	12	
n	4	
σ	103	

In addition to the constraints necessary to provide cubic symmetry to the crystal field contribution (Equation 2.24), it is a common practice to constrain the ratios of the remaining crystal field parameters, and sometimes the ratios of Coulomb parameters, as necessary to obtain a reasonable fit [13, 65]. An example of this occurs in the $SrCl_2$:Yb^{2+} calculation by Pan et al. [71]. This is found to be necessary in some of the calculations of Chapter 6, but this is not required for the first sequence of fits: all parameters were allowed to vary

[a] $B^4_0 = B^4$, $B^4_{\pm 4} = \sqrt{\frac{5}{14}}B^4$.

[b] $B^6_0 = B^6$, $B^6_{\pm 4} = -\sqrt{\frac{7}{2}}B^6$.

freely wherever possible. The parameters that are most frequently constrained were the $R^k\,(ds)$ configuration interaction parameters. These were typically averaged from a number of fits, varying in initial parameter values, with all other parameters fixed. Regardless of the method used, these parameter values often have little or no effect on the overall calculation.

4.2.1.1 Fit results

Table 4.3 contains the resultant parameters fitted to each level of the *ab initio* calculation, and Table 4.4 contains the energy levels calculated for the SO-CI level. For the spin–orbit inclusive fits, the stability of each fit was tested by taking a large number of trials, varying the initial parameter values for each fit through a wide range of values. Several distinct local minima in the solution space were obtained through these trials. The solutions were ranked by standard deviation, in order to select only viable candidates for the fit. The values of the free–ion parameters between these distinct local minima cover only a small range of values. The average standard deviation for these local minima was $\sigma = 195$ cm^{-1}. Of the parameters, the $4f^{13}5d$ parameters vary the least, converging to a small range of values for each parameter. The $G^3\,(fs)$ parameter also follows this trend, converging to values comparable to the free–ion prediction. This result is to be expected since the *ab initio* calculation predicts predominantly $6s$ character for the excited electron at the fitted minima [5].

The largest variation arises in the $R^2\,(ds)$ and $R^3\,(ds)$ parameters. As the matrix representations of the r_2 and r_3 operators have no diagonal elements, there is only a weak mixing of some $5d$ and $6s$ states. The resultant energies of the calculation are insensitive to small variations in $R^2\,(ds)$ and $R^3\,(ds)$ parameters, hence the uncertainties of these fits are correspondingly large. The $R^2\,(ds)$ and $R^3\,(ds)$ parameters tend to converge to positive and negative values, of similar magnitude, with equal frequency. If we examine the energy levels in Table 4.4, we observe that some of the states without a dominant $6s$ contribution vary slightly between the two fits. As the only parameter that has changed is the $6s$ configuration average energy, $\Delta_E(fs)$, there must be some mixing of $6s$ character in these states, which arises due to the $R^k\,(ds)$ parameters and operators. That the size of this mixing results in an energy shift on the order of a few wavenumbers for a change in $\Delta_E(fs)$ parameter of ≈ 4500 cm^{-1} demonstrates why the fitting process has difficulty optimising these parameters.

Table 4.3 Parameter values for the effective Hamiltonian of $SrCl_2$:Yb^{2+} fitted to three levels of *ab initio* calculation of Sánchez-Sanz et al. [5]. The labels CASSCF, CASPT2 and SO-CI refer to the level of the reference calculation (as defined in Chapter 3). All parameter values and uncertainties (σ) are in cm^{-1}. At the CASPT2 and SO-CI levels of the calculation, the states with predominantly $6s$ character exhibit double–well potentials. To fit to the minima corresponding to the A_{1u} delocalised states, only the average configurational energy shift parameter, $\Delta_E\,(fs)$, needs to be changed. The rest of the parameters are held at the values for the fit to the global minima. Note: $\Delta_E\,(fs) = \Delta_E\,(fd) + \Delta_E\,(ds)$.

	CASSCF		CASPT2		SO-CI	
Parameter	Value	$\pm\sigma$	Value	$\pm\sigma$	Value	$\pm\sigma$
$\Delta_E(fd)$	12060	(494)	41895	(337)	41800	(195)
$\zeta(f)$					2943	(19)
$\zeta(d)$					1149	(105)
$F^2(fd)$	23412	(1196)	17776	(845)	18411	(412)
$F^4(fd)$	11338	(2269)	13665	(1623)	12994	(1051)
$G^1(fd)$	7702	(350)	4888	(340)	5404	(219)
$G^3(fd)$	8766	(1303)	9356	(906)	8693	(838)
$G^5(fd)$	6834	(1618)	5250	(1191)	7214	(1280)
$G^3(fs)$	6998	(1605)	2767	(952)	2883	(822)
$R^2(ds)$	1948		1948		1948	
$R^3(ds)$	1990		1990		1990	
$B^4(f)$	−674	(622)	401	(382)	−200	(279)
$B^6(f)$	−161	(309)	−45	(215)	−515	(333)
$B^4(d)$	−18881	(481)	−20190	(312)	−20132	(189)
Long R_{Cl} minima:						
$\Delta_E(ds)$	9560	(287)	11061	(169)	11118	(62)
Short R_{Cl} minima (A_{1u} exciton):						
$\Delta_E(ds)$			15480	(148)	15745	(92)
Fit details:						
N	33		34		71	
n	12		12		14	
σ	484		330		193	

Table 4.4 Energy levels for the Yb^{2+} $4f^{14} \rightarrow 4f^{13}5d/4f^{13}6s$ effective Hamiltonian, in $SrCl_2$, calculated using the parameters in Table 4.3 for the SO-CI level (spin–orbit) level calculation. Energy levels for both the long and short R_{Cl} minima fits are presented. The ΔE are the difference between the effective Hamiltonian and reference energy levels. All values are in cm^{-1}. It can be seen that these are mostly identical, with differences only occuring on the eigenvectors that have sufficient contributions from $6s$ basis states. States with predominant $6s$ character have been labelled. Some states without predominant $6s$ character also vary by a few cm^{-1}, due to the $R^k\,(ds)$ parameters. While it is possible to label most irreps with a dominant $^{S}L_J$ multiplet label, there are a sufficient number of highly mixed states that it is impractical to present the states grouped by multiplet label.

			Long R_{Cl}		Short R_{Cl}		
		Ab initio	Energy		Energy		$\left\vert^{S}L_J\right\rangle$
Irrep		Reference	H_{cf}	ΔE	H_{cf}	ΔE	
1	A_{1g}	0	0	0	0	0	$^1S_0$
1	E_u	27781	27722	59	27722	59	$^3P_2$
1	T_{2u}	27828	27754	74	27754	74	$^3P_2$
1	T_{1u}	30598	30359	239	30359	239	$^3H_5$
1	A_{2u}	30357	30513	-156	30513	-156	$^3D_3$
2	T_{2u}	30332	30540	-208	30540	-208	*mixed*
2	E_u	31125	31125	0	31125	0	$^3H_5$
1	A_{1u}	31151	31189	-38	31189	-38	$^3F_4$
2	T_{1u}	31269	31240	29	31240	29	*mixed*
3	T_{2u}	31538	31335	203	31335	203	$^3H_6$
3	T_{1u}	31606	31521	85	31522	84	$^3H_5$
3	E_u	32590	32952	-362	32952	-362	$^3G_5$
4	T_{1u}	32795	33122	-327	33122	-327	*mixed*
4	T_{2u}	33058	33422	-364	33422	-364	$^1G_4$
4	E_u	37305	37609	-304	37609	-304	$^3H_6$
5	T_{2u}	37343	37632	-289	37632	-289	$^3H_6$
2	A_{1u}	38163	38028	135	38028	135	$^3P_0$
5	T_{1u}	38103	38126	-23	38126	-23	$^3P_1$
6	T_{2u}	39920	39896	24	39896	24	$^3H_6$
2	A_{2u}	40269	39971	298	39971	298	$^3H_6$
6	T_{1u}	40105	40053	52	40053	52	$^3H_6$

Continued on next page...

Table 4.4 *Continued*

Irrep		*Ab initio* Reference	Long R_{Cl} Energy H_{cf}	Long R_{Cl} Energy ΔE	Short R_{Cl} Energy H_{cf}	Short R_{Cl} Energy ΔE	$\left\|^{S}L_{J}\right\rangle$
5	E_u	40023	40162	-139	40162	-139	*mixed*
3	A_{1u}	40194	40321	-127	40321	-127	$^3H_6$
7	T_{2u}	40484	40362	122	40362	122	$^1D_2$
6	E_u	40623	40406	217	40406	217	$^3H_4$
7	T_{1u}	40540	40580	-40	40580	-40	*mixed*
8	T_{1u}	41142	41094	48	41094	48	$^3D_3$
8	T_{2u}	41479	41185	294	41185	294	$^3F_4$
9	T_{2u}	41624	41456	168	41456	168	*mixed*
10	T_{2u}	41781	41567	214	41567	214	$^3H_4$
7	E_u	41988	42011	-23	42011	-23	$^3F_2$
9	T_{1u}	42536	42264	272	42264	272	$^3G_5$
10	T_{1u}	42769	42382	387	42382	387	*mixed*
8	E_u	42533	42603	-70	42603	-70	$^3G_5$
11	T_{1u}	43163	42893	270	42894	269	$^1G_4$
9	E_u	43007	42920	87	42920	87	*mixed*
4	A_{1u}	43183	43209	-26	43209	-26	$^1G_4$
11	T_{2u}	43365	43388	-23	43388	-23	$^1G_4$
3	A_{2u}	43151	43457	-306	43457	-306	$^3F_3$
12	T_{1u}	43507	43581	-74	43581	-74	*mixed*
12	T_{2u}	43752	43714	38	43714	38	$^3G_5$
13	T_{2u}	44025	44114	-89	44114	-89	$^3G_4$
4	A_{2u}	44489	44381	108	44381	108	$^3G_3$
13	T_{1u}	45076	44713	363	44713	363	$^3G_5$
5	A_{1u}	47118	47381	-263	47381	-263	$^3P_0$
10	E_u	48218	48204	14	48272	-54	$^3F_4\,(6s)$
14	T_{1u}	48309	48278	31	48339	-30	$^3F_4\,(6s)$
14	T_{2u}	48288	48284	4	48349	-61	$^3F_4\,(6s)$
6	A_{1u}	48433	48454	-21	48521	-88	$^3F_4\,(6s)$
15	T_{2u}	48828	48719	109	48644	184	$^1F_3\,(6s)$
5	A_{2u}	48700	48753	-53	48693	7	$^1F_3\,(6s)$

Continued on next page...

Table 4.4 *Continued*

Irrep		*Ab initio* Reference		Long R_{Cl} Energy		Short R_{Cl} Energy		$\left\|^{S}L_J\right\rangle$
				H_{cf}	ΔE	H_{cf}	ΔE	
15	T_{1u}	48801		48839	-38	48781	20	$^1F_3/^3F_3\,(6s)$ [a]
16	T_{1u}	49905		49822	83	49822	83	$^3D_1$
11	E_u	50291		50253	38	50254	37	$^3F_2$
16	T_{2u}	50612		50546	66	50547	65	$^3H_4$
17	T_{2u}	50820		50878	-58	50878	-58	*mixed*
12	E_u	50862		51024	-162	51024	-162	$^3D_2$
17	T_{1u}	51298		51700	-402	51700	-402	$^1P_1$
18	T_{1u}	51854		51930	-76	51934	-80	*mixed*
18	T_{2u}	53012		52851	161	52852	160	$^3G_3$
6	A_{2u}	53218		53143	75	53162	56	$^1F_3$
19	T_{2u}	53475		53315	160	53324	151	$^1F_3$
19	T_{1u}	53512		53419	93	53421	91	$^3G_3$
13	E_u	53560		53703	-143	53703	-143	$^3G_4$
20	T_{1u}	54064		54192	-128	54194	-130	$^3G_4$
7	A_{1u}	54067		54307	-240	54307	-240	*mixed*
		Long	Short					
20	T_{2u}	58601	63359	58591	10	63281	78	$^3F_2\,(6s)$
14	E_u	58594	63461	58623	-29	63314	147	$^3F_2\,(6s)$
21	T_{2u}	58995	63550	58984	11	63549	1	$^3F_3\,(6s)$
7	A_{2u}	59048	63363	58996	52	63536	-173	$^3F_3\,(6s)$
21	T_{1u}	58937	63582	59028	-91	63581	1	$^3F_3/^1F_3\,(6s)$ [a]

4.2.1.2 Comparison with experimental fit

If we look at Table 4.2, we see that the Coulomb parameters calculated for a free Yb^{2+} ion significantly overestimate the values fitted to experimental observations. If we compare this with the values in Table 4.3, the free–ion calculations still overestimate the F^2 and G^1

[a] These irreps consist of nearly 50% of each of the two ^SL_J multiplet contributions. The other mixed states consist of much less dominant contributions from two or more basis ^SL_J multiplets.

Coulomb terms at CASPT2 and SO-CI levels, but most of the remaining Coulomb terms are larger than the free–ion estimates. At each level of the *ab initio* calculations, the fitted Coulomb parameters are greater than those fitted to the experimental spectrum. The free–ion calculations are expected to overestimate these values, as they use Hartree–Fock radial wavefunction approximations, and should hence be an upper limit on reasonable values. The CASSCF level calculation is very consistent with the free–ion values. As mentioned in Chapter 3, the CASSCF level calculation is an optimisation of a Slater determinant basis, in the same iterative manner as the Hartree–Fock equations are solved. Therefore, the similarity in values is expected.

The f crystal field parameters are not consistent with the values of Pan et al., indicated in Table 4.2. At both the CASSCF and SO-CI levels, both f crystal field parameters are negative, whereas we expect the B^6 parameter to be positive, based on the fit to experimental levels [71]. At the CASPT2 level, the signs of both of these parameters are reversed from the expected directions. Looking at the magnitudes of the parameters, we see that the CASSCF level parameters agree best with the experimental parameters. At the CASPT2 level, the magnitudes of these parameters decrease from the CASSCF values, indicating a weaker f crystal field. Finally, at the SO-CI level, the relative magnitudes of the B^4 and B^6 parameters are reversed. While the strong d crystal field interaction is reproduced well by the *ab initio* calculation, the variation in the resulting parameters between calculation levels indicates that the weaker f crystal field interactions are not reproduced well.

Figure 4.4 shows the position of the absorbing T_{1u} irreps arising from the fitted effective Hamiltonian compared to those of the SO-CI calculation. Both the long– and short–distance minima are shown. There is a good agreement between the two calculations, which indicates that spectra simulated using these energy levels/eigenvectors might look similar to the reference calculation. However, when we consider every irrep, as in Figure 4.5, we can see that the order of irreps is not conserved between the two kinds of calculations. This will not directly affect any spectrum simulated using these calculated energy levels, as only the T_{1u} irreps have an allowed transition with the ground configuration. In the calculations performed by Sánchez-Sanz et al., the wavefunction resulting from the CASPT2 level calculation is projected onto the much smaller space of the spin–orbit Hamiltonian. This projection is stated to have not conserved the energy order of irreps [5]. The energy order is therefore very unlikely to be able to be reproduced using this effective Hamiltonian.

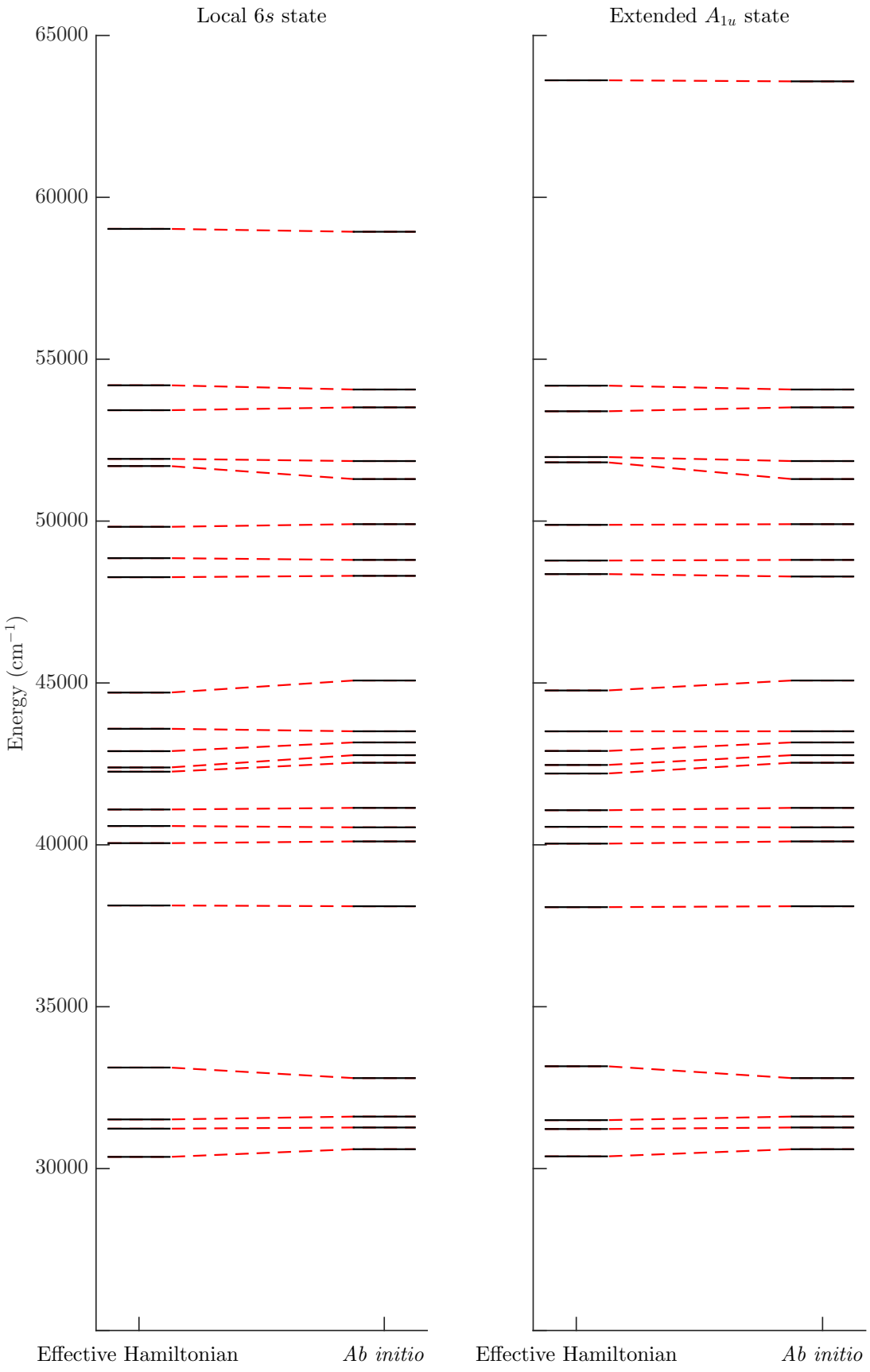

Figure 4.4 Absorbing T_{1u} states, matching the fitted effective Hamiltonian energy levels to the long and short minima regions of Figure 4.3.

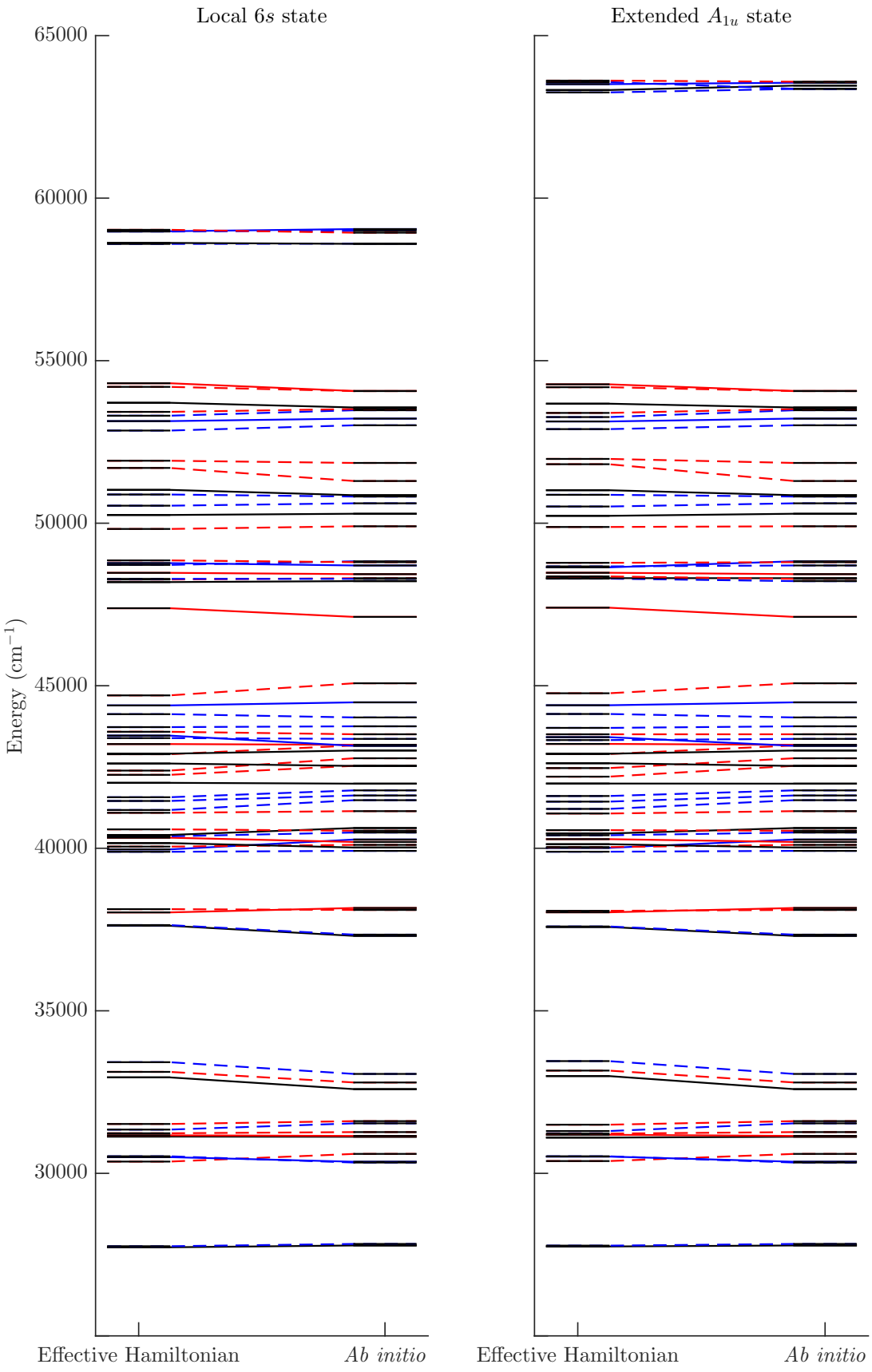

Figure 4.5 All irreps, matching the fitted effective Hamiltonian energy levels to the long and short minima regions of Figure 4.3.

4.2.2 Fit by impurity–ligand separation

The data provided by Sanchez-Sanz et al. provides potential energy curves for the states across a range of impurity–ligand separations (R_{Cl}). The data consists of energy levels at seventeen different R_{Cl} in the range 2.4748 Å – 3.2997 Å. An effective Hamiltonian was fitted to the energy curves at each of the different separations. This is equivalent to modelling an instantaneous vertical energy transition, ignoring any relaxation that would occur in the system if it were given time to evolve (ie. no broadening). This is, of course, not a physical process.

As many of the energy curve minima occur near the ground $4f^{14}$ state energy minimum, the parameters fitted to the minima in the previous section (Table 4.3) can be used as initial values for the fitting process. Each adjacent impurity–ligand separation is sufficiently similar that the parameter values fitted to the first fit provide suitable initial values for the adjacent fits. This process is then repeated to fit an effective Hamiltonian at each R_{Cl}.

The resulting parameters from these fits are shown in Figures 4.6 – 4.8, plotted against impurity–ligand separation. Figure 4.6 shows the CASSCF level parameters, Figure 4.7 shows the CASPT2 level parameters, and Figure 4.8 shows the SO-CI level parameters.

The best fits were obtained at impurity–ligand separations that correspond to either minimum of the double–well potential curves, at the SO-CI level of the reference calculation. For the longer ion separation potential well, the fits ranged in standard deviation from 130 cm^{-1} to 190 cm^{-1}, with the best parameter fit to the energy levels occurring at $R_{\mathrm{Cl}} = 3.1164$ Å, near the ground–state minimum. The shorter separation well, corresponding to A_{1u} exciton–like behavior, has a minimum standard deviation of $\sigma = 156\ \mathrm{cm}^{-1}$ at $R_{\mathrm{Cl}} = 2.7498$ Å. However, the accuracy of the fit decreases rapidly as the impurity–ligand separation decreases, with the standard deviation climbing to $\sigma > 500\ \mathrm{cm}^{-1}$. At the point of discontinuity between the $6s$ electron and A_{1u} exciton regimes ($R_{\mathrm{Cl}} = 2.8414$ Å) there is a reasonable fit to the energies, with a standard deviation of $\sigma = 190\ \mathrm{cm}^{-1}$. This suggests that as the system becomes highly compressed, the *ab initio* calculation starts to provide a less viable solution, as the electron interactions become increasingly difficult to associate with those of the effective Hamiltonian model.

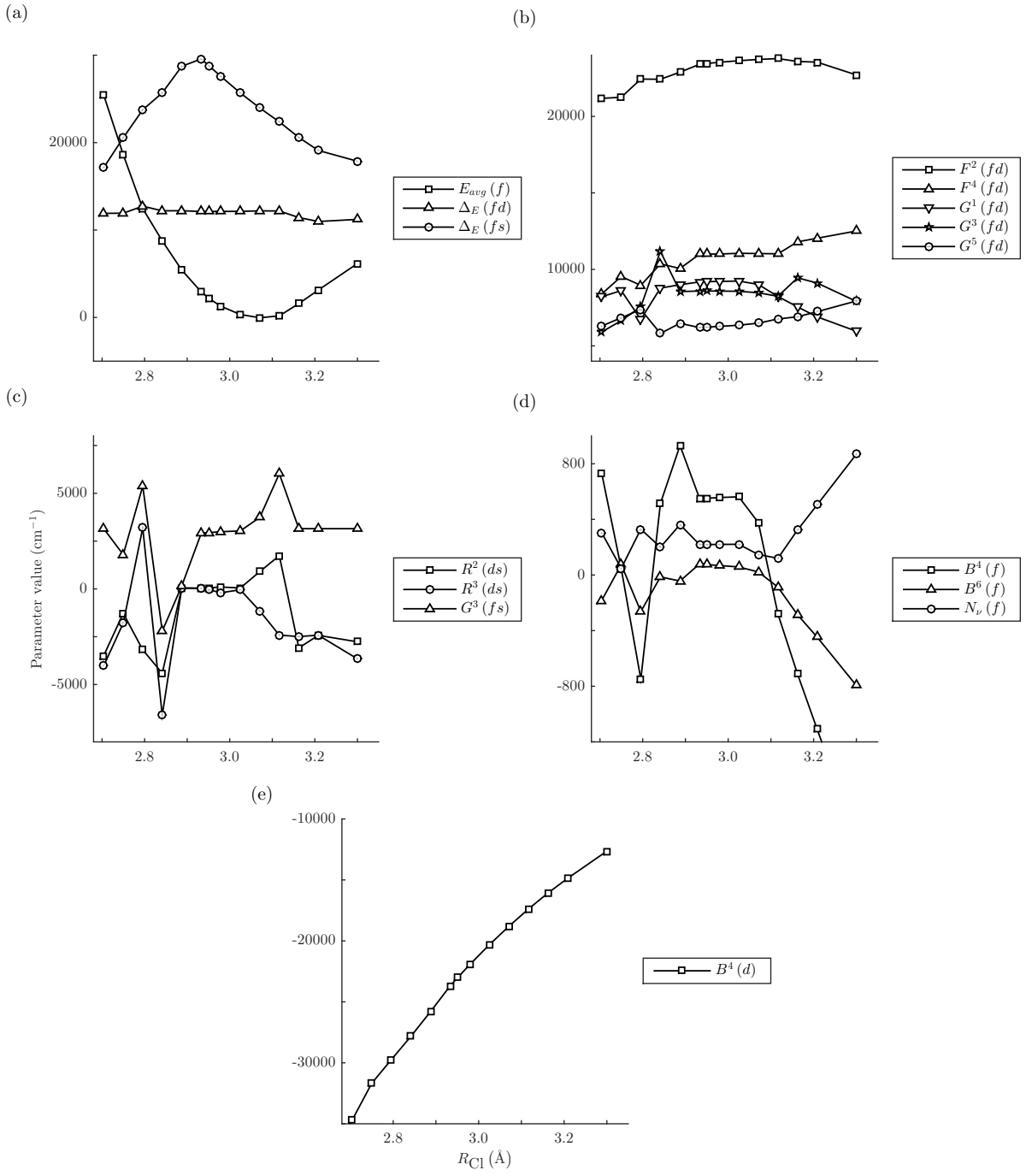

Figure 4.6 Parameters for the $4f^{14} \rightarrow 4f^{13}5d/4f^{13}6s$ effective Hamiltonian, optimised by fitting to energies of $SrCl_2$:Yb^{2+} using the CASSCF level calculation of Sánchez-Sanz et al. [5]. The plots are split into groups of comparable parameters: (a) Average configuration energy parameters. (b) fd Coulomb parameters. (c) fs Coulomb parameters. (d) $4f$ crystal field parameters. (e) $5d$ crystal field parameter.

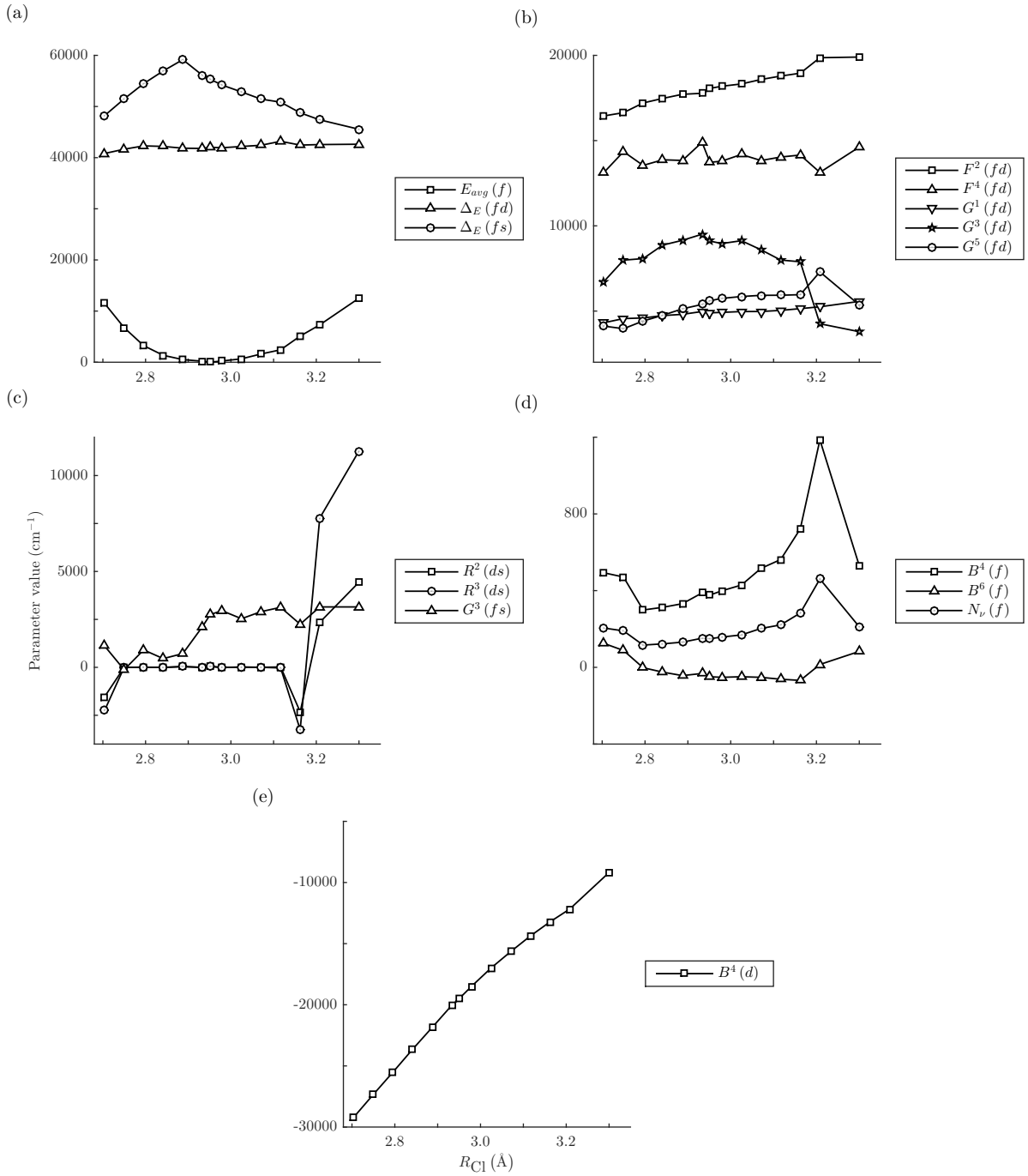

Figure 4.7 Parameters for the $4f^{14} \rightarrow 4f^{13}5d/4f^{13}6s$ effective Hamiltonian, optimised by fitting to energies of $SrCl_2$:Yb^{2+} using the MS-CASPT2 level calculation of Sánchez-Sanz et al. [5]. The plots are split into groups of comparable parameters: (a) Average configuration energy parameters. (b) fd Coulomb parameters. (c) fs Coulomb parameters. (d) $4f$ crystal field parameters. (e) $5d$ crystal field parameter.

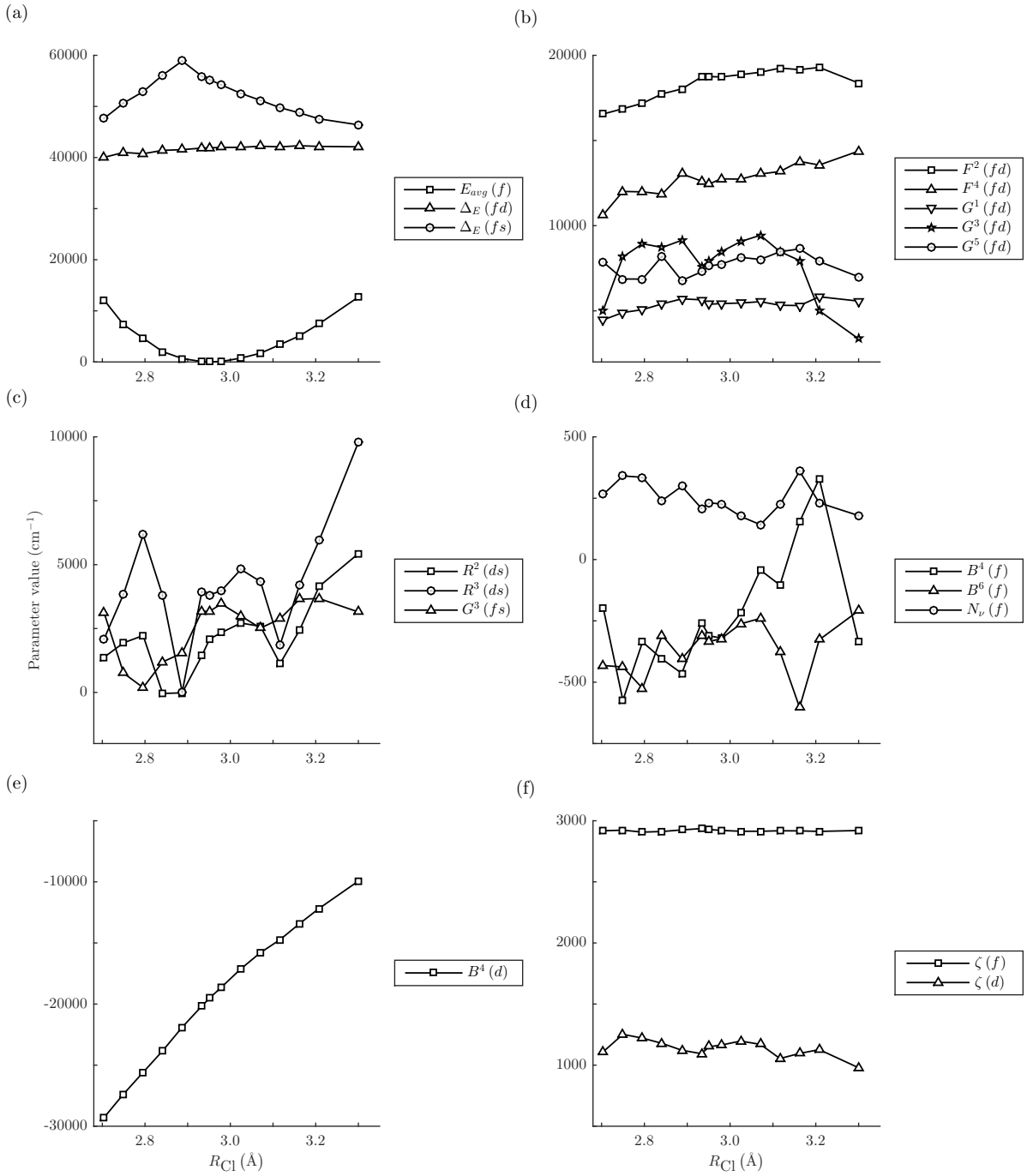

Figure 4.8 Parameters for the $4f^{14} \rightarrow 4f^{13}5d/4f^{13}6s$ effective Hamiltonian, optimised by fitting to energies of $SrCl_2$:Yb^{2+} using the spin–orbit level calculation (SO-CI) of Sánchez-Sanz et al. [5]. The plots are split into groups of comparable parameters: (a) Average configuration energy parameters. (b) fd Coulomb parameters. (c) fs Coulomb parameters. (d) $4f$ crystal field parameters. (e) $5d$ crystal field parameter. (f) Spin–orbit parameters.

4.2.2.1 SO-CI level

We begin our analysis by examining the highest level of the calculation, as this is where the trends in the parameters are the clearest. Looking at the SO-CI fit, in Figure 4.8, we see that most of the potential curve shape in Figure 4.3 is controlled by the average configuration energy parameter, $E_{\text{avg}}(f)$. This term consists of all symmetric effects of the Hamiltonian, such as kinetic energy of the electrons. The $\Delta_E(fd)$ is a near–constant offset, as the $4f^{13}5d$ curves all have very similar shape to the ground $4f^{14}$ curve. The $4f^{13}6s$ average has a discontinuity at 2.85 Å, as seen in $\Delta_E(fs)$, reflecting an avoided crossing between localized and delocalized states of the excited electron. As stated in the reference, at longer distances these states are predominantly $4f^{13}6s$ in character, as the electron is more closely associated with the ytterbium ion, but at shorter distances they have significant delocalization, and can be considered an ITE state [5].

Several trends are observable in the remaining parameter values as they vary with length. The f spin–orbit parameter, $\zeta(f)$, is very nearly constant with increased impurity–ligand separation, but the d spin–orbit parameter, $\zeta(d)$, decreases slightly with increased separation.

The $F^k(fd)$ and $G^k(fd)$ Coulomb parameters show a general decline with decreasing ion separation. This can be explained by the nephelauxetic effect interpretation, where the valence electrons become increasingly delocalized as the bonding between an ion and its ligand increases. Spreading the valence d–electron distributions further from the ion, while leaving the shielded f–electron distributions unchanged decreases the overlap of the f– and d–electron wavefunctions, which, by the Slater integral definition in Equation 2.34, reduces the Coulomb interactions [75]. This is demonstrated in the schematic in Figure 4.9.

The decrease in the d spin–orbit parameter with increasing impurity–ligand separation can probably also be attributed to the nephelauxetic effect. If we consider the definition of the spin–orbit parameter (Equation 2.39), and make the very rough assumption that the nephelauxetic effect can be approximated by stretching and renormalising the P_{nl} radial probability functions, we require that the magnitude of the potential experienced by the d electron decreases with increasing radius in order to reproduce this observed trend in the d spin–orbit parameter. Under the central–field approximation, the potential experienced by the electrons would be approximately r^{-3} [51], neglecting shielding due to other electrons. While this is a poor approximation for the actual potential experienced by the d electon, it does agree with the observed trend, and departures from the model

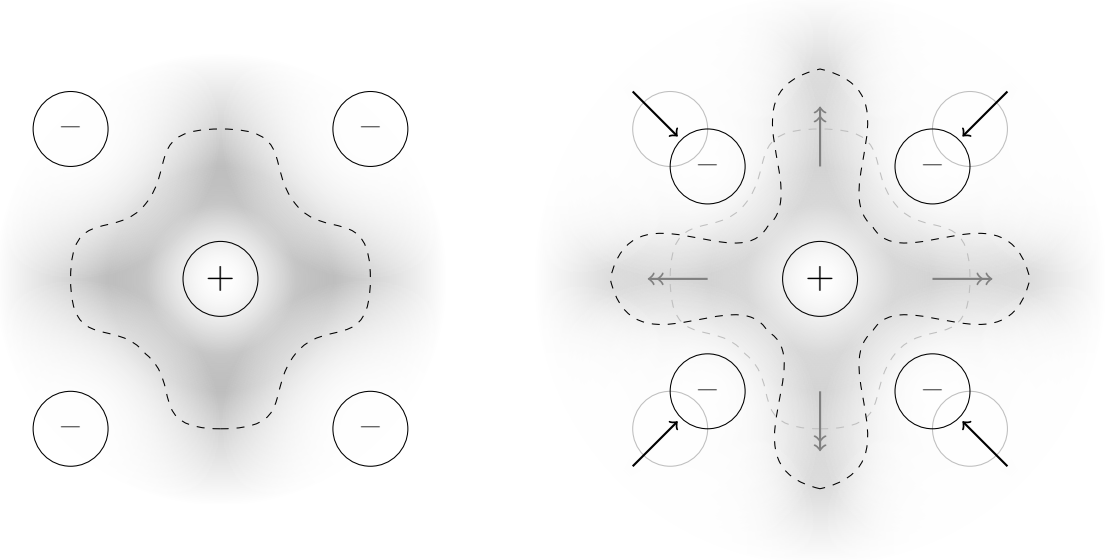

Figure 4.9 An illustration of the nephelauxetic (electron cloud expanding) effect. The electron orbital is demonstrated in a simple schematic, as the shaded region following the shape of the dashed line. As the cage of ligands around a cation site are compressed, the outermost electron orbitals of the cation extend into the interstitial regions, instead of simply contracting. This causes Coulomb interactions between the valence electrons of the cation to decrease, as the electron wavefunction overlap decreases.

are unlikely to effect this long–term behaviour of the potential.

The $SrCl_2$ $4f$ crystal field parameters $B^4(f)$ and $B^6(f)$ exhibit a reasonably smoothly varying region, $R_{Cl} = 2.75$ Å $- 3.05$ Å, with greater fluctuations in parameter values outside of this region. In this smoothly varying region, the parameter magnitudes increase as the ligands are contracted (decreasing R_{Cl}). This is expected, as the magnitude of the crystal field effects are influenced by the proximity to neighbouring elements of the host crystal. This is expected to follow a power–law dependence, as given in Equation 2.30. The expected power–law models, using a point–charge model, have been fitted to the parameters in this region in Figure 4.10. The models fit the variation of the parameters reasonably well, and in particular, reproduce the total f crystal field strength, N_ν, well.

That the parameter variations are reproduced sufficiently accurately by a point–charge model power–law is an interesting feature. The reference *ab initio* calculations use relativistic core *ab initio* model potentials (AIMPs) [69] to describe the nearest lattice constituents to the impurity site (those within $4a_0$), and then point–charges for the contributions from more distant ions [5]. The AIMPs are calculated from the Hartree–Fock

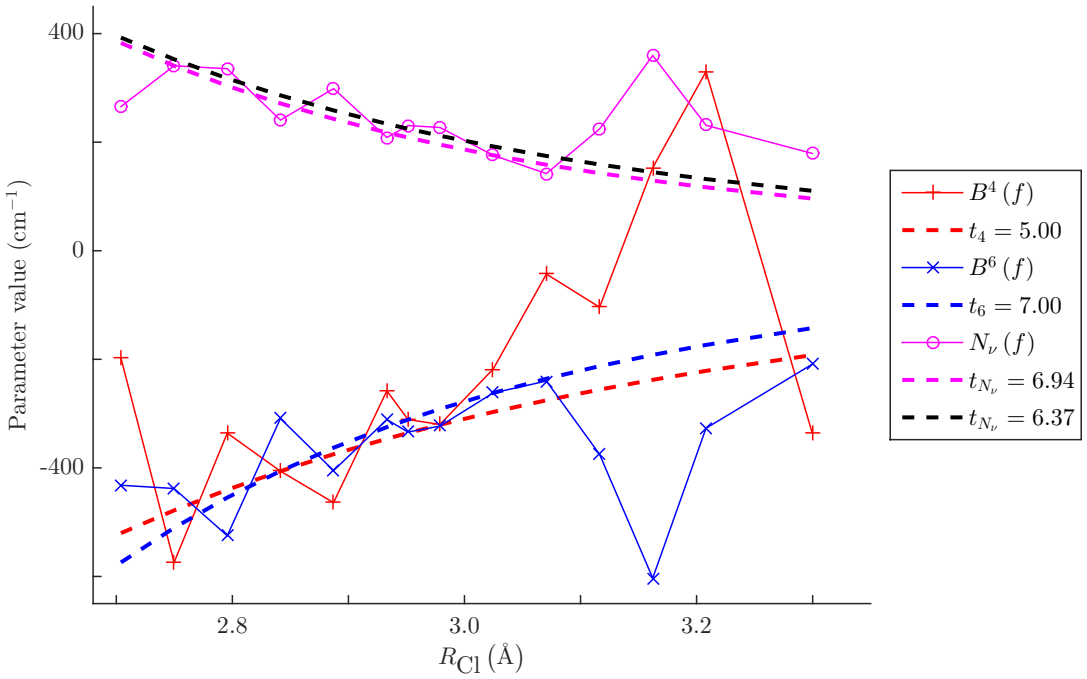

Figure 4.10 Point–charge power–law fits to the f crystal field parameters, $B^4(f)$ and $B^6(f)$; and the total f crystal field strength, N_ν, for the SO-CI level calculation of $SrCl_2:Yb^{2+}$, using Equation 2.30. The $B^4(f)$ and $B^6(f)$ parameters have been fitted to the theoretical point–charge model, (ie. $t_4 = 5$ and $t_6 = 7$), using the smoothly changing region of the parameters ($R_{Cl} = 2.75$ Å $- 3.05$ Å). The dashed lines show the power–law models. The total field strength, N_ν, has both a single power–law exponent fitted to it (dashed magenta line); and has been modelled from the $B^4(f)$ and $B^6(f)$ power–law curves (dashed black line).

definitions of the appropriate ions. These potentials should provide a more accurate description of the interaction of the impurity with the electrons of the host lattice than simple point–charges, as the valence electrons of these ions are explicitly involved in the *ab initio* calculation. In this case, however, the effects of these AIMPs are reproducable using just the point–charge model of the crystal field Hamiltonian.

Likewise, the $5d$ crystal field parameter, $B^4(d)$, shows a smooth increase in magnitude as the ligands contract, and does so for all levels of the reference calculation. The SO-CI level parameter variation may be approximated by a power–law dependence of $R_{Cl}^{-5.43}$, as demonstrated in Figure 4.11. This dependence is steeper than a simple point–charge crystal field model (R_{Cl}^{-5}) [76]. However, this is considerably closer to the point–charge model than typical experimental observations, which have much greater power–law coefficients than predicted by the model. The power–law coefficient for lanthanides with chloride ligands are typically observed to be in the range $t_4 = 12 - 16$ [14, 59].

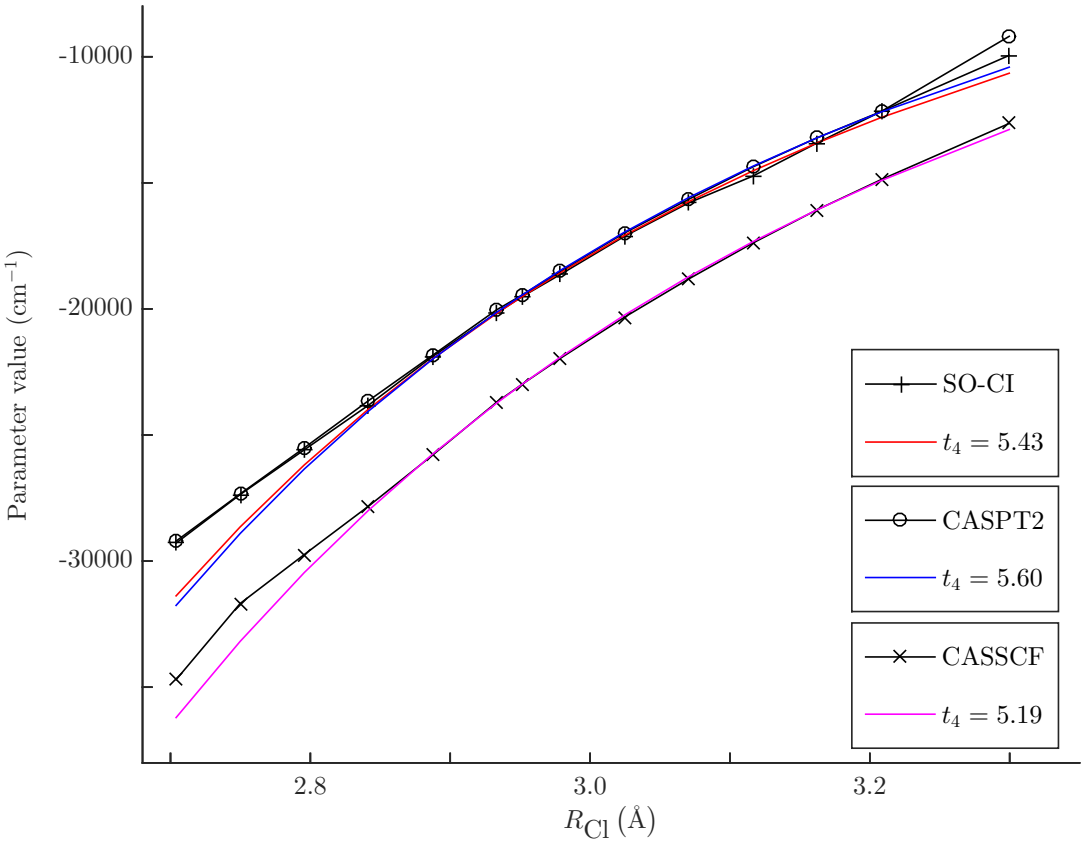

Figure 4.11 Point–charge power–law fits to the d crystal field parameter, $B^4(d)$, for the different calculation levels of $SrCl_2$:Yb^{2+}, using Equation 2.30. The CASPT2 and SO-CI levels have very similar parameter values at all R_{Cl}, and hence have a very similar power–law fit. The reference point, R_0, is chosen to be 2.9514 Å, as the best effective Hamiltonian fits for all levels of calculation occur in this central region.

The signs of the f crystal field parameters are consistent with the fit to the curve minima, which does not match the expected crystal field parameters based on experimental observations, as stated previously.

We have already noted the discontinuity in $\Delta_E\,(fs)$ at 2.85 Å as the excited electron switches between $6s$ character at long impurity–ligand separations, and delocalized character at short separations. In theory, we would expect a similar discontinuity to occur in the remaining $6s$ parameters. The $R^2\,(ds)$ and $R^3\,(ds)$ parameters fluctuate too much and are too uncertain to draw any conclusions. However, the $G^3\,(fs)$ parameter does appear to exhibit a discontinuity, dropping in value by a factor of three at the discontinuity at $R_{\mathrm{Cl}} = 2.85$ Å. If the excited electron becomes delocalized, as in the case of ITEs, it would be expected that the magnitude of the Coulomb interaction between the excited electron and the $4f^{13}$ core would decrease, which indicates that this change in strength of the $G^3\,(fs)$ parameter is a good model of this excitonic behavior. The $G^3\,(fs)$ parameter fluctuates too much in each region to be able to distinguish any nephelauxetic effect as the ligands contract. By observation, a gradient similar to those on the fd Coulomb parameters could feasibly fit the $G^3\,(fs)$ parameter in the longer R_{Cl} region ($R_{\mathrm{Cl}} > 2.85$ Å).

4.2.2.2 CASPT2 level

At the CASPT2 level (Figure 4.7), similar patterns are observed. Again, the overall shapes of the potential energy curves are determined by the average configuration energy terms. There is very little difference between the corresponding values of the configuration average parameters of the SO-CI and CASPT2 levels of calculation, other than some noise. This is a good outcome, as the differences should lie primarily in the addition of spin–orbit parameters.

The fd Coulomb parameters are similarly well–behaved, varying slightly from the higher–level calculation, mostly towards the extreme ends of the data. The nephelauxetic effect can again be observed in the parameters, as they mostly decrease as the ligands contract. The nephelauxetic effect is also apparent in the $G^3\,(fs)$ parameter, which varies much more smoothly than for the SO-CI level. The parameter also exhibits a very clear discontinuity, causing the parameter to decrease by a factor of approximately 3 – 4, about the point of the discontinuity.

The $R^2\,(ds)$ and $R^3\,(ds)$ parameters tend to near–zero values for a large range of separa-

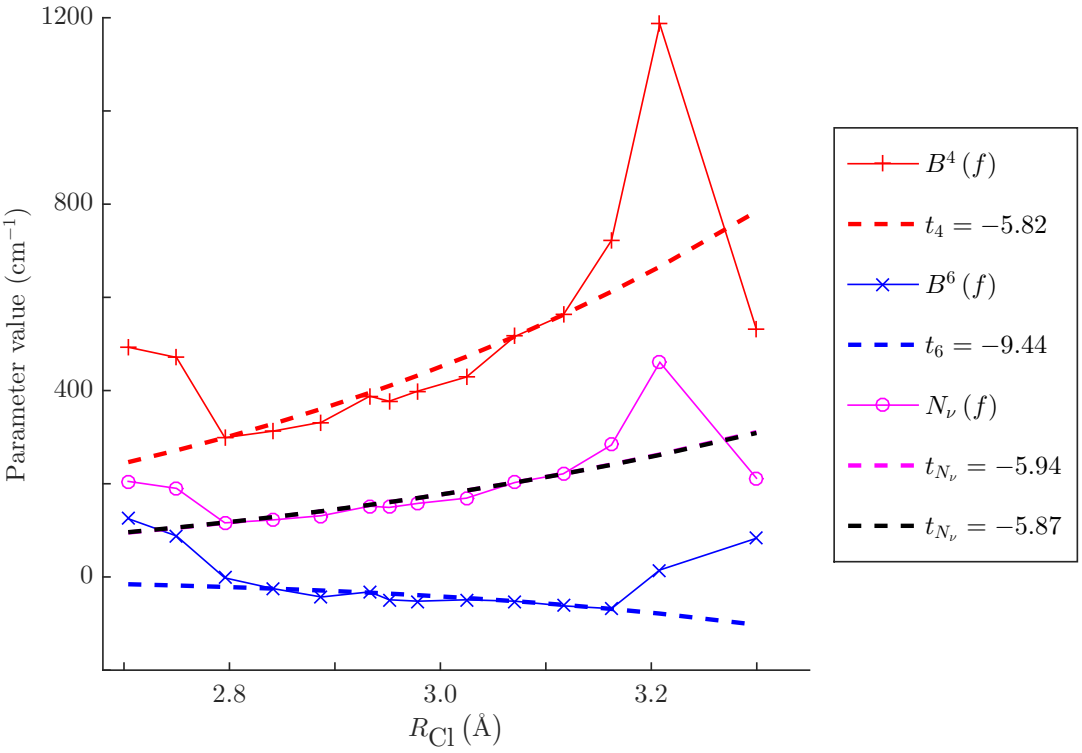

Figure 4.12 Point–charge power–law fits to the f crystal field parameters, $B^4(f)$ and $B^6(f)$; and the total f crystal field strength, N_ν, for the CASPT2 level calculation of $SrCl_2$:Yb^{2+}. A good fit to these power–law models can be obtained for the parameters in the region, $R_{Cl} = 2.80$ Å $- 3.15$ Å, however the coefficient has the opposite sign than is expected. The total field strength, N_ν, has both a single power–law exponent fitted to it (dashed magenta line); and has been modelled from the $B^4(f)$ and $B^6(f)$ power–law curves (dashed black line).

tions. This suggests that these particular configuration interaction terms are not included at this level of calculation.

The most interesting feature at this level of calculation occurs in the f crystal field parameters. These parameters extracted from the *ab initio* calculations are observed to *increase* with increasing impurity–ligand separation, instead of decreasing, as is expected based on the decreasing level of interaction between the impurity and the ligands; and the observed behaviour at the highest level of calculation. As demonstrated in Figure 4.12, the parameter variation can still be modelled well with a power–law relationship, albeit with a negative power–law coefficient. The fitted parameter values are fairly stable, converging to these values for a range of initial parameters, so this is unlikely to be an error in the fitting process. The parameter values are of a similar magnitude to the parameters fitted to the potential curve minima, at this level of calculation. They also exhibit the same

reversal of expected parameter signs, as noted for the fit to the curve minima.

This is clearly a flaw in the *ab initio* calculation at this level. Regardless of the signs or magnitudes of the individual crystal field parameters, the increase in magnitude with increasing separation observed here is non–physical.

4.2.2.3 CASSCF level

At the lowest calculation level (CASSCF, Figure 4.6), the discontinuity in the configurational shift parameter, $\Delta_E\,(fs)$, is the least pronounced of the three levels.

The fd Coulomb parameters are reasonably well behaved, and a clear nephelauxetic trend is observable in the F^2, F^4 and G^5 parameters as they vary with impurity–ligand separation. The $R^k\,(ds)$ configuration interaction parameters are very close to zero in the central region of the fit (corresponding to the minima of the d–levels, where the best fits to the energy levels are observed). The parameter values fluctuate greatly outside of this region. These zero values in the best–fitting region indicate that these configuration interaction terms are not considered at this level of calculation. This is in agreement with the observations of these parameters at the higher level CASPT2 calculation.

It is harder to define a discontinuity in the $G^3\,(fs)$ parameter, as the parameter varies greatly for R_{Cl} immediately smaller than at the discontinuity at $R_{\mathrm{Cl}} = 2.85$ Å. It also does not appear to exhibit any nephelauxetic effect, unlike at the other calculation levels.

The $4f$ crystal field parameters also vary considerably. These parameters are roughly constant through the central minima region, and then vary wildy outside of it. There are insufficient consistent data points to attempt to fit power–law curves to these parameters, and initial observations would tend to suggest that the coefficients would probably have the wrong sign, similar to the CASPT2 level.

This level of calculation is the most distant from reproducing experimental observations, and this introduces difficulty in fitting the effective Hamiltonian to these energies. The standard deviations for these fits are all consistently higher than for the corresponding CASPT2 fits (which have the same number of data points). This is expected, however, as this is the most basic level of *ab initio* calculation, and hence is lacking the corrections present in the higher level calculations for various physical effects.

4.3 $CsCaBr_3$:Yb^{2+}

An *ab initio* calculation of similar rigour has been conducted by Sánchez-Sanz et al. for the $CsCaBr_3$:Yb^{2+} system [70]. This system does not exhibit any excitonic emission or "pre–excitonic" structure in the calculated potential energy curves. $CsCaBr_3$:Yb^{2+} has six–coordinate octahedral symmetry, as opposed to the eight–coordinate cubic symmtery of $SrCl_2$:Yb^{2+}. As the octahedral and cubic sites are both described by the octahedral point group, these materials are described by the same crystal field Hamiltonian. However, as the octahedral coordination has a different physical arrangement of ligands, the crystal field parameters are expected to be quite different between the two systems. The free–ion parameters however, should remain relatively unchanged.

As with the $SrCl_2$:Yb^{2+} calculations, data for three levels of the *ab initio* calculation has been provided [72]. Figure 4.13 shows the provided potential energy curves for this system, at the spin–orbit level calculation.

4.3.1 Fit to the *ab initio* energy level minima

The parameter values from the $SrCl_2$:Yb^{2+} fitting of Pan et al. were used as initial parameter estimates for the $5d$ effective Hamiltonian terms, and the $6s$ terms were calculated using Hartree–Fock radial wavefunctions calculated for a free Yb^{2+} ion (listed in Table 4.5). For cubic and octahedral systems with the same lattice constant, the d crystal field parameters relate to each other by [1]:

$$B^4\left(d\right)_{\text{octahedral}} = \frac{-9}{8} B^4\left(d\right)_{\text{cubic}}. \tag{4.5}$$

Similarly, the f crystal field parameters are expected to change signs from the $SrCl_2$:Yb^{2+} values. The initial value for the $5d$ crystal field parameter was set using the value fitted to the minima of $SrCl_2$:Yb^{2+} and this relationship as an approximation. The difference in the lattice constants of the two hosts can be ignored, as the strength of the $5d$ crystal field interaction in excited lanthanides is of sufficient magnitude that the parameter can be easily fitted to the system from a very large range of initial estimates. The minima of the potential wells at each level of the calculation were used as target energies for the fitting process. Based on the observations of the parameters extracted from $SrCl_2$:Yb^{2+}, the R^k parameters are only introduced at the SO-CI level. The resulting parameters for the fits to each level of the calculation are shown in Table 4.5, and the energy levels and $^{S}L_{J}$ multiplet assignments for the SO-CI level calculation are shown in Table 4.6.

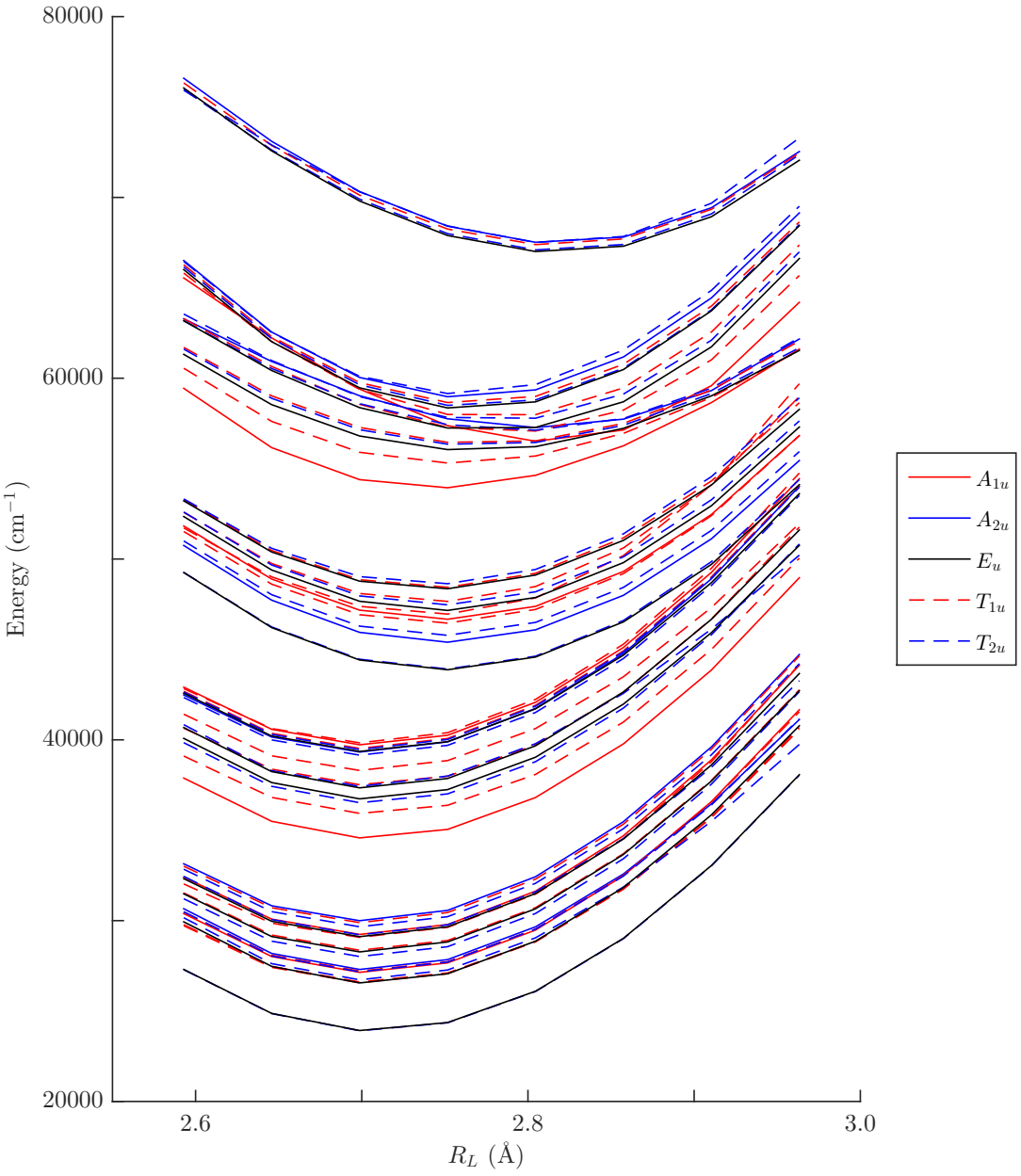

Figure 4.13 Potential energy curves of excited–state $CsCaBr_3:Yb^{2+}$ calculated by Sánchez-Sanz et al. [70], showing the variation of energy as a function of impurity–ligand separation (R_L). The calculation includes $4f^{13}5d$ and $4f^{13}6s$ excited states. The ground $4f^{14}$ curve (A_{1g} irrep), which has a minimum at $R_{\mathrm{Cl}} = 2.954$ Å, is omitted.

Table 4.5 Parameter values for the effective Hamiltonian of $CsCaBr_3$:Yb^{2+} fitted to experimental observations [71]; calculated for a free Yb^{2+} ion [23]; and fitted to *ab initio* calculations of Ref. [5]. The labels CASSCF, CASPT2 and SO-CI refer to the level of the reference calculation. All parameter values and uncertainties (σ) are in cm^{-1}.

	CASSCF		CASPT2		SO-CI		$SrCl_2$:Yb^{2+}	Free-ion
Parameter	Value	$\pm\sigma$	Value	$\pm\sigma$	Value	$\pm\sigma$	[71]	[23]
$\Delta_E(fd)$	13904	(269)	39814	(396)	39801	(243)	38382	
$\zeta(f)$					2927	(20)	2950	2899
$\zeta(d)$					749	(109)	1211	1290
$F^2(fd)$	21382	(703)	15569	(1055)	16849	(506)	14355	23210
$F^4(fd)$	9864	(1287)	12430	(1924)	9534	(1425)	7222	10646
$G^1(fd)$	8763	(221)	3451	(437)	4381	(435)	4693	10059
$G^3(fd)$	7170	(701)	7129	(1039)	7008	(973)	5382	8046
$G^5(fd)$	6198	(960)	4345	(1502)	7795	(1611)	4349	6085
$\Delta_E(ds)$ [a]	21288	(159)	21566	(234)	21568	(101)		
$G^3(fs)$	2699	(882)	2287	(1294)	1607	(1519)		3168
$R^2(ds)$					−70	(2469)		−305
$R^3(ds)$					8779	(1444)		1468
$B^4(f)$ [b]	596	(334)	1596	(492)	1374	(368)	−725	
$B^6(f)$ [c]	88	(173)	−89	(260)	−351	(428)	292	
$B^4(d)$ [b]	35197	(245)	39613	(340)	39689	(153)	−20442	
Fit summary:								
N	33		33		71			
n	12		12		16			
σ	269		396		241			

[a] $\Delta_E(fs) = \Delta_E(fd) + \Delta_E(ds)$.

[b] $B^4_0 = B^4$, $B^4_{\pm4} = \sqrt{\frac{5}{14}}B^4$.

[c] $B^6_0 = B^6$, $B^6_{\pm4} = -\sqrt{\frac{7}{2}}B^6$.

Table 4.6 Energy levels for the Yb^{2+} $4f^{14} \rightarrow 4f^{13}5d/4f^{13}6s$ effective Hamiltonian in $CsCaBr_3$, calculated using the parameters in Table 4.5 for the SO-CI level (spin–orbit) level calculation. The ΔE are the difference between the effective Hamiltonian and reference energy levels. All values are in cm^{-1}. While it is possible to label most irreps with a dominant $^{S}L_J$ multiplet label, there are a sufficient number of highly mixed states that it is impractical to present the states grouped by multiplet label. States have been labelled with the dominant $^{S}L_J$ multiplet contribution where applicable.

		Energy						Energy			
		Ab initio	Calculated		$\|^{S}L_J\rangle$			*Ab initio*	Calculated		$\|^{S}L_J\rangle$
Irrep		Reference	H_{cf}	ΔE		Irrep		Reference	H_{cf}	ΔE	
1	A_{1g}	0	0	0	$^1S_0$	8	E_u	43872	44148	-276	$^3H_6$
1	E_u	23902	23971	-69	$^3P_2$	11	T_{2u}	43912	44198	-286	$^3H_6$
1	T_{2u}	23890	23984	-94	$^3P_2$	4	A_{2u}	45396	45680	-284	$^3D_2$
1	T_{1u}	26555	26553	2	*mixed*	12	T_{2u}	45775	46067	-292	$^3D_3$
2	T_{2u}	26718	26588	130	$^3H_5$	12	T_{1u}	46445	46201	244	*mixed*
1	A_{2u}	27292	26632	660	$^3H_6$	5	A_{1u}	46665	46486	179	$^3F_4$
3	T_{2u}	27160	26765	395	$^3H_6$	9	E_u	47153	47073	80	$^3F_4$
2	E_u	26544	26791	-247	$^3H_5$	13	T_{1u}	46938	47082	-144	*mixed*
2	T_{1u}	26599	26835	-236	*mixed*	13	T_{2u}	47461	47274	187	*mixed*
1	A_{1u}	27132	27070	62	$^3H_6$	14	T_{1u}	47641	47760	-119	*mixed*
3	T_{1u}	27200	27090	110	$^3H_5$	10	E_u	48343	48372	-29	$^3G_5$
4	T_{2u}	28008	27923	85	$^3F_4$	15	T_{1u}	48424	48501	-77	$^3G_5$
4	T_{1u}	28355	28250	105	*mixed*	14	T_{2u}	48619	48513	106	$^1G_4$
3	E_u	28264	28552	-288	$^3G_4$	6	A_{1u}	53932	54088	-156	*mixed*
4	E_u	29107	28896	211	$^3F_4$	16	T_{1u}	55304	55439	-135	*mixed*
5	T_{2u}	29209	29185	24	$^3G_5$	11	E_u	56008	56164	-156	$^3F_2$
5	T_{1u}	29073	29489	-416	$^1G_4$	15	T_{2u}	56283	56247	36	$^1F_3$
2	A_{1u}	29231	29545	-314	*mixed*	17	T_{1u}	56376	56341	35	*mixed*
6	T_{2u}	29655	29583	72	$^1F_3$	12	E_u	57103	56832	271	$^3F_4$
2	A_{2u}	29992	29862	130	$^1F_3$	18	T_{1u}	57009	56849	160	$^3F_4$
6	T_{1u}	29884	30025	-141	$^3G_5$	7	A_{1u}	56502	56863	-361	$^3F_4$
3	A_{1u}	34560	34389	171	$^3P_0$	16	T_{2u}	57112	56911	201	$^3F_4$
7	T_{1u}	35916	35959	-43	*mixed*	17	T_{2u}	57653	57365	288	$^3F_4$
7	T_{2u}	36508	36420	88	$^3H_4$	5	A_{2u}	57270	57371	-101	$^3F_3$

Continued on next page...

Table 4.6 *Continued*

		Energy						Energy			
		Ab initio	Calculated		$\left\|^{S}L_J\right\rangle$			*Ab initio*	Calculated		$\left\|^{S}L_J\right\rangle$
Irrep		Reference	H_{cf}	ΔE		Irrep		Reference	H_{cf}	ΔE	
5	E_u	36725	36563	162	$^3H_4$	19	T_{1u}	57810	57494	316	*mixed*
8	T_{2u}	37421	37286	135	$^1D_2$	13	E_u	58304	57882	422	*mixed*
6	E_u	37335	37395	-60	$^1D_2$	18	T_{2u}	58436	58014	422	$^3G_3$
8	T_{1u}	37504	37561	-57	*mixed*	20	T_{1u}	58604	58786	-182	$^1F_3$
9	T_{1u}	38301	38437	-136	$^1H_5$	6	A_{2u}	58936	58827	109	$^3G_3$
9	T_{2u}	39146	38914	232	$^3F_2$	19	T_{2u}	59135	59092	43	$^3G_4$
3	A_{2u}	39319	39318	1	$^1F_3$	14	E_u	66964	67113	-149	$^3F_2$
7	E_u	39350	39335	15	*mixed*	20	T_{2u}	67050	67186	-136	$^3F_2$
10	T_{2u}	39459	39377	82	$^1F_3$	21	T_{1u}	67353	67264	89	*mixed*
10	T_{1u}	39518	39560	-42	*mixed*	21	T_{2u}	67466	67564	-98	*mixed*
4	A_{1u}	39716	40093	-377	*mixed*	7	A_{2u}	67473	67678	-205	$^3F_3$
11	T_{1u}	39830	40183	-353	*mixed*						

4.3.1.1 Results

It can be seen from the fit results in Table 4.5 that the f crystal field parameters changed signs relative to the corresponding values in $SrCl_2$:Yb^{2+} as expected, with the exception of the $B^6(f)$ parameter at the CASSCF level. The strength of the f crystal field at the CASSCF level is much smaller than at higher levels of the calculation. The d crystal field is roughly twice as strong as that of $SrCl_2$:Yb^2+ at all levels of the calculation. If we approximate that the f crystal fields should relate by a similar factor, then the expected $B^4(f)$ parameter is approximately $B^4(f) = 1450\ cm^{-1}$. This is roughly observed at both CASPT2 and SO-CI level calculations. Similarly, we expect roughly $B^6(f) = -584\ cm^{-1}$, which is stronger than is observed at any level of the calculation. The SO-CI level parameter is the closest to this estimate.

The CASSCF level again most closely resembles the free–ion parameters. The Coulomb parameters are larger than the values fitted to experimental observations of $SrCl_2$:Yb^{2+}, with two exceptions: the $G^1(fd)$ parameter at the CASPT2 and SO-CI levels, and the $G^3(fd)$ parameter at the CASPT2 level. The $G^3(fs)$ parameter decreases as the calculation level increases. At the SO-CI level, it is roughly half of the free–ion value.

As can be seen in Table 4.6, the energy order of irreps is not preserved between the *ab initio* calculation and the fitted effective Hamiltonian. Additionally, the states experience a greater degree of mixing than was observed in the $SrCl_2:Yb^{2+}$ effective Hamiltonian calculations, with more eigenvectors unable to be assigned a dominant contribution from a single $^{S}L_{J}$ multiplet.

4.3.2 Fit by impurity–ligand separation

The range over which the impurity–ligand separation is varied is much smaller for this calculation than for the $SrCl_2:Yb^{2+}$ calculation. Parameters were fitted at each impurity–ligand separation, following the method used for the $SrCl_2:Yb^{2+}$ system. Since the range of separations encompasses the centre of the potential well, and does not extend too far up the sides, a fairly good fit is achieved at each distance.

The resulting parameters from these fits are shown in Figures 4.14 – 4.16, plotted against impurity–ligand separation, R_L. Figure 4.14 shows the CASSCF level parameters, Figure 4.15 shows the CASPT2 level parameters, and Figure 4.16 shows the SO-CI level parameters.

4.3.2.1 Results

Looking at the SO-CI level calculation, the shape of the potential curves is given by the configurational energy average of the ground $4f^{14}$ state, $E_{\text{avg}}(f)$. The configurational shift for the $5d$ states is reasonably constant, and the configurational shift for the $6s$ states decreases slightly as the ligand cage expands.

As with $SrCl_2:Yb^{2+}$, the $4f$ spin–orbit parameter is constant with varying impurity–ligand distance due to the shielding of the $4f$ orbitals. However, the $5d$ spin–orbit parameter increases with increasing ligand distance, unlike the $SrCl_2:Yb^{2+}$ system. This effect is probably due to the presence of the Cs^+ ions in the lattice. As the d electron becomes increasingly delocalised from the Yb^{2+} impurity due to the nephelauxetic effect, it will experience an increased interaction with the Cs^+ ion, due to increased proximity.

The $F^k(fd)$ and $G^k(fd)$ Coulomb parameters at all levels of the calculation clearly vary in accordance with the nephelauxetic effect. The $G^3(fs)$ parameter shows a marked variation with respect to impurity–ligand separation at CASSCF and CASPT2 levels. This variation is much more distinct than in the $SrCl_2:Yb^{2+}$ fits. It is also not obscured

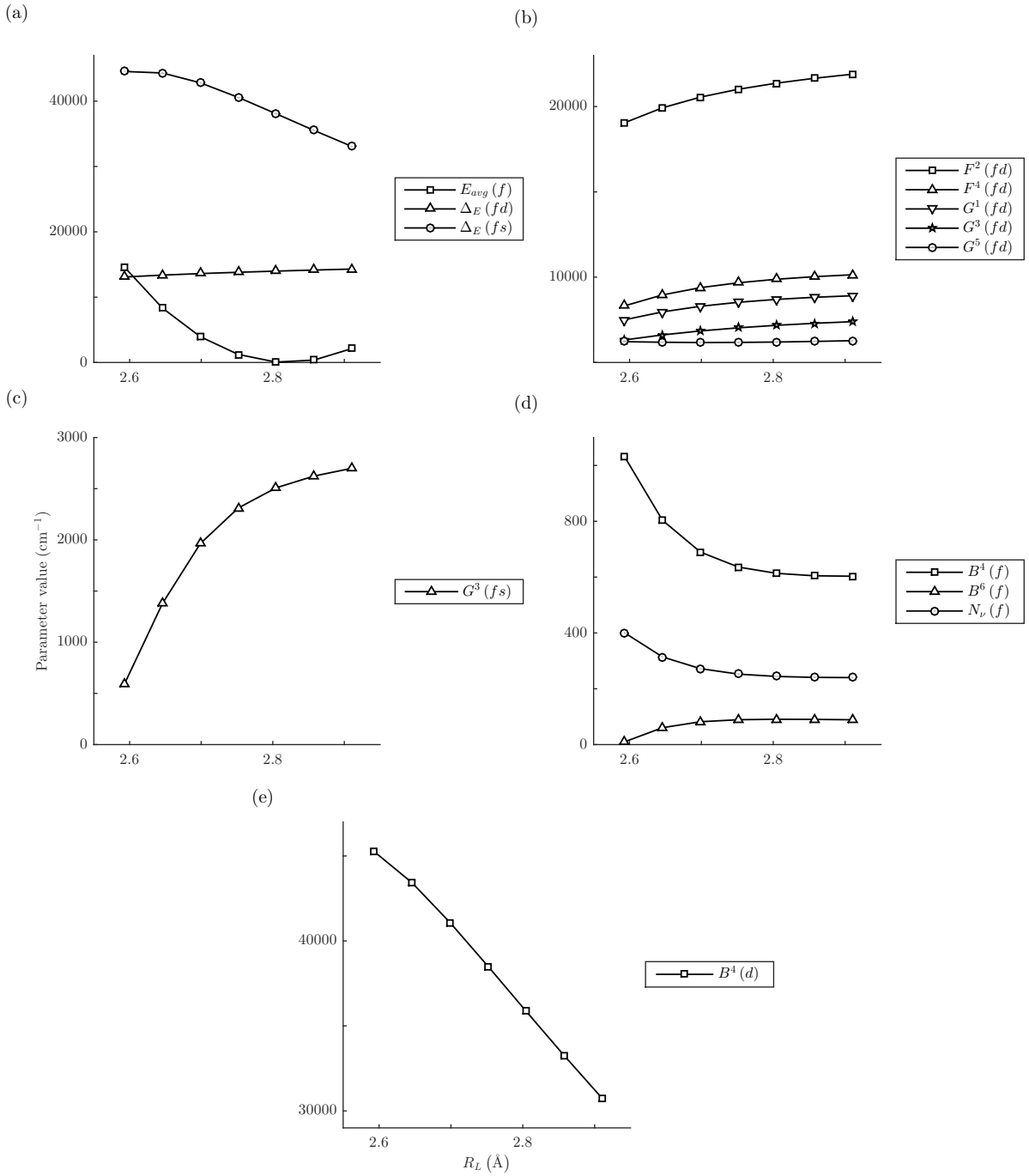

Figure 4.14 Parameters for the $4f^{14} \rightarrow 4f^{13}5d/4f^{13}6s$ effective Hamiltonian, optimised by fitting to energies of $CsCaBr_3$:Yb^{2+} using the CASSCF level calculation of Sánchez-Sanz et al. [70]. The plots are split into groups of comparable parameters: (a) Average configuration energy parameters. (b) fd Coulomb parameters. (c) fs Coulomb parameters. (d) $4f$ crystal field parameters. (e) $5d$ crystal field parameter.

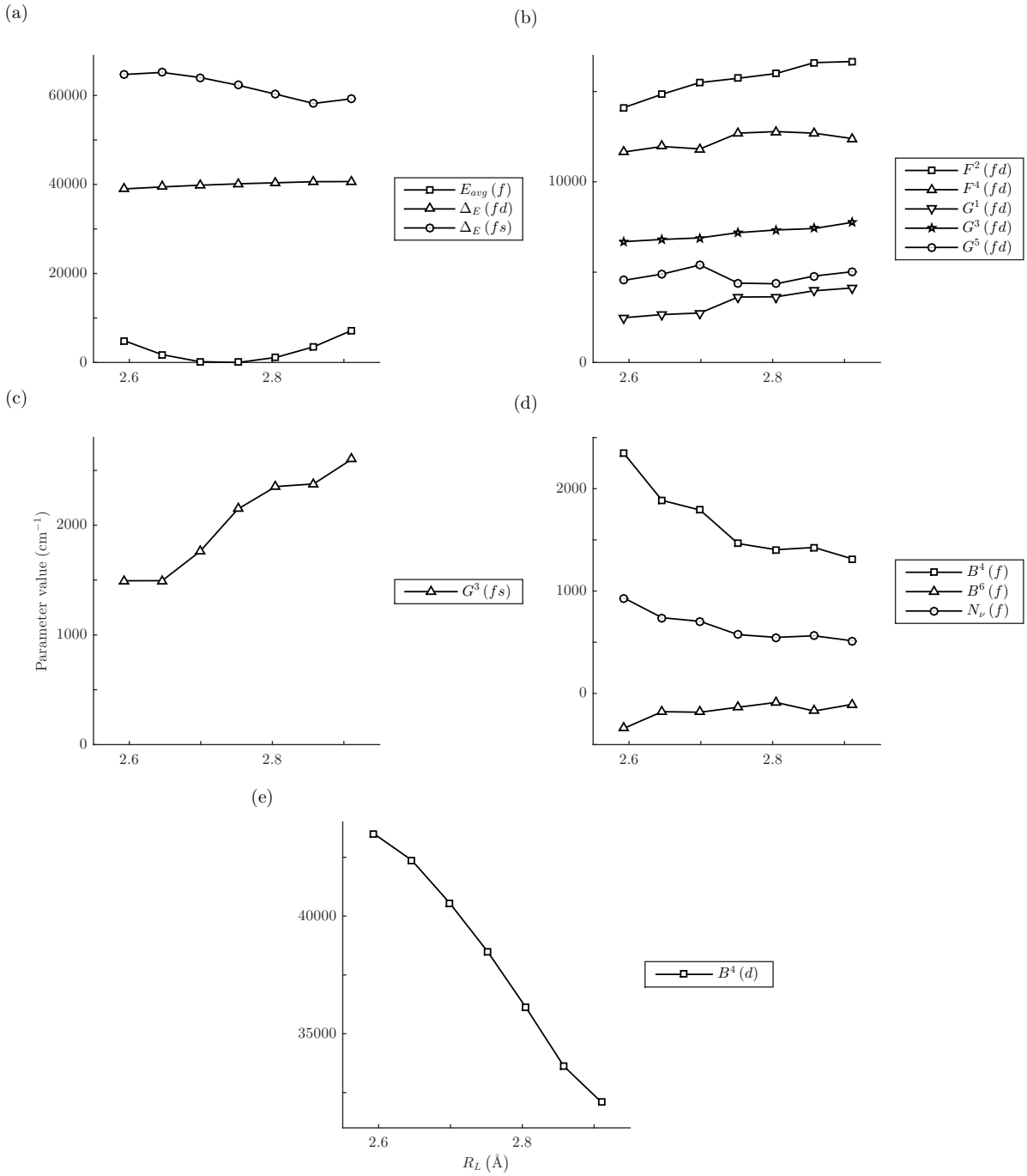

Figure 4.15 Parameters for the $4f^{14} \rightarrow 4f^{13}5d/4f^{13}6s$ effective Hamiltonian, optimised by fitting to energies of $CsCaBr_3:Yb^{2+}$ using the CASPT2 level calculation of Sánchez-Sanz et al. [70]. The plots are split into groups of comparable parameters: (a) Average configuration energy parameters. (b) fd Coulomb parameters. (c) fs Coulomb parameters. (d) $4f$ crystal field parameters. (e) $5d$ crystal field parameter.

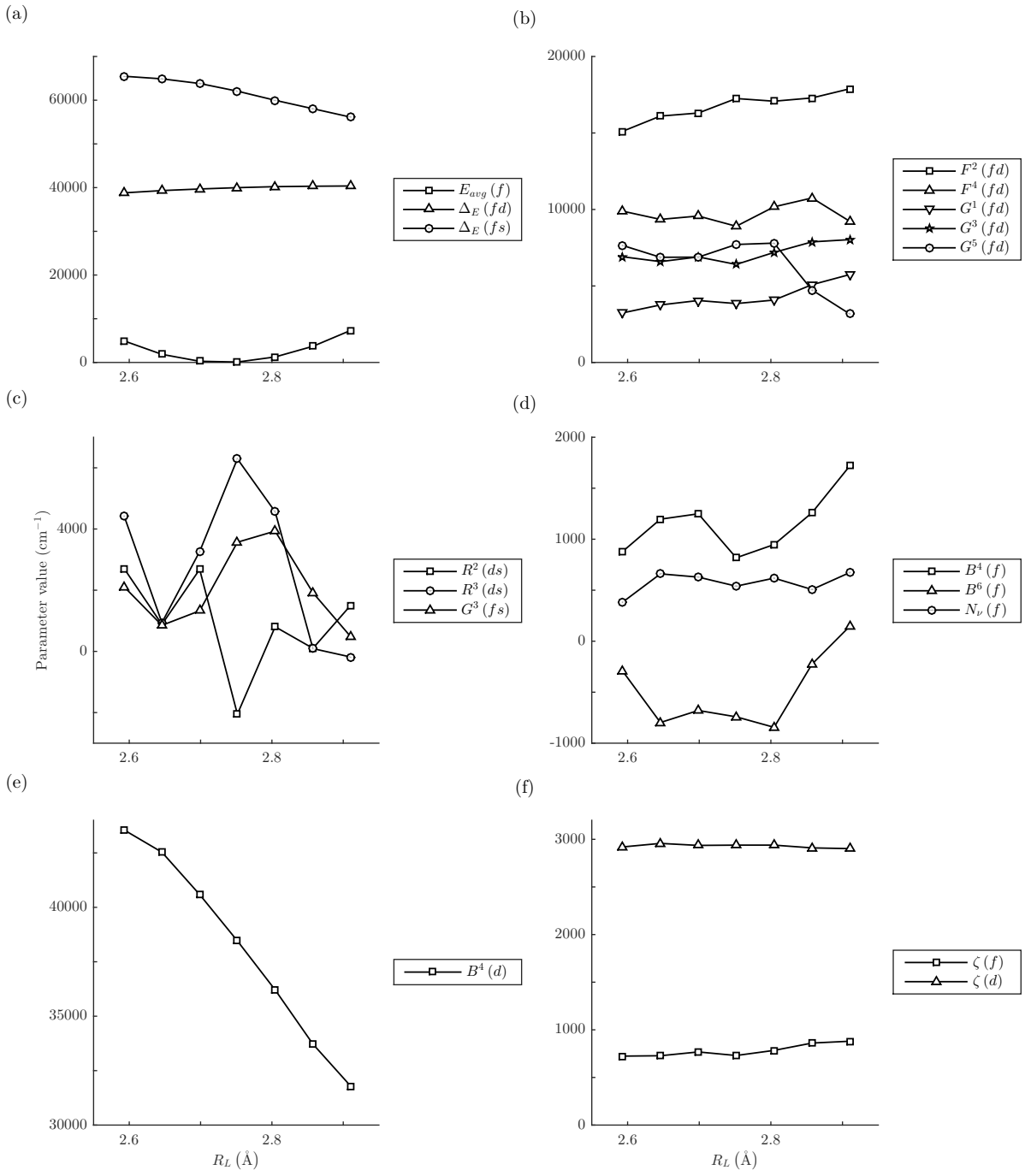

Figure 4.16 Parameters for the $4f^{14} \rightarrow 4f^{13}5d/4f^{13}6s$ effective Hamiltonian, optimised by fitting to energies of $CsCaBr_3$:Yb^{2+} using the spin–orbit level calculation (SO-CI) of Sánchez-Sanz et al. [70]. The plots are split into groups of comparable parameters: (a) Average configuration energy parameters. (b) fd Coulomb parameters. (c) fs Coulomb parameters. (d) $4f$ crystal field parameters. (e) $5d$ crystal field parameter. (f) Spin–orbit parameters.

by any discontinuities. At the SO-CI level, there is no clear trend in the $G^3\,(fs)$ parameter. This is perhaps a product of the introduction of the configuration interaction terms, which introduce substantial noise in the fitting process. However, these results are reproduceable from several initial parameter values, which suggest that these are the stable solutions. At the CASPT2 level, the values for the $G^3\,(fs)$ parameter at the two extreme fits are questionable, as incomplete sets of reference energy levels were provided at these R_L. This is also the cause of the sudden increase in the $6s$ average configuration energy parameter at the greatest R_L, at this calculation level.

The $5d$ crystal field also varies smoothly with changing R_L, but the shape of the curve does not match the power–law expression in Equation 2.30. At best, the central, roughly linear region can be modelled with power–law curves with coefficients of approximately $t_4 = 3$, which is smaller than expected using a point–charge model. At CASSCF and CASPT2 levels, the $4f$ crystal field parameters also vary smoothly with changing R_L. The CASPT2 level parameters fit to the theoretical point–charge model power–laws well, as demonstrated in Figure 4.17. At CASSCF level, the $B^4\,(f)$ parameter curves too steeply to fit the expected power–law curve, and while the $B^6\,(f)$ parameter shows the correct shape, it appears to have an offset above the zero axis. At SO-CI level, the $4f$ crystal field parameters vary too greatly to fit to the expected model. At the CASPT2 and SO-CI calculation levels, the signs of both f crystal field parameters are consistent with the fits to the potential curve minima, which, in turn, agreed with the expected signs based on the site symmetry.

4.4 Summary

An effective Hamiltonian, acting on the space $4f^{14} \rightarrow 4f^{13}5d/4f^{13}6s$, was fitted to the energy levels of $SrCl_2$:Yb^{2+} and $CsCaBr_3$:Yb^{2+} determined by *ab initio* calculations, in order to extract the equivalent physical parameters from these calculations. A fit was made to the minima of the energy curves of each system, and to each position along the potential curves, modelling a hypothetical instantaneous transmission at fixed impurity–ligand separation. In addition, these fits were performed at each level of the *ab initio* calculation provided. The extraction of these parameters allowed a number of analyses of these calculations to be made.

For any given fit, the $CsCaBr_3$:Yb^{2+} had a slightly higher standard deviation both for the overall fit, and all of the parameters involved, despite the two systems having the

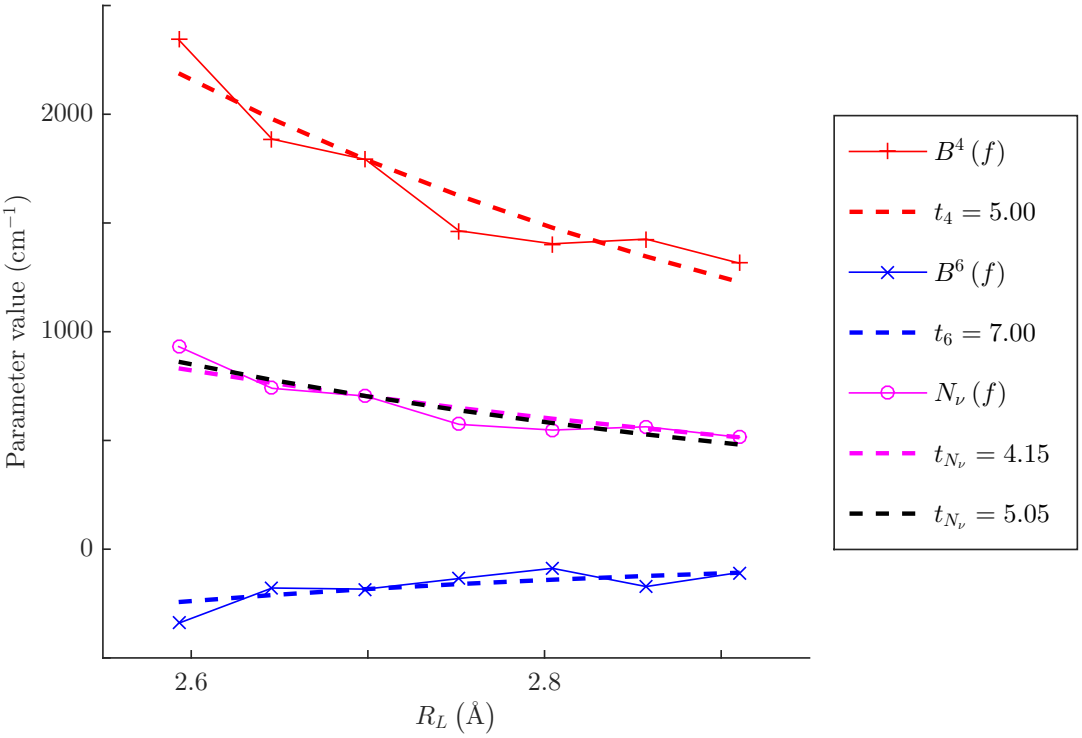

Figure 4.17 Point–charge power–law fits to the f crystal field parameters, $B^4(f)$ and $B^6(f)$; and the total f crystal field strength, N_ν, for the CASPT2 level calculation of $CsCaBr_3$:Yb^{2+}. The power–law coefficients for the $B^4(f)$ and $B^6(f)$ parameters are fixed at the expected theoretical values, $t_4 = 5$ and $t_6 = 7$ [14]. The total field strength, N_ν, has both a single power–law exponent fitted to it (dashed magenta line); and has been modelled from the $B^4(f)$ and $B^6(f)$ power–law curves (dashed black line).

same number of reference energy levels used in all of the fitting procedures. The ability of the effective Hamiltonian to fit to the *ab initio* energy curves was significantly improved near the positions of the minima of the curves, and degraded towards the edges of the potential curves. None of the fits were able to reproduce the energy order of the irreps of the reference calculations.

The magnitudes of the Coulomb parameters were observed to vary with increasing ligand displacement for both crystal systems at all levels of the calculation. This can be explained in terms of the nephelauxetic effect, where the expansion of the ligand cage around the impurity allows the valence electron distribution to collapse inwards, or conversely, the contraction of the ligand cage causes the valence electron distribution to move into the interstitial sites. The overall effect is a change in the orbital overlap of the $5d$ and $4f$ valence electrons, resulting in the observed changes to the Coulomb parameters.

At the SO-CI level calculations, the spin–orbit interaction parameters were easily fitted, due to the magnitude of the spin–orbit interaction upon the crystal system. The $4f$ spin–orbit parameter did not vary with changing impurity–ligand separation, as the $4f$ electron distribution is largely shielded from the ligands by the outer electrons. Only slight trends were observed in the $5d$ spin–orbit parameter, and these can be attributed to the change in electron distribution described by the nephelauxetic effect.

Similarly, due to the strength of the $5d$ crystal field interaction, the corresponding parameter was well–defined, and provided clear trends with changing impurity–ligand separation. The $SrCl_2$:Yb^{2+} $5d$ crystal field parameter exhibited a power–law dependence of $R_{\mathrm{Cl}}^{-5.43}$, which is slightly different than the expected R_{Cl}^{-5}. The variation of the $CsCaBr_3$:Yb^{2+} $5d$ crystal field parameter is not reproduced well by the simple power–law model described by theory.

The extraction of crystal field parameters from the *ab initio* calculations allowed us to identify a problem with the CASPT2 level f crystal field parameters in $SrCl_2$:Yb^{2+}, where the f crystal field parameters vary in a non–physical way with increasing impurity–ligand separation. As the impurity–ligand separation increases, the influence of the crystal lattice on the f electrons is expected to decrease, due to the decreased overlap of electron wavefunctions. This is observed at the higher SO-CI level of calculation, but not at the CASPT2 level, where it increases with a smooth power–law dependence.

The $G^3(fs)$ parameter fluctuates considerably at the SO-CI level of the $CsCaBr_3$:Yb^{2+} calculation. Comparatively, in the $SrCl_2$:Yb^{2+} system, this parameter is more stable in

the central region of the data, close to the minima of the potential curves. There is a clear discontinuity in this parameter value, introduced at the point where the double–well potential crosses from a predominantly $6s$ character state, to a delocalised symmetrical A_{1u} state. This is expected behaviour, as the significantly delocalised state should experience a considerably different Coulomb interaction with the remaining localised electrons. This, along with the low standard deviation fit at the delocalised A_{1u} minima suggest that this effective Hamiltonian can be used as a good approximation to the delocalised electron state.

The $R^2(ds)$ and $R^3(ds)$ configuration interaction parameters are very difficult to fit, owing to their weak interactions in the overall effective Hamiltonian. There are only a few non-zero matrix elements in the representations of the corresponding operators, which means that these operators only introduce a very weak mixing of $6s$ states into the predominantly $5d$ character states. It is observed that the magnitude of this mixing results in a change of energy on the order of a few wavenumbers in these mixed states for a substantial change in the diagonal $6s$ average configuration energy parameter, on the order of 5000 cm^{-1}. The action of these operators was, however, shown to be sufficient for fitting purposes, as demonstrated in the CASPT2 level fit of $SrCl_2$:Yb^{2+}. There is no configuration interaction accounted for at this level of the reference calculation, and for the central region of the provided data, the parameters reliably fit to near–zero values.

Chapter 5

Spectroscopic parameters from experiment and *ab initio* calculation: CaF_2:Yb^{2+}

In the previous chapter we fitted an effective Hamiltonian to the energy levels produced by two *ab initio* calculations, in order to extract the equivalent crystal field parameters from those calculations and compare with the directly computed quantities. Additionally, we modelled a delocalised electron state by means of an adjustment to the parameters of a localised $6s$ electron state. These parameters provided a good model for this extended state, and should be able to model the intended impurity trapped exciton (ITE) states in other materials.

In this chapter, we fit an effective Hamiltonian to experimental spectra for two materials that do exhibit excitonic emission: CaF_2:Yb^{2+} and SrF_2:Yb^{2+}. The effective Hamiltonian model for these is reduced to a $4f^{14} \rightarrow 4f^{13}5d$ space, as the dominant structure observed in these spectra arise due to the $f \leftrightarrow d$ transitions. The $6s$ states are not fitted directly, as there is insufficient information in the observed spectra to fit to localised $6s$ states, due to the weak f-s electric dipole strength.

We then extract physical parameters from an *ab initio* calculation for CaF_2:Yb^{2+} of similar detail to those referenced in the previous section. The parameters fitted to experimental spectra are used as a comparison for these extracted parameters. The *ab initio* calculation models potential energy surfaces across a small range of impurity–ligand separations about the minimum of the $4f^{14}$ ground state potential energy curve, as with the calculations

in the previous chapter. An effective Hamiltonian is fitted to the energy levels of this calculation, using the methods discussed in the previous chapter.

Absorption spectra are simulated using the eigenvectors from the effective Hamiltonian fits to both the experimental data, and the *ab initio* calculations. The structure of vibronic levels presented in the *ab initio* calculations is also simulated. Lastly, the ITE states are modelled using the fitted fd parameters, and modified fs parameters.

5.1 Experimental CaF_2:Yb^{2+} spectra

The first material we shall examine is CaF_2:Yb^{2+}. This material exhibits the anomalous emission band referred to as an impurity–trapped exciton, frequently seen in Yb^{2+} and Eu^{2+} compounds [27–32]. In addition to this, CaF_2 has a wide band gap, such that all Yb^{2+} $5d$ levels lie at energies below the conduction band [77]. This provides an abundance of spectral information for the $5d$ levels, which makes it an ideal material for fitting effective Hamiltonian parameters to experimental levels.

Hughes-Currie et al. [77] performed VUV excitation experiments on CaF_2:Yb^{2+}, in order to probe the trap state causing anomalous emission. Using an excitation setup, a VUV photon source is tuned across a range of energies, exciting the ground state electrons into $5d$, and higher, excited states, while emission is monitored at a specific wavelength. In this study, the emission was monitored primarily at three different energies: near the peak energy of the anomalous emission associated with the ITE state; near the peak energy of the known self–trapped excitons that exist in the structure of CaF_2; and lastly at an intermediate energy to these two. The ITE state is populated by non-radiative processes from the $5d$ energy levels of the Yb^{2+} ion, indicated by the presence of the $5d$ absorption profile clearly visible in the excitation spectrum. This indicates that the ITE state is energetically favourable to the $5d$ levels, with reference to the ground state.

We use this excitation spectrum, in addition to existing low–temperature absorption spectra, [28], to determine the positions of the four distinct clusters of spectral peaks for cubic Yb^{2+}. These four groupings of peaks correspond to the splitting of energy levels due to the two biggest interactions: the $5d$ crystal field interaction, splitting the d levels into t_2 and e irreps; and the $4f$ spin–orbit interaction, which splits the levels into high–spin and low–spin states. The size of these interactions allows them to be easily fitted to the experimental spectra. This is demonstrated by the schematic in Figure 5.1. The remainder

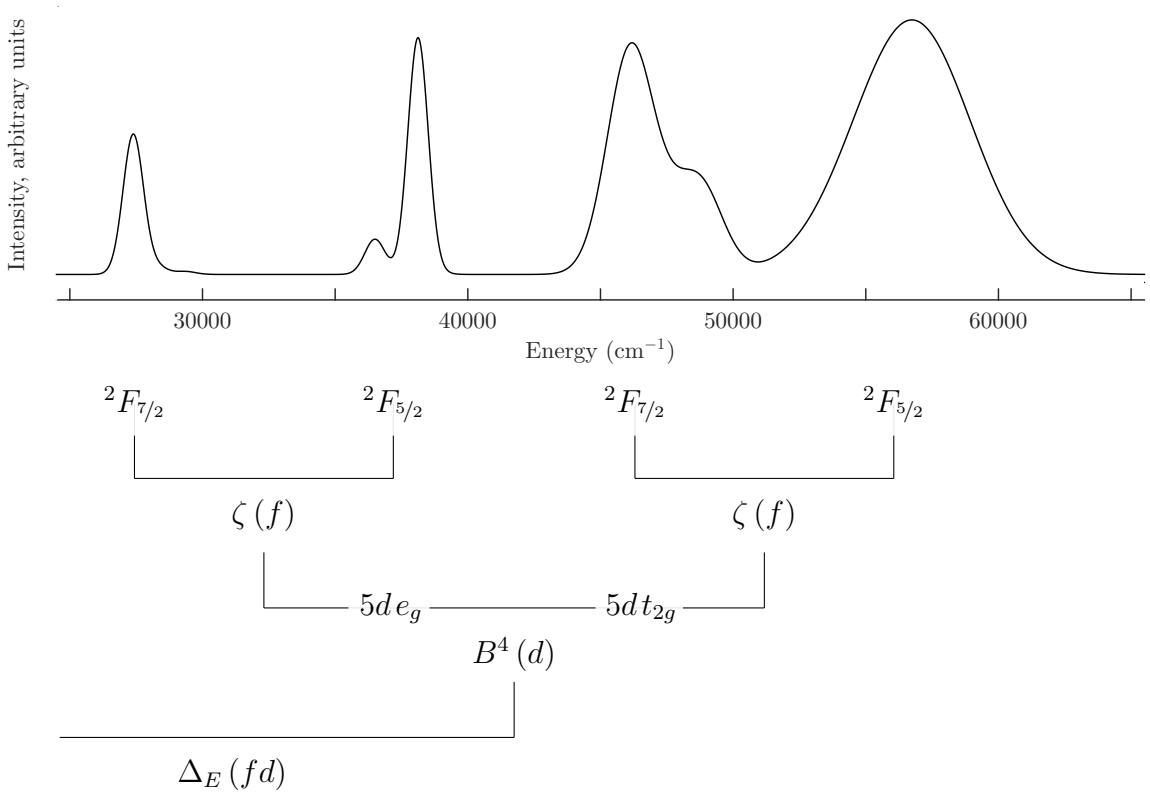

Figure 5.1 A schematic of the effects of the two strongest parameters in the CaF_2:Yb^{2+} system, with reference to a simulated absorption spectra. The $5d$ crystal field parameter has the strongest splitting effect on the spectrum, splitting the states into $5de_g$ and $5dt_{2g}$ irreps. The next strongest splitting is due to the f spin–orbit parameter, which splits the system into high–spin, $^2F_{7/2}$, and low–spin, $^2F_{5/2}$, states. These two parameters are the most strongly defined in any fitting procedure, and are sufficent to reproduce the main structure of the spectrum. The d spin–orbit and f-d Coulomb interactions provide the majority of the remaining structure.

of the structure can be determined by identifying the positions of zero–phonon lines in the experimental spectra, and fitting to these.

By the selection rules of the electric dipole operator, the only states that can interact radiatively (emission or absorption) with the $4f^{14}$ ground state are the T_{1u} irreps. The selection rule for an allowed transition is that the direct product of the dipole operator with an initial irrep must include the final irrep, in order for the dipole moment to be non–zero. That is:

$$\Gamma_{\text{final}} \subset \Gamma_{\text{ED}} \otimes \Gamma_{\text{initial}} \tag{5.1}$$

The $6s$ states do not strongly absorb, due to the $f \rightarrow s$ transition being forbidden by the

selection rule $\Delta L = 0, \pm 1$. Similarly, direct absorption into the ITE state is extremely weak, with dipole strengths four orders of magnitude smaller than $f \leftrightarrow d$ transitions [32]. Thus, from these experimental data, we shall only identify states to assign to a $4f^{14} \rightarrow 4f^{13}5d$ Hamiltonian:

$$H_{\text{eff}}^{\text{Yb}^{2+}} = H_{4f^{14}} + H_{4f^{13}5d}, \tag{5.2}$$

using Equations 4.1 and 4.2. As CaF_2:Yb^{2+} has the same crystal structure as $SrCl_2$:Yb^{2+} (Figure 4.1), the crystal field Hamiltonian has the same terms (Equation 2.24).

5.1.1 Fit results

The parameters of Pan et al. [71] for $SrCl_2$:Yb^{2+} are used as initial parameter estimates for the fitting process. The Coulomb parameters are held fixed at these values, as there are insufficient reference points that can be easily extracted from the experimental spectra.

The CaF_2 lattice has the same coordination as $SrCl_2$, so the crystal field parameters should have the same signs. $SrCl_2$ is the larger crystal ($SrCl_2$ $a_0 = 6.9767$Å, CaF_2 $a_0 = 5.46295$Å [78]), so we expect the crystal field parameters for CaF_2 to be correspondingly larger, due to the increased overlap of electron orbitals of the impurity and ligands. As illustrated in Figure 5.1, the $B^4\,(d)$ parameter has the strongest influence on the system, and can easily be fitted, irrespective of the initial parameter estimate. The f crystal field parameters are small in magnitude, and have only a small influence on the system. As the lattice has the same coordination, these parameters are not expected to change drastically, and thus the $SrCl_2$ crystal field parameters provide good initial estimates.

The fit is completed manually, by inspection. The positions of zero–phonon lines (ZPL) are estimated from the Huang–Rhys parameters provided in the reference *ab initio* calculation used later in this chapter [35, 79]. The linewidths are chosen to match the observed spectra. The simulation of the spectra shall be discussed shortly. The process was repeated iteratively, until a good fit was reached with respect to both the ZPL and the overall spectrum, with a physically reasonable set of parameters. The resultant parameter values are presented in Table 5.1.

As the parameter fit was achieved using a manual method, the individual parameter uncertainties presented in Table 5.1 are approximated by running the resultant fit through a single iteration of the fitting process via CFIT, and extracting the internal uncertainty readout. These are to be taken as indicative values only.

Table 5.1 Crystal field parameters, calculated for a free Yb^{2+} ion; fitted to a $SrCl_2$:Yb^{2+} system (used as initial parameter values); and fitted to excitation data of a CaF_2:Yb^{2+} system. All parameter values are measured in cm^{-1}. The $4f$ and $5d$ B_q^k crystal field parameters are necessarily different from the reference $SrCl_2$:Yb^{2+} values. The fit to the excitation spectrum was conducted manually. The individual parameter uncertainties presented are indicative only.

	Yb^{2+}	$SrCl_2$:Yb^{2+}		CaF_2:Yb^{2+}	
	Free–ion [23]	Expt. [71]	*Ab initio* [73]	Excitation fit	
Parameter	Value	Value	Value	Value	$\pm\sigma$
$\Delta_E\,(fd)$		38382	41802	42700	(683)
$\zeta\,(f)$	2899	2950	2939	2950	(116)
$\zeta\,(d)$	1290	1211	1166	1204	(622)
$F^2\,(fd)$	23210	14355	18393	14355	
$F^4\,(fd)$	10646	7222	13099	7222	
$G^1\,(fd)$	10059	4693	5408	4693	
$G^3\,(fd)$	8046	5382	8901	5382	
$G^5\,(fd)$	6085	4349	7165	4349	
$\Delta_E\,(ds)$ [a]			11093		
$G^3\,(fs)$	3168		2604		
$R^2\,(ds)$	−305		1990		
$R^3\,(ds)$	1468		2449		
$B^4\,(f)$ [b]		−725	−194	−869	(1840) [c]
$B^6\,(f)$ [b]		292	−592	350	(739) [c]
$B^4\,(d)$ [b]		−20442	−20100	−37726	(1043)
Fit details:					
N				10	
n				6	
σ				886	

[a] $\Delta_E\,(fs) = \Delta_E\,(fd) + \Delta_E\,(ds)$.

[b] Cubic crystal field: $B_0^4 = B^4$, $B_{\pm4}^4 = \sqrt{\frac{5}{14}}B^4$, and $B_0^6 = B^6$, $B_{\pm4}^6 = -\sqrt{\frac{7}{2}}B^6$.

[c] Crystal field parameters held at a fixed ratio to match the fit to $SrCl_2$:Yb^{2+} by Pan et al. [71].

The resulting spin–orbit parameters agree with the initial parameters, and free–ion values. As expected, the main difference is in the crystal field parameters. The d crystal field parameter for CaF_2:Yb^{2+} is significantly larger in magnitude than the value for $SrCl_2$:Yb^{2+}. The f crystal field increases in magnitude by a small amount. The $B^4(f)$ crystal field parameter is in rough agreement with that of Senanayake et al., fitted to infra–red excitation of CaF_2:Yb^{2+} [80]: $B^4(f) = -800$ cm^{-1}. There is a slight disagreement in the $B^6(f)$ parameter, as a different ratio B^4/B^6 has been used.

5.1.2 Simulating the spectrum

The transition intensities for each state are calculated using the f–shell empirical software suite. The theory for this is covered in section 2.4.1. As the T_{1u} irreps are the only absorbing states present, they have the only non–zero transition intensities. The simulated spectrum is generated by convolving the transition intensities with Gaussian curves of the appropriate line–width, to match the observed excitation spectrum. The reference spectra and absorption spectrum simulated using the fitted parameters from Table 5.1 are presented in Figure 5.2. The vertical lines represent the transition intensities of the eighteen absorbing T_{1u} irreps. For display, these are normalised relative to the irrep with the strongest transition intensity.

A limitation to consider is that the spectrum we are simulating is an absorption spectrum, while the reference spectrum for the higher energy region is an excitation spectrum. The intensities of the $5d$ peaks of the two spectra are not comparable, as while the intensities observed in an absorption spectrum can be related to the transition strengths of the states involved, the overall intensity observed in the excitation spectrum can be affected by any number of other processes in the material. Any non–radiative relaxation from the states responsible for the monitored radiative emission will decrease the intensity of the excitation spectrum. Hence, we only use the the excitation spectrum as a rough estimate of overall shape, not intensity.

An issue observed in the comparison between the fitted and observed spectra is the inability to reproduce the position of the $4f^{13}\left(^2F_{7/2}\right)5dt_{2g}$ group of spectral peaks, in the $40\,000 - 50\,000$ cm^{-1} region. The splitting between the groups of peaks is defined very strongly by the spin–orbit parameter, and cannot be resolved for both the $5de_g$ peaks or $5dt_{2g}$ peaks simultaneously. This is demonstrated in Figure 5.3, where the spin–orbit interaction is increased in magnitude from zero strength to the fitted strength of 2950 cm^{-1}.

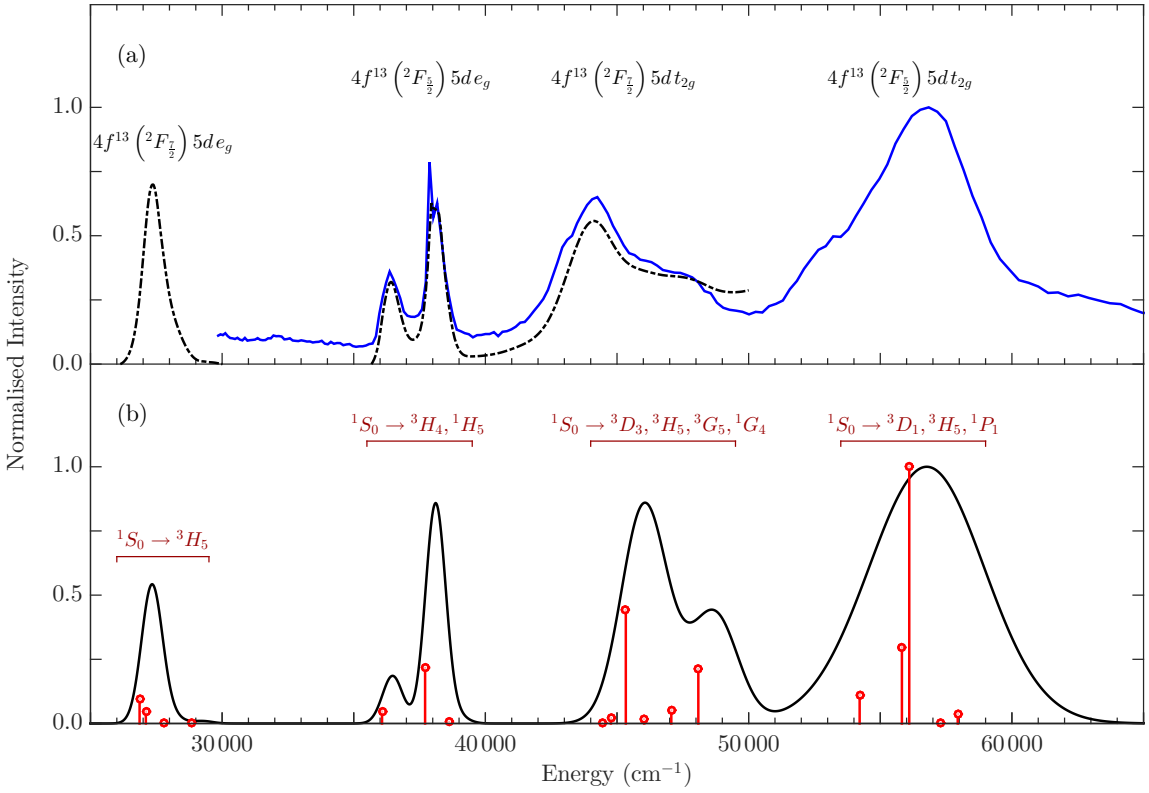

Figure 5.2 Comparison of measured absorption and excitation spectra with an absorption spectrum simulated using the parameters in Table 5.1. (a) The excitation [77] (solid blue) and absorption [28] (dashed black) spectra. (b) The simulated absorption spectrum (solid black) and positions of absorbing T_{1u} irreps (vertical red lines). The multiplets involved in the transitions for each group of peaks are indicated.

The spin–orbit parameter required to fit the splitting between the high–spin and low–spin $5dt_{2g}$ peaks is 3583 cm^{-1}, which is substantially higher than the values measured for $SrCl_2$:Yb^{2+} and the calculated free–ion value, which agrees well. If we look at the definition of the spin–orbit interaction, from Equation 2.39, the value of the spin–orbit parameter can be increased by expanding the electron wavefunction, or by altering the potential of the system. The $4f$ electron wavefunctions undergo minimal changes under external influences upon the system, due to shielding by the outermost electron shells. The $5d$ spin–orbit parameter, while less strongly defined, still fits both regions of the spectrum simultaneously, which indicates that the $5d$ wavefunction does not change between lower and higher energy regions. This indicates that the best explanantion for this discrepency in spin–orbit parameter fitting is probably a poor choice of ZPL positions and Gaussian parameters.

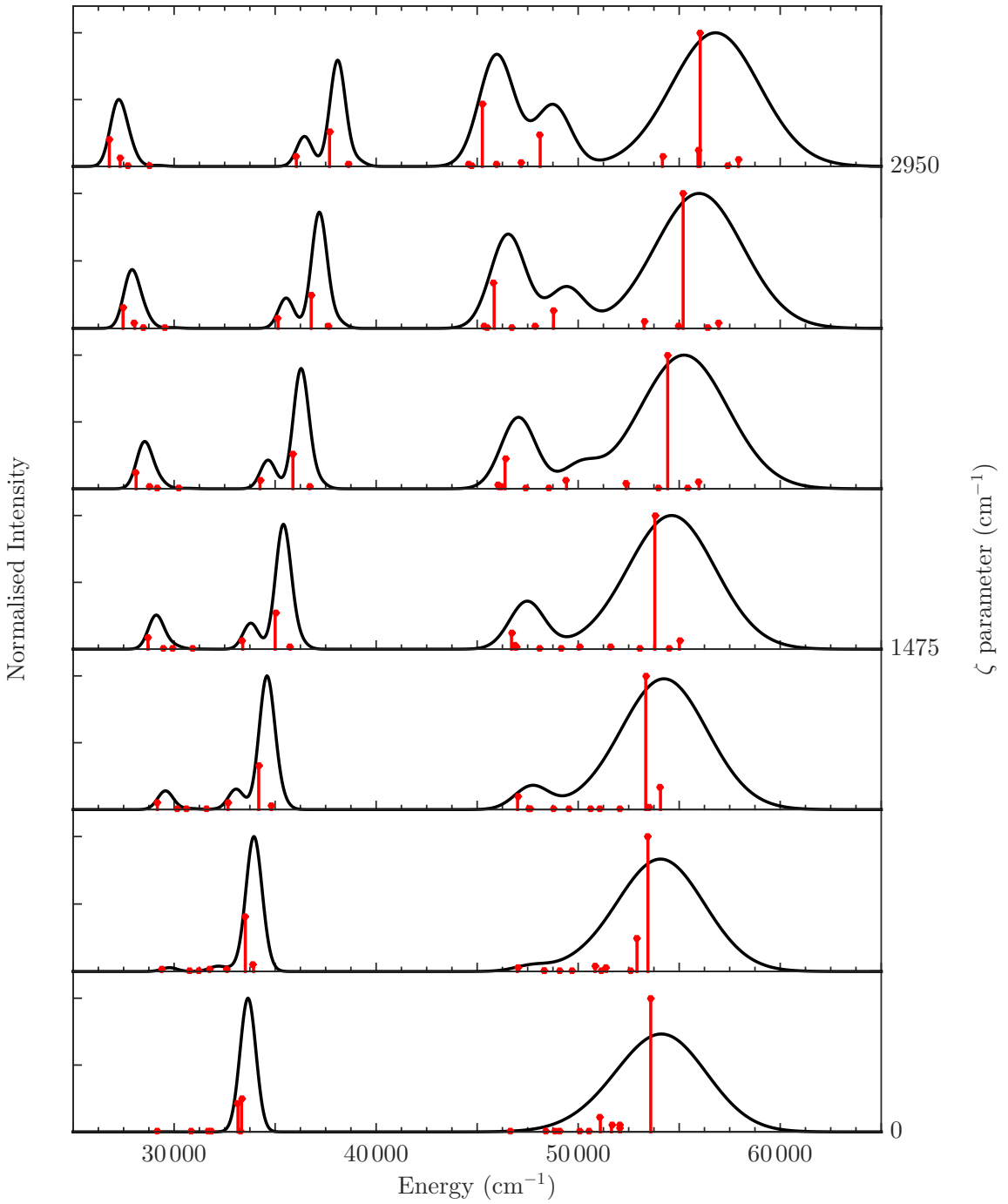

Figure 5.3 Transitions of CaF_2:Yb^{2+} as the spin–orbit interaction is increased from 0 cm^{-1} to the fitted value of 2950 cm^{-1}. The parameter controls the splitting of the two peaks in the spin–orbit free solution (the e_g and t_{2g} irreps of the d crystal field splitting) into four sets of peaks fitted to the observed excitation and absorption spectra, and is hence very strongly determined in the fitting process by the location of these peaks.

5.2 Fit to experimental SrF_2:Yb^{2+} absorption

Low–temperature (10 K) absorption spectra of SrF_2:Yb^{2+} were obtained by Hughes–Currie et al. [37], and used in conjunction with existing absorption and emission data for this material [28] to provide reference energies with which to fit the effective Hamiltonian for this system. The SrF_2 lattice is a similar size to the CaF_2 lattice, (SrF_2, $a_0 = 5.7996$ Å; CaF_2, $a_0 = 5.46295$ Å), and, as it has the same structure, has the same cubic site symmetry for the Yb^{2+} impurity. The spectra for these two materials are visibly very similar, and can hence be described by very similar sets of parameters.

For this fit, as with the fit to excitation data for CaF_2:Yb^{2+}, the Coulomb parameters are held fixed at the values determined by Pan et al. for $SrCl_2$:Yb^{2+} [71]. Additionally, the f crystal field parameters are also held fixed at the CaF_2:Yb^{2+} values, as the two hosts have similar lattice sizes, and the effect of the f crystal field on the overall spectrum is minimal. This was tested, using crystal field parameters for SrF_2:Yb^{2+} fitted by Senanayake et al. [80]: $B^4(f) = -600$ cm^{-1}, $B^6/B^4 = 0.35$. This caused negligible change to the simulated spectrum.

The fitted positions of the absorbing T_{1u} irreps are presented in Figure 5.4, with the simulated and measured spectra. The fitted parameters are presented in Table 5.2. As can be seen from the fitted parameters, the greatest difference between the two host crystals is the magnitude of the d crystal field parameter. This can be observed directly in the spectra of the two materials, by the proximity of the high–spin $4f^{13}\left(^2F_{7/2}\right)5d\,t_{2g}$ and low–spin $4f^{13}\left(^2F_{5/2}\right)5d\,e_g$ states. This is also illustrated in the schematics in Figures 5.1 and 5.3. In the spectra of CaF_2:Yb^{2+}, Figure 5.2, the distance between the high–spin $4f^{13}\left(^2F_{7/2}\right)5d\,t_{2g}$ and low–spin $4f^{13}\left(^2F_{5/2}\right)5d\,e_g$ peaks is approximately 9000 cm^{-1}, whereas for SrF_2:Yb^{2+}, the peaks are separated by only 4000 cm^{-1}.

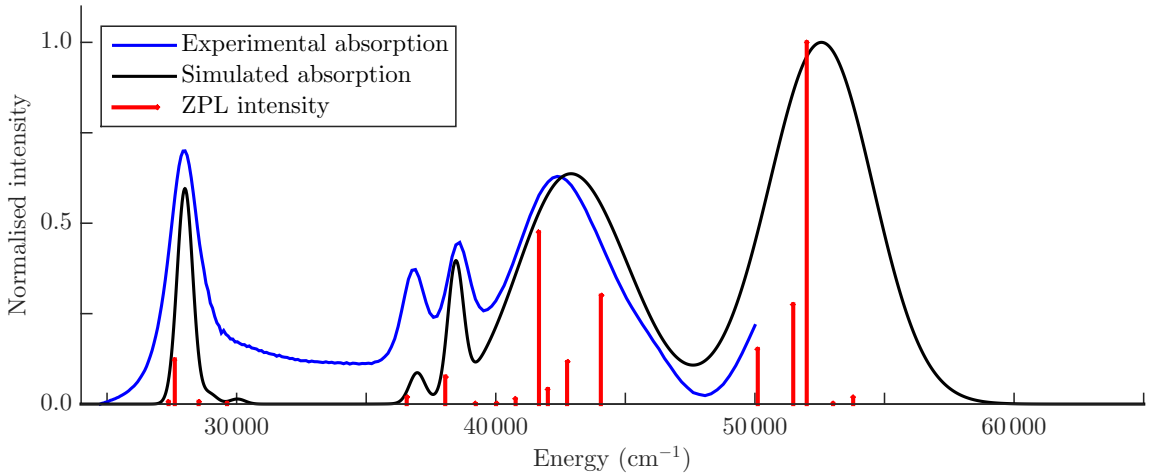

Figure 5.4 Measured and simulated absorption spectra for SrF_2:Yb^{2+}, and calculated zero–phonon lines. The height of the vertical lines indicate the relative electric dipole strength for the transition from the A_{1g} ground state to the corresponding T_{1u} irrep, normalised relative to the strongest dipole strength.

Table 5.2 Parameter values calculated for a free Yb^{2+} ion [23]; for the effective Hamiltonian of CaF_2:Yb^{2+} and SrF_2:Yb^{2+}; and values for $SrCl_2$:Yb^{2+} fitted to experimental observations [71]. All parameter values are in cm^{-1}. The free ion parameters are largely unaffected by the host crystal, and can simply be held fixed. The f crystal field parameters for SrF_2:Yb^{2+} are held at the CaF_2:Yb^{2+} values.

		Host		
Parameter	Free ion	$SrCl_2$:Yb^{2+}	CaF_2:Yb^{2+}	SrF_2:Yb^{2+}
$\Delta_E\,(fd)$		38382	42700	40470
$\zeta\,(f)$	2899	2950	2950	2950
$\zeta\,(d)$	1290	1211	1204	1204
$F^2\,(fd)$	23210	14355	14355	14355
$F^4\,(fd)$	10646	7222	7222	7222
$G^1\,(fd)$	10059	4693	4693	4693
$G^3\,(fd)$	8046	5382	5382	5382
$G^5\,(fd)$	6085	4349	4349	4349
$B^4\,(f)$ [a]		-725	-869	-869
$B^6\,(f)$ [a]		292	350	350
$B^4\,(d)$ [a]		-20442	-37726	-27323

[a] Cubic crystal field: $B^4_0 = B^4$, $B^4_{\pm4} = \sqrt{\frac{5}{14}}B^4$, and $B^6_0 = B^6$, $B^6_{\pm4} = -\sqrt{\frac{7}{2}}B^6$.

5.3 Fit to *ab initio* CaF_2:Yb^{2+} energy level structure calculations

In this section we compare the effective Hamiltonian fitted to experimental data with one fitted to an *ab initio* calculation on the same system. In a similar calculation to their $SrCl_2$:Yb^{2+} and $CsCaBr_3$:Yb^{2+} work [5, 70], Barandiarán and Seijo have provided *ab initio* energy levels for the CaF_2:Yb^{2+} system [79]. The range of impurity–ligand separations modelled in this study is significantly smaller than those of the reference calculations used in the previous chapter. This removes some of the inferior fits from either extreme of the range. This does, however, limit our ability to observe smaller trends in the parameters, such as those due to the nephelauxetic effect. The potential curves provided are shown in Figure 5.5.

The system was described using the same $4f^{14} + 4f^{13}5d + 4f^{13}6s$ effective Hamiltonian as in the previous chapter (Equation 4.4). Initial parameters are taken from the fit to the excitation spectrum of CaF_2:Yb^{2+}.

As with the previous chapter, two stages of analysis have been performed. The first uses the minima of the potential curves of Barandiarán and Seijo, [79], as target energy levels to fit the effective Hamiltonian. The second simulates a vertical (instantaneous) transition with the system held at a fixed impurity–ligand separation, at each separation provided in the reference calculation.

5.3.1 Fit to potential curve minima

For the fit to the minima of the potential curves provided by Barandiarán and Seijo, [79], all parameters are allowed to vary freely, with the $B^4(f)$ and $B^6(f)$ crystal field parameters constrained to a fixed ratio. This ratio is chosen to be the same proportion as the same parameters in the fit to $SrCl_2$:Yb^{2+} of Pan et al. [71]. The results of the fitting process are presented in Table 5.3.

Parameters are fitted to both spin–orbit free and spin–orbit inclusive levels of the *ab initio* calculation. The non–spin–orbit parameters in these two fits have very similar fitted parameter values. As will be discussed in the next chapter, this is not frequently observed in these calculations, and was not observed in the previous calculation for $SrCl_2$:Yb^{2+}.

The fd Coulomb parameters of the fit to the *ab initio* calculation are consistent with the

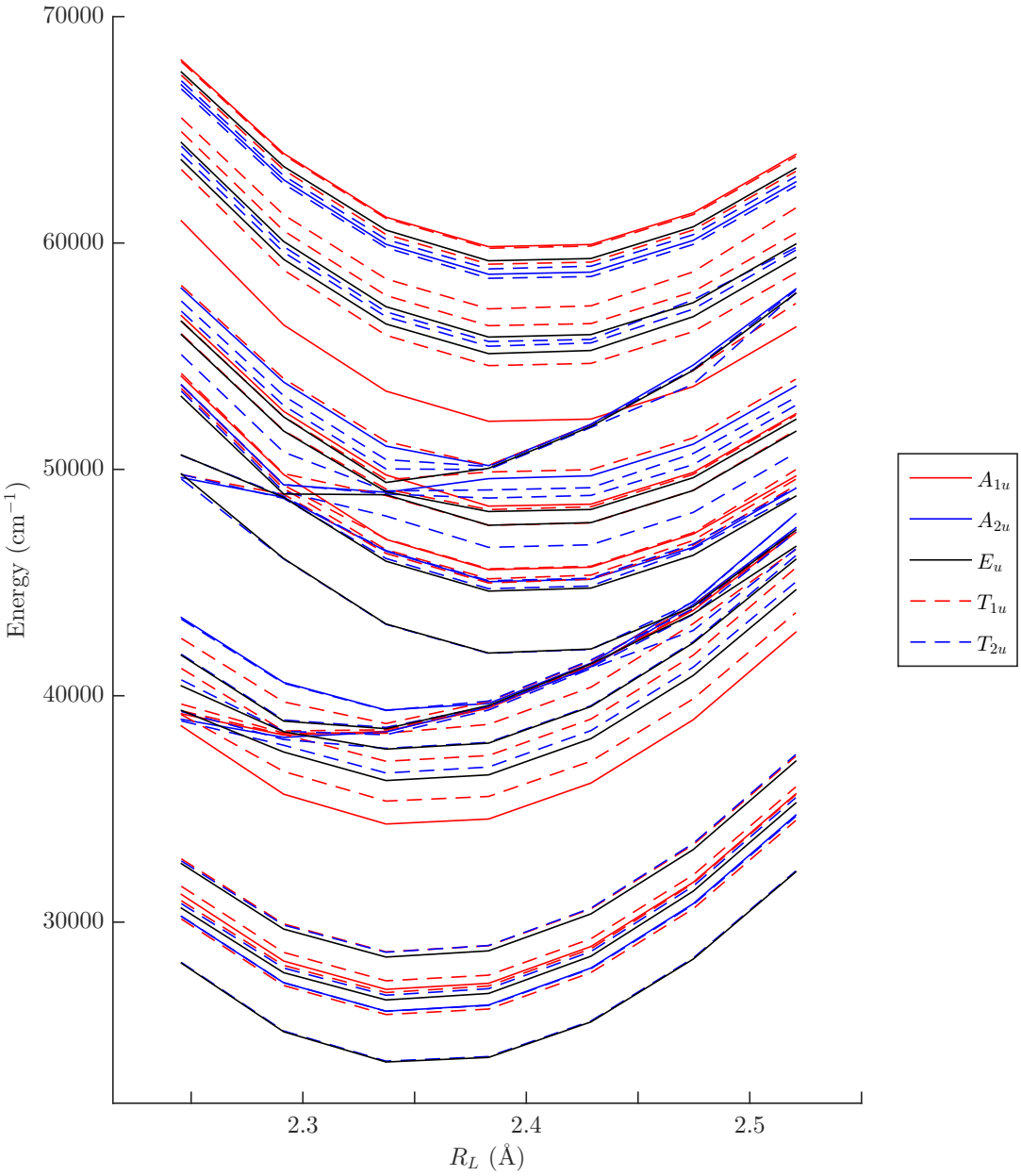

Figure 5.5 Calculated energy levels as a function of impurity–ligand separation (R_L) for the CaF_2:Yb^{2+} system of Barandiarán and Seijo [79]. Unlike the $SrCl_2$:Yb^{2+} calculation in Figure 4.3, there is no clear double–well feature in the potential curve. Some states do have a favourable minimum at about $R_L = 2.2914$ Å, which is a shorter than the equilibrium of most of the states. The $4f^{14}$ curve, which has a minimum at 2.3831 Å, is omitted. The range of separations between impurity and ligand is much less than the previous analysis.

Table 5.3 Parameters fitted to an excitation spectrum and to *ab initio* energy levels of the CaF_2:Yb^{2+} system. The fits to the *ab initio* calculations are for the highest spin–free level (MS-RASPT2) and the spin–orbit level of calculation (RASSI-SO) [79]. All parameter values are measured in cm^{-1}.

	Excitation fit		*Ab initio* fits			
	CaF_2:Yb^{2+}		MS-RASPT2		RASSI-SO	
Parameter	Value	$\pm\sigma$	Value	$\pm\sigma$	Value	$\pm\sigma$
$\Delta_E\,(fd)$	42700	(683)	42938	(348)	42980	(304)
$\zeta\,(f)$	2950	(116)			3021	(25)
$\zeta\,(d)$	1204	(622)			1676	(154)
$F^2\,(fd)$	14355		19478	(870)	19342	(605)
$F^4\,(fd)$	7222		11326	(1634)	11845	(1705)
$G^1\,(fd)$	4693		5085	(356)	5283	(433)
$G^3\,(fd)$	5382		8450	(912)	8891	(1421)
$G^5\,(fd)$	4349		2906	(1243)	4832	(2290)
$\Delta_E\,(ds)$ [a]			−193	(174)	277	(146)
$G^3\,(fs)$			537	(973)	2992	(1645)
$R^2\,(ds)$					6977	(2295)
$R^3\,(ds)$					3930	(1210)
$B^4\,(f)$ [b]	−869	(1840) [c]	−570	(269) [c]	−478	(438) [c]
$B^6\,(f)$ [b]	350	(739) [c]	229	(108) [c]	192	(176) [c]
$B^4\,(d)$ [b]	−37726	(1043)	−40578	(300)	−39873	(251)
Fit details:						
N	10		34		71	
n	6		11		15	
σ	886		341		301	

[a] $\Delta_E\,(fs) = \Delta_E\,(fd) + \Delta_E\,(ds)$.

[b] Cubic crystal field: $B^4_0 = B^4$, $B^4_{\pm4} = \sqrt{\frac{5}{14}}B^4$, and $B^6_0 = B^6$, $B^6_{\pm4} = -\sqrt{\frac{7}{2}}B^6$.

[c] Crystal field parameters held at a fixed ratio to match the fit to $SrCl_2$:Yb^{2+} by Pan et al. [71].

fit to $SrCl_2$:Yb^{2+} [73]. The exception is the $G^5\,(fd)$ parameter, as this value does not split the states strongly, and hence allows for more variation in the value during the fitting process. The f spin–orbit parameter for the fit to the *ab initio* calculation agrees with both the free–ion and previously–fitted f spin–orbit parameter values.

The main differences between the *ab initio* fit and the fit directly to the excitation spectrum are in the $B^4\,(d)$ crystal field parameter and the d spin–orbit parameter. The $R^2\,(ds)$ and $R^3\,(ds)$ parameters do differ from the corresponding values in previous fits, but these parameters only introduce very weak mixing of states and hence large values of these parameters do not have a large influence on the fit.

The fitted f crystal field parameters are much smaller than the corresponding values fitted to the excitation spectrum. The $B^4\,(f)$ parameter is smaller than the value fitted to $SrCl_2$:Yb^{2+} by Pan et al. [71], and to SrF_2:Yb^{2+} by Senanayake et al. [80]. As both $SrCl_2$ and SrF_2 have a larger lattice than CaF_2, this is not the expected result. However, the $B^4\,(f)$ parameter value fitted to the *ab initio* calculation of $SrCl_2$:Yb^{2+} is also considerably smaller than the value of Pan et al, which could indicate that the *ab initio* calculation understates the f crystal field influences to some extent.

5.3.2 Comparison of simulated spectra

Barandiarán and Seijo also provided a simulated spectrum produced from their *ab initio* calculation [79]. A comparison of this spectrum with those of the effective Hamiltonian (fitted to the experimental spectra and *ab initio* energy minima) is presented in Figure 5.6.

The energies of the states in the fit to the excitation spectrum is such that three of the four groups of peaks are reasonably aligned, but the high–spin $4f^{13}\left(^2F_{7/2}\right)5dt_{2g}$ peaks in the $40\,000 - 50\,000$ cm^{-1} range do not correctly align. The *ab initio* calculation places all states closer to the observed spectrum on average. The results of these two approaches differ by approximately 2000 cm^{-1} in the $B^4\,(d)$ parameter. By observation, the fit to the experimental spectrum demonstrates the largest $B^4\,(d)$ value that will reasonably reproduce the spectrum. The *ab initio* calculation therefore overstates the strength of this interaction.

The difference in the d spin–orbit parameter can be seen in the low–spin $4f^{13}\left(^2F_{5/2}\right)5de_g$ peaks in the $35\,000 - 40\,000$ cm^{-1} range. The experimental data has the two peaks slightly closer together than *ab initio* calculation, which causes the fitted parameter values to differ

by approximately 500 cm^{-1}.

The $E(fs)$ parameter can be changed considerably with no visible effect upon the predicted absorption spectrum, as the absorption intensities of the T_{1u} states with predominantly $6s$ character are very small relative to the predominantly $5d$ character states. This is the expected result according to the transition election rules, as discussed at the beginning of the chapter.

Additionally, the vibronics for the system are compared in Figure 5.7. The first spectrum demonstrates the vibronic structure calculated by Barandiarán and Seijo. The second spectrum is simulated using the effective Hamiltonian fitted to the minima of the potential curves. (This is the same spectrum as part (d) of Figure 5.6). The last spectrum shows the vibronic progressions determined using each T_{1u} state as a zero phonon line. The vibrational frequencies for each irrep are taken from values determined by the *ab initio* reference calculation. The Huang–Rhys parameters calculated from these values are used to create the vibronic progressions for the $5de_g$ peaks, whereas the Huang–Rhys parameters for the $5dt_{2g}$ states had to be adjusted to fit the reference spectrum. The vibronic progressions appear to provide a good correction to the relative intensities of the spectral peaks.

5.3.3 Fit by impurity–ligand separation

The effective Hamiltonian is then fitted to each impurity–ligand separation (R_L) of the energy curves provided, as per the method stated in the previous chapter. The results for these fits are presented in Table 5.4 for the highest level spin–orbit free calculation, and Table 5.5 for the spin–orbit inclusive calculation. As the range of ligand distances is smaller than the previous study, the parameters are largely well–behaved in these fits. The parameters that do vary are the crystal field terms, the configurational average energy, $\Delta E(fs)$, and the fs exchange Coulomb parameter, $G^3(fs)$. These variations are shown in Figures 5.8 and 5.9.

The crystal field parameters change predictably, decreasing in magnitude as the ligands become more distant, causing the orbital overlap between impurity and ligand electrons to decrease. At the RASSI-SO level calculation, the f crystal field parameters fit very well to a power–law model, albeit with a much larger coeffecient, $t_4 = t_6 = 10.55$, than the expected $t_4 = 5$ and $t_6 = 7$. This is shown in Figures 5.10 and 5.11. As the ratios of the parameters were fixed for the fitting process, the fitted coefficients are necessarily

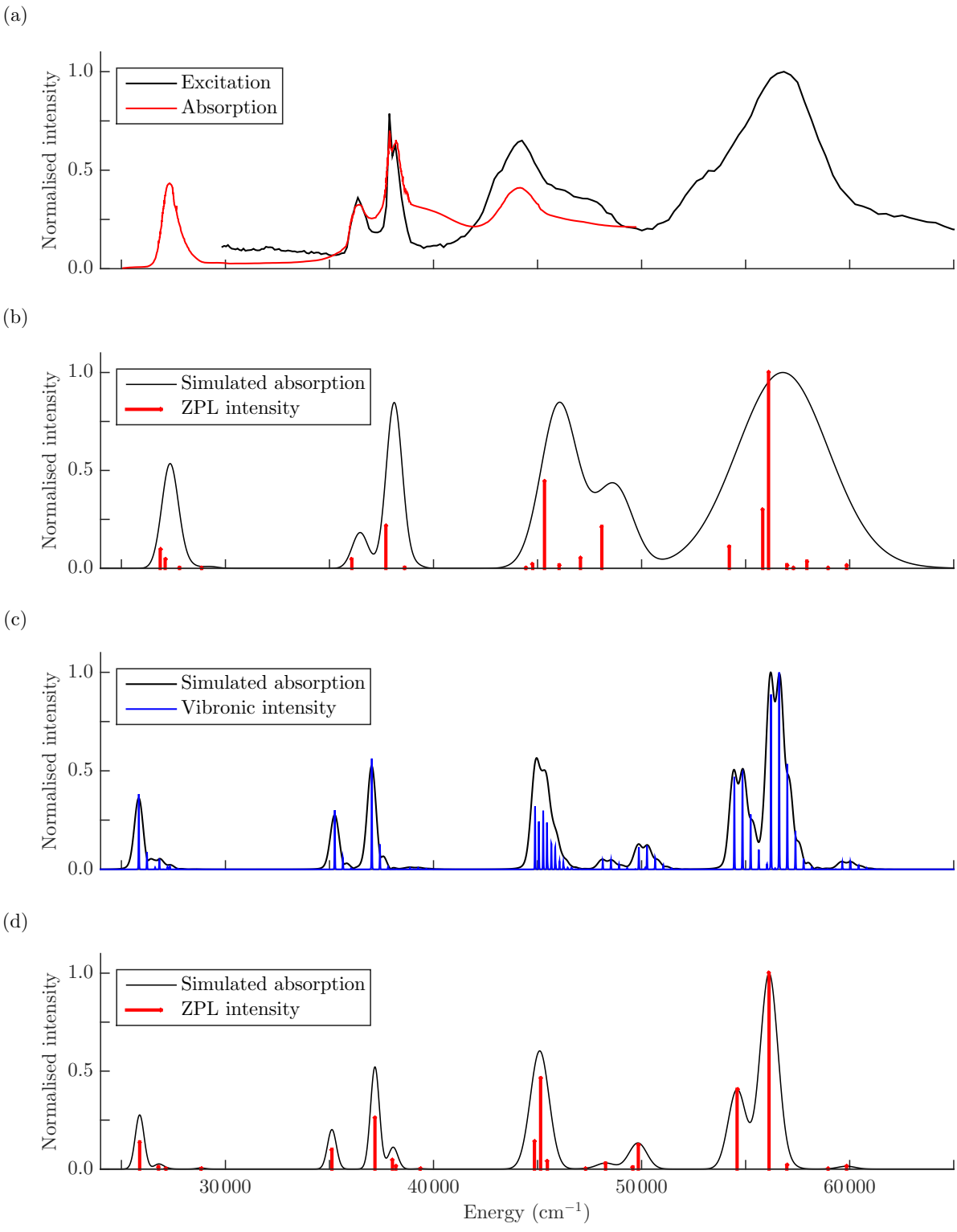

Figure 5.6 Comparison of experimental and simulated spectra for CaF_2:Yb^{2+}. (a) Absorption [28] and excitation [77] spectra of CaF_2:Yb^{2+}. (b) Simulated absorption spectrum from effective Hamiltonian parameters fitted to the experimental absorption and excitation spectra. ($4f^{14} \rightarrow 4f^{13}5d$, 18 T_{1u} irreps). (c) Simulated absorption spectrum from *ab initio* calculation [79]. (d) Simulated absorption spectrum from effective Hamiltonian parameters fitted to the *ab initio* spectrum. ($4f^{14} \rightarrow 4f^{13}5d/4f^{13}6s$, 21 T_{1u} irreps). The linewidths of the peaks in the simulated spectra in (b) and (d) are chosen to match those of (a) and (c) respectively.

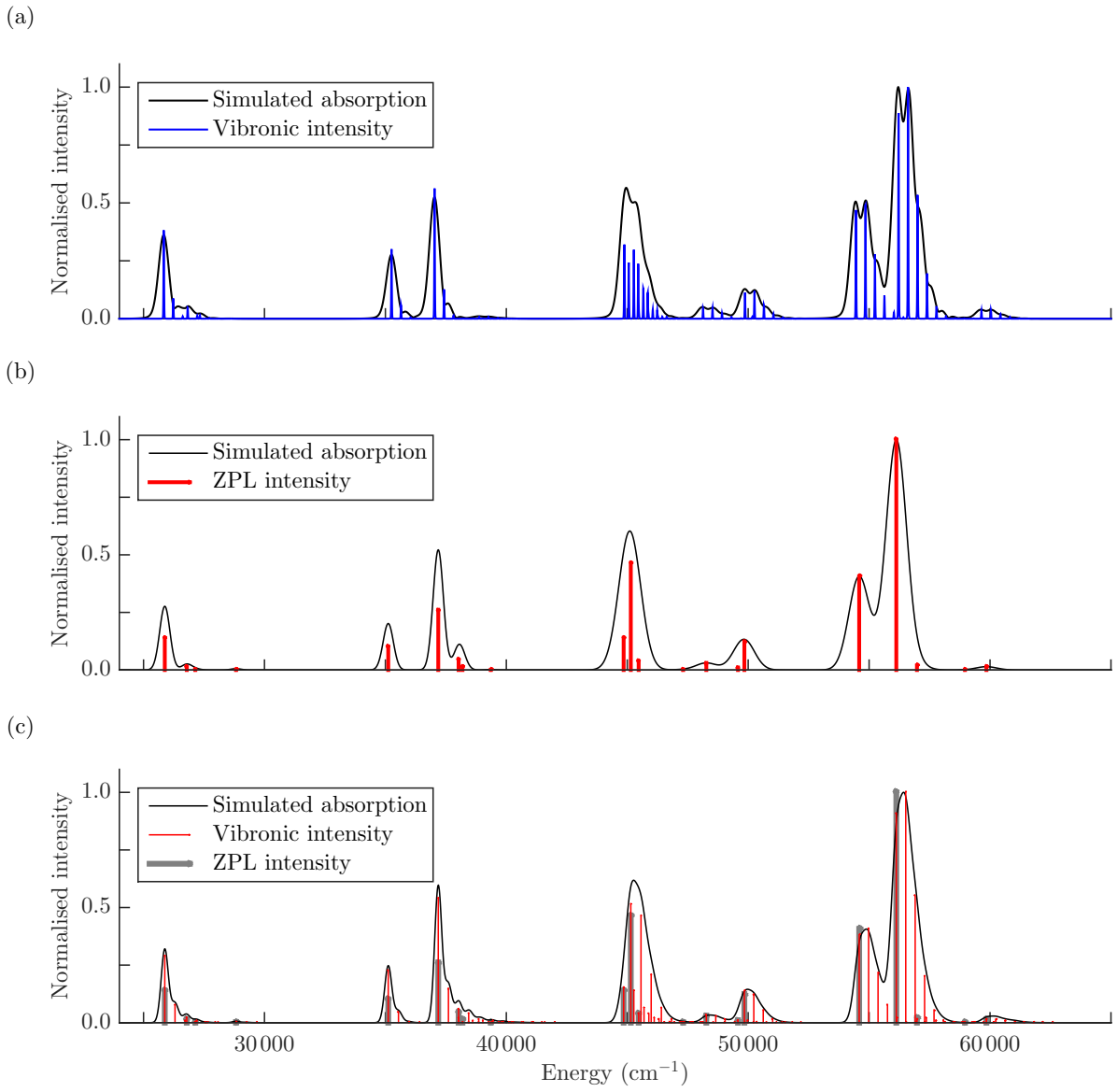

Figure 5.7 Comparison of simulated vibronic spectra for CaF_2:Yb^{2+}. (a) Seijo et al. *ab initio* absorption spectrum for CaF_2:Yb^{2+}. (b) Energy levels of absorbing states determined by an effective Hamiltonian fitted to the *ab initio* calculation. (c) Reconstruction of the vibronics using Huang–Rhys parameters from the *ab initio* calculation.

Table 5.4 Crystal field parameters fitted to the energy levels of CaF_2:Yb^{2+}, for each impurity–ligand separation of the MS-RASPT2 level (spin–orbit free) calculation provided by Barandiarán and Seijo [79]. All parameter values and σ are measured in cm^{-1}. Impurity–ligand separations, R_L, are measured in Å. Individual parameter uncertainties obtained from the CFIT program have been omitted here.

	Impurity–ligand separation, R_L (Å)						
Parameter	2.2456	2.2914	2.3372	2.3821	2.4289	2.4747	2.5206
E_{avg}	5784	2129	274	0	1120	3474	6926
$\Delta_E\,(fd)$	43967	43871	43518	43102	42696	42413	42136
$F^2\,(fd)$	18493	19417	19722	19807	19816	18752	18344
$F^4\,(fd)$	9842	10818	11148	11213	11181	10374	7090
$G^1\,(fd)$	4711	4969	5063	5078	5057	4696	4383
$G^3\,(fd)$	7040	7858	8147	8216	8243	7949	7190
$G^5\,(fd)$	2858	2863	2960	3007	3144	3681	3836
$\Delta_E\,(ds)$[a]	−6150	−3263	−875	878	2017	2175	2110
$G^3\,(fs)$	−84	445	715	936	925	902	1169
$B^4\,(f)$[b,c]	−827	−714	−575	−468	−366	32	331
$B^6\,(f)$[b,c]	332	287	231	188	147	−13	−133
$B^4\,(d)$[b]	−50240	−47090	−43615	−40177	−36900	−34195	−31521
Fit details:							
N	33	33	33	33	33	33	33
n	11	11	11	11	11	11	11
σ	314	340	340	334	328	338	501

[a] $\Delta_E\,(fs) = \Delta_E\,(fd) + \Delta_E\,(ds)$.

[b] Cubic crystal field: $B^4_0 = B^4$, $B^4_{\pm4} = \sqrt{\frac{5}{14}}B^4$, and $B^6_0 = B^6$, $B^6_{\pm4} = -\sqrt{\frac{7}{2}}B^6$.

[c] Crystal field parameters held at a fixed ratio to match the fit to $SrCl_2$:Yb^{2+} by Pan et al. [71].

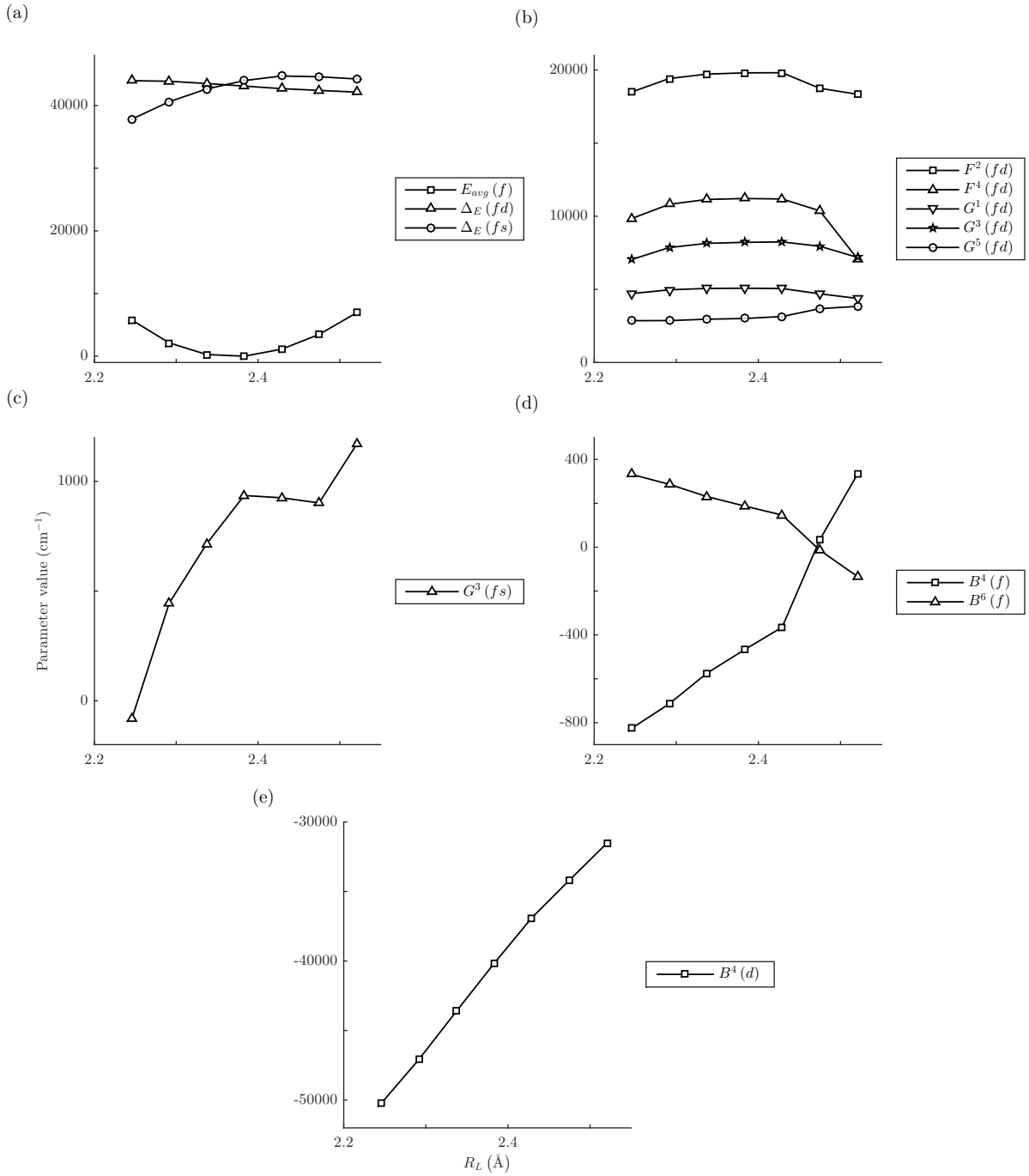

Figure 5.8 Parameters for the $4f^{14} \rightarrow 4f^{13}5d/4f^{13}6s$ effective Hamiltonian, optimised by fitting to energies of CaF_2:Yb^{2+} using the MS-RASPT2 level calculation of Barandiaran and Seijo [79], from Table 5.4. The plots are split into groups of comparable parameters: (a) Average configuration energy parameters. (b) fd Coulomb parameters. (c) fs Coulomb parameters. (d) $4f$ crystal field parameters. (e) $5d$ crystal field parameter.

Table 5.5 Crystal field parameters fitted to the energy levels of CaF_2:Yb^{2+}, for each impurity–ligand separation of the SO-CI level (spin–orbit inclusive) calculation provided by Barandiarán and Seijo [79]. All parameter values and σ are measured in cm^{-1}. Impurity–ligand separations, R_L, are measured in Å. Individual parameter uncertainties obtained from the CFIT program have been omitted here.

	Impurity–ligand separation, R_L (Å)						
Parameter	2.2456	2.2914	2.3372	2.3821	2.4289	2.4747	2.5206
E_{avg}	5784	2129	274	0	1120	3474	6923
$\Delta_E\,(fd)$	44044	43957	43606	43191	42788	42445	42115
$\zeta\,(f)$	2988	2993	2999	2999	3003	2997	2995
$\zeta\,(d)$	1324	1508	1541	1544	1531	1514	1485
$F^2\,(fd)$	18533	19169	19537	19629	19804	19381	18983
$F^4\,(fd)$	10660	11429	11337	11394	11239	10918	11053
$G^1\,(fd)$	5419	5169	5221	5215	5156	4761	4835
$G^3\,(fd)$	7548	8892	9270	9275	9140	8806	9294
$G^5\,(fd)$	2710	4770	5262	5313	5776	7376	5297
$\Delta_E\,(ds)$[a]	−6089	−3268	−890	863	1969	2306	2610
$G^3\,(fs)$	1050	756	944	831	398	2361	742
$R^2\,(ds)$	7398	2416	1199	1277	2156	576	2592
$R^3\,(ds)$	3722	1030	764	1882	3447	3424	3900
$B^4\,(f)$[b,c]	−787	−747	−595	−485	−403	−515	301
$B^6\,(f)$[b,c]	316	300	239	195	162	207	−121
$B^4\,(d)$[b]	−49561	−46518	−43013	−39574	−36264	−33410	−30595
Fit details:							
N	71	71	71	71	71	71	71
n	15	15	15	15	15	15	15
σ	199	231	232	222	208	224	237

[a] $\Delta_E\,(fs) = \Delta_E\,(fd) + \Delta_E\,(ds)$.

[b] Cubic crystal field: $B^4_0 = B^4$, $B^4_{\pm4} = \sqrt{\frac{5}{14}}B^4$, and $B^6_0 = B^6$, $B^6_{\pm4} = -\sqrt{\frac{7}{2}}B^6$.

[c] Crystal field parameters held at a fixed ratio to match the fit to $SrCl_2$:Yb^{2+} by Pan et al. [71].

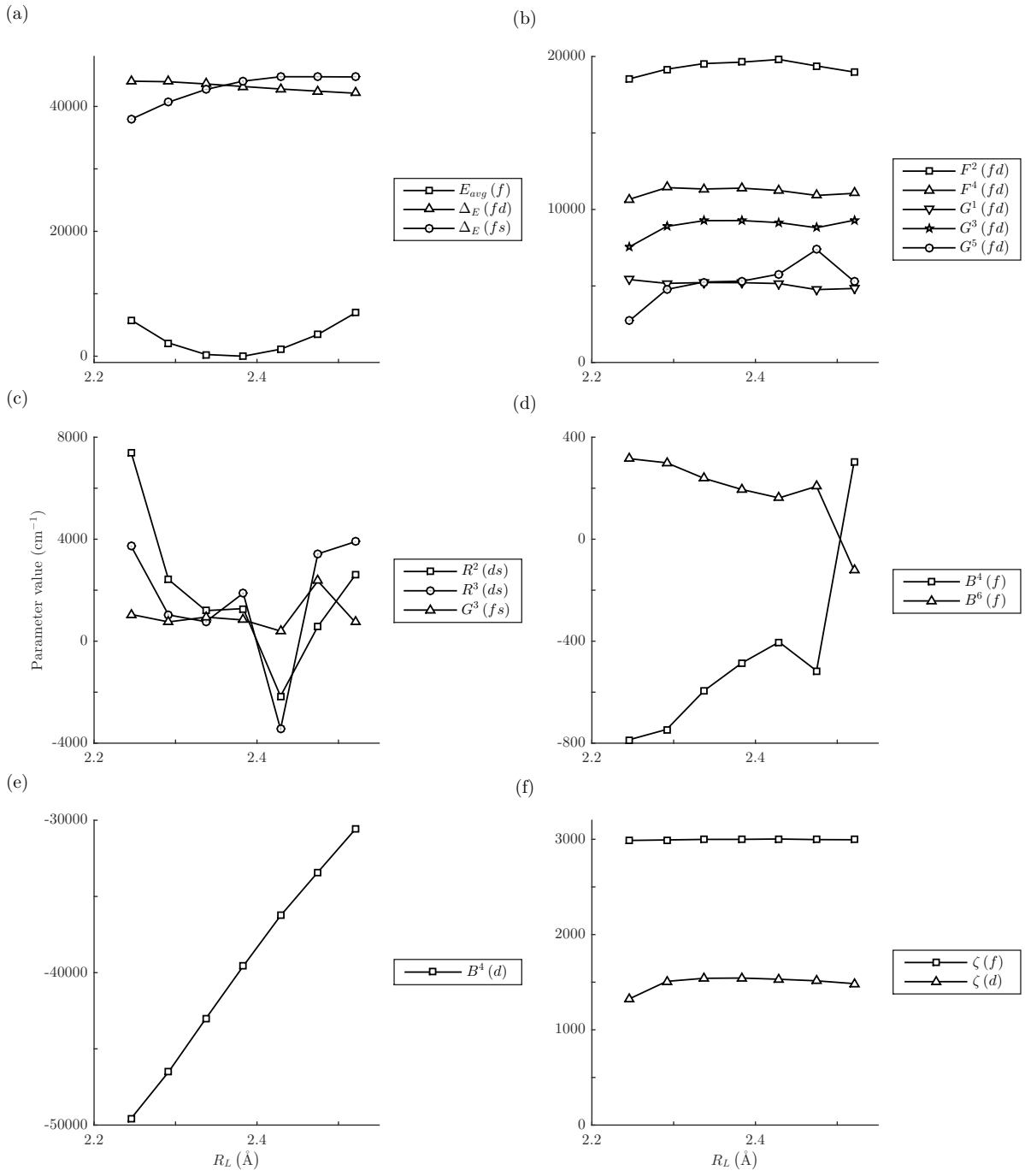

Figure 5.9 Parameters for the $4f^{14} \rightarrow 4f^{13}5d/4f^{13}6s$ effective Hamiltonian, optimised by fitting to energies of CaF_2:Yb^{2+} using the spin–orbit level calculation (SO-CI) of Barandiaran and Seijo [79], from Table 5.5. The plots are split into groups of comparable parameters: (a) Average configuration energy parameters. (b) fd Coulomb parameters. (c) fs Coulomb parameters. (d) $4f$ crystal field parameters. (e) $5d$ crystal field parameter. (f) Spin–orbit parameters.

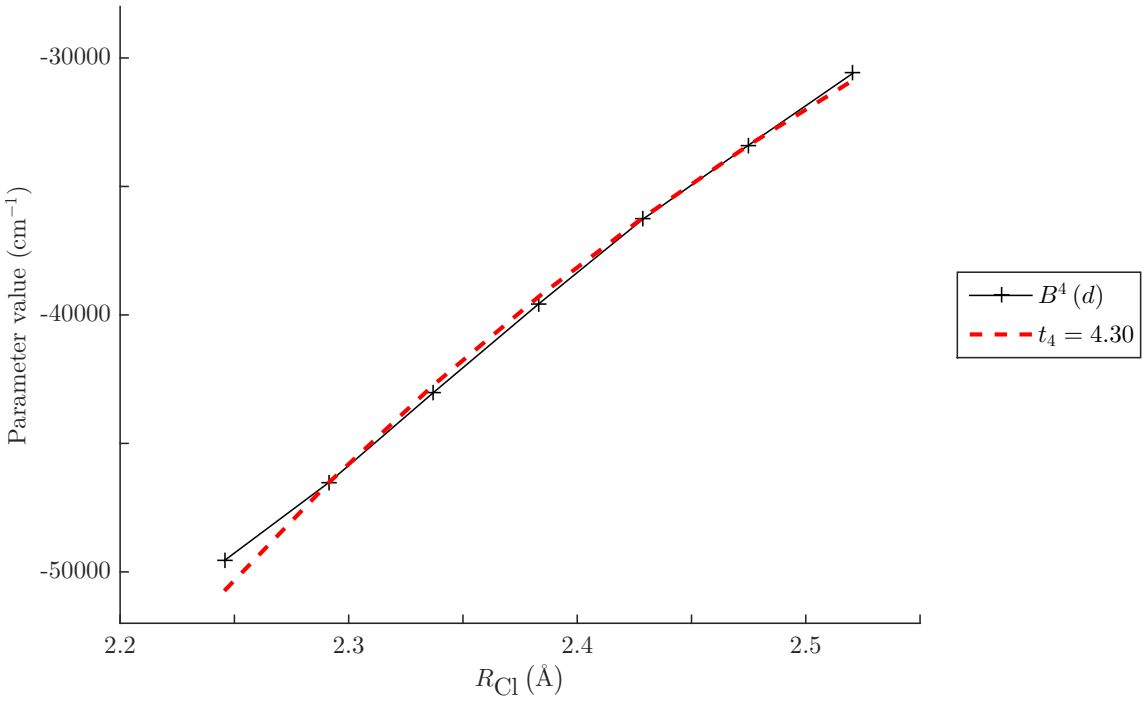

Figure 5.10 Power–law fit for the d crystal field parameter, at the RASSI-SO calculation level.

identical, but should, in theory, lie between the expected t_4 and t_6 values. The total f crystal field strength value, N_ν, is not shown, as having the parameters held at a fixed ratio renders analysis of this quantity pointless.

More interesting is the behaviour of the $\Delta_E(fs)$ and $G^3(fs)$ parameters. Unlike the fit to $SrCl_2$:Yb^{2+} in the previous chapter, there is no discontinuity introduced by the formation of double–well potentials. Instead the $\Delta_E(fs)$ parameter increases in value accross the range of ligand distances given, possibly with a quadratic dependence. For the spin–orbit inclusive calculation, the $G^3(fs)$ parameter appears to be reasonably stable apart from the longest two longest ligand displacements, whereas the spin–orbit free calculation has a gradual increase in value of this parameter with increasing ligand displacement. Since the range of ligand displacements covered is not large, the interpretation of these behaviours is limited.

Another limitation of this data range is that no clear nephelauxetic effect can be observed in the Coulomb parameters. The parameters are, by inspection, reasonably stable, with the exception of the $F^4(fd)$ parameter at MS-RASPT2 level, and the $G^5(fd)$ parameter at the RASSI-SO level. A slight decrease of the d spin–orbit parameter can be seen as the impurity–ligand separation increases. This was attributed to the nephelauxetic effect in the previous chapter.

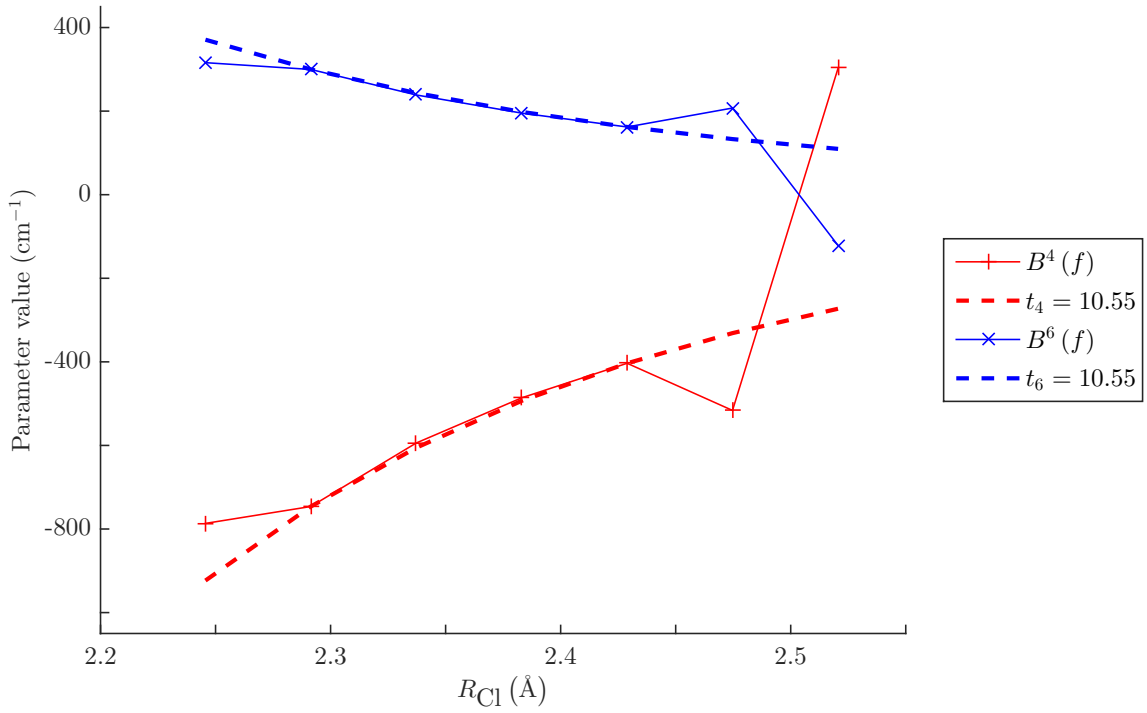

Figure 5.11 Power–law fit for the f crystal field parameters, at the RASSI-SO calculation level.

5.4 Search for the impurity–trapped exciton

Lastly, one of the aims of the *ab initio* study of CaF_2:Yb^{2+} electronic structure was to model the impurity–trapped exciton present in this material, in a similar fashion to the "pre–excitonic" states observed in the $SrCl_2$:Yb^{2+} calculations [5, 6]. However, the *ab initio* calculation was unable to provide highly delocalised electron states at a lower energy than the $5d$ levels [79]. Instead, it is argued that the anomalous emission observed in this material is an intervalence charge transfer luminescence, allowed by the clustering of Yb^{3+} and Yb^{2+} defects in the material [35]. There is presently, however, considerable evidence for the impurity–trapped exciton model [27–29, 32, 39].

Here, we use the parameters and observations from the previous sections to model the expected delocalised electron states, in a similar fashion to the $SrCl_2$:Yb^{2+} model in the previous chapter.

We observed in the previous chapter that the only parameters necessary to adjust the positions of the $6s$ states are the corresponding configuration average energy parameter, $\Delta_E(fs)$, and possibly the $G^3(fs)$. We can avoid modelling the discontinuity, and hence any need to adjust the $G^3(fs)$ parameter, by ignoring the actual $6s$ configuration states,

and simply treating all of these states as the extended electron states.

The parameters that have been fitted to experimental observations and *ab initio* calculations of the CaF_2:Yb^{2+} system are used as a basis for this model. As very little variation is observed in the Coulomb and spin–orbit parameters with changing impurity–ligand separation for the data range covered in the *ab initio* calculation, these are held fixed for the purposes of this model. Any nephelauxetic effects are assumed to be negligible over the range of the simulation. The shape of the ground state potential curve is calculated using a harmonic oscillator potential, and a vibronic frequency determined by the *ab initio* calculation: $\nu_{a_1} = 417\ \mathrm{cm}^{-1}$. To model the exciton states, the fs Coulomb parameter is scaled to a third of its free–ion value, as was observed in the fit to the $SrCl_2$:Yb^{2+} system in the previous chapter. A gradient is chosen for the $\Delta_E\,(fs)$ parameter, to match the peak of the observed exciton emission, $\Delta E = 17\,300\ \mathrm{cm}^{-1}$ [27]. The positions of the exciton states are modelled using the quoted shift of potential curves of -0.17 Å in CaF_2:Yb^{2+} from Moine et al. [28]. The resulting potential energy curves from this model are presented in Figure 5.12.

As observed in Figure 5.12, the minima of the potential curves used to model the extended electrons lie above the lowest $5d$ levels. This clearly will not reproduce the expected physical behaviour, as the state is not energetically favourable. As we have noted previously, the lowest $5d$ energy levels produced by the *ab initio* calculation are too low in energy when compared to the observed absorption spectrum, in Figure 5.6, due to the overstated strength of the $5d$ crystal field interaction. This seems to be a likely candidate for why the exciton state does not work here.

An alternative set of curves were modelled (not shown here) for comparison, using estimated energies from the schematic of Mahlik et al. [81]. These placed the exciton states at an energetically favourable position below the $5d$ levels, but at the slightly shorter offset of -0.15 Å.

5.5 Summary

An effective Hamiltonian was fitted to both experimental absorption and excitation data spectra and an *ab initio* calculation of energy levels in the excitonic material, CaF_2:Yb^{2+}. An effective Hamiltonian was also fitted to an absorption spectrum of SrF_2:Yb^{2+}, which also exhibits excitonic emission. The fits to experimental spectra were conducted on the

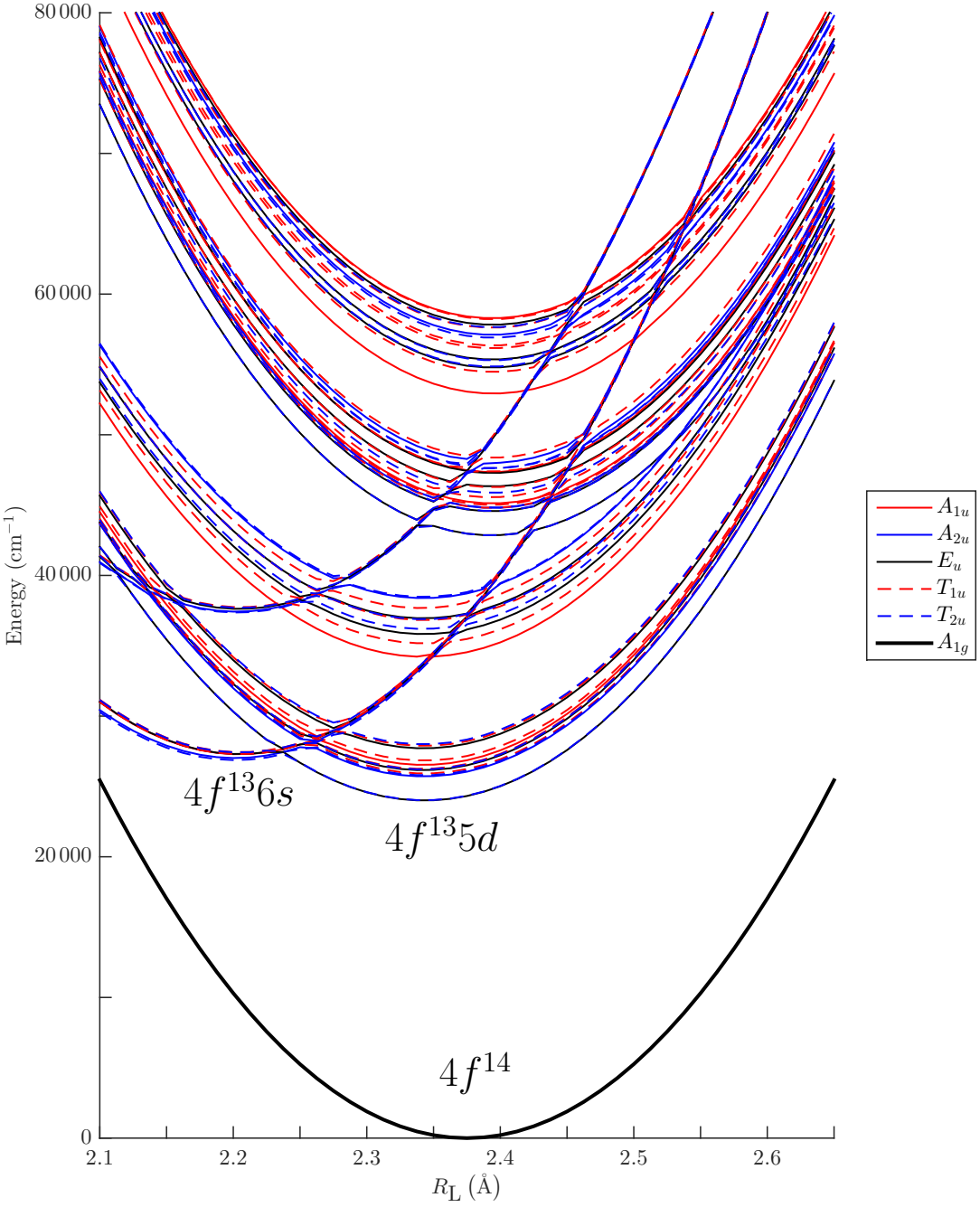

Figure 5.12 A simulation to reproduce the potential energy surfaces required to model the impurity–trapped exciton in CaF_2:Yb^{2+}. The parameters are chosen using the fits to the *ab initio* calculations for the CaF_2:Yb^{2+} system. The Coulomb and spin–orbit interactions are held constant throughout the range of impurity–ligand separations covered, as no clear nephelauxetic effect is observed in the parameters over this range of data in the reference calculation. The shape of the potential curves is modelled using harmonic oscillator potentials, and the vibronic frequencies calculated in the reference calculation [79].

space $4f^{14} \rightarrow 4f^{13}5d$, as the low intensity of $f \leftrightarrow s$ transitions prevents any $6s$ features from being clearly observable in the experimental spectra.

Existing parameters from a fit to $SrCl_2$:Yb^{2+} were used as starting parameters for the fitting processes. These were held fixed wherever possible, particularly for the Coulomb parameters, as there were only a small number of reference energy levels available.

The $f \rightarrow d$ absorption spectra of each material were simulated from the fitted effective Hamiltonian parameters, by convolving the electric dipole moments of the absorbing irreps (the T_{1u} irreps from the selection rules of the transition) with Gaussian functions, with line–widths fitted to the observed spectra. The fits to both CaF_2:Yb^{2+} and SrF_2:Yb^{2+} reproduce the corresponding observed spectra well, with the exception of one group of peaks in the CaF_2:Yb^{2+} spectrum. The $4f^{13}\left(^2F_{7/2}\right)5dt_{2g}$ peaks are shifted slightly from the observed positions. With the given parameter fit to this spectrum, it is impossible to pick an f spin–orbit parameter to fit the splitting of both the $5de_g$ peaks and $5dt_{2g}$ peaks simultaneously. The value required to fit the spin–orbit splitting of the $5dt_{2g}$ peaks is 3583 cm^{-1}. This is substantially higher than the $SrCl_2$:Yb^{2+} reference value of 2950 cm^{-1}, which agrees with all other fits in this chapter.

The equivalent effective Hamiltonian parameters for an *ab initio* calculation for the CaF_2:Yb^{2+} system are extracted. The extracted *ab initio* parameters and fitted experimental parameters disagreed with each other, with respect to the crystal field parameters. The *ab initio* f crystal field parameters are weaker than the parameters fitted to the observed spectra, but the *ab initio* d crystal field is much stronger than the experimental counterpart. As a result, the *ab initio* calculation overstates the influence of the d crystal field, and the predicited energy levels are split too far.

The Coulomb parameters fitted to the *ab initio* are physically reasonable, and are largely in agreement, apart from the $G^5\left(fd\right)$ parameter, with the values fitted to $SrCl_2$:Yb^{2+} in the previous chapter. The f spin–orbit parameters agree with the experimental and free–ion values.

The spectrum simulated by the reference *ab initio* calculation was also reproduced, using a spectrum simulated from the extracted effective Hamiltonian parameters. This was reproduced in two ways. The first was to simply convolve the absorbing irreps with a broad Gaussian function. The second was to simulate the vibronic progression associated with each absorbing irrep, to provide the shape of the simulated spectrum. Both of these methods were able to reproduce the *ab initio* spectrum.

An analysis of the effective Hamiltonian parameters as a function of impurity–ligand separation for CaF_2:Yb^{2+} was conducted, as per the previous chapter, using the *ab initio* potential energy curves as reference energy levels for the effective Hamiltonian fits. The short range of impurity–ligand separations covered by the reference calculation means that the Coulomb parameters are reasonably stable, and do not exhibit any clear nephelauxetic effect. The f spin–orbit parameter is also steady, while a slight decrease can be seen in the d spin–orbit parameter as the impurity–ligand separation increases. This was also observed in $SrCl_2$:Yb^{2+} in the previous chapter, and was attributed to the nephelauxetic effect. The crystal field parameters at the highest calculation level can be modelled well using power–law dependencies. At the highest level of calculation, the $G^3\,(fs)$ Coulomb parameter seems to be very stable.

Using the parameters extracted from the *ab initio* calculations, a model of the CaF_2:Yb^{2+} system including an excitonic state was constructed, to reproduce the known excitonic emission energy from this material. It is sufficient to adjust the $\Delta_E\,(fs)$ parameter to achieve this. The values of the $B^4\,(d)$ crystal field parameter extracted from the *ab initio* calculation are too large to match the observed absorption spectrum, causing a lower energy than expected for the lowest $5d$ states. This prevents the exciton state from being energetically favourable when using a value of -0.17 Å for the potential curve displacement, as determined by Moine et al. [28].

Chapter 6

Spectroscopic parameters from *ab initio* calculations of more complex systems

In the previous two chapters, we have focused our analysis on the $5d$ and $6s$ excited configurations of divalent ytterbium, and the impurity–trapped exciton that can form from these. We have used the semi–empirical effective Hamiltonian to extract the physical parameters that describe these models from *ab initio* calculations of the energy level structure of these materials.

Divalent ytterbium has a reasonably simple effective Hamiltonian. The ground configuration is a full shell, and hence consists of only a single state, and the lowest excited configurations contain a total of two valence electrons, each in a different shell. Therefore, a minimal number of electron interaction operators are required to describe this system.

In this chapter, we extend our analyses to lanthanide ions of increasing complexity, in order to test the ability to extract parameters from larger Hamiltonian systems. *Ab initio* calculations of a similar rigour to those used as a reference in the previous chapters have been published for a number of lanthanide materials, including ions of praseodymium, samarium, europium, and terbium [44, 67, 68, 82, 83]. There are also several *ab initio* studies of cerium materials (for example, Pascual et al. [4]), but the Ce^{3+} system is simpler than the Yb^{2+} system already studied, as it only has one valence electron. This can give us information about the crystal field that the lanthanide is embedded in, but has no Coulomb parameters. The equivalent crystal field parameters from these systems can be

determined by direct calculation from the eigenvectors of the *ab initio* calculation [8, 46], which is a preferable method. This is not used for the larger systems due to the complexity of these systems.

The reference calculations not only include $4f^N$ states, but also the excited $4f^{N-1}5d$ configuration states. The purpose of this chapter is to use the advantage provided by the vast number of reference energy levels for these $5d$ states to allow the large number of parameters that describe these systems to be fitted with relative freedom – a process that cannot normally occur when using experimental data, as electronic transitions to the $5d$ levels result in broad bands, which limit the number of reference energy levels. These fitted parameters are then compared with existing predictions of $4f^{N-1}5d$ effective Hamiltonian parameters for these materials.

The reference *ab initio* calculations that are chosen for use as targets for the analysis are those for which the resultant *ab initio* energy levels have been published. We fit an effective Hamiltonian to extract the crystal field parameters of the *ab initio* calculations of trivalent praseodymium in Lu_2O_3 and CaF_2; trivalent terbium in BaF_2; and divalent europium in CaF_2. No excitonic or other trap states have been modelled in these calculations. Wherever possible, both the spin–free and spin–orbit inclusive levels of these calculations are examined. Parameters fitted to observed experimental energy levels or calculated from the free–ion definitions are used as a comparison for the extracted parameters. Experimental levels for La_2O_3:Pr^{3+} are fitted to provide reference parameters with which to compare the Lu_2O_3:Pr^{3+} parameters.

6.1 Trivalent praseodymium

The simplest increase in complexity from the $4f^{14} \leftrightarrow 4f^{13}5d$ system is to consider trivalent praseodymium: $4f^2 \leftrightarrow 4f5d$. The ground configuration has all $4f^N$ Hamiltonian terms excluding the three–body interactions. The excited configuration, $4f5d$, is nearly identical to that of $4f^{13}5d$, apart from the signs of some matrix elements. The effective Hamiltonian for this system is $H_{\text{eff}} = H_{4f^2} + H_{4f5d}$, where:

$$\begin{aligned} H_{4f^2} = {} & E_{\text{avg}} \cdot I + \sum_k F^k f_k + \alpha L\left(L+1\right) + \beta G\left(G_2\right) + \gamma G\left(R_7\right) \\ & + \zeta A_{\text{so}}\left(f\right) + \sum_{i=0,2,4} M^i m_i + \sum_{i=2,4,6} P^i p_i + H_{\text{CF}}\left(f\right), \end{aligned} \tag{6.1}$$

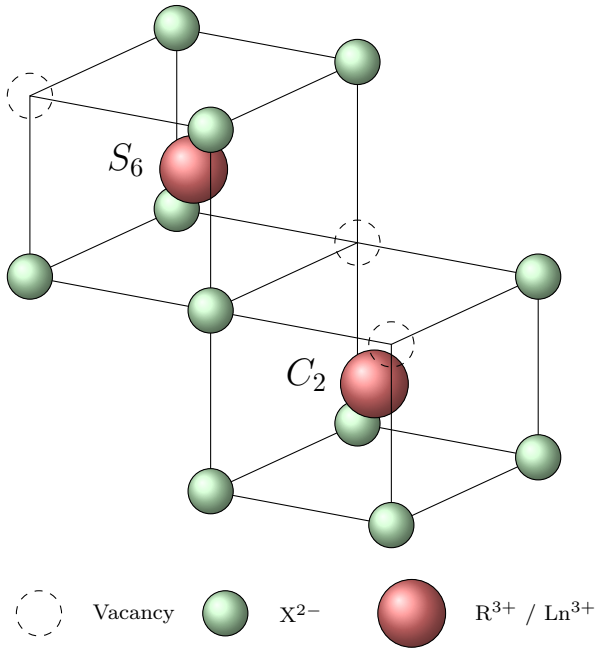

Figure 6.1 A schematic of the substitutional impurity site symmetries in cubic structure R_2X_3.

and

$$H_{4f5d} = \Delta_E\left(fd\right)\delta_E\left(fd\right) + \sum_{k=2,4} F^k f_k\left(fd\right) + \sum_{k=1,3,5} G^k g_k\left(fd\right) + \zeta A_{\mathrm{so}}\left(d\right) + H_{\mathrm{CF}}\left(d\right). \tag{6.2}$$

There are two reference *ab initio* calculations from which we extract the equivalent effective Hamiltonian parameters: Lu_2O_3:Pr^{3+} [82] and CaF_2:Pr^{3+} [68]. In CaF_2:Pr^{3+}, the divalent metal cation has been replaced by a trivalent lanthanide ion. Unlike the CaF_2:Yb^{2+} case, this will cause a change in structure of the crystal, in order to compensate for the difference in charge of the substituted ion. There are a number of charge–compensating mechanisms available, which can result in different site symmetries for the impurity. In the CaF_2:Pr^{3+} calculation, the Pr^{3+} impurity still occupies an octahedral site. Experimental energy levels for CaF_2:Pr^{3+} and free–ion Pr^{3+} are also reported in this reference.

The Lu_2O_3 host material has a cubic R_2X_3 structure, which has a large unit cell containing many molecules [78]. There are, therefore, multiple substitution sites for the Pr^{3+} impurity to occupy within this lattice. The Lu_2O_3:Pr^{3+} calculation is for Pr^{3+} occupying S_6 and C_2 sites [82]. A schematic of these site symmetries within Lu_2O_3 is demonstrated in Figure 6.1, based on the schematic by Antic-Fidancev et al. [58].

For an approximate experimental reference, we use effective Hamiltonian parameters from

a fit to La_2O_3:Pr^{3+} by Moune et al. [84]. This material has a hexagonal stucture [78], where the lanthanum ions occupy C_{3v} symmetry sites. The validity of this as a reference shall be discussed shortly.

6.1.1 The fitting process

For each of these fits, the $4f^2$ configuration parameters are fitted independently of the excited $4f5d$ configuration. As there are no configuration interaction terms present which explicitly mix the basis states of the two configurations, the fitted parameters for each configuration will have no impact upon the positions of the energy levels of the other (besides the E_{avg} and $\Delta_E\,(fd)$ parameters).

The $4f^2$ configuration parameters fitted to these systems are presented in Table 6.1. The parameters for the C_{3v} symmetry fit of the La_2O_3 host are from Moune et al. [84], and have been reproduced here for comparison. The energy levels of the S_6 site of the La_2O_3 host; the C_2 and S_6 sites of the Lu_2O_3 host; and the O_h site of the CaF_2 host have been fitted in this work, along with the the free–ion levels for Pr^{3+} modelled by *ab initio* calculation by Pascual et al. [68]. In the appendices, the $4f^2$ configuration energy levels for the spin–free Lu_2O_3:Pr^{3+} are presented in Table B.1, and the $4f^2$ configuration energy levels of the remaining spin–orbit inclusive calculations are presented in Table B.2.

The $4f5d$ configuration parameters fitted to these systems are presented in Table 6.2. These consist of parameters extracted from the *ab initio* reference calculations (Lu_2O_3:Pr^{3+}, CaF_2:Pr^{3+}, and free–ion Pr^{3+}), and $4f5d$ parameters for O_h site CaF_2:Pr^{3+} calculated by van Pieterson et al. [18] for comparison.

6.1.2 "Descent of symmetry"

The crystal field Hamiltonian is necessarily different for each site symmetry. The necessary parameters for each available symmetry are listed in Table 1.7 of Liu [14]. For C_{3v} site symmetry, the required crystal field parameters are:

$$\begin{aligned} H_{\text{CF},\,C_{3v}} = {} & B_0^2 C_0^{(2)} + B_0^4 C_0^{(4)} + B_3^4 \left(C_3^{(4)} - C_{-3}^{(4)} \right) \\ & + B_0^6 C_0^{(6)} + B_3^6 \left(C_3^{(6)} - C_{-3}^{(6)} \right) + B_6^6 \left(C_6^{(6)} + C_{-6}^{(6)} \right). \end{aligned} \tag{6.3}$$

Table 6.1 Effective Hamiltonian parameters fitted to experimentally observed and *ab initio* calculations of $4f^2$ energy levels of Pr^{3+} ions embedded in the host materials: Lu_2O_3, La_2O_3, and CaF_2 (at various site symmetries); and for the free–ion. Uncertainties of fitted parameters are indicated in brackets. Some fits did not allow all parameters to vary at once, but instead by turn, in a sequence of fits. All parameter values are in cm^{-1}. Except for the C_{3v} fit by Moune et al., the parameters presented here are the results of fits conducted in this work, to the energy levels reported in the indicated references.

	La_2O_3:Pr^{3+}				Lu_2O_3:Pr^{3+}				CaF_2:Pr^{3+}				Free–ion Pr^{3+}			
	Experiment [84]		Experiment [84]		*Ab initio* [82]				Experiment [68]		*Ab initio* [68]		Experiment [68]		*Ab initio* [68]	
Site symmetry:	C_{3v}		S_6		C_2		S_6		O_h		O_h					
Parameter	Value	$\pm\sigma$	Value	$\pm\sigma$	Value	$\pm\sigma$	Value	$\pm\sigma$	Value	$\pm\sigma$	Value	$\pm\sigma$	Value	$\pm\sigma$	Value	$\pm\sigma$
E_{avg}			10073	(2)	8660	(46)	9150	(321)	10326	(5)	11270	(135)	10176	(11)	11117	(32)
F_2	66566	(95)	66778	(17)	72785	(361)	79107	(2640)	68610	(41)	82373	(1398)	70878	(371)	82614	(1109)
F_4	49529	(233)	49988	(48)	45843	(701)	49138	(510)	49421	(92)	53333	(4166)	49404	(957)	50718	(2862)
F_6	32575	(182)	33101	(35)	27919	(654)	29182	(4640)	33248	(57)	31429	(2261)	31055	(1106)	31475	(3302)
α	21	(1)	21	(0)	79	(3)	54	(20)	22	(1)	63	(14)	24	(0)	56	(1)
β	-712	(44)	-716	(10)	-1028	(268)	-476	(1251)	−687	(42)	−566		-590	(11)	-245	(35)
γ	1370		1200		3674	(250)	1659	(1201)	1406	(49)	2972	(767)	2273	(342)	1990	(1023)
ζ	736	(6)	737	(1)					757	(3)	830	(87)	764	(2)	801	(5)
M^0 [a]	1	(1)	1	(1)					2		2		2	(0)	0	(1)
P^2 [b]	196	(145)	194	(10)					−87		−87		250	(42)	51	(135)
B_0^2	-812	(54)	-807	(13)	-753	(262)	-2697	(1501)								
$\mathrm{Re}(B_2^2)$					2011	(177)										
B_0^4	475	(20)	459	(33)	-675	(625)	-1541	(3660)	−2873	(58)	−2132	(1268)				
$\mathrm{Re}(B_2^4)$					1665	(544)										
$\mathrm{Im}(B_2^4)$					1741	(561)										
$\mathrm{Re}(B_3^4)$	1568		-217	(125)			-2821	(382)								
$\mathrm{Im}(B_3^4)$			1556	(18)			1737	(620)								

Continued on next page...

[a] Ratios held at $M^2 = 0.56\ M^0,\ M^4 = 0.31\ M^0$ [18].
[b] Ratios held at $P^4 = 0.5\ P^2,\ P^6 = 0.1\ P^2$ [18].

Table 6.1 *Continued*

	La_2O_3:Pr^{3+}				Lu_2O_3:Pr^{3+}				CaF_2:Pr^{3+}				Free–ion Pr^{3+}			
	Experiment [84]		Experiment [84]		*Ab initio* [82]				Experiment [68]		*Ab initio* [68]		Experiment [68]		*Ab initio* [68]	
Site symmetry:	C_{3v}		S_6		C_2		S_6		O_h		O_h					
Parameter	Value	$\pm\sigma$	Value	$\pm\sigma$	Value	$\pm\sigma$	Value	$\pm\sigma$	Value	$\pm\sigma$	Value	$\pm\sigma$	Value	$\pm\sigma$	Value	$\pm\sigma$
$\mathrm{Re}(B_4^4)$					2625	(500)			−1717 [c]		−1274 [c]					
$\mathrm{Im}(B_4^4)$					800	(1099)										
B_0^6	475	(131)	458	(36)	295	(756)	1774	(3920)	1147	(25)	491	(844)				
$\mathrm{Re}(B_2^6)$					-1535	(541)										
$\mathrm{Im}(B_2^6)$					80	(900)										
$\mathrm{Re}(B_3^6)$	-45	(85)	46	(167)			755	(402)								
$\mathrm{Im}(B_3^6)$			21	(26)			469	(652)								
$\mathrm{Re}(B_4^6)$					678	(607)			−2146 [d]		−919 [d]					
$\mathrm{Im}(B_4^6)$					70	(821)										
$\mathrm{Re}(B_6^6)$	345	(132)	-355	(36)	651	(588)	623	(844)								
$\mathrm{Im}(B_6^6)$			81	(120)	184	(1072)	1240	(422)								
N_ν	2396		2390		5840		5073		4622		3108					
Fit details:																
N	42		42		49		33		15		37		12		12	
n	14		16		21		16		7		9		10		10	
σ	34		38		306		259		14		815		5		16	

[c] For O_h symmetry, $B_4^4 = \sqrt{\frac{5}{14}} B_0^4$.

[d] For O_h symmetry, $B_4^6 = -\sqrt{\frac{7}{2}} B_0^6$.

Table 6.2 Effective Hamiltonian parameters fitted to experimentally observed and *ab initio* calculations of $4f5d$ energy levels of Pr^{3+} ions embedded in the host materials: Lu_2O_3 and CaF_2 (at various site symmetries); and for the free–ion. Uncertainties of fitted parameters are indicated in brackets. Some fits did not allow all parameters to vary at once, but instead by turn, in a sequence of fits. All parameter values are in cm^{-1}. Except for the calculation of O_h CaF_2:Pr^{3+} by van Pieterson et al., the parameters presented here are the results of fits conducted in this work, to the energy levels reported in the indicated references.

	Lu_2O_3:Pr^{3+}				CaF_2:Pr^{3+}				Free–ion Pr^{3+}			
	Ab initio [82]				Experiment [18]		*Ab initio* [68]		Experiment [68]		*Ab initio* [68]	
Site symmetry:	C_2		S_6		O_h		O_h					
Parameter	Value	$\pm\sigma$	Value	$\pm\sigma$	Value	$\pm\sigma$	Value	$\pm\sigma$	Value	$\pm\sigma$	Value	$\pm\sigma$
$\Delta_E\,(fd)$	36014	(17)	36699	(2428)	52760		51116	(160)	57087	(45)	53812	(63)
$F^2\,(fd)$	18887	(262)	20303	(915)	30271		17847	(1647)	21817	(507)	24032	(536)
$F^4\,(fd)$	11003	(430)	10786	(1801)	15094		9526	(3346)	16550	(782)	16750	(822)
$G^1\,(fd)$	7221	(114)	6611	(464)	12903		6632	(985)	10351	(176)	9969	(187)
$G^3\,(fd)$	6157	(290)	4613	(1184)	11160		9550	(3040)	12320	(611)	12922	(640)
$G^5\,(fd)$	6827	(981)	6827		8691		1246	(3683)	8544	(832)	9456	(888)
$\zeta\,(f)$ [a]					751		1033	(78)	926	(35)	961	(37)
$\zeta\,(d)$					1149		746	(379)	1018	(60)	1062	(65)
$B_0^2\,(d)$	-51	(214)	-14198	(4745)								
$\mathrm{Re}(B_2^2\,(d))$	5498	(106)										
$B_0^4\,(d)$	-7930	(170)	-20554	(4677)	−44016		−51404	(478)				

Continued on next page...

[a] The f–electron spin–orbit interaction will change slightly, due to the new configuration. The f crystal field terms may also change slightly, but this is ignored, as the change should be minimal due to the shielding from the ligands provided by outer orbitals.

Table 6.2 *Continued*

	Lu_2O_3:Pr^{3+}				CaF_2:Pr^{3+}				Free–ion Pr^{3+}			
	Ab initio [82]				Experiment [18]		*Ab initio* [68]		Experiment [68]		*Ab initio* [68]	
Site symmetry:	C_2		S_6		O_h		O_h					
Parameter	Value	$\pm\sigma$	Value	$\pm\sigma$	Value	$\pm\sigma$	Value	$\pm\sigma$	Value	$\pm\sigma$	Value	$\pm\sigma$
$\mathrm{Re}(B_2^4(d))$	-244	(206)										
$\mathrm{Im}(B_2^4(d))$	5149	(127)										
$\mathrm{Re}(B_3^4(d))$			-26593	(4532)								
$\mathrm{Im}(B_3^4(d))$			10919	(10298)								
$\mathrm{Re}(B_4^4(d))$	6574	(141)			−26306		−30720 [b]					
$\mathrm{Im}(B_4^4(d))$	577	(212)										
N_ν	16177		47438		60592		70761					
Fit details:												
N	91		61				97		31		31	
n	14		10				10		9		9	
σ	353		315				771		155		164	

[b] For O_h symmetry, $B_4^4 = \sqrt{\frac{5}{14}} B_0^4$.

For the S_6 site symmetry, the required parameters are (Equation 2.25):

$$\begin{aligned} H_{\mathrm{CF},\,S_6} = {} & B_0^2 C_0^{(2)} + B_0^4 C_0^{(4)} + \mathrm{Re}\left(B_3^4\right)\left(C_3^{(4)} - C_{-3}^{(4)}\right) + i\,\mathrm{Im}\left(B_3^4\right)\left(C_3^{(4)} + C_{-3}^{(4)}\right) \\ & + B_0^6 C_0^{(6)} + \mathrm{Re}\left(B_3^6\right)\left(C_3^{(6)} - C_{-3}^{(6)}\right) + i\,\mathrm{Im}\left(B_3^6\right)\left(C_3^{(6)} + C_{-3}^{(6)}\right) \\ & + \mathrm{Re}\left(B_6^6\right)\left(C_6^{(6)} + C_{-6}^{(6)}\right) + i\,\mathrm{Im}\left(B_6^6\right)\left(C_6^{(6)} - C_{-6}^{(6)}\right). \end{aligned} \tag{6.4}$$

Lastly, for the low–symmetry C_2 site, 14 parameters are required:

$$\begin{aligned} H_{\mathrm{CF},\,C_2} = {} & B_0^2 C_0^{(2)} + B_0^4 C_0^{(4)} + B_0^6 C_0^{(6)} + B_2^2\left(C_2^{(2)} + C_{-2}^{(2)}\right) \\ & + \mathrm{Re}\left(B_2^4\right)\left(C_2^{(4)} + C_{-2}^{(4)}\right) + i\,\mathrm{Im}\left(B_2^4\right)\left(C_2^{(4)} - C_{-2}^{(4)}\right) \\ & + \mathrm{Re}\left(B_4^4\right)\left(C_4^{(4)} + C_{-4}^{(4)}\right) + i\,\mathrm{Im}\left(B_4^4\right)\left(C_4^{(4)} - C_{-4}^{(4)}\right) \\ & + \mathrm{Re}\left(B_2^6\right)\left(C_2^{(6)} + C_{-2}^{(6)}\right) + i\,\mathrm{Im}\left(B_2^6\right)\left(C_2^{(6)} - C_{-2}^{(6)}\right) \\ & + \mathrm{Re}\left(B_4^6\right)\left(C_4^{(6)} + C_{-4}^{(6)}\right) + i\,\mathrm{Im}\left(B_4^6\right)\left(C_4^{(6)} - C_{-4}^{(6)}\right) \\ & + \mathrm{Re}\left(B_6^6\right)\left(C_6^{(6)} + C_{-6}^{(6)}\right) + i\,\mathrm{Im}\left(B_6^6\right)\left(C_6^{(6)} - C_{-6}^{(6)}\right) \end{aligned} \tag{6.5}$$

The large number of parameters at low–symmetry sites, such as C_2 and even S_6 symmetry, are frequently handled by approximating the group as a higher symmetry group by ignoring the imaginary components. This is sometimes referred to as the "descent of symmetry" [3]. For example, ignoring the imaginary components of S_6 symmetry results in a C_{3v} site symmetry, as these two symmetries can share a common axis. Similarly, C_2 symmetry may be approximated by C_{2v} in this manner, again effectively fixing the orientation of the rotational axis. This has been used by Carnall et al. for their fits of lanthanide ions in the C_2 site of LaF_3 [13]. This is beneficial to the fitting process, as a decrease in the number of crystal field parameters relaxes the required amount of data to produce a viable fit.

This process has not been used for the parameter fitting process on *ab initio* levels, as we have an abundance of energy levels provided by these calculations. It is used instead to justify our choice of La_2O_3:Pr^{3+} as a reference with which to compare Lu_2O_3:Pr^{3+}. The effect that this approximated increase in symmetry has on the quality of fit is examined by fitting the S_6 symmetry crystal field Hamiltonian to the experimental energy levels of the C_{3v} site in La_2O_3:Pr^{3+}, and comparing the resultant parameters with those obtained from the C_{3v} fit of Moune et al. [84]. The C_{3v} irreps are relabeled to match the available S_6 irreps. These are conveniently compatable, as shown in Table 6.3.

Table 6.3 Conversion of C_{3v} irreps to S_6 irreps

C_{3v} Irrep		S_6 Irrep
A_1	$\rightarrow$	A_g
A_2		
E	$\rightarrow$	E_g

We see from the parameters in Table 6.1, that the fit to the higher symmetry group is of similar accuracy to the fit to the lower symmetry group, with the overall standard deviation of the C_{3v} fit of $\sigma = 34$ cm^{-1}, and for the S_6 fit with $\sigma = 38$ cm^{-1}. The crystal field parameters are also sufficiently similar to make this process a reasonable approximation, with the exception of the B_3^4 parameter. This parameter is $B_3^4 = 1568$ cm^{-1} in C_{3v} symmetry, and $B_3^4 = (-217 + i\,1556)$ cm^{-1} in S_6 symmetry, which appears to be a change of phase. Comparing the other crystal field parameters with complex components in S_6 symmetry, the overall magnitude of the parameter seems to be fairly consistent with the corresponding parameter in C_{3v} symmetry. As a consequence, the total crystal field strength parameters, N_ν, of these two symmetries are very similar. The effect on the calculated energy levels is demonstrated in Table B.2.

On this basis, we now have a set of S_6 symmetry crystal field parameters for La_2O_3:Pr^{3+} with which we can compare the S_6 symmetry site of Lu_2O_3:Pr^{3+}.

6.1.3 Comparison of parameters

6.1.3.1 The $4f^2$ parameters

The parameters fitted to the energy levels calculated by *ab initio* methods differ from the reference experimental parameters. First, we consider just the free–ion parameters, as these should be largely independent of the host crystal. The $F^k\,(f)$ Coulomb terms are fairly consistent across the fits to experimental levels, with $F^2 = 66\,000 - 71\,000$ cm^{-1}, $F^4 = 49\,000 - 50\,000$ cm^{-1}, and $F^6 = 31\,000 - 33\,000$ cm^{-1}. The F^2 Coulomb parameter is overstated by all *ab initio* calculations, typically by a large margin. The F^4 parameter is fairly consistent with the experimental values. The F^6 parameter for the Lu_2O_3:Pr^{3+} calculations are slightly understated.

The M^i and P^i magnetic interaction parameters have mostly been held fixed, or are

unnecessary, for the fits to *ab initio* calculations, (as the Lu_2O_3:Pr^{3+} calculations are only to a spin–orbit free level).

Using our approximated S_6 symmetry site of La_2O_3:Pr^{3+} to compare with the same site in Lu_2O_3:Pr^{3+}, we would expect the crystal field parameters to have the same signs, if not a similar magnitude. The lutetium ion is smaller than lanthanum ion, which should result in a smaller crystal lattice [78], and hence have stronger crystal field interactions with the impurity ions. We see from Table 6.1, that the Lu_2O_3:Pr^{3+} f crystal field interactions are all much larger in magnitude than those of the La_2O_3:Pr^{3+} reference, in agreement with this expectation. The total crystal field strength parameter for this material is over twice as large as that of La_2O_3:Pr^{3+}. Additionally, the signs are mostly preserved, apart from B_0^4 and the real component of B_6^6. The relative magnitudes of the crystal field interactions within each site do not appear to be consistent.

The crystal field parameters of the C_2 site of Lu_2O_3:Pr^{3+} which are common to the S_6 site, ($B_q^k, q = 0$, and B_6^6), are much closer in magnitude to the corresponding La_2O_3:Pr^{3+} values. The remaining C_2 parameters are much larger in magnitude.

The *ab initio* energy levels of the O_h site of CaF_2:Pr^{3+} are particularly difficult to reproduce. The best fit to these levels at $4f^2$ level has a standard deviation of $\sigma = 815$ cm^{-1}. The experimental levels quoted from the same reference are easily reproduced, with $\sigma = 14$ cm^{-1}. From the same reference, the *ab initio* levels for the free Pr^{3+} ion are more easily reproduced, but the fit is still worse, by standard deviation, than the fit to the corresponding experimental levels. Neither *ab initio* calculation reproduces the observed levels well, as can be seen in the reference itself, and by the large differences between the parameters, particularly those of the Coulomb interactions.

Figure 6.2 demonstrates the average SL term energies for the parameters extracted from *ab initio* calculations (Lu_2O_3:Pr^{3+} and CaF_2:Pr^{3+}), compared to the equivalent parameters from the experimental references, and the free Pr^{3+} ion. The SL term energies of the three experimental observations (La_2O_3:Pr^{3+}, CaF_2:Pr^{3+} and the free Pr^{3+} ion), are very consistent, with some minor differences due to the slight differences in Coulomb parameter values.

The energy levels reproduced from the parameters extracted from the *ab initio* calculations vary considerably more. The *ab initio* CaF_2:Pr^{3+} has good agreement with the lowest SL terms of the experimental observations, but deviates highly for the higher–energy SL terms. This is due to the very strong Coulomb interaction in this *ab initio* calculation. The

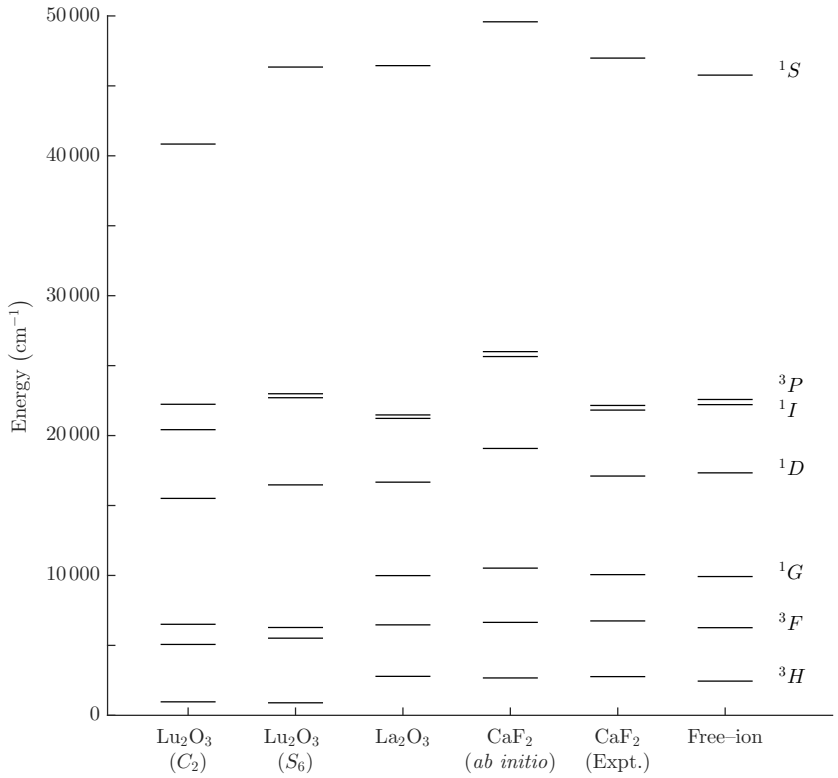

Figure 6.2 Average SL term energies for Lu_2O_3:Pr^{3+} (C_2 and S_6 sites), La_2O_3:Pr^{3+}, CaF_2:Pr^{3+} (*ab initio* and experimental) and experimental free–ion Pr^{3+}, calculated using the fitted effective Hamiltonian energy levels.

behaviour observed in the energy levels here is very similar to that shown in Figure 1 of Morrison and Rajnak, for energy levels determined using Hartree–Fock parameter values [85].

The S_6 symmetry site of Lu_2O_3:Pr^{3+} matches well for the higher SL terms, but has very low values for the lower energy terms. The C_2 symmetry site of Lu_2O_3:Pr^{3+} varies a bit more. The lower energies agree with the S_6 site, but the highest level (^1S) does not.

Looking at Table 6.1, we see that the α parameters extracted from the *ab initio* calculations are all considerably larger than the values fitted to the experimental counterparts.

The α, β and γ parameters quantify the electron correlation effect correction by means of configuration interaction: mixing additional states to describe this effect. They are added to the Hamiltonian as the Hartree–Fock Coulomb description does not account for correlation [85]. The *ab initio* calculations account for this by means of an MP2 perturbation (as discussed in Chapter 3). This lack of correlation effects is also what causes the empirical decrease of the Coulomb values when fitting experimental energy levels.

Table 6.4 Direct *ab initio* calculation of correlation correction parameters, α, β, and γ for Pr^{3+} [85], compared to the values obtained by extracting these parameters from *ab initio* energy level calculations of materials containing Pr^{3+}. All values are in cm^{-1}. The β parameter for CaF_2:Pr^{3+} is not fitted, but held at a fixed value.

	α	β	γ
Morrison and Rajnak:			
2^{nd}-order bound states	87.67	-1221.00	2260.45
Modified 2^{nd}-order single-electron excitation to continuum	-93.77	1340.01	-2477.02
2^{nd}-order two electrons to continuum	46.69	-774.15	1750.40
3^{rd}-order	-8.27	7.18	127.54
Magnetic orbit-orbit interaction within $4f^2$	-4.38	32.05	-49.84
Total calculated	27.94	-615.91	1611.53
Extracted from *ab initio* energy levels:			
Lu_2O_3:Pr^{3+} (S_6)	54	-476	1659
Lu_2O_3:Pr^{3+} (C_2)	79	-1028	3674
CaF_2:Pr^{3+}	63	[-566]	2972
Free–ion Pr^{3+}	56	-245	1990

That the *ab initio* correlation parameters are so large is probably related to the Coulomb parameters tending towards larger values. If the Coulomb values are too close to the Hartree–Fock values, and not scaled sufficiently to account realistically for the electron correlation, then the correlation parameters might be larger to compensate.

Alternatively, direct *ab initio* calculations of the correlation parameters have been conducted [85]. Morrison and Rajnak identified that in order to produce values that reasonably reproduce the empirically determined values, many contributions to the correlation had to be considered, including interactions between the bound electrons and the continuum states. If important contributions to these parameters are overlooked, and only mixing with bound states of the ion are considered, the value of α calculated was 87.67 cm^{-1}, which is not too dissimilar from the values extracted from the *ab initio* calculations: 54–

79 cm^{-1}. The full summary from the calculation of Morrison and Rajnak is presented in Table 6.4, compared to the parameters extracted from the *ab initio* calculations. From here, we can see that even if third–order bound states and magnetic orbit–orbit interactions are considered, the calculated α value will be very large. This could be the case with the *ab initio* energy level calculations.

It is suspected that similar problems might apply to the extraction of transition–intensity parameters [49]. The poor agreement between experimental and *ab initio* parameters in that case may be because the *ab initio* calculation does not properly take into account the effect of continuum states on the dipole polarizability.

6.1.3.2 The $4f5d$ parameters

The parameters quoted by van Pieterson et al. [18] are mostly calculated values using the Hartree–Fock radial distributions generated by Cowan's RCN code [23]. As the Hartree–Fock functions tend to overstate the strength of the Coulomb interactions by a significant factor due to the absence of electron correlation effects [85], these are the parameters that we would like to be able to fit to observed levels. Fitting all five Coulomb interaction parameters requires many experimental levels, spanning different multiplets. The *ab initio* calculations provide us with these levels, which experimental observations cannot. However, this still relies upon the *ab initio* calculations accurately describing these interactions to provide good values for these parameters.

Looking at the parameters fitted to the quoted experimental levels of the free–ion, presented in Table 6.2, we find that we require the $F^2\,(fd)$ parameter to be roughly two thirds of its value calculated using the Hartree–Fock functions. The *ab initio* calculations for Lu_2O_3:Pr^{3+} and CaF_2:Pr^{3+} reproduce this strength of parameter nicely. The remaining Coulomb parameters of both the Lu_2O_3:Pr^{3+} and CaF_2:Pr^{3+} *ab initio* calculations are significantly smaller than the calculated Hartree–Fock values, as we expect to observe. The *ab initio* calculation of the free–ion Pr^{3+} overstates the F^2 and G^5 parameters, while the remaining parameters agree with the fit to experimental levels of the free–ion.

The spin–orbit parameters for the CaF_2:Pr^{3+} calculation appear to have been reversed. The f spin–orbit parameter, for the single f electron in the $4f5d$ configuration, is approximately 300 cm^{-1} greater than the value quoted by van Pieterson et al. Similarly, the d spin–orbit parameter is approximately 300 cm^{-1} smaller. The reference also reports to have scaled all relevant $4f^N$ configuration parameters recurring in the $4f^{N-1}5d$ config-

uration by a factor of 1.06. In previous chapters, we have found this to be unneccesary for Yb^{2+}, as the difference in fitted values between the configurations was negligible compared to the scale of the parameter value. It is therefore unlikely that the f spin–orbit parameter should be this much larger in the $4f5d$ configuration.

In CaF_2:Pr^{3+}, the d crystal field parameter for the *ab initio* calculation is much stronger than the value reported by van Pieterson et al. A similar observation was noted for the d crystal field parameter in *ab initio* CaF_2:Yb^{2+} in the previous chapter.

As with the $4f^2$ configuration parameters, the C_2 site of Lu_2O_3:Pr^{3+} has smaller magnitude crystal field interactions than for the S_6 site, for the parameters common between them. Unfortunately, there are insufficient reported experimental fd level observations for La_2O_3:Pr^{3+} against which to fit parameters, so no comparison can be made here.

6.2 Trivalent terbium

The next lanthanide ion that we shall examine is trivalent terbium, as this occupies the central region of the period of lanthanides and hence has one of the most complex electronic energy level structures. This is partially shown in the Dieke diagram in Figure 1.1, although a large portion of the energy levels lie above the 50 000 cm^{-1} vertical axis cut–off. The only ions with a greater complexity $4f^n$ structure are the Gd^{3+} and Eu^{2+} ions.

Trivalent terbium has a ground state configuration of $4f^8$, and an excited configuration of $4f^75d$. The effective Hamiltonian for this ion is $H_{\text{eff}} = H_{4f^8} + H_{4f^75d}$, where:

$$\begin{aligned} H_{4f^8} = {} & E_{\text{avg}} \cdot I + \sum_k F^k f_k + \zeta A_{\text{so}}(f) + \alpha L(L+1) + \beta G(G_2) + \gamma G(R_7) \\ & + \sum_{i=0,2,4} m_i M^i + \sum_{i=2,4,6} p_i P^i + \sum_i t_i T^i + H_{\text{CF}}(f), \end{aligned} \tag{6.6}$$

$$\begin{aligned} H_{4f^75d} = {} & H_{4f^7}(d) + \Delta_E(fd) + \sum_{k=2,4} F^k f_k(fd) + \sum_{k=1,3,5} G^k g_k(fd) \\ & + \zeta A_{\text{so}}(d) + H_{\text{CF}}(d). \end{aligned} \tag{6.7}$$

The H_{4f^75d} effective Hamiltonian contains the term $H_{4f^7}(d)$, which is a complete set of duplicate f–electron parameters (identical to the H_{4f^8} Hamiltonian terms) describing the f-f electron interactions of the $4f^75d$ excited configuration. The presence of the $5d$ electron alters the $4f$ electron orbitals, and hence these parameters may have different values than the corresponding values for the $4f^8$ configuration. In their analyses of lanthanide–doped materials, van Pieterson et al. report scaling the duplicate f–electron parameters

for the excited $4f^{N-1}5d$ configurations by a factor of 1.06 times the corresponding ground configuration values [18, 19].

The *ab initio* calculation from which we are extracting the parameters is for BaF_2:Tb^{3+} [44]. In this, the $4f^8$ levels are reported to the spin–orbit level of calculation, and $4f^7 5d$ levels are reported to both spin–free level and spin–orbit inclusive levels. The BaF_2 host has the same structure as CaF_2 (Figure 4.1), and has multiple possible symmetry sites present, due to the charge compensation upon substitution of the Tb^{3+} ion. The lanthanide impurity in the *ab initio* calculation has cubic site symmetry, so only requires two crystal field parameters per f–electron configuration, and a single d crystal field parameter.

6.2.1 The fitting process

To handle the large number of available parameters, the fitting process is carried out in stages. The $4f^8$ ground configuration parameters are fitted first. These parameters are then used as a basis for the $4f^7$ parameters of the excited state configuration. Once a fit has been achieved for the $4f^8$ configuration, the groups of related parameters are constrained at that ratio for the fit to the $4f^7 5d$ configuration. The $4f^7 5d$ parameters are fitted using their definitions as initial estimates [23]. The values for the electron correlation parameters and three–body interaction parameters are taken from those of Gd^{3+} from Carnall et al. [13].

Two series of fits are conducted for the $4f^8$ configuration parameters. For the first, the levels used for the fitting process are those involved in the experimentally observed $^5D_4 \rightarrow {}^7F_J$ 'green', and $^5D_3 \rightarrow {}^7F_J$ 'blue' emission spectra of transitions within the $4f^8$ configuration. This is the extent of the energy level structure published in the reference. Calculated energy levels for all septet and quintet multiplets are also supplied, but as these largely coincide with the onset of the $4f^8 \leftrightarrow 4f^7 5d$ transitions there are no current experimental observations to compare to the higher energy levels. Table B.3 lists the energy levels resulting from the fitted effective Hamiltonian, and those of the reference *ab initio* calculations, for the lowest energy multiplets of the $4f^8$ configuration. The parameters for the fits are presented in Table 6.5. The effective Hamiltonian fit to the lowest $4f^8$ levels does not reproduce the higher calculated levels well, with increasing disagreement at higher energies.

The second series of fits are conducted using the full $4f^8$ configuration data set provided,

at both spin–free and spin–orbit inclusive levels of the *ab initio* calculation. Parameters for the fit are presented in Table 6.6. Two different fits are presented for each level of this calculation: the first has all three–body interaction parameters and Trees parameters, (α, β, and γ), held fixed; whereas the second allows all interactions to vary freely (apart from the spin–own–orbit and spin–other–orbit corrections, for the spin–orbit inclusive level).

Lastly, the parameters fitted to the $4f^7 5d$ configuration are presented in Table 6.7. The $4f^8$ configuration parameters used are those from the fit to the *ab initio* levels in the range of the observed emission lines only. The *ab initio* energy levels are supplied for the lowest few multiplets of this configuration. The fitting process occurs on a truncated effective Hamiltonian matrix, as the full matrix is inhibitively large for the fitting process. The final parameters are applied to the full effective Hamiltonian of the system, with only a single diagonalisation process, to ensure that the reference energy levels do not migrate far under the influence of the states not present in the truncated system. The interaction with these states is typically quite small.

6.2.2 Comparison of parameters

6.2.2.1 The $4f^8$ configuration

A very good fit to the reference energy levels is achieved within the energy range of the observed emissions. The three–body interactions, Trees parameters, and magnetic correction terms are all held fixed for these fitting processes. The F^2 Coulomb parameter is consistent for all three fits presented in Table 6.5. However, both fits to the experimental emission lines provide a much greater value for the F^4 parameter, and a much smaller value for the F^6 parameter, than the *ab initio* calculation.

The spin–orbit parameter for the *ab initio* calculation lies at the average of the two experimental spin–orbit parameter values. These experimental values differ by only 100 cm^{-1}. This value is slightly larger than that of the LaF_3:Tb^{3+} calculation of Carnall et al.

The biggest difference between the two experimental emissions is in the crystal field parameters. The crystal field parameters are not constrained to a specific ratio for these fits. The fit to the green emission, ($^5D_4 \rightarrow {}^7F_J$), suggests a much stronger crystal field than the fit to the blue emission, ($^5D_3 \rightarrow {}^7F_J$). The fit to the *ab initio* calculation produces crystal field parameters in better agreement with those of the blue emission lines.

Table 6.5 Parameters for an octahedral crystal field Hamiltonian fitted to the ^7F and lowest ^5D multiplets of the $4f^8$ levels of BaF_2:Tb^{3+}. The parameters are fitted to *ab initio* energy levels for these multiplets, and to experimental observations of the green ($^5D_4 \rightarrow {}^7F_J$) and blue ($^5D_3 \rightarrow {}^7F_J$) emission spectra [44, 86]. The LaF_3:Tb^{3+} values are from the fit to experimental levels by Carnall et al. [13], and are presented for a comparison. The crystal field parameters for LaF_3 have been omitted, due to the different site symmetry. All parameter values are in cm $^{-1}$.

			Fit to experimental emissions					
	Ab initio		Green		Blue		LaF_3:Tb^{3+}	
Parameter	Value	$\pm\sigma$	Value	$\pm\sigma$	Value	$\pm\sigma$	Value	$\pm\sigma$
E_{avg}	62744	(337)	62651	(3224)	62553	(1053)		
F^2	72778	(1000)	71257	(8261)	71867	(2797)	88995	
F^4	45941	(994)	72589	(12996)	72757	(4995)	62919	
F^6	60705	(1033)	39762	(8449)	39652	(2585)	47252	
α	18.92		18.92		18.92		18.40	
β	-600		-600		-600		-590.9	
γ	1575		1575		1575		1650	
T_2	300		300		300		320	
T_3	42		42		42		40	
T_4	62		62		62		50	
T_6	-295		-295		-295		-395	
T_7	350		350		350		303	
T_8	310		310		310		317	
ζ	1759	(9)	1804	(53)	1716	(53)	1707	
M_{tot}	2		2		2		2.39	
P_{tot}	919		919		919		373	
B^4	-1364	(124)	-2754	(1898)	-1368	(793)		
B^6	502	(72)	1088	(804)	658	(437)		
Fit details:								
N	28		11		14			
n	7		7		7			
σ	43		145		167			

Table 6.6 Parameters for an octahedral crystal field Hamiltonian operating on the space of all septet and quintet SL multiplets of the $4f^8$ levels of BaF_2:Tb^{3+}. Parameters are presented for both spin–orbit free and spin–orbit inclusive levels of calculation. Two fits have been presented at each level of calculation: one where all three–body interactions and Trees parameters are held fixed, and one where these parameters are allowed to vary. Due to the large number of energy levels available as reference levels, the fitted values for these interactions are very stable. All parameter values are in cm $^{-1}$.

	Spin–orbit free				All interactions			
Parameter	Value	$\pm\sigma$	Value	$\pm\sigma$	Value	$\pm\sigma$	Value	$\pm\sigma$
E_{avg}	70529	(205)	70403	(50)	74282	(63)	74232	(33)
F^2	101724	(541)	102088	(202)	101085	(179)	101878	(170)
F^4	65583	(1557)	65780	(486)	67829	(536)	66102	(411)
F^6	49841	(1351)	48065	(555)	48145	(452)	47759	(456)
α	18.92		50	(1)	18.92		48	(1)
β	-600		-868	(125)	-600		-928	(101)
γ	1575		1197	(104)	1575		1351	(82)
T_2	300		387	(47)	300		443	(41)
T_3	42		-59	(56)	42		-42	(51)
T_4	62		113	(88)	62		-13	(77)
T_6	-295		326	(73)	-295		262	(85)
T_7	350		-375	(103)	350		-412	(89)
T_8	310		-40	(85)	310		-5	(78)
ζ					1799	(25)	1776	(12)
M_{tot}					2		2	
P_{tot}					919		919	
B^4	-1377	(899)	-1043	(174)	-1672	(412)	-1232	(191)
B^6	1151	(309)	563	(83)	1065	(165)	729	(95)
Fit details:								
N	62		62		314		314	
n	6		15		7		16	
σ	629		133		410		198	

Looking at the parameters fitted to the entire space of septet and quintet SL multiplets, (Table 6.6), we see that they are significantly different from those of the fit to the *ab initio* energy levels in the range of the experimental data only. The higher energy levels determined by the *ab initio* calculation are clearly not reproduced well by the parameters from Table 6.5. The F^2 Coulomb parameter required is much larger, although the F^4 and F^6 values are in much better agreement with the parameters fitted to the observed emission lines. These values for F^4 and F^6 agree very well with the LaF_3:Tb^{3+} parameters. The required size of this F^2 parameter to reproduce the higher *ab initio* energy levels indicates that the *ab initio* Coulomb values are still closer to the Hartree–Fock values than are observed in experiment, as was observed in CaF_2:Pr^{3+}.

At each level of calculation, a fit is conducted with and without allowing the three–body interactions to vary. The fitted values for these interactions tend to be of similar magnitude to the fixed counterparts, although the sign is regularly not conserved. Given the number of reference energy levels used in the fit, and the stability of these values when fitted, these values do not seem unreasonable. The overall standard deviation of the fit is significantly improved when these are allowed to vary. These parameters are seldom varied all at once, since they are not strongly defined. Even with 146 energy levels available for fitting in LaF_3:Tb^{3+}, Carnall et al. only allowed T^6, T^7, and T^8 to vary [13].

Similarly, the Trees parameters are allowed to vary with the three–body interactions. The biggest change is in the magnitude of the α parameter. As seen with the parameters of the *ab initio* calculations of Pr^{3+}, these tend to a much larger value than the fixed parameter. As mentioned previously, the high F^2 Coulomb parameter may be the cause of the large correction to the electron correlation.

The spin–orbit parameter is the only magnetic interaction allowed to vary. These parameters agreed with the previous values.

The crystal field parameters for the fits where the three–body interactions are allowed to vary agree reasonably well with the values of the corresponding parameters for the *ab initio* fit, and fit to the blue emission lines, in the Table 6.5. In the fits where the three–body interactions are held fixed, the B^4 crystal field parameters are in agreement, but the B^6 parameters are larger than the previous values.

Table 6.7 Parameters for an octahedral crystal field Hamiltonian fitted to the lowest multiplets of the $4f^7 5d$ levels of BaF_2:Tb^{3+}. The parameters are fitted to *ab initio* energy levels for these multiplets, and supplied from a calculation for CaF_2:Tb^{3+} by van Pieterson et al. [19]. The reference effective Hamiltonian calculation sets the duplicate $4f^N$ parameters to be 1.06 times the value of the $4f^8$ parameters. For the fits to the *ab initio* calculations, all duplicate parameters, excluding the spin–orbit and Coulomb interactions, are kept fixed at the same value as the corresponding parameters for the $4f^8$ configuration. All parameter values are in cm $^{-1}$.

	Fit to *ab initio* calculation				Reference
	Spin–orbit free		Spin–orbit inclusive		CaF_2:Tb^{3+}
Parameter	Value	$\pm\sigma$	Value	$\pm\sigma$	Value
$4f^8$ configuration parameters:					
E_{avg}	53598	(467)	61243	(610)	
F^2	72778		72778		94335
F^4	45941		45941		66694
F^6	60705		60705		50087
α	18.92		18.92		18.4
β	-600		-600		-590.9
γ	1575		1575		1650
T_2	300		300		320
T_3	42		42		40
T_4	62		62		50
T_6	-295		-295		-395
T_7	350		350		303
T_8	310		310		317
$\zeta\,(f)$			1988	(164)	1707
M_{tot}			2		2.39
P_{tot}			919		373
$B^4\,(f)$	-1408		-1408		-2185
$B^6\,(f)$	481		481		733.6

Continued on next page...

Table 6.7 *Continued*

	Fit to *ab initio* calculation				Reference
	Spin–orbit free		Spin–orbit inclusive		CaF_2:Tb^{3+}
Parameter	Value	$\pm\sigma$	Value	$\pm\sigma$	Value
$4f^7 5d$ configuration parameters:					
$\Delta_E\,(fd)$	91437	(1286)	75690	(809)	81991
${}^{F^k(f)_d}/_{F^k(f)_f}$	1.34	(0.02)	1.08	(0.01)	1.06
$\zeta\,(f)_d$			1556	(312)	1809
$\zeta\,(d)$			1438	(755)	1557
$F^2\,(fd)$	10997	(958) [a]	5821	(944) [a]	19665
$F^4\,(fd)$	5577	(486) [a]	2952	(479) [a]	9469
$G^1\,(fd)$	5286	(460) [a]	2881	(453) [a]	8083
$G^3\,(fd)$	4281	(373) [a]	2266	(367) [a]	6935
$G^5\,(fd)$	3252	(283) [a]	1721	(279) [a]	5376
$B^4\,(d)$	-31680	(984)	-28875	(1142)	-41595
Fit details:					
N	7		72		
n	5		8		
σ	466		876		

[a] The fd Coulomb parameters are held at a fixed ratio, and fitted as a single parameter, rather than five independent parameters.

6.2.2.2 The $4f^7 5d$ configuration

For the $4f^7 5d$ configuration, the spin–free system is fitted first. The magnetic interaction parameters are then added and allowed to vary to fit the full spin–orbit system. The $4f^8$ configuration parameters are those fitted to the *ab initio* calculation of the visible emission lines.

The fd Coulomb parameters are allowed to vary as a single parameter (ie. scaled at a fixed ratio to each other). For the spin–free calculation, these fit to approximately a factor of 0.6 of the calculated values using Cowan's RCN code [23]. At the spin–orbit inclusive level, these parameters are scaled to approximately 0.3 times the calculated values.

The $F^k\,(f)$ Coulomb parameters for the excited configuration are fitted at the fixed ratio of the $4f^8$ configuration. For the spin–free calculation, these fit to a factor of 1.34 times the corresponding ground configuration parameters. At the spin–orbit inclusive level, this is only a factor of 1.08. A value of 1.06 is reported to fit well to observed spectra by van Pieterson et al. These seem to be in good agreement.

The diagonal matrix element, E_{avg}, is much smaller at the spin–free level than the spin–orbit level, but correspondingly, the d–level configuration shift, $\Delta_E\,(fd)$, is much larger. The introduction of spin–orbit interactions alone to the *ab initio* calculations should not affect the diagonal matrix elements at all, as the operators are orthogonal. The $B^4\,(d)$ is also affected, decreasing in magnitude by 3000 cm^{-1} with the addition of the magnetic interactions.

The d crystal field parameters are considerably smaller in magnitude than that of the reference CaF_2:Tb^{3+} calculation. This is expected, as the BaF_2 host has a much larger lattice, (BaF_2, a_0 = 6.2001 Å; CaF_2, a_0 = 5.46295 Å [78]), and hence the crystal field interactions should be weaker.

It is difficult to achieve a good parameter fit to the spin–orbit level calculation, even with the much larger set of reference energy levels. This is due in a large part to the lack of configuration interaction terms in the effective Hamiltonian. The higher energy levels for the $4f^8$ configuration and the lower energy levels for $4f^7 5d$ configurations in this effective Hamiltonian calculation are freely interspersed, whereas for the *ab initio* calculation, the states clearly bunch up and repel between interacting states between the two configurations. Moune et al. improved the fit to the $4f^2$ configuration of La_2O_3:Pr^{3+} by a significant proportion by including a $4f6p$ configuation, and appropriate configuration

interaction terms to adjust the $4f^2$ levels [84]. Much like the configuration interaction matrix elements that we constructed for Yb^{2+} in the previous chapters, the $4f^2 \leftrightarrow 4f6p$ configuration interaction matrix elements are fairly simple to construct, as there are only two electrons in the system. Similar terms are decidely non–trivial to construct for the $4f^8 \leftrightarrow 4f^7 6p$ terbium system. Additionally, the addition of crystal field configuration interaction correction terms breaks the degeneracy of the cubic site, which destroys most convenient methods of labelling the reference energy levels.

As a potential alternative, Lee et al. [87] demonstrated that the addition of correlation crystal field terms to the La_2O_3:Pr^{3+} system had a roughly equivalent action to the Coulomb and crystal field configuration interaction terms added by Moune et al., when these were projected onto the $4f^2$ configuration space. It might therefore be easier to simply add the correlation crystal field to the Hamiltonian, to see if these parameters can increase the accuracy of the fit to the *ab initio* calculation. Due to time constraints, this is beyond the scope of this thesis.

6.3 Divalent europium

Finally, we examine divalent europium. As stated previously, this ion, along with Gd^{3+}, has the the most extensive electronic structure, owing to the half–filled $4f$ shell. The vast majority of this structure lies above the vertical axis limit of 50 000 cm^{-1} of the Dieke diagram in Figure 1.1. The higher energy levels in the model extend well past 100 000 cm^{-1}.

Divalent europium has a ground state configuration of $4f^7$, and an excited configuration of $4f^6 5d$. The full basis of the $4f^7$ configuration consists of 3432 states, while the excited $4f^6 5d$ configuration has 30030 states (3003 $4f^6$ states $\times$ 10 d electron orbitals). This is a very large system to diagonalise, taking a few minutes of processing time on the hardware used for these calculations. Given that the parameter–fitting process uses gradient–based methods to converge to a solution, the matrix is diagonalised many times for each iteration of the fitting process. In order to vastly reduce this time requirement, we truncate the system to just the relevant states for the calculation (that is, those reported in the reference). This leaves us with 296 $4f^7$ basis states and 490 $4f^6 5d$ basis states, which can be fitted in a much more reasonable amount of time.

The effective Hamiltonian is $H_{\text{eff}} = H_{4f^7} + H_{4f^6 5d}$, where H_{4f^7} and $H_{4f^6 5d}$ have the same

forms as the $4f^8$ and $4f^7 5d$ Hamiltonian terms for trivalent terbium, (Equations 6.6 and 6.7).

The reference calculation for this material is an *ab initio* calculation of CaF_2:Eu^{2+} by Aiga et al. [67]. The Eu^{2+} ion occupies a cubic site in the CaF_2 lattice. The calculation includes spin–orbit free octet and sextet multiplets of the $4f^7$ and $4f^6 5d$ configurations; and a spin–orbit inclusive level of calculation for the octet multiplets of both configurations.

The parameters of van Pieterson et al. for Eu^{3+} (in a $LiYF_4$ host) are used as initial parameter estimates for the fitting processes. The appropriate crystal field parameters for a CaF_2 host have also been chosen. Initially, just the $4f^7$ configuration is fitted, and then these parameter values are used for the duplicate f configuration parameters in the $4f^6 5d$ configuration, as with the Tb^{3+} fits.

6.3.1 Irrep labelling discrepency

There is, however, a disagreement between the irrep labels assigned by the reference *ab initio* calculation and by this work. The irreps reported for the $4f^7$ sextet states of the *ab initio* calculation appear in energy order for each class of irrep. That is, all T_{2u} irreps occur at lower energies than all T_{1u} irreps, and similarly, all A_{1u} irreps occur at lower energies than all A_{2u} irreps. This is not observed in the effective Hamiltonian, nor can it be reproduced by any physically realistic combination of parameters. Additionally, the number of each type of irrep present is not consistent. The effective Hamiltonian produces six each of the T_{1u} and T_{2u}, where Aiga et al. report five T_{2u} and seven T_{1u} irreps. They also report an additional A_{1u} and A_{2u} irrep, and one less E_u irrep in this configuration. If the reported states have been incorrectly labelled, this is possibly due to the *ab initio* calculation occuring on the D_{2h} subgroup of the O_h symmetry site, where the reported irrep decomposition for both T_{2u} and T_{1u} O_h irreps is $B_{1u} + B_{2u} + B_{3u}$ under D_{2h}. Hence the octahedral irreps would be indistinguishable.

Similarly, some of the irrep assignments for the sextet states of the $4f^6 5d$ configuration do not agree. The octet states of the excited configuration have the interesting property that the irrep labelling scheme used here also cannot distinguish the T_{1g} and T_{2g} irreps, or A_{1g} and A_{2g} irreps. The assigned block labels for each corresponding pair of irreps are identical. It is, however, sufficient to identify the irreps by the energy order indicated by Aiga et al.

The change of irrep labels brings the best fit for the spin–free fit down from a standard deviation in the tens of thousands of wavenumbers to 1579 cm^{-1}. The addition of the spin–orbit parameters for the spin–orbit inclusive level of calculation significantly improves upon this value.

The spin–orbit states of this calculation are labelled by the irreps of the octahedral double group, O_h':

Irrep	Dimension
Γ_6	2
Γ_7	2
Γ_8	4

Once again, we find that the number of irreps listed by Aiga et al. is not in agreement with the number of irreps provided by the effective Hamiltonian. Based on group theory, the ground state should split into three irreps: $\Gamma_6 + \Gamma_7 + \Gamma_8$, for a total dimension of eight [1]. Aiga et al. report four degenerate states for the zero energy point. Two of these states, and a number of other multiply degenerate states, are identified as potentially being two–dimensional components of Γ_8 irreps. The remaining irreps are identified as Γ_6, Γ_7 or Γ_8 irreps based on the order of irreps from the effective Hamiltonian calculation.

This is a limiting factor in that these results rely upon the assumption that the irrep order achieved by adding the spin–orbit interaction parameters to the spin–free parameters is very much consistent with that of the *ab initio* calculation. As the actual irrep labels for these states have not been supplied in the reference, this assumption is a requirement for any fitting process to be able to occur.

6.3.2 Comparison of parameters

The parameters from the fits to CaF_2:Eu^{2+} are presented in Table 6.8. The energy levels produced by these calculations are presented in Tables B.4 and B.5, of Appendix B.

6.3.2.1 Spin–free fit

The spin free effective Hamiltonian is first fitted to the $4f^7$ configuration, to obtain estimates for the Coulomb parameters and crystal field parameters for this configuration.

Table 6.8 Parameters for a spin–orbit free octahedral crystal field Hamiltonian fitted to the octet and sextet multiplets of the $4f^7$ and $4f^6 5d$ levels of CaF_2:Eu^{2+}. The parameters are fitted to *ab initio* energy levels for these multiplets; calculated from definition for Eu^{3+} [18] (substituting applicable crystal field parameters for a CaF_2 host); and supplied from a calculation for CaF_2:Eu^{2+} by Burdick et al. [65]. Except where specified, the fits to the *ab initio* calculations set the duplicate $4f^N$ parameters to be the same value as the $4f^7$ parameters. The Eu^{3+} calculation sets these to 1.06 times the value of the $4f^7$ parameters. Additionally, in the calculation by Burdick et al., there are correlation crystal field parameters present, which have not been listed here. All parameter values are in cm $^{-1}$.

	Fit to *ab initio* calculation				Reference			
	Spin–orbit free		Spin–orbit inclusive		Eu^{3+} [18]		Eu^{2+} [65]	
Parameter	Value	$\pm\sigma$	Value	$\pm\sigma$	Value	$\pm\sigma$	Value	$\pm\sigma$
$4f^7$ configuration parameters:								
E_{avg}	79817	(1141)	79996	(232)				
F^2	85763	(2470) [a]	85763		83125		74848	
F^4	44107	(1270) [a]	44107		59268		49598	
F^6	40278	(1160) [a]	40278		42560		38643	
α	18.92		18.92		20.16		18.9	
β	-600		-600		-566		-600	
γ	1575		1575		1500		1575	
T_2	300		300		300		300	
T_3	40		40		40		42	
T_4	60		60		60		62	
T_6	-300		-300		-300		-295	
T_7	370		370		370		350	
T_8	320		320		320		310	
$\zeta\,(f)$			1338		1338		1170	
M_{tot}			2.1		2.1		2.0	
P_{tot}			360		360		919	
$B^4\,(f)$	-1544	(1204)	-1544		-1900		-2386	
$B^6\,(f)$	2036	(1612)	2036		500		966	

Continued on next page...

[a] The F^k Coulomb parameters are held at a fixed ratio for the fitting process, presenting just a single parameter.

Table 6.8 *Continued*

	Fit to *ab initio* calculation				Reference			
	Spin–orbit free		Spin–orbit inclusive		Eu^{3+} [18]		Eu^{2+} [65]	
Parameter	Value	$\pm\sigma$	Value	$\pm\sigma$	Value	$\pm\sigma$	Value	$\pm\sigma$
$4f^6 5d$ configuration parameters:								
$\Delta_E\,(fd)$	55819	(679375)	55741	(93355)	73057		23500	
${}^{F^k(f)_d}/_{F^k(f)_f}$	1.65	(12.53)	1.66	(1.72)	1.06		1.09	
${}^{B^k(f)_d}/_{B^k(f)_f}$	-0.93	(0.43)	-0.23	(0.20)	1.06		1.00	
$\zeta\,(f)_d$			1211	(65)	1418		1275	
$\zeta\,(d)$			1273	(386)	1419		760	
$F^2\,(fd)$	9394	(1191) [b]	10958	(631) [b]	30300		14000	
$F^4\,(fd)$	4764	(604) [b]	5557	(320) [b]	15038		7100	
$G^1\,(fd)$	4516	(573) [b]	5268	(304) [b]	12914		6730	
$G^3\,(fd)$	3657	(464) [b]	4266	(246) [b]	11135		5450	
$G^5\,(fd)$	2778	(352) [b]	3240	(187) [b]	8659		4140	
$B^4\,(d)$	-40009	(1337)	-42650	(269)	-44016		-33600	
Fit details:								
N	47		96					
n	8		8					
σ	1579		403					

The Coulomb parameters are then fixed at the resulting ratio, and simply scaled collectively as a single parameter for the subsequent fits. This $F^k\,(f)$ parameter is allowed to vary for the $4f^6 5d$ configuration fit. The F^2 and F^6 Coulomb parameters agree well with the corresponding values from van Pieterson et al., while the F^4 parameter is significantly larger. The f crystal field parameters agree in sign with the reference, but differ in relative magnitudes.

For the $4f^6 5d$ configuration, the duplicate $F^k\,(f)$ parameters are scaled to 1.65 times the $4f^7$ values, which is much greater than the factor of 1.06 used by van Pieterson et al. The fd Coulomb parameters are also scaled at a fixed ratio to each other. These parameters fit to about a third of the calculated free–ion values. Lastly, the d crystal field parameter differs from the reference value by only 4000 cm^{-1}, which appears to be in rough agreement.

[b] The fd Coulomb parameters are held at a fixed ratio.

The stated parameter uncertainty for the average d configuration energy, $\Delta_E(fd)$, is rather large. It is unlikely that this value should be this large, as the interaction is quite strongly defined by the location of the $4f^6 5d$ states compared to the ground $4f^7$ configuration states. This parameter is very stable, and reliably fits to this value for a variety of perturbations from the initial parameters.

6.3.2.2 Spin–orbit fit

For the spin–orbit level fit, the $4f^7$ spin–orbit parameter is held fixed while the $4f^6 5d$ f and d spin–orbit parameters are allowed to vary. These both yield very similar values, as observed in the values of van Pieterson et al. These values are slightly smaller than the reference parameter values, and slightly smaller than the fixed $4f^7$ spin–orbit parameter.

The fd Coulomb parameters are allowed to vary again, and settle to a very similar set of values to the spin–free system. The F^k f Coulomb parameter for the $4f^6 5d$ configuration is allowed to vary again, but there is little change from the spin–free value. Similarly, the configuration average energy term, $\Delta_E(fd)$, also agrees with the spin–free value. The fd Coulomb terms are smaller even than those of Burdick et al., which have already been reduced significantly from the Hartree–Fock values of van Pieterson et al. [18, 65]. The $F^k(f)$ parameters, however, are extremely large, to an extent greater than observed in the previous analyses in this chapter. The small fd Coulomb parameters might be a partial compensation for the size of the f Coulomb parameters.

The biggest change occurs in the crystal field parameters. The duplicate f crystal field parameters in the spin–free system have a reversed sign from the $4f^7$ configuration equivalents, but the magnitudes are roughly preserved. The spin–orbit solution, however, has much weaker parameters for these interactions, scaling them to -0.23 of the $4f^7$ configuration values. The d crystal field is closer in magnitude to the reference parameter value for the CaF_2 host.

Again, the $\Delta_E(fd)$ parameter has a much larger estimated uncertainty than seems reasonable.

6.4 Summary

Effective Hamiltonian parameters are fitted to *ab initio* calculations of three different lanthanide ions, residing in different host materials, in order to extract crystal field parameters from these calculations. Pr^{3+} ions in Lu_2O_3 and CaF_2 hosts provide crystal field parameters for S_6, C_2, and O_h sites. The C_{3v} impurity site of La_2O_3:Pr^{3+} crystal is treated as an S_6 site to provide an experimental comparison to the S_6 impurity site of the cubic Lu_2O_3 host. Parameters for these fits are presented and discussed. It is observed that the parameters extracted from the *ab initio* calculations at $4f^N$ level are typically (but not exclusively) overstated compared to experimental observations. The F^2 Coulomb parameter is a notable example. This is demonstrated to cause increasing disagreement with experimental observations as we examine higher energy states, and is particularly apparent in the CaF_2:Pr^{3+} material.

The fd Coulomb values extracted from the *ab initio* calculations are typically much smaller than the calculated Hartree–Fock values, which is in line with expected observations of experimental levels [85]. The *ab initio* calculations appear to scale these Coulomb terms to correct for electron correlation effects quite well. For these systems, the fd Coulomb parameters are able to be freely varied, which cannot normally occur due to the absence of sufficient experimental levels to fit these parameters.

The d crystal field parameters tend to have large values. The CaF_2:Pr^{3+} d crystal field is stronger than the experimental observation. Interestingly, the S_6 site of Lu_2O_3:Pr^{3+} has a much larger total d crystal field strength than the C_2 site, despite both having similar total crystal field strengths for the f crystal field.

It is observed that the electron correlation parameter, α, is consistently significantly larger than the experimental values, when allowed to fit to the *ab initio* calculations. As the basic level of *ab initio* calculation is a Hartree–Fock type calculation (or equivalent), the electron correlation is not considered, and is added subsequently as a correction. The large values for α extracted from the *ab initio* calculations are consistent with the possibility that only contributions to the electron correlation from bound states have been considered in the corrections applied to the *ab initio* calculation, ignoring the large contributions from continuum states [85]. This raises the possibility that a similar shortcoming of the *ab initio* model may be responsible for the disagreements in extracted and experimental parameters observed in a study of one of the references, to extract transition–intensity parameters from *ab initio* models [49].

Octahedral site symmetry BaF_2:Tb^{3+} and CaF_2:Eu^{2+} are also examined. These materials have the most complicated electronic structure of the lanthanide series, as they occupy the region around the half–filled f–electron shell. Because of this, all effective Hamiltonian parameters, and, frequently, additional corrective terms, are required to describe these systems. Due to the large number of energy levels available as targets for the fitting processes, most of these parameters can be allowed to vary. It is, however, impractical to simply allow every parameter to vary at once, as the solution space has a very large number of local minima. Additionally, some of the interactions are very weakly defined, and hence difficult to fit.

The three–body interactions are able to be varied for the BaF_2:Tb^{3+}, which results in parameters that are mostly similar in magnitude to the experimental parameters, but differ frequently in sign. Allowing these to vary significantly improves the accuracy of the overall fit, decreasing the standard deviation by a factor of 2–3.

The lowest energy states of the *ab initio* BaF_2:Tb^{3+} calculation fit very well to the observed emission spectra in this region. Correspondingly, the parameters extracted from just these energy levels of the *ab initio* calculation agree well with the parameters fitted to the emission spectra. However, when the the entire set of energy levels calculated by the *ab initio* calculation are used, the extracted parameters exhibit the same large F^2 Coulomb parameter as seen in the other analyses.

It is observed that the *ab initio* BaF_2:Tb^{3+} energy levels appear to bunch up at the interface between the ground and excited configurations, and on this basis, we predict that there are configuration interaction terms present that are not accounted for in the chosen effective Hamiltonian. A possible solution to this, other than introducing a $6p$ excited configuration, and calculating configuration interaction operators, is to add correlation crystal field parameters to the $4f^n$ Hamiltonian, as the action of the configuration interaction and correlation crystal fields were shown to be equivalent by Lee et al. [87]. This is left as a potential study for the future.

Lastly, there is a major disagreement between the irrep labels assigned to the states of the *ab initio* calculation for CaF_2:Eu^{2+}, and the labels assigned by the effective Hamiltonian calculation. This discrepency is likely due to the difficulty in assigning octahedral irrep labels to states of the *ab initio* calculation, as the calculation was conducted in D_{2h} symmetry due to the symmetry limitations of the quantum chemical software. The labels of the *ab initio* calculation were reassigned, which allowed the parameters to be extracted from these calculations.

The fd Coulomb parameters in this material were roughly a third of the size of the Hartree–Fock values, and smaller even than the parameters of Burdick et al., which were scaled to about half of the Hartree–Fock values to account for the missing electron correlation effect. The duplicate $F^k\,(f)$ parameters are unrealistically large in this calculation, being approximately 1.65 times the Hartree–Fock values.

Chapter 7

Conclusions and Future Work

In this thesis, we have empirically extracted effective Hamiltonian parameters from *ab initio* energy level structure calculations for a variety of lanthanide materials. These parameters describe the strengths of the physical interactions occurring within the system, and are not typically available directly from the *ab initio* calculations. These parameters are useful, as they provide a direct means of comparison with experimental observations, and behave in predictable trends across the series of lanthanides. We use the extracted parameters to make a number of observations on each system.

In Chapter 4, we extract parameters from the *ab initio* calculations of $SrCl_2$:Yb^{2+} and $CsCaBr_3$:Yb^{2+} energy levels. The parameters are fitted to the minima of the potential energy curves supplied in the references, and to instantaneous vertical transitions at various positions along the potential energy curves.

While the Coulomb parameters fitted to the *ab initio* minima are smaller than the Hartree–Fock values, they are still greater than the parameters fitted to experimental observations. The f spin–orbit interaction was reproduced well, as was the d crystal field. The impurity–trapped exciton–like state present in the $SrCl_2$:Yb^{2+} calculation was able to be reasonably modelled by adjustment of a single parameter: the $\Delta_E\,(fs)$ configuration average energy parameter.

The fits to the instantaneous transitions allow us to explore trends in the parameter values as the cage of ligands surrounding the lanthanide impurity varies in size. We were able to use these extracted parameters to check for the expected behaviours in the system. The nephelauxetic effect was clearly observed at several levels of the *ab initio* calculations, with the Coulomb parameters decreasing in strength as the ligand

cage contracts. The d spin–orbit parameters were also observed to vary slightly with changing proximity of the ligand cage. For $SrCl_2$:Yb^{2+} the parameter increased as the cage contracted, whereas for $CsCaBr_3$:Yb^{2+} the parameter decreased. These effects were attributed to the nephelauxetic effect, and the composition of the host lattices. We also identified that at the highest level of *ab initio* calculation for $SrCl_2$:Yb^{2+}, the behaviour of the f crystal field parameters with variation of the ligand cage size matches the expected behaviour if the crystal field is treated as a system of point charges. The actual model of the crystal field used by the *ab initio* calculation is more extensive than this, so it is interesting that the extracted parameter behaviour matches that of the simpler point–charge model.

We also used the extracted parameters to identify an issue with the behaviour of the highest spin–free level of calculation for the $SrCl_2$:Yb^{2+} system, where the crystal field parameters vary in a non–physical way: decreasing in strength as the ligand cage contracts. As the interaction of the electrons with the ligands should increase with increased proximity to the ligands, the parameter strength should be increasing. This incorrect interaction is not immediately apparent simply by looking at the energy levels of the *ab initio* calculation, which is an example of the advantage of having access to the physical parameters of the system.

In Chapter 5, we fit an effective Hamiltonian to the $4f^{13}5d$ configuration of an experimental CaF_2:Yb^{2+} excitation spectrum, and then extract parameters from the *ab initio* calculations of energy levels for the same material. The experimental parameters are largely based on values from an existing calculation for $SrCl_2$:Yb^{2+}, as there were insufficient points of reference in the spectrum to allow all parameters to be freely fitted. An absorption spectrum was simulated from these values, and matches well with the observed spectrum apart from one set of peaks, corresponding to the $4f^{13}\left(^2F_{7/2}\right)5dt_{2g}$ states. These are shifted due to a disagreement with the fitted f spin–orbit parameter value between the e and t_2 $5d$ irrep states.

An identical analysis to that of Chapter 4 was performed on the *ab initio* calculations of CaF_2:Yb^{2+}: parameters were fitted to both the minima of the potential curves, and to vertical transitions at several positions along the potential curves.

The parameters show a disagreement between the crystal field strengths fitted to the minima of the *ab initio* potential energy curves, and those of the fit to the experimental spectrum. The f crystal field of the *ab initio* calculation is weaker than the observed values, whereas the d crystal field is stronger. The strength of the d crystal field parameter

prevents the spectrum simulated by the *ab initio* calculation from completely reproducing the observed spectrum, as the e and t_2 $5d$ irreps are split too far apart.

The fits to vertical transitions along the potential curves were again used to observe any trends present in the *ab initio* calculation, as the size of the ligand cage about the impurity changes. The range of sizes of the ligand cage covered by the *ab initio* calculation is insufficient to observe any clear nephelauxetic effect in the Coulomb parameters. There is a slight decrease in d spin–orbit value with increasing ligand cage size, as observed for $SrCl_2$:Yb^{2+}. This is attributed to the nephelauxetic effect, by the same arguments. The values of the f crystal field parameters can again be modelled very well by power–law dependencies, but the coefficient is much higher that expected for a simple point–charge model. The $k = 4$ coefficient, in particular, is much closer in value to previous experimental observations for similar systems.

The parameters extracted from the CaF_2:Yb^{2+} *ab initio* calculation were used in an attempt to model the impurity–trapped exciton state that is observed in this material. Fitting the exciton state to the observed energy and equilibrium impurity–ligand distance shift from literature does not create an energetically favourable state compared to the lowest $5d$ levels, using the parameters from the *ab initio* calculation. This is again attributed to the large value for the d crystal field parameter.

In Chapter 6, we extract parameters from the *ab initio* calculations of energy levels of Lu_2O_3:Pr^{3+}, CaF_2:Pr^{3+}, BaF_2:Tb^{3+}, CaF_2:Eu^{2+} and the free Pr^{3+} ion, in order to test that the process is successful on lanthanide systems of increasing complexity.

The $4f^2 + 4f5d$ system Hamiltonian parameters were extracted from the materials containing Pr^{3+} ions. A typical observation is that the Coulomb parameters, in particular the F^2 parameter, tend to be larger than the values fitted to experimental levels, and closer to the Hartree–Fock values. The electron correlation parameter, α, also tends to a large value when extracted from the *ab initio* calculations, usually more than twice the value of the experimental result. It is observed that the values of these parameters are consistent with previous direct calculations of the electron correlation parameters by *ab initio* means, if only the contributions from bound states are considered. The references show that there is significant contribution to the calculation from continuum states that, if overlooked, can lead to a very large value for the α parameter. We suggest that this is the case here.

The fd Coulomb terms from the *ab initio* calculations are typically much smaller than the

Hartree–Fock values. This is a good result, as the Hartree–Fock values are too large due to the absence of electron correlation effects. As with the CaF_2:Yb^{2+} fit, the d crystal field parameters tend towards large values, with the exception of the C_2 site of Lu_2O_3:Pr^{3+}.

The $4f^8 + 4f^7 5d$ and $4f^7 + 4f^6 5d$ system Hamiltonian parameters were extracted from BaF_2:Tb^{3+} and CaF_2:Eu^{2+}. These Hamiltonians contain a large number of parameters, and cannot be easily fitted to experimental levels, unless a suitably large number are identified. Both of these calculations have very small fd Coulomb interactions, smaller even than the values fitted to experimental observations.

The lowest energy levels of the *ab initio* calculation for BaF_2:Tb^{3+} provided parameters which agree well with experimental parameters. This was unsurprising, as the lowest *ab initio* levels were in excellent agreement with the experimental levels. However, the complete set of *ab initio* levels provide parameters that do not agree well with the experimental parameters. The F^2 Coulomb parameter was very large again, as was observed in the previous materials. Due to the large number of *ab initio* energy levels used in the fitting process, the three–body interactions were allowed to vary freely. This resulted in an improvement in the overall standard deviation by a factor of 2–3. The values varied a little in magnitude, and frequently in sign, from the experimental observations. There were no obvious outliers.

A limitation to the fit was observed in the bunching of energy levels at the interface between the $4f^8$ and $4f^7 5d$ configurations in the *ab initio* energy levels, that could not be reproduced with the given effective Hamiltonian. This shows that there are interactions between the configurations that have not been included in the Hamiltonian. To introduce the configuration interaction terms would require the introduction of a $6p$ configuration as the Coulomb configuration interaction has no matrix elements between the $4f$ and $5d$ orbitals. An alternative is to introduce correlation crystal field interactions, as these were shown in the references to have equivalent action to the configuration interaction terms. This is beyond the scope of this thesis due to time constraints.

A disagreement was observed between the irrep labels of the *ab initio* CaF_2:Eu^{2+} calculation and the effective Hamiltonian states. The labels of the *ab initio* calculation were reassigned, but this limited the extent to which the parameters of the fit could be varied at the spin–orbit level calculation.

In most of the fits to these materials, we have observed a few consistent features of the *ab initio* calculations:

- The ground $4f^N$ configuration Coulomb parameters, in particular the F^2 parameter, are larger than the experimental values, sometimes by a considerable amount. This indicates that these interactions are not fully scaled to incorporate electron correlation effects.

- The α electron correlation parameter is similarly shown to be very large in *ab initio* calculations, often 2–3 times that fitted to experimental observations. This may occur if the *ab initio* calculations overlook important contributions to the electron correlation from the continuum states.

- The d crystal field is frequently (but not always) very strong when compared to experimental observations. This could be a property of the embedding potentials used by these calculations.

These features indicate where potential improvements for the *ab initio* models lie.

7.1 Overall context of this research

The usefulness of the research presented in this thesis is as a potential aid to the continuing development of *ab initio* calculations for large systems such as these materials. While recent *ab initio* calculations can reproduce observed spectral features rather well, they still do not portray a completely accurate picture of the physical interactions that occur in these systems, as is evidenced by the difference between the effective Hamiltonian parameters fitted to experimental observations and those extracted from the *ab initio* calculations.

Using effective Hamiltonian parameters to quantify these interactions for the *ab initio* calculations provides us with a direct measure of how well the calculation can reproduce the actual process that occurs. This provides an interface between the *ab initio* calculation methods, and the experimental spectroscopy that these calculations have aimed to reproduce.

The methods used here may allow us to identify potential issues in the *ab initio* interpretations, as is suggested is the case for the *ab initio* handling of the electron correlation corrections. This will allow us to further develop these models, and continue to improve the accuracy of first principles calculations.

7.2 Future work

As suggested previously, the calculation for BaF_2:Tb^{3+} could benefit from the addition of correlation crystal field interaction terms to approximate the effects of the missing configuration interaction between the ground and excited configurations that is present in the *ab initio* calculation. This is a feasible short term project. On a longer timescale, a calculation involving the actual configuration interaction terms and the inclusion of the higher $6p$ states would also be of merit.

Ab initio analyses exist for lanthanide ions not covered in this thesis. The extraction of parameters from a complete series of *ab initio* would be of use, to observe any periodic trends in the parameters. Similarly, a number of *ab initio* studies of the actinides exist, and the equivalent physical parameters of these would provide a useful comparison for those of the lanthanide series.

Appendix A

Extra definitions

A.1 n–j symbol determination

The 3–j symbol can be calculated using the analytic definition of the Clebsch–Gordon coefficient [51]:

$$\begin{aligned}
&\langle j_1 m_1, j_2 m_2 \mid JM \rangle = \delta\left(m_1 + m_2,\, M\right) \\
&\times \left[\frac{(2J+1)\,(j_1+j_2-J)!\;(j_1-m_1)!\;(j_2-m_2)!\;(J+M)!\;(J-M)!}{(j_1+j_2+J+1)!\;(J+j_1-j_2)!\;(J+j_2-j_1)!\;(j_1+m_1)!\;(j_2+m_2)!}\right]^{1/2} \\
&\times \sum_r (-1)^{j_1-m_1+r}\,\frac{(j_1+m_1+r)!\;(j_2+J-m_1-r)!}{r!\;(J-M-r)!\;(j_1-m_1-r)!\;(j_2-J+m_1+2)!}.
\end{aligned} \tag{A.1}$$

The 6–j symbol can be calculated in terms of 3–j symbols as shown [51]:

$$\begin{Bmatrix} j_1 & j_2 & j_3 \\ j_4 & j_5 & j_6 \end{Bmatrix} = \sum_{\text{all } m} (-1)^{j_1-m_1+j_2-m_2+j_3-m_3+j_4-m_4+j_5-m_5+j_6-m_6} \tag{A.2}$$
$$\times \begin{pmatrix} j_1 & j_2 & j_3 \\ -m_1 & -m_2 & -m_3 \end{pmatrix} \begin{pmatrix} j_1 & j_5 & j_6 \\ m_1 & -m_5 & m_6 \end{pmatrix} \begin{pmatrix} j_2 & j_6 & j_4 \\ m_2 & -m_6 & m_4 \end{pmatrix} \begin{pmatrix} j_3 & j_4 & j_5 \\ m_3 & -m_4 & m_5 \end{pmatrix}.$$

Similarly, the 9–j symbol can also be calculated in terms of 3–j symbols [51]:

$$\begin{Bmatrix} j_{11} & j_{12} & j_{13} \\ j_{21} & j_{22} & j_{23} \\ j_{31} & j_{32} & j_{33} \end{Bmatrix} = \sum_{\text{all } m} \begin{pmatrix} j_{11} & j_{12} & j_{13} \\ m_{11} & m_{12} & m_{13} \end{pmatrix} \begin{pmatrix} j_{21} & j_{22} & j_{23} \\ m_{21} & m_{22} & m_{23} \end{pmatrix} \begin{pmatrix} j_{31} & j_{32} & j_{33} \\ m_{31} & m_{32} & m_{33} \end{pmatrix}$$
$$\times \begin{pmatrix} j_{11} & j_{21} & j_{31} \\ m_{11} & m_{21} & m_{31} \end{pmatrix} \begin{pmatrix} j_{12} & j_{22} & j_{32} \\ m_{12} & m_{22} & m_{32} \end{pmatrix} \begin{pmatrix} j_{13} & j_{23} & j_{33} \\ m_{13} & m_{23} & m_{33} \end{pmatrix}. \tag{A.3}$$

Appendix B

Calculated energy levels

This section contains tables of energy levels calculated using the parameters reported in this thesis.

B.1 Spin–orbit free Pr^{3+}–doped hosts

Table B.1 *Ab initio* calculation and S_6 symmetry crystal field fit of Lu_2O_3:Pr^{3+}. All energies are in cm^{-1}.

Site Symmetry:			S_6 site				C_2 site		
Multiplet	Irrep		H_{CF}	*Ab initio*	ΔE	Irrep	H_{CF}	*Ab initio*	ΔE
^3H	1	^3A_g	-39	95	134	1 ^3B	-200	0	200
	1	^3E_g	34	0	-34	1 ^3A	-178	150	328
	2	^3E_g	519	610	91	2 ^3B	118	100	-18
	2	^3A_g	659	800	141	2 ^3A	554	630	76
	3	^3E_g	1185	1250	65	3 ^3B	773	810	37
	3	^3A_g	1267	1130	-137	3 ^3A	903	840	-63
	4	^3E_g	2242	1980	-262	4 ^3B	1422	1455	33
						4 ^3A	1464	1255	-209
						5 ^3B	1776	1730	-46
						6 ^3B	1973	1865	-108
						5 ^3A	2001	1795	-206

Continued on next page...

Table B.1 *Continued*

Site Symmetry:			S_6 site					C_2 site		
Multiplet	Irrep		H_{CF}	*Ab initio*	ΔE	Irrep		H_{CF}	*Ab initio*	ΔE
^{3}F	4	^3A_g	4782	4800	18	6	^3A	4513	4385	-128
	5	^3A_g	5300	5355	55	7	^3B	4549	4810	261
	5	^3E_g	5379	5325	-54	8	^3B	4839	4920	81
	6	^3E_g	5900	5780	-120	7	^3A	5204	5195	-9
	6	^3A_g	5973	6075	102	9	^3B	5316	5095	-221
						8	^3A	5366	5365	-1
						10	^3B	5689	5690	1
^{1}G	1	^1E_g	5523	5540	17	1	^1B	5515	5645	130
	1	^1A_g	5582	5655	73	1	^1A	5590	5715	125
	2	^1A_g	5943	5895	-48	2	^1A	5813	5905	92
	2	^1E_g	5952	6095	143	2	^1B	6023	5805	-218
	3	^1E_g	7134	7065	-69	3	^1B	6555	6380	-175
	3	^1A_g	7765	7645	-120	3	^1A	6720	6760	40
						4	^1A	7020	7035	15
						5	^1A	7504	7560	56
						4	^1B	7828	7760	-68
^{1}D	4	^1E_g	15597	15685	88	6	^1A	14576	14400	-176
	4	^1A_g	16687	16357	-330	7	^1A	14887	14910	23
	5	^1E_g	17245	17480	235	5	^1B	15311	15395	84
						6	^1B	16083	16315	232
						8	^1A	16683	16520	-163

Continued on next page...

Table B.1 *Continued*

Site Symmetry:			S_6 site					C_2 site		
Multiplet	Irrep		H_{CF}	*Ab initio*	ΔE	Irrep		H_{CF}	*Ab initio*	ΔE
^{1}I	5	^1A_g	21142	21070	-72	7	^1B	20405	20735	330
	6	^1E_g	21281	21575	294	9	^1A	20417	20285	-132
	7	^1E_g	21645	21650	5	8	^1B	20907	20945	38
	6	^1A_g	22068	21530	-538	10	^1A	20917	20865	-52
	7	^1A_g	22517	22125	-392	11	^1A	21746	21540	-206
	8	^1E_g	23285	23430	145	9	^1B	21892	21730	-162
	9	^1E_g	24137	24375	238	12	^1A	22427	22295	-132
	8	^1A_g	24317	24515	198	10	^1B	22605	22355	-250
	9	^1A_g	24428	24560	132	13	^1A	22725	22735	10
						11	^1B	22962	22395	-567
						14	^1A	22991	23180	189
						12	^1B	24511	25065	554
						15	^1A	24576	24955	380
^{3}P	7	^3E_g	22462	22665	203	11	^3B	19247	18985	-262
	7	^3A_g	24043	23840	-203	9	^3A	20641	21395	754
						12	^3B	21374	20875	-499
^{1}S	10	^1A_g	46345	46345	0	16	^1A	40840	40840	0

B.2 Spin–orbit inclusive Pr^{3+}–doped hosts

Table B.2 Energy levels for Irrep states in La_2O_3:Pr^{3+} at both S_6 and C_{3v} symmetry sites, and at CaF_2:Pr^{3+} O_h sites. Effective Hamiltonians have been fitted to experimentally observed levels for La_2O_3:Pr^{3+}, and to both experimental levels and *ab initio* levels for CaF_2:Pr^{3+}. All fits are to a spin–orbit inclusive level. All energies are in cm^{-1}.

	La_2O_3:Pr^{3+} S_6 site					La_2O_3:Pr^{3+} C_{3v} site					CaF_2:Pr^{3+} O_h site							
Multiplet	Irrep		Energy levels			Irrep		Energy levels			Irrep		Energy levels					
			Expt.	H_{CF}	ΔE			Expt.	H_{CF}	ΔE			*Ab initio*	H_{CF}	ΔE	Expt.	H_{CF}	ΔE
$^3H_4$	1	A_g	0	25	25	1	A_1	0	33	33	1	T_{2g}	0	-277	277	0	-17	-17
	1	E_g	110	146	36	1	E	110	150	40	1	A_{1g}	193	242	-49		498	
	2	E_g	472	430	-42	2	E	472	435	-37	1	E_g	386	179	206		668	
	2	A_g	573	523	-50	1	A_2	573	547	-26	1	T_{1g}	448	209	239	540	555	15
	3	A_g	644	643	-1	2	A_1	644	625	-19								
	3	E_g	707	724	17	3	E	707	712	5								
$^3H_5$	4	A_g	2215	2208	-7	2	A_2	2215	2210	-5	2	E_g	2121	2222	-101	2300	2314	14
	4	E_g	2247	2250	3	4	E	2247	2253	6	2	T_{1g}	2411	2179	232	2325	2323	-2
	5	E_g	2353	2387	34	5	E	2353	2389	36	3	T_{1g}	2695	2530	165		2678	
	5	A_g	2551	2521	-30	3	A_1	2551	2536	-15	2	T_{2g}	2750	2490	260	2693	2687	-6
	6	A_g	2635	2622	-13	3	A_2	2635	2603	-32								
	6	E_g	2676	2682	6	6	E	2676	2678	2								
	7	E_g		2772		7	E		2762									

Continued on next page...

Table B.2 *Continued*

	La_2O_3:Pr^{3+} S_6 site					La_2O_3:Pr^{3+} C_{3v} site					CaF_2:Pr^{3+} O_h site						
Multiplet	Irrep		Energy levels			Irrep		Energy levels			Irrep		Energy levels				
			Expt.	H_{CF}	ΔE			Expt.	H_{CF}	ΔE			*Ab initio*	H_{CF}	ΔE	Expt.	H_{CF}	ΔE
$^3H_6$	7	A_g	4292	4285	-7	4	A_1	4292	4290	-2	2	A_{1g}	4391	4479	-88		4405	
	8	E_g	4342	4344	2	8	E	4342	4347	5	3	T_{2g}	4664	4563	101	4279	4288	9
	9	E_g	4460	4469	9	9	E	4460	4469	9	4	T_{1g}	4773	4571	202		4517	
	8	A_g		4626		4	A_2		4643		3	E_g	4930	4953	-23		4838	
	9	A_g	4644	4692	48	5	A_1	4644	4660	16	4	T_{2g}	5065	4962	103	4889	4870	-19
	10	E_g		4837		10	E		4826		1	A_{2g}	5212	5051	161		5069	
	11	E_g	4916	4883	-33	11	E	4916	4876	-40								
	10	A_g		4951		5	A_2		4932									
	11	A_g		4978		6	A_1		4961									
$^3F_2$	12	E_g	5165	5154	-11	12	E	5165	5157	-8	4	E_g	5634	5356	278		5541	
	12	A_g		5284		7	A_1		5272		5	T_{2g}	5844	5325	519	5558	5564	-6
	13	E_g	5265	5269	4	13	E	5265	5291	26								
$^3F_3$	13	A_g	6479	6464	-15	8	A_1	6479	6459	-20	6	T_{2g}	7037	6688	349	6606	6607	1
	14	E_g	6526	6571	45	14	E	6526	6572	46	5	T_{1g}	7180	6848	332	6955	6955	0
	15	E_g	6612	6605	-7	15	E	6612	6607	-5	2	A_{2g}	7442	6952	490		7193	
	14	A_g		6549		6	A_2		6558									
	15	A_g		6676		7	A_2		6679									

Continued on next page...

Table B.2 *Continued*

Multiplet	La_2O_3:Pr^{3+} S_6 site					La_2O_3:Pr^{3+} C_{3v} site					CaF_2:Pr^{3+} O_h site						
	Irrep		Energy levels			Irrep		Energy levels			Irrep		Energy levels				
			Expt.	H_{CF}	ΔE			Expt.	H_{CF}	ΔE			*Ab initio*	H_{CF}	ΔE	Expt.	H_{CF}	ΔE
$^3F_4$	16	A_g	6949	6941	-8	9	A_1	6949	6946	-3	5	E_g	6769	7272	-503		7224	
	16	E_g	6949	6907	-42	16	E	6949	6911	-8	3	A_{1g}	7494	7510	-16		7510	
	17	E_g	7047	7062	15	17	E	7047	7061	14	6	T_{1g}	7499	7385	115	7367	7368	1
	17	A_g		7114		8	A_2		7110		7	T_{2g}	7755	7131	624		7331	
	18	E_g	7179	7191	12	18	E	7179	7182	3								
	18	A_g	7243	7259	16	10	A_1	7243	7251	8								
$^1G_4$	19	E_g	9771	9699	-72	19	E	9771	9712	-59	6	E_g	9742	10394	-652		9383	
	19	A_g	9771	9726	-45	11	A_1	9771	9744	-27	7	T_{1g}	10526	10704	-178		10367	
	20	E_g	9906	9925	19	20	E	9906	9917	11	4	A_{1g}	10733	11153	-420		11183	
	20	A_g		10058		9	A_2		10038		8	T_{2g}	10887	10217	670		9823	
	21	E_g	10184	10229	45	21	E	10184	10217	33								
	21	A_g	10364	10401	37	12	A_1	10364	10406	42								
$^1D_2$	22	E_g	16365	16354	-11	22	E	16365	16368	3	7	E_g	17820	18751	-931	16756	16771	15
	22	A_g	16829	16884	55	13	A_1	16829	16899	70	9	T_{2g}	20271	19297	974	17345	17330	-15
	23	E_g	16930	16877	-53	23	E	16930	16870	-60								
$^3P_0$	23	A_g	20274	20272	-2	14	A_1	20274	20268	-6	5	A_{1g}	24080	24256	-176	20855 [a]	20856	1
$^3P_1$	24	A_g		20717		10	A_2		20693		8	T_{1g}	24774	24986	-212		21482	
	24	E_g	20916	20921	5	24	E	20916	20920	4								

Continued on next page...

[a] This level is approximated using the centre of the indicated range of positions given by Carnall et al. [16].

Table B.2 *Continued*

	La_2O_3:Pr^{3+} S_6 site					La_2O_3:Pr^{3+} C_{3v} site					CaF_2:Pr^{3+} O_h site						
Multiplet	Irrep		Energy levels			Irrep		Energy levels			Irrep		Energy levels				
			Expt.	H_{CF}	ΔE			Expt.	H_{CF}	ΔE			*Ab initio*	H_{CF}	ΔE	Expt.	H_{CF}	ΔE
$^1I_6$	25	A_g		20686		15	A_1		20714		3	A_{2g}	23476	25671	-2195		21233	
	25	E_g	20741	20728	-13	25	E	20741	20731	-10	8	E_g	23849	25598	-1749		21250	
	26	E_g	20821	20850	29	26	E	20821	20845	24	6	A_{1g}	25462	26560	-1098		22613	
	26	A_g		20953		11	A_2		20938		10	T_{2g}	25983	25619	364		21244	
	27	A_g		21275		16	A_1		21266		11	T_{2g}	26668	26158	510		22175	
	27	E_g		21409		27	E		21387		9	T_{1g}	27142	26415	727		22357	
	28	E_g		21622		28	E		21600									
	28	A_g	21924	21907	-17	17	A_1	21924	21906	-10								
	29	A_g		21922		12	A_2		21918									
$^3P_2$	29	E_g	21924	21903	-21	29	E	21924	21897	-27	9	E_g	25896	26190	-294		22626	
	30	E_g	22168	22187	19	30	E	22168	22182	14	12	T_{2g}	27327	26417	910		22941	
	30	A_g		22267		18	A_1		22267									
$^1S_0$	31	A_g		46446		19	A_1		45993		7	A_{1g}	49455	49580	-125	46986 [b]	46986	0

[b] This level is taken from an observation of LaF_3:Pr^{3+}. The level in CaF_2:Pr^{3+} is typically obscured [16].

B.3 $^5D_{4/3} \rightarrow {}^7F_J$ emission of BaF_2:Tb^{3+}

Table B.3 *Ab initio* calculation and O_h symmetry crystal field fits to BaF_2:Tb^{3+}. All energies are in cm^{-1}.

			Fit to *ab initio* calc.			Fit to green emission			Fit to blue emission		
Multiplet	Irrep		*Ab initio*	H_{cf}	ΔE	$^5D_4 \rightarrow {}^7F_J$	H_{cf}	ΔE	$^5D_3 \rightarrow {}^7F_J$	H_{cf}	ΔE
$^7F_6$	1	E_g	0	32	-32	0	51	-51	0	135	-135
	1	T_{2g}	5	34	-29		51			131	
	1	A_{2g}	10	36	-26		51			122	
	2	T_{2g}	190	204	-14	300	332	-32	275	301	-26
	1	T_{1g}	225	232	-7		377			320	
	1	A_{1g}	265	267	-2		441			352	
$^7F_5$	2	T_{1g}	2040	2024	16	2370	2220	150	2270	2166	104
	2	E_g	2035	2024	11	2140	2220	-80	2035	2168	-133
	3	T_{1g}	2205	2172	33	2535	2455	80	2440	2301	139
	3	T_{2g}	2330	2299	30		2712			2473	
$^7F_4$	3	E_g	3320	3290	30	3440	3467	-27	3315	3315	-40
	4	T_{2g}	3320	3305	15	3670	3534	136	3575	3575	138
	4	T_{1g}	3510	3480	30		3802		3830	3584	246
	2	A_{1g}	3810	3780	30		4435			3949	

Continued on next page...

Table B.3 *Continued*

			Fit to *ab initio* calc.			Fit to green emission			Fit to blue emission		
Multiplet	Irrep		*Ab initio*	H_{cf}	ΔE	$^5D_4 \rightarrow {}^7F_J$	H_{cf}	ΔE	$^5D_3 \rightarrow {}^7F_J$	H_{cf}	ΔE
$^7F_3$	2	A_{2g}	4270	4289	-19	4385	4457	-72	4175	4314	-139
	5	T_{2g}	4395	4415	-20	4570	4660	-90	4510	4463	47
	5	T_{1g}	4460	4467	-7		4834			4516	
$^7F_2$	4	E_g	4980	5006	-26	5120	5112	-8	4975	4954	21
	6	T_{2g}	5315	5304	8		5925			5280	
$^7F_1$	6	T_{1g}	5660	5667	-7		6093		5460	5565	-105
$^7F_0$	3	A_{1g}	5880	5895	-15		6239		5630	5751	-121
$^5D_4$	7	T_{2g}	20845	20761	84	20620	20510	110		20636	
	5	E_g	20865	20832	33		20558			20655	
	7	T_{1g}	20865	20880	-15		20622			20694	
	4	A_{1g}	20870	20950	-80		20711			20749	
$^5D_3$	8	T_{1g}	26380	26325	55		26300			26218	
	8	T_{2g}	26345	26320	25		26304			26235	
	3	A_{2g}	26310	26411	-101		26354		26250	26236	14

B.4 CaF_2:Eu^{2+} Spin–free energy levels

Table B.4 Energy levels fitted to a spin–free *ab initio* calculation of CaF_2:Eu^{2+} [67]. All energies are in cm^{-1}.

	$4f^7$ configuration					$4f^6 5d$ configuration			
	Irrep	*Ab initio*	H_{CF}	ΔE		Irrep	*Ab initio*	H_{CF}	ΔE
Octet states:									
1	$^8A_{1u}$	0	659	-659	1	$^8T_{2g}$	28069	28983	-914
					2	$^8T_{1g}$	28472	29610	-1138
					3	$^8T_{1g}$	29682	30263	-581
					4	$^8T_{2g}$	30730	30978	-248
					1	^8E_g	29037	31509	-2472
					2	^8E_g	48072	47706	366
					5	$^8T_{1g}$	47991	48367	-376
					6	$^8T_{2g}$	48233	48435	-202
					7	$^8T_{1g}$	49120	49319	-199
					1	$^8A_{2g}$	51459	49400	2059
					8	$^8T_{2g}$	51056	49508	1548
					3	^8E_g	50814	49743	1071
					2	$^8A_{1g}$	51863	50029	1834
					9	$^8T_{1g}$	51459	51265	194
Sextet states:									
1	$^6T_{2u}$	29278	29406	-128	1	$^6T_{2g}$	32666	32814	-148
1	$^6T_{1u}$	33069	33135	-66	1	$^6T_{1g}$	35651	34020	1631
1	$^6A_{1u}$	33391	33157	235	2	$^6T_{2g}$	36376	34639	1737
2	$^6T_{1u}$	33714	33198	516	2	$^6T_{1g}$	38474	36012	2462
1	^6E_u	33553	33206	347	1	^6E_g	36296	36639	-343
1	$^6A_{2u}$	33714	33216	498	3	$^6T_{2g}$	50895	51433	-538
2	$^6T_{2u}$	33633	33695	-61	2	^6E_g	50895	52740	-1845
3	$^6T_{1u}$	35730	35498	232	3	$^6T_{1g}$	51137	53235	-2098
2	^6E_u	35811	35525	286	4	$^6T_{2g}$	55734	53753	1981
3	$^6T_{2u}$	47909	48406	-497	4	$^6T_{1g}$	56621	54245	2376
4	$^6T_{1u}$	48313	49113	-800	1	$^6A_{1g}$	51056	54498	-3442
2	$^6A_{1u}$	48716	49188	-472	1	$^6A_{2g}$	51298	54681	-3383
3	^6E_u	48071	49924	-1854	3	^6E_g		54976	
2	$^6A_{2u}$	54039	49937	4102	5	$^6T_{2g}$	56541	55873	668
5	$^6T_{1u}$	49119	49968	-849					
4	$^6T_{2u}$	49845	50248	-403					
5	$^6T_{2u}$	54120	54259	-139					
4	^6E_u		54315						
6	$^6T_{1u}$	54523	54404	119					

Continued on next page...

Table B.4 *Continued*

	$4f^7$ configuration				$4f^6 5d$ configuration		
Irrep	*Ab initio*	H_{CF}	ΔE	Irrep	*Ab initio*	H_{CF}	ΔE
6 $^6T_{2u}$	54362	54768	-407				

B.5 CaF_2:Eu^{2+} Spin–orbit energy levels

Table B.5 Energy levels fitted to a full spin–orbit level *ab initio* calculation of CaF_2:Eu^{2+} [67]. Effective Hamiltonian energy levels without a corresponding reference energy level have been omitted. All energies are in cm^{-1}.

Irrep		*Ab initio*	H_{CF}	ΔE	Irrep		*Ab initio*	H_{CF}	ΔE
$4f^7$:									
1	Γ_{6u}	0	0	0					
1	Γ_{8u}	0	0	0					
1	Γ_{7u}	0	0	0					
$4f^6 5d\,(e_g)$:					$4f^6 5d\,(t_{2g})$:				
1	Γ_{8g}	25407	26253	-846	34	Γ_{8g}	46217	46144	73
1	Γ_{7g}	25407	26406	-999	35	Γ_{8g}	47104	46344	760
2	Γ_{8g}	25730	26496	-767	17	Γ_{6g}	47104	46744	359
2	Γ_{7g}	26859	26861	-2	36	Γ_{8g}	47668	46804	865
1	Γ_{6g}	26456	27063	-608	17	Γ_{7g}	46217	46856	-640
3	Γ_{8g}	26859	27100	-241	18	Γ_{6g}	47668	47259	409
4	Γ_{8g}	26940	27464	-525	18	Γ_{7g}	47749	47313	436
2	Γ_{6g}	27504	27519	-15	37	Γ_{8g}	47749	47456	293
5	Γ_{8g}	27504	27655	-151	38	Γ_{8g}	48152	47857	296
6	Γ_{8g}	27907	27881	26	39	Γ_{8g}	48233	47977	256
3	Γ_{7g}	27907	27944	-36	19	Γ_{6g}	48152	48038	114
7	Γ_{8g}	28311	28008	303	19	Γ_{7g}	48314	48104	209
3	Γ_{6g}	27665	28068	-403	40	Γ_{8g}	48233	48111	122
8	Γ_{8g}	28311	28566	-255	41	Γ_{8g}	48394	48330	65
4	Γ_{7g}	28230	28624	-394	20	Γ_{7g}	48798	48376	422
4	Γ_{6g}	28472	28631	-159	20	Γ_{6g}	48394	48554	-160
5	Γ_{6g}	29359	28820	539	42	Γ_{8g}	48798	48582	215
9	Γ_{8g}	28472	28834	-362	43	Γ_{8g}	48878	48672	207
5	Γ_{7g}	28553	28862	-310	21	Γ_{7g}	49040	48694	346
10	Γ_{8g}	29279	28924	354	21	Γ_{6g}	48878	48739	140
6	Γ_{6g}	29440	29372	68	22	Γ_{7g}	49443	48836	607

Continued on next page...

Table B.5 *Continued*

Irrep		*Ab initio*	H_{CF}	ΔE	Irrep		*Ab initio*	H_{CF}	ΔE
11	Γ_{8g}	29521	29473	47	44	Γ_{8g}	49040	48870	170
6	Γ_{7g}	29279	29514	-235	45	Γ_{8g}	49282	49153	128
12	Γ_{8g}	29521	29685	-164	22	Γ_{6g}	49201	49201	0
13	Γ_{8g}	30085	29807	278	23	Γ_{7g}	49766	49368	398
7	Γ_{7g}	30327	30044	284	46	Γ_{8g}	49362	49383	-21
14	Γ_{8g}	30327	30076	251	23	Γ_{6g}	49604	49486	119
7	Γ_{6g}	30811	30104	707	47	Γ_{8g}	49766	49507	258
15	Γ_{8g}	30650	30424	226	48	Γ_{8g}	49846	49640	206
16	Γ_{8g}	31295	30530	765	24	Γ_{7g}	49927	49719	208
8	Γ_{6g}	30811	30544	267	25	Γ_{7g}	50008	49788	219
9	Γ_{6g}	31376	30702	674	49	Γ_{8g}	49927	49795	132
17	Γ_{8g}	31295	30780	515	24	Γ_{6g}	49846	49858	-12
8	Γ_{7g}	30650	30816	-167	50	Γ_{8g}	50008	49954	54
18	Γ_{8g}	31376	30838	537	51	Γ_{8g}	50088	50043	45
9	Γ_{7g}	31860	31291	569	52	Γ_{8g}	50169	50203	-34
19	Γ_{8g}	31860	31408	452	25	Γ_{6g}	50088	50204	-116
					53	Γ_{8g}	50169	50471	-302
					26	Γ_{6g}	50250	50518	-268
					26	Γ_{7g}	50250	50565	-315
					54	Γ_{8g}	50330	50688	-358
					27	Γ_{7g}	50491	50699	-208
					55	Γ_{8g}	50572	50783	-211
					27	Γ_{6g}	50653	50834	-181
					56	Γ_{8g}	50572	50939	-367
					28	Γ_{7g}	50653	50947	-295
					57	Γ_{8g}	50733	51096	-363
					28	Γ_{6g}	50814	51114	-300
					58	Γ_{8g}	51137	51172	-35
					59	Γ_{8g}	51217	51342	-124
					29	Γ_{7g}	51298	51553	-255
					29	Γ_{6g}	50975	51765	-790
					60	Γ_{8g}	51298	51786	-488
					31	Γ_{7g}	51379	51893	-514
					30	Γ_{6g}	51217	51975	-758
					63	Γ_{8g}	51379	52071	-692

References

[1] B. Henderson and G. F. Imbusch, *Optical spectroscopy of inorganic solids.* Clarendon Press, Oxford, 1989.

[2] D. J. Newman and B. K. C. Ng, *Crystal Field Handbook.* Cambridge, UK: Cambridge University Press, 2000.

[3] B. Wybourne, *Spectroscopic Properties of Rare Earths.* New York: John Wiley and Sons, Inc., 1965.

[4] J. L. Pascual, J. Schamps, Z. Barandiarán, and L. Seijo, "Large anomalies due to insufficiency of Madelung embedding in *ab initio* calculations of $4f-5d$ and $4f-6s$ excitations of lanthanides in ionic crystals: The BaF_2:Ce^{3+} crystal," *Phys. Rev. B*, vol. 74, p. 104105, 2006.

[5] G. Sánchez-Sanz, L. Seijo, and Z. Barandiarán, "Yb^{2+}-doped $SrCl_2$: Electronic structure of impurity states and impurity-trapped excitons," *J. Chem. Phys.*, vol. 133, p. 114509, 2010.

[6] G. Sánchez-Sanz, L. Seijo, and Z. Barandiarán, "Electronic spectra of Yb^{2+}-doped $SrCl_2$," *J. Chem. Phys.*, vol. 133, p. 114506, 2010.

[7] C.-K. Duan and P. A. Tanner, "What use are crystal field parameters? A chemist's viewpoint," *J. Phys. Chem. A*, vol. 114, pp. 6055–6062, 2010.

[8] L. Hu, M. F. Reid, C.-K. Duan, S. Xia, and M. Yin, "Extraction of crystal-field parameters for lanthanide ions from quantum-chemical calculations," *J. Phys.-Condens. Mat.*, vol. 23, p. 045501, 2011.

[9] M. Grinberg and S. Mahlik, "Impurity-trapped excitons: Experimental evidence and theoretical concept," *J. Non-Cryst. Solids*, vol. 354, pp. 4163–4169, 2008.

[10] S. V. Eliseeva and J.-C. G. Bünzli, "Rare earths: jewels for functional materials of the future," *New J. Chem.*, vol. 35, pp. 1165–1176, 2011.

[11] M. Nilsson, L. Rippe, N. Ohlsson, T. Christiansson, and S. Kröll, "Initial experiments concerning quatum information processing in rare-earth-ion doped crystals," *Phys. Scr.*, pp. 178–185, 2002.

[12] J.-C. G. Bünzli and S. V. Eliseeva, "Intriguing aspects of lanthanide luminescence," *Chem. Sci.*, vol. 4, pp. 1939–1949, 2013.

[13] W. Carnall, G. Goodman, K. Rajnak, and R. Rana, "A systematic analysis of the spectra of the lanthanides doped into single crystal LaF_3," *J. Chem. Phys.*, vol. 90, pp. 3443–3457, 1989.

[14] G. Liu, "Electronic Energy Level Structure," in *Spectroscopic Properties of Rare Earths in Optical Materials*, G. Liu and B. Jacquier, Eds. Springer, 2005, ch. 1, pp. 95–127.

[15] P. Dorenbos, "The 5d level positions of the trivalent lanthanides in inorganic compounds," *J. Lumin.*, vol. 91, pp. 155–176, 2000.

[16] W. Carnall, P. Fields, and R. Sarup, "$^1S_0$ level of Pr^{3+} in crystal matrices and energy-level parameters for the $4f^2$ configuration of Pr^{3+} in LaF_3," *J. Chem. Phys.*, vol. 51, pp. 2587–2591, 1969.

[17] G. H. Dieke, H. M. Crosswhite, and H. Crosswhite, *Spectra and Energy Levels of Rare Earth Ions in Crystals.* New York: Interscience Publishers, Inc., 1968.

[18] L. van Pieterson, M. F. Reid, R. T. Wegh, S. Soverna, and A. Meijerink, "$4f^n \rightarrow 4f^{n-1}5d$ transitions of the light lanthanides: experiment and theory," *Phys. Rev. B*, vol. 65, pp. 045 113–1–16, 2002.

[19] L. van Pieterson, M. F. Reid, G. W. Burdick, and A. Meijerink, "$4f^n \rightarrow 4f^{n-1}5d$ transitions of the heavy lanthanides: experiment and theory," *Phys. Rev. B*, vol. 65, pp. 045 114–1–13, 2002.

[20] M. F. Reid, L. van Pieterson, and A. Meijerink, "Trends in parameters for the $4f^N \leftrightarrow 4f^{N-1}5d$ spectra of lanthanide ions in crystals," *J. Alloy Compd.*, vol. 344, pp. "240–245", 2002.

[21] C. A. Morrison and R. P. Leavitt, "Many-body calculations for the heavy atoms," *J. Chem. Phys.*, vol. 71, p. 2366, 1979.

[22] K. Ogasawara, S. Watanabe, H. Toyoshima, T. Ishii, M. G. Brik, H. Ikeno, and I. Tanaka, "Optical spectra of trivalent lanthanides in $LiYF_4$ crystal," *J. Solid State Chem.*, vol. 178, pp. 412–418, 2005.

[23] R. D. Cowan, *The Theory of Atomic Structure and Spectra*. Berkeley and Los Angeles, California: University of California Press, 1981.

[24] M. F. Reid, J.-P. R. Wells, R. J. Reeves, P. S. Senanayake, A. Reynolds, A. Meijerink, G. Bellochi, G. Berden, B. Redlich, L. van der Meer, and C.-K. Duan, "Excited-state structure and dynamics of high-energy states in lanthanide materials," Conference presentation slides, 2010.

[25] D. S. McClure and C. Pedrini, "Excitons trapped at impurity centers in highly ionic crystals," *Phys. Rev. B*, vol. 32, pp. 8465–8468, 1985.

[26] D. S. McClure and C. Pedrini, "Photoionization of divalent rare earth ions in fluorite-type crystals," *J. de Physique*, vol. 46, pp. 397–401, 1985.

[27] P. Dorenbos, "Anomalous luminescence of Eu^{2+} and Yb^{2+} in inorganic compounds," *J. Phys.-Condens. Mat.*, vol. 15, pp. 2645–2665, 2003.

[28] B. Moine, B. Courtois, and C. Pedrini, "Luminescence and photoionization processes of Yb^{2+} in CaF_2, SrF_2 and BaF_2," *J. de Physique*, vol. 50, p. 2105, 1989.

[29] B. Moine, B. Courtois, and C. Pedrini, "Photoconductivity and fluorescence properties of divalent ytterbium ions in fluoride crystals," *J. Lumin.*, vol. 48-49, pp. 501–504, 1991.

[30] B. Moine, C. Pedrini, and B. Courtois, "Photoionization and luminescences in BaF_2:Eu^{2+}," *J. Lumin.*, vol. 50, pp. 31–38, 1991.

[31] B. Moine, B. Courtois, and C. Pedrini, "Fluorescence, photoconductivity and polarization properties of divalent rare earth ions in fluoride crystals," *J. Lumin.*, vol. 45, pp. 248–250, 1990.

[32] C. Pedrini, M. F. Joubert, and D. S. McClure, "Photoionization processes of rare-earth dopant ions in ionic crystals," *J. Lumin.*, vol. 125, p. 230, 2007.

[33] E. G. Reut, "Nature of luminescence of divalent Eu and Yb ions in fluorite-type crystals," *Opt. Spectr.*, vol. 40, pp. 55–57, Jan 1976.

[34] A. A. Kaplyanskii, V. N. Medvedev, and P. L. Smolyanskii, "Spectra, kinetics, and polarization of the luminescence of CaF_2:Yb^{2+} crystals," *Opt. Spectr.*, vol. 41, pp. 615–619, Dec 1976.

[35] Z. Barandiarán and L. Seijo, "Intervalence charge transfer luminescence: Interplay between anomalous and $5d-4f$ emissions in Yb-doped fluorite-type crystals," *J. Chem. Phys.*, vol. 141, p. 234704, 2014.

[36] B. Ordejon, L. Seijo, and Z. Barandiarán, "Geometry and electronic structure of impurity-trapped excitons in Cs_2GeF_6 : U^{4+} crystals. The 5f(1)7s(1) manifold," *J. Chem. Phys.*, vol. 126, p. 194712, 2007.

[37] R. B. Hughes-Currie, "Spectroscopy of excitons in ytterbium-doped flouride lattices," Ph.D. dissertation, University of Canterbury, 2015.

[38] P. S. Senanayake, "Two-colour excitation of impurity trapped excitons in wide bandgap insulators," Ph.D. dissertation, University of Canterbury, 2013.

[39] P. S. Senanayake, J.-P. R. Wells, M. F. Reid, G. Berden, A. Meijerink, and R. J. Reeves, "Impurity-trapped excitons and electron traps in CaF_2:Yb^{2+} and SrF_2:Yb^{2+} probed by transient photoluminescence enhancement," *J. Lumin.*, vol. 133, pp. 81–85, 2013.

[40] M. F. Reid, P. S. Senanayake, J.-P. R. Wells, G. Berden, A. Meijerink, A. J. Salkeld, C.-K. Duan, and R. J. Reeves, "Transient photoluminescence enhancement as a probe of the structure of impurity-trapped excitons in CaF_2:Yb^{2+}," *Phys. Rev. B*, vol. 84, p. 113110, 2011.

[41] B. Judd, *Operator Techniques in Atomic Spectroscopy.* Princeton, New Jersey: Princeton University Press, 1998.

[42] E. U. Condon and G. H. Shortley, *The Theory of Atomic Spectra.* London: Cambridge University Press, 1935.

[43] G. Karlstrom, R. Lindh, P. Malmqvist, B. Roos, U. Ryde, V. Veryazov, P. Widmark, M. Cossi, B. Schimmelpfennig, P. Neogrady, and L. Seijo, "MOLCAS: a program package for computational chemistry," *Comp. Mater. Sci.*, vol. 28, no. 2, pp. 222–239, Oct 2003.

[44] J. L. Pascual, Z. Barandiarán, and L. Seijo, "Ab initio theoretical study of the $4f^8$ and $4f^7 5d$ manifolds of Tb^{3+}-doped BaF_2 cubic sites," *J. Lumin.*, vol. 145, pp. 808–817, 2014.

[45] B. Ordejon, V. Vallet, J.-P. Flament, L. Seijo, and Z. Barandiarán, "The $5f^16d^1 \rightarrow 5f^2$ luminescence spectrum of U^{4+} in Cs_2GeF_6 crystals – A quantum chemical study," *J. Lum.*, vol. 126, pp. 779–783, 2007.

[46] M. F. Reid, C.-K. Duan, and H. Zhou, "Crystal-field parameters from *ab initio* calculations," *J. Alloys Comp.*, vol. 488, pp. 591 – 594, 2009.

[47] J. Wen, L. Ning, C.-K. Duan, Y. Chen, Y. Zhang, and M. Yin, "A theoretical study on the structure and energy spectral properties of Ce^{3+} ions doped in various fluoride compounds," *J. Phys. Chem. C*, vol. 116, pp. 20 513–20 521, 2012.

[48] J. Wen, C.-K. Duan, L. Ning, Y. Huang, S. Zhan, J. Zhang, and M. Yin, "Spectroscopic distinctions between two types of Ce^{3+} ions in X2-Y_2SiO_5: A theoretical investigation," *J. Phys. Chem. A*, vol. 118, pp. 4988–4994, 2014.

[49] J. Wen, M. F. Reid, L. Ning, J. Zhang, Y. Zhang, C.-K. Duan, and M. Yin, "*Ab-initio* calculations of Judd-Ofelt intensity parameters for transitions between crystal-field levels," *J. Lumin.*, vol. 152, pp. 54–57, 2014.

[50] C.-K. Duan, M. F. Reid, and S. Xia, "Parameterized analysis of the ab initio calculation of Pr^{3+} energy levels," *J. Lumin.*, vol. 122, pp. 939–941, 2007.

[51] I. Lindgren and J. Morrison, *Atomic Many-Body Theory*, 2nd ed. Springer-Verlag Berlin Heidelberg, 1986.

[52] M. Weissbluth, *Atoms and Molecules*. New York: Academic Press, 1978.

[53] M. F. Reid and D. J. Newman, "Correlation crystal fields," in *Crystal Field Handbook*, D. J. Newman and B. Ng, Eds. Cambridge University Press, 2000, ch. 6, pp. 122–141.

[54] G. W. Burdick and M. F. Reid, "$4f^N \rightarrow 4f^{N-1}5d$ transitions," in *Handbook on the Physics and Chemistry of the Rare Earths*, K. A. Gschneidner Jr., J. C. Bunzli, and V. K. Percharsky, Eds. North Holland, 2007, vol. 37, ch. 232, pp. 61–91.

[55] K. R. Lea, M. J. M. Leask, and W. P. Wolf, "Raising of angular momentum degeneracy of f-electron terms by cubic crystal fields," *J. Phys. Chem. Solids*, vol. 23, no. Oct, pp. 1381–1405, 1962.

[56] G. Liu and B. Jacquier, Eds., *Spectroscopic Properties of Rare Earths in Optical Materials*. Springer, 2005.

[57] F. Auzel and O. L. Malta, "A scalar crystal field strength parameter for rare earth ions: meaning and usefulness," *J. de Physique*, vol. 44, pp. 201–206, 1983.

[58] E. Antic-Fidancev, J. Hölsä, and M. Lastusaari, "Crystal field energy levels of Eu^{3+} and Yb^{3+} in the C_2 and S_6 sites of the cubic C-type R_2O_3," *J. Phys.-Condens. Mat.*, vol. 15, pp. 863–876, 2003.

[59] M. F. Reid and F. S. Richardson, "Free-ion, crystal-field, and spin-correlated crystal-field parameters for lanthanide ions in $Cs_2NaLnCl_6$ and Cs_2NaYCl_6:Ln^{3+} systems," *J. Chem. Phys.*, vol. 83, pp. 3831–3836, Oct 1985.

[60] C. W. Nielson and G. F. Koster, *Spectroscopic coefficients for the p^n, d^n and f^n configurations*. Cambridge, Mass.: MIT Press, 1963.

[61] M. Blume and R. E. Watson, "Theory of spin-orbit coupling in atoms .1. derivation of spin-orbit coupling constant," *P. Roy. Soc. Lond. A Mat.*, vol. 270, no. 1340, pp. 127–143, 1962.

[62] J. E. Hansen, B. R. Judd, and H. Crosswhite, "Matrix elements of scalar three-electron operators for the atomic f shell," *Atomic Data and Nuclear Data Tables*, vol. 62, pp. 1–49, 1996.

[63] M. F. Reid, "Correlation crystal field analyses with orthogonal operators," *J. Chem. Phys.*, vol. 87, pp. 2875–2884, 1987.

[64] M. F. Reid, "Transition intensities," in *Spectroscopic Properties of Rare Earths in Optical Materials*, G. Liu and B. Jacquier, Eds. Springer, 2005, ch. 2, pp. 95–127.

[65] G. W. Burdick, A. Burdick, V. Deev, C.-K. Duan, and M. F. Reid, "Simulation of two-photon absorption spectra of Eu^{2+}: CaF_2 by direct calculation," *J. Lumin.*, vol. 118, no. 2, pp. 205–219, Jun 2006.

[66] P. H. Butler, *Point Group Symmetry Applications*. Plenum Press, 1981.

[67] F. Aiga, R. Hiramatsu, and K. Ishida, "Ab initio theoretical study of $4f \rightarrow 5d$ transitions in Eu^{2+}-doped CaF_2," *J. Lumin.*, vol. 145, pp. 951–955, Jan 2014.

[68] M. Krośnicki, A. Kędziorski, L. Seijo, and Z. Barandiarán, "Ab initio theoretical study on the $4f^2$ and $4f5d$ electronic manifolds of cubic defects in CaF_2:Pr^{3+}," *J. Phys. Chem. A*, vol. 118, pp. 358–368, 2014.

[69] L. Seijo and Z. Barandiarán, "Relativistic *ab-initio* model potential calculations for molecules and embedded clusters," in *Theoretical and Computational Chemistry*, P. Schwerdtfeger, Ed. Elsevier, 2004, vol. 14, ch. 7, pp. 417–475.

[70] G. Sánchez-Sanz, L. Seijo, and Z. Barandiarán, "Spin-forbidden and spin-enabled $4f^{14} \rightarrow 4f^{13}5d^{1}$ transitions of Yb^{2+}-doped $CsCaBr_3$," *J. Chem. Phys.*, vol. 131, p. 024505, 2009.

[71] Z. Pan, C.-K. Duan, and P. A. Tanner, "Electronic spectra and crystal field analysis of Yb^{2+} in $SrCl_2$," *Phys. Rev. B*, vol. 77, p. 085114, 2008.

[72] Z. Barandiarán, G. Sánchez-Sanz, and L. Seijo, "Electronic structure of Yb^{2+}-doped $SrCl_2$ and $CsCaBr_3$," Private Communication, 2012.

[73] A. J. Salkeld, M. F. Reid, J.-P. R. Wells, G. Sánchez-Sanz, L. Seijo, and Z. Barandiarán, "Effective Hamiltonian parameters for ab initio energy-level calculations of $SrCl_2$:Yb^{2+} and $CsCaBr_3$:Yb^{2+}," *J Phys.-Condens. Mat.*, vol. 25, no. 41, OCT 2013.

[74] T. S. Piper, J. P. Brown, and D. S. McClure, "fd and $f^{13}d$ configurations in a crystal field and spectrum of Yb^{2+} in cubic crystals," *J. Chem. Phys.*, vol. 46, p. 1353, 1967.

[75] C. E. Schaffer and C. K. Jorgensen, "The nephelauxetic series of ligands corresponding to increasing tendency of partly covalent bonding," *J. Inorg. Nucl. Chem.*, vol. 8, pp. 143 – 148, 1958.

[76] D. J. Newman and B. Ng, "The superposition model of crystal fields," *Rep. Prog. Phys.*, vol. 52, pp. 699–763, 1989.

[77] R. B. Hughes-Currie, A. J. Salkeld, K. V. Ivanovskikh, M. F. Reid, J.-P. R. Wells, and R. J. Reeves, "Excitons and interconfigurational transitions in CaF_2:Yb^{2+} crystals," *J. Lumin.*, vol. 158, pp. 197–202, Feb 2015.

[78] R. W. G. Wyckoff, *Crystal Structures*. New York: Interscience Publishers, Inc., 1963, vol. 1,2.

[79] Z. Barandiarán and L. Seijo, "Electronic structure of Yb^{2+}-doped CaF_2," Private Communication, 2014.

[80] P. S. Senanayake, J.-P. R. Wells, M. F. Reid, R. B. Hughes-Currie, G. Berden, R. J. Reeves, and A. Meijerink, "Frequency non-degenerate sequential excitation of the impurity trapped exciton in strontium fluoride crystals doped with ytterbium," *J. Appl. Phys.*, vol. 117, p. 133109, 2015.

[81] S. Mahlik, A. Lazarowska, M. Grinberg, J.-P. R. Wells, and M. F. Reid, "Pressure dependence of the emission in CaF_2:Yb^{2+}," *J. Phys.-Condens. Mat.*, vol. 27, p. 305501, 2015.

[82] J. L. Pascual, Z. Barandiarán, and L. Seijo, "Ab initio theoretical study of luminescence properties of Pr^{3+}-doped Lu_2O_3," *Theor. Chem. Acc.*, vol. 129, pp. 545–554, 2011.

[83] J. L. Pascual, Z. Barandiarán, and L. Seijo, "Relation between high-pressure spectroscopy and $f^{n-1}d^1$ excited-state geometry: A comparison between theoretical and experimental results in SrF_2:Sm^{2+}," *Phys. Rev. B*, vol. 76, p. 104109, 2007.

[84] O. K. Moune, M. D. Faucher, C. K. Jayasankar, and A. M. Lejus, "Electronic transisitions, crystal field analysis and anomalous levels splittings in the optical spectrum of Pr^{3+} in La_2O_3 and Pr_2O_3," *J. Lumin.*, vol. 85, pp. 59–70, 1999.

[85] J. C. Morrison and K. Rajnak, "Many-body calculations for the heavy atoms," *Phys. Rev. A*, vol. 4, pp. 536–542, Aug 1971. [Online]. Available: http://link.aps.org/doi/10.1103/PhysRevA.4.536

[86] M. Witkowski and A. J. Wojtowicz, "High and low spin energy states of the Tb^{3+} $4f^7 5d$ configuration in BaF_2," *Opt. Mat.*, vol. 33, pp. 1535–1539, 2010.

[87] M. J. Lee, M. F. Reid, M. D. Faucher, and G. W. Burdick, "Comparison between correlation crystal field calculations using extended basis sets and two-electron operators," *J. Alloys Compd.*, vol. 323–324, pp. 636–639, 2001.

Publications

Chapter 4

The results of Chapter 4 were published in the paper:

Salkeld, A.J., Reid, M.F., Wells, J-P.R., Sanchez-Sanz, G., Seijo, L. and Barandiaran, Z. (2013) "Effective Hamiltonian parameters for ab initio energy-level calculations of $SrCl_2$:Yb^{2+} and $CsCaBr_3$:Yb^{2+}." *Journal of Physics: Condensed Matter* 25(41): 415504.

Chapter 5

Part of the analysis in Chapter 5 contributed to the paper:

Hughes-Currie, R.B., Salkeld, A.J., Ivanovskikh, K.V., Reid, M.F., Wells, J-P.R. and Reeves, R.J. (2015) "Excitons and interconfigurational transitions in CaF_2:Yb^{2+} crystals." *Journal of Luminescence* 158: 197-202.

Parts of this work were also presented at DPC'13:

Salkeld, A.J., Hughes-Currie, R.B., Senanayake, P.S., Ivanovskikh, K.V., Reid, M.F., Wells, J-P.R., Reeves, R.J. and Meijerkink, A. (2013) "Energy levels and dynamics of CaF_2:Yb^{2+} under UV and VUV excitation." Fuzhou, China: 18^{th} International Conference on Dynamical Processes in Excited States of Solids (DPC'13), 4-9 Aug 2013.

Chapter 6

A manuscript based on the results of Chapter 6 is in preparation.